Diffractive production of vector mesons in Deep Inelastic Scattering within k_t-factorization approach

Dissertation

zur

Erlangung des Doktorgrades (Dr. rer. nat.)

der

Mathematisch-Naturwissenschaftlichen Fakultät

der

Rheinischen Friedrich-Wilhelms-Universität Bonn

vorgelegt von

Igor Ivanov

aus

Russland

Bonn 2002

Angefertigt am Institut für Kernphysik
des Forschungszentrums Jülich GmbH

mit Genehmigung der Mathematisch-Naturwissenschaftlichen Fakultät der
Rheinischen Friedrich-Wilhelms-Universität Bonn

1. Referent: Prof. Dr. J. Speth

2. Referent: Prof. Dr. H.R. Petry

Tag der Promotion:

Abstract

In this work we give a theoretical description of the elastic vector meson production in diffractive DIS developed within the k_t-factorization formalism. Since the k_t-factorization scheme does not require large values of $Q^2+m_V^2$, we conduct an analysis that is applicable to all values of Q^2 from photo- up to highly virtual production of vector mesons. The basic quantity in this approach — the unintegrated gluon structure function — was for the first time extracted from the experimental data on F_{2p}, thoroughly investigated, and consistently used in the vector meson production calculation. Moreover, by limiting ourselves to the lowest Fock state of the vector meson, we were able to construct in a closed form the theory of spin-angular coupling in the vector meson. This allowed us for the first time to address the production of a vector meson in a given spin-angular state. We performed an extensive analytical and numerical investigation of the properties of $1S$, $2S$, and D-wave vector meson production reactions. Treating the physical ground state vector mesons as purely $1S$ states, we observed a good overall agreement with all available experimental data on vector meson production. For the excited states, our analysis predicts a picture which is remarkably different from $1S$-state, so that such reactions can be regarded as potential sources of new information on the structure of excited states in vector mesons.

to

Claudia I

and

Claudia II

Contents

Chapter 1

Introduction

In the past 30 years particle physics theory has proved numerous times to provide a good, consistent, unified description of the great variety of nuclear, low and high energy particle physics experiments. Being based on the ideas of quantum field theory, gauge approach to fundamental interactions, symmetry and naturalness considerations, the Standard Model has managed to explain virtually all phenomena in electromagnetic, weak and strong interactions, and to predict new particles and effects. Although questions of fundamental origin lie beyond the scope of the Standard Model, its precision in description, for example, electromagnetic phenomena, reaches the magnitude of 10^{-10}.

However, the current situation is not that optimistic in the domain of strong interactions. The gauge–based formulation — Quantum Chromodynamics (QCD) — seems to offer a reasonably good description only of sufficiently energetic processes (more accurately, only when every vertex involves at least one highly virtual particle), thanks to asymptotic freedom. The major difficulty lies in the behavior of the QCD coupling constant $\alpha_s(Q^2)$, which exhibits infrared growth and becomes comparable to unity at $Q^2 \sim 1$ GeV^2. The net result is that perturbation theory — the most successful treatment of various high-energy processes — fails to give even qualitative description of low-energy, essentially non-perturbative phenomena. Additional difficulties arise from the non-abelian nature of QCD, chiral symmetry breaking, non-trivial QCD vacuum, instantons etc.

On the other hand, many separate concepts have been developed that do not rely on perturbative QCD (pQCD) and provide reasonably good description of phenomena in their applicability regions. The fundamental problem of the theory of strong interactions is that these heterogeneous approaches do not match[1]. They do not comprise a unified picture of strong interactions. Given such a lack of universal, rigorously derived results, one must admit that the subject of our investigation belongs to the realm of phenomenology rather than rigorous theory.

[1] Just one example of poor accordance among various approaches: the quark generated ladder diagrams do not appear to correspond uniquely to any of the experimentally observed Regge trajectories. Another example is the vague status of $\alpha_s = \text{const}$ Balitskii-Fadin-Kuraev-Lipatov equation (BFKL) results in true QCD.

1.1 Diffractive processes and pomeron

In the light of these problems, the careful examination of regions where two or more approaches overlap (or conversely, where none of the concepts exhausts the interaction) are of great interest. Diffractive Deep Inelastic Scattering (DIS) is exactly one of these fields.

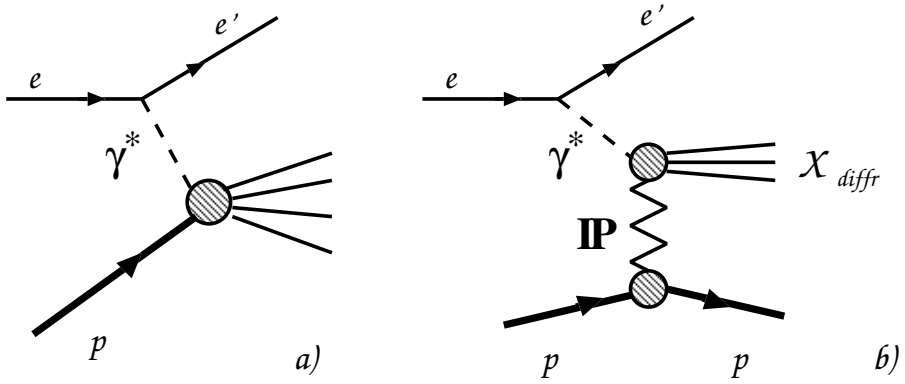

Figure 1.1: Examples of deep inelastic scattering process: *(a)* hard DIS and *(b)* diffractive DIS. In the latter case $M^2_{diffr} \ll s$ and the process proceeds via pomeron t-channel exchange.

A typical hard DIS process (Fig.1.1a) occurs when a virtual photon[2] strikes a proton to produce a hard system X with large invariant mass squared[3] s and large enough multiplicity, final state hadrons being distributed over whole rapidity range approximately smoothly.

However, as was noted long ago, sometimes the proton survives, being only slightly deflected, and a virtual photon turns into a so-called diffractive system X_{diffr} with invariant mass $M^2_{diffr} \ll s$. In this process the proton and the diffractive system are naturally separated by a large rapidity gap. A condition necessary for the rapidity gap formation is $Q^2 \ll s$, or in terms of Bjorken x

$$x = \frac{Q^2}{s} \ll 1\,. \tag{1.1}$$

This is one of the most common cases of diffractive DIS (DDIS) processes. In fact, the class of diffractive processes is not confined to DIS; it is much broader. There are many other reactions which possess the generic features — the rapidity gap and smallness of M^2_{diffr} — and therefore can be classified as diffractive processes (for a recent review see [1]).

How can a typical diffractive process occur? Certainly, it must be a kind of peripheral interaction: if the photon struck directly one of the valence quarks, the proton would 'explode', providing no way for the large rapidity gap formation. What remains is the possibility of the t–channel exchange by a not-too-energetic 'particle' (Fig.1.1b), which would be a natural mechanism of the experimentally observed weak proton deflection and small M^2_{diffr}. Further experimental features suggest that this 'particle' should be chargeless and colorless, its interaction with other particles should be of strong (not electromagnetic or weak) nature, its 'propagation' should be independent of the specific process (γp, $\gamma\gamma$, pp, $p\bar{p}$, etc), and it should

[2]We will always imply that the virtual photon is emitted by an electron, which means the photon is always space-like: if q is the photon momentum, then $Q^2 \equiv -q^2 > 0$.

[3]In hard DIS phenomenology this quantity is usually labeled W^2. However, for simplicity, we will use notation s.

be of spin 1, due to the approximately s-independent pp cross section. In the early 60s this 'particle' was dubbed *pomeron* (symbol $\mathbb{P}$).

Further properties come from combining the Regge picture and BFKL results with experimental observations (for a detailed review of Regge theory see [2]). They include, first of all, the asymptotic equality of total pp and $p\bar{p}$ cross sections (the Pomeranchuk theorem). Formulated long ago, it was experimentally verified only recently. Then, the Regge theory predicts the power-like s-dependence of the total pp cross section $\sigma \propto s^{2(\alpha_{\mathbb{P}}-1)}$, which has also been experimentally observed, with intercept $\delta_{\mathbb{P}} \equiv \alpha_{\mathbb{P}} - 1 \approx 0.08$. On the other hand, the BFKL equation [3, 4] succeeded in reproducing such power-like dependence in QCD, but in the simple case $\alpha_s = \text{const}$. In this approach the hard pomeron is treated as two reggeized gluons — an ansatz used currently in diffraction phenomenology with great success. However, the predictive power of the BFKL approach for the numerical value of the pomeron intercept is still limited and not all issues concerning the sensitivity of the result to the infrared region have been understood. For further reading on pomerons, a topic very intriguing by itself, we refer to [5].

1.2 Vector meson production in diffractive DIS

There are several possible final states X in a typical diffractive DIS (DDIS) process $\gamma^* p \to Xp$: system X can be a real photon, a $q\bar{q}$ continuum pair forming two jets, or a $q\bar{q}$ bound state, for example, a vector meson. Let us now focus specifically on exclusive vector meson production in diffractive DIS. This reaction has been studied extensively in fixed target DIS experiments at CERN and FNAL and more recently by the H1 and ZEUS collaborations at HERA.

Despite the great deal of theoretical work on vector meson production in diffractive DIS [6, 7, 8, 9], there is a number of issues that have not yet been carefully analyzed and still need closer investigation. One of them concerns the vector meson production in a seeming soft region, namely at small values of Q^2 and m_V^2 (or, to put it short, at small values of $Q^2 + m_V^2$). Indeed, the majority of early calculations treated the vector meson productions in the DGLAP-inspired approach, the production amplitudes being expressed in terms of the integrated gluon density $G(x, Q^2)$. Certainly, this line of calculation is not applicable at small enough values of $Q^2 + m_V^2$, say at $Q^2 + m_V^2 \lesssim 1$ GeV^2. However it is necessary to understand that the DGLAP-based approach not only *can* be avoided but also *should* be avoided when one studies diffractive scattering. Indeed, at high energies and small-to-moderate values of Q^2, the dynamics of the amplitudes is governed by large logarithms of $\log(1/x)$ rather than $\log(Q^2)$, and the correct and the most natural method to treat processes in this kinematical region is the k_t-factorization approach. This approach does not place any restriction on the value of Q^2 as long as one works at large enough energies.

Although the strategy of the evaluation of the vector meson production amplitudes within the k_t-factorization approach is essentially clear, making reliable numerical prediction is not a straghtforward task. The impediment consists in the presence of purely soft, non-perturbative quantities in the calculation, namely the gluon content of the proton and the wave function of the vector meson.

The presence of the former quantity is a specific feature of the particular final state we

investigate, however the unintegrated gluon density

$$\mathcal{F}(x,Q^2) = \frac{\partial G(x,Q^2)}{\partial \log Q^2}\,, \tag{1.2}$$

is the basic quantity in all k_t-factorization calculations. Unfortunately, no reliable Ansatz or parametrization has been developed, and this gap needs to be filled.

Another issue that has never been brought under scrutiny is the spin-angular coupling inside the vector meson. In an off-forward scattering $\gamma^*_{\lambda_\gamma} \to V_{\lambda_V}$ the s-channel helicity flip amplitudes can be non-vanishing. Because of the well-known quark helicity conservation in high energy QCD scattering, such a helicity flip is possible only due to the internal motion and spin–angular momentum coupling of quarks in a vector meson. This issue was accurately analyzed only in very recent papers [6, 7], where it was shown that helicity non-conserving amplitudes are not negligible, as had been thought before. Thus, the helicity flip amplitudes would offer a great deal of unique information on internal constituent motion and spin–angular momentum structure of vector mesons, inaccessible in other experiments. In addition, the vector meson decays are self-analyzing and the full set of helicity amplitudes can be measured experimentally. For unpolarized incident leptons, the angular distribution of decay products is parameterized in terms of 15 spin-density matrix elements, which can be calculated via five — two helicity conserving plus three helicity violating — basic helicity amplitudes [10].

Certainly, the helicity structure of the vector meson production amplitudes must be analyzed only along with a careful treatment of the spinorial structure of the $q\bar{q} \to V$ transition. It is thus rather surprising that the above issue of sensitivity of the production amplitudes to the spin-angular momentum coupling has not been addressed before. Namely in a typical vector meson production calculation, a vector meson has been implicitly taken as a $1S$ state and at the same time an unjustified ansatz was used for the $q\bar{q} \to V$ transition spinorial structure, namely of $\bar{u}'\gamma_\mu u \cdot V_\mu$ type. Being a mere analogy of $q\bar{q}\gamma$ vertex, this ansatz in fact corresponds neither to a pure S- nor to a pure D-wave state, but to a superposition. Only in [11] were the cases of $1S$ and $2S$ vector mesons compared and the necessity of similar calculations for D wave states was stressed. Such calculations, however, have been missing in the literature until now.

In addition to purely theoretical needs, there are more issues that call upon a thorough analysis of the D-wave effects. For instance, different spin properties of the S- and D-wave production may resolve the long standing problem of the D-wave vs. $2S$-wave assignment for the $\rho'(1480)$ and $\rho'(1700)$ mesons (as well as the ω' and ϕ' mesons). Furthermore, the deuteron, which is a spin-1 ground state in the pn system, is known to have a substantial D-wave admixture, which mostly derives from the tensor forces induced by pion exchange between nucleons. Recently, there has been much discussion [12] of the non-perturbative long-range pion exchange between light quarks and antiquarks in a vector meson, which is a natural source of the S-D mixing in the ground state ρ and ω mesons.

In the present work we addressed both issues. We performed an accurate determination of the unintegrated gluon density from the experimental data on the structure function F_{2p} and gave its convenient and ready-to-use parametrizations. In addition, we constructed a consistent description of the vector mesons with spin-angular coupling taken into account, which enabled us to calculate diffractive production amplitudes for pure S-wave and D-wave states as well as for an arbitrary S/D wave mixture. This resulted in a complete theory of

the vector meson production in diffractive DIS within the k_t-factorization approach.

1.3 The strategy of the thesis

The main text of this thesis is comprised of three parts. Part I is an introduction to the k_t-factorization approach. Here we calculate some basic scattering processes, such as the virtual Compton scattering, and introduce the concept of the differential densities of partons. The discussion on the similarities and distinctions between the DGLAP-motivated description and k_t-factorization description of diffractive processes can also be found here.

In Part II we turn to the vector meson production amplitudes. These are preceeded by the theory of vector meson structure within the truncated Fock space, that is, when the vector meson is assumed to be a bound state only of a $q\bar{q}$ pair. Upon obtaining the closed analytical expessions for vector meson production amplitudes, we perform the twist expansion and illustrate some of the most salient properties of the S-wave and D-wave vector meson amplitudes.

Part III contains the numerical analysis of the expressions obtained and the concrete prediction of various experimentally observed quantities. At first we perform an extraction of the differential gluon density of the proton and thoroughly investigate its properties. Having brought the differential glue under control, we turn to the vector meson production amplitudes and give a large number of predictions for $1S$-, $2S$-, and D-wave states. Whenever the experimental results are avaliable, we confront our predictions with the data. This Part concludes with a detailed consideration of the effect of the Coulomb tail of the vector meson wave function and of the S/D-wave mixing.

Finally, we summarize our main findings in Conclusions. Some lengthy calculations can be found in Appendices.

The results presented in this thesis were derived by the author. The text is based on publications [13] and [14], and on works in progress [15]. Preliminary results have been presented as talks at workshops [16, 17].

Part I

Basics of k_t-factorization scheme

Chapter 2

Virtual Compton scattering

We start our introduction to the k_t-factorization scheme with a calculation of the imaginary part of the forward virtual Compton scattering amplitude. By means of the optical theorem, it is related to the total photoabsorption cross section and to the structre functions of the proton.

There three purposes to begin with this quantity. First, during this calculation we will follow all steps and discuss all major feature of the k_t-factorization scheme of calculations. Being rather simple, the Compton scattering amplitude will keep us from being distracted by inessential technical complications that would arise in other diffractive reactions.

The second purpose is to derive the well-known expression for the structure function F_{2p} in terms of the unintegrated gluon density of the proton, the basic quantity in any k_t-factorization calculation. These expressions will be used later, when we discuss the determination of the unintegrated glue from the experimental data.

The third aim is to use the simplicity of this amplitude to gain as much insight into the dynamics of photon-proton peripheral interactions. This information will be used later in deriving the vector meson production amplitudes thanks to a remarkable similarity between the virtual Compton scattering and the vector meson electroproduction processes. Indeed, in the proton rest frame, both can be viewed as follows: a photon dissociates into a $q\bar{q}$ pair, which interacts with gluon content of the proton and then is projected onto the final state. The hard dynamics in both cases are the same, the only difference lying in the final state projection.

2.1 Modeling virtual photoabsorption in QCD

The quantity that is measured in deep inelastic leptoproduction is the total cross section of photoabsorption $\gamma^*_\mu p \to X$, summed over all hadronic final states X, where $\mu, \nu = \pm 1, 0$ are helicities of (T) transverse and (L) longitudinal virtual photons. One usually starts with the imaginary part of the amplitude $A_{\mu\nu}$ of forward Compton scattering $\gamma^*_\mu p \to \gamma^*_\nu p'$, which by the optical theorem gives the total cross cross section of photoabsorption of virtual photons:

$$\sigma_T^{\gamma^* p}(x_{bj}, Q^2) = \frac{1}{\sqrt{(W^2 + Q^2 - m_p^2)^2 + 4Q^2 m_p^2}} \mathrm{Im} A_{\pm\pm} \,, \tag{2.1}$$

$$\sigma_L^{\gamma^* p}(x_{bj}, Q^2) = \frac{1}{\sqrt{(W^2 + Q^2 - m_p^2)^2 + 4Q^2 m_p^2}} \mathrm{Im} A_{00} \,, \tag{2.2}$$

where W is the total energy in the $\gamma^* p$ c.m. system, m_p is the proton mass, Q^2 is the virtuality of the photon and $x_{bj} = Q^2/(Q^2 + W^2 - m_p^2)$ is the Bjorken variable. Hereafter we will suppress the subscript bj and use $x \equiv x_{bj}$.

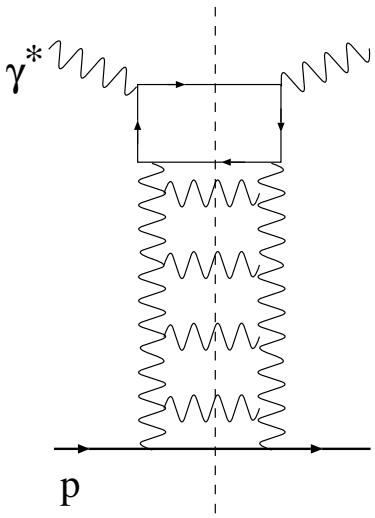

Figure 2.1: *The pQCD modeling of DIS in terms of multiproduction of parton final states.*

In perturbative QCD (pQCD) one models virtual photoabsorption in terms of the multiple production of gluons, quarks and antiquarks (Fig. 2.1). The experimental integration over the full phase space of hadronic states X is substituted in the pQCD calculation by integration over the whole phase space of QCD partons

$$\int |M_X|^2 d\tau_X \Rightarrow \sum_n |M_n|^2 \prod \int_0^1 \frac{dx_i}{x_i} d^2\vec{\kappa}_i \,, \tag{2.3}$$

where the integration over the transverse momenta of partons goes over the whole allowed region

$$0 \leq \vec{\kappa}_i^2 \leq \frac{1}{4} W^2 = \frac{Q^2(1-x)}{4x} \,. \tag{2.4}$$

The core of the so-called DGLAP approximation [18] is an observation that at finite x the dominant contribution to the multiparton production cross sections comes from a tiny part of the phase space,

$$\begin{aligned} 1 \geq x_1 \geq x_2 ... \geq x_{n-1} \geq x_n \geq x \quad &, \\ 0 \leq \vec{\kappa}_1^2 \ll \vec{\kappa}_2^2 ... \ll \vec{\kappa}_{n-1}^2 \ll \vec{k}^2 \ll Q^2 \quad &, \end{aligned} \tag{2.5}$$

in which the upper limit of integration over transverse momenta of partons is much smaller than the kinematical limit (2.4). At very small x this limitation of the transverse phase space becomes much too restrictive and the DGLAP approximation is doomed to failure.

Hereafter we focus on how lifting the restrictions on the transverse phase space changes our understanding of the gluon structure function of the nucleon at very small x; that is, at very

large $\frac{1}{x}$. In this kinematical region the gluon density $g(x,Q^2)$ is much higher than the density of charged partons $q(x,Q^2), \bar{q}(x,Q^2)$. As Fadin, Kuraev and Lipatov [19] have shown, to the leading $\log \frac{1}{x}$ (LL$\frac{1}{x}$) approximation the dominant contribution to photoabsorption comes, in this regime, from multigluon final states of Fig. 2.1. Alternatively, in the LL$\frac{1}{x}$, splitting of gluons into gluons dominates over the splitting of gluons into $q\bar{q}$ pairs. As a matter of fact, for the purposes of the present analysis, we do not need the full BFKL dynamics. In the k_t-factorization only the $q\bar{q}$ loop is treated explicitly to the LL$\frac{1}{x}$ approximation. In this regime the Compton scattering can be viewed as an interaction of the nucleon with the light cone $q\bar{q}$ Fock states of the photon via the exchange by gluons (Fig. 2.2), and the Compton scattering amplitude takes the form

$$A_{\nu\mu} = \Psi^*_{\nu,\lambda\bar{\lambda}} \otimes A_{q\bar{q}} \otimes \Psi_{\mu,\lambda\bar{\lambda}} \tag{2.6}$$

Here $\Psi_{\mu,\lambda\bar{\lambda}}$ is the Q^2 and $q,\bar{q}$ helicity $\lambda,\bar{\lambda}$ dependent light cone wave function of the photon. The $q\bar{q}$-proton scattering kernel $A_{q\bar{q}}$, arising from the pomeron exchange, does not depend on, and conserves exactly, the $q,\bar{q}$ helicities.

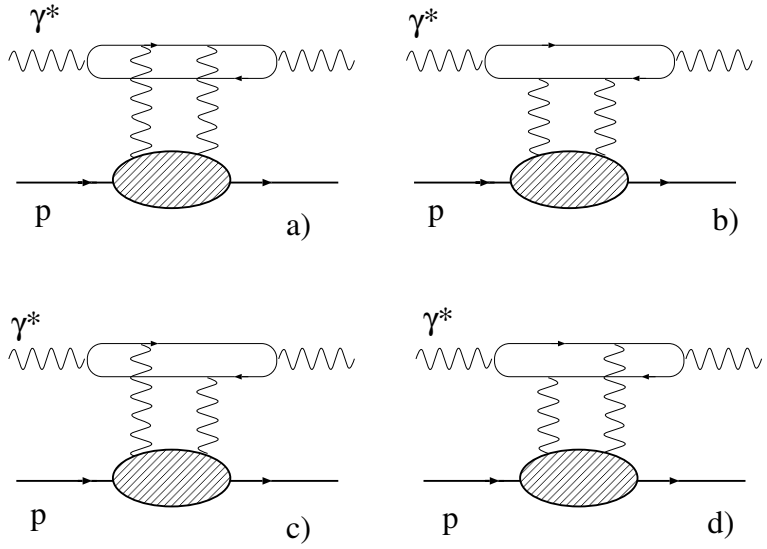

Figure 2.2: *The k_t-factorization representation for DIS at small x.*

The resummation of diagrams of Fig. 2.1 defines the unintegrated gluon structure function of the target, which is represented in diagrams of Fig. 2.2 as the fliied ellipse.

2.2 Details of the calculation

Suppose that there were no interaction between the gluons exchanged in t-channel, so that the full calculation of the Compton scattering amplitude would amount only to summing the Born diagrams. Consider one of such diagrams, e.g., Fig.2.2a, but without the ellipse. A virtual photon turns into a $q\bar{q}$ pair, which interacts with a proton via two-gluon exchange. The general expression for this amplitude is:

$$iA = \int \frac{d^4k}{(2\pi)^4} \int \frac{d^4\kappa}{(2\pi)^4}\ \bar{u}'(-ig\gamma^{\nu'}t^{B'})i\frac{\hat{p}-\hat{\kappa}+m}{[(p-\kappa)^2-m^2+i\epsilon]}(-ig\gamma^{\mu'}t^{A'})u$$

$$\cdot(-i)\frac{g_{\mu\mu'}\delta_{AA'}}{\kappa^2-\mu^2+i\epsilon}\cdot(-i)\frac{g_{\nu\nu'}\delta_{BB'}}{\kappa^2-\mu^2+i\epsilon}\cdot e_f^2$$
$$\cdot\frac{Sp\left\{(-ie)\hat{e}\;i(\hat{k}-\hat{q}+m)\;(-ie)\hat{e}^*\;i(\hat{k}+m)\;(-ig\gamma^\nu t^B)\;i(\hat{k}+\hat{\kappa}+m)\;(-ig\gamma^\mu t^A)\;i(\hat{k}+m)\right\}}{\left[k^2-m^2+i\epsilon\right]^2\left[(k+\kappa)^2-m^2+i\epsilon\right]\left[(k-q)^2-m^2+i\epsilon\right]} \tag{2.7}$$

Let's first calculate the numerator.

Color factor

If we consider photon scattering off a single quark, we have

$$\frac{1}{N_c}Sp\{t^{B'}t^{A'}\}\cdot\delta_{AA'}\delta_{BB'}Sp\{t^Bt^A\}=\frac{1}{N_c}\frac{1}{2}\delta_{AB}\frac{1}{2}\delta_{AB}=\frac{1}{2}\frac{1}{2N_c}(N_c^2-1)=\frac{1}{2}C_F=\frac{2}{3} \tag{2.8}$$

However, we should take into account that quarks are sitting inside a colorless proton, whose color structure is

$$\psi_{color}=\frac{1}{\sqrt{6}}\epsilon^{abc}q^aq^bq^c\,. \tag{2.9}$$

In this case there are two ways a pair of gluons can couple three quark lines. In the first, both gluons couple to the same quark. Since the quark momentum does not change after these two interactions, the nucleon stays in the same state: $\langle N|N\rangle=1$. In the second case, gluon legs are attached to different quark lines, so that extra momentum κ circulates between quarks, which gives rise to the factor $\langle N|\exp(i\kappa r_1-i\kappa r_2)|N\rangle$, i.e. to the two-body form factor. Therefore, for the lower line, instead of

$$\frac{1}{N_c}Sp\{t^Bt^A\}=\frac{1}{N_c}\frac{1}{2}\delta_{AB} \tag{2.10}$$

one has

$$\begin{aligned}&\frac{1}{6}\epsilon^{abc}\left(3\delta_{aa'}\delta_{bb'}t^A_{cc''}t^B_{c''c'}+6\delta_{aa'}t^A_{bb'}t^B_{cc'}\langle N|\exp(i\kappa r_1-i\kappa r_2)|N\rangle\right)\epsilon^{a'b'c'}\\ =\;&Sp\{t^At^B\}-Sp\{t^At^B\}\langle N|\exp(i\kappa r_1-i\kappa r_2)|N\rangle\\ =\;&\frac{1}{2}\delta_{AB}(1-\langle N|\exp(i\kappa r_1-i\kappa r_2)|N\rangle)\,.\end{aligned} \tag{2.11}$$

Note also that a similar calculation for N_c number of colors would yeild the same result. Thus, the overall color factor is

$$2V(\kappa)\equiv 2(1-\langle N|\exp(i\kappa r_1-i\kappa r_2)|N\rangle). \tag{2.12}$$

As is known, the highest power s contribution comes from so–called nonsense components of gluon propagator (density matrix) decomposition:

$$g_{\mu\mu'}=\frac{2p'_\mu q'_{\mu'}}{s}+\frac{2p'_\mu q'_{\mu'}}{s}+g^\perp_{\mu\mu'}\;\approx\;\frac{2p'_\mu q'_{\mu'}}{s}\,. \tag{2.13}$$

Therefore, the lower trace is calculated trivially:

$$\frac{1}{2}Sp\{\hat{p}'\hat{q}'\hat{p}'\hat{q}'\}=s^2\,. \tag{2.14}$$

Combining all factors, one has for the numerator of Eq.(2.7),

$$\begin{aligned} & (4\pi\alpha_s)^2\ 4\pi\alpha_{em}\ e_f^2 \cdot 2\frac{4}{s^2}s^2 \cdot Sp\left\{\hat{e}\ (\hat{k}-\hat{q}+m)\ \hat{e}^*\ (\hat{k}+m)\ \hat{q}'\ (\hat{k}+\hat{\kappa}+m)\ \hat{q}'\ (\hat{k}+m)\right\} \\ = \ & (4\pi\alpha_s)^2\ 4\pi\alpha_{em}\ e_f^2 \cdot 8 \cdot 2s^2 \cdot I^{(a)}(\gamma^* \to \gamma^*)\,. \end{aligned} \tag{2.15}$$

Note that we factored out $2s^2$ because it will appear later in all trace calculations. The resulting expression for amplitude (2.7) is then

$$\begin{aligned} A \ = \ & (4\pi\alpha_s)^2\ 4\pi\alpha_{em}\ 16e_f^2\ s^2 \cdot \int \frac{d^4k}{(2\pi)^4}\int \frac{d^4\kappa}{(2\pi)^4} \cdot \frac{1}{[(p-\kappa)^2-m^2+i\epsilon]\,[\kappa^2-\mu^2+i\epsilon]^2} \\ & \cdot \frac{\tilde{I}(\gamma^* \to \gamma^*)}{[k^2-m^2+i\epsilon]^2\,[(k+\kappa)^2-m^2+i\epsilon]\,[(k-q)^2-m^2+i\epsilon]}\,. \end{aligned} \tag{2.16}$$

One can now immediately write similar expressions for three other diagrams (Fig. 2.2 b,c,d). Indeed, they will differ from Eq.(2.16) only by the last line. Aside from different expressions for traces, the quark line propagator structures will read:

$$\begin{aligned} &(b) \qquad [k^2-m^2+i\epsilon][(k-q)^2-m^2+i\epsilon][(k+\kappa)^2-m^2+i\epsilon][(k+\kappa-q)^2-m^2+i\epsilon] \\ &(c) \qquad [k^2-m^2+i\epsilon][(k-q)^2-m^2+i\epsilon][(k-\kappa)^2-m^2+i\epsilon][(k-\kappa-q)^2-m^2+i\epsilon] \\ &(d) \qquad [k^2-m^2+i\epsilon][(k-q)^2-m^2+i\epsilon][(k-\kappa)^2-m^2+i\epsilon][(k-q)^2-m^2+i\epsilon] \end{aligned} \tag{2.17}$$

2.3 Denominator and trace evaluation

We now turn to calculation of denominators. As usual, we implement Sudakov's decomposition and

$$\begin{aligned} k &= yp' + zq' + \vec{k} \\ \kappa &= \alpha p' + \beta q' + \vec{\kappa} \\ q &= q' - xp'\,, \end{aligned} \tag{2.18}$$

and make use of relation

$$d^4k = \frac{1}{2}s\,dy\,dz\,d^2\vec{k}\,. \tag{2.19}$$

The complete analysis of denominator hierarchy and their integrals is performed in Appendix A. We show there that, for example, for diagram A, the imaginary part of the desired integral is given by

$$Im\left\{\int \frac{dy\ dz\ d\alpha\ d\beta}{\text{propagators}}\right\} = \frac{4\pi^2}{s^3}\int_0^1 dz\ \frac{1-z}{z}\frac{1}{[\vec{k}^2+m^2+z(1-z)Q^2]^2}\frac{1}{[\vec{\kappa}^2+\mu^2]^2}\,. \tag{2.20}$$

The results for the other three diagrams differ only by replacements $\vec{k} \to \vec{k}+\vec{\kappa}$ in quark propagators wherever appropriate. The whole expression for the imaginary part of the amplitude is then

$$ImA \ = \ s\frac{32}{(2\pi)^2}e_f^2 \cdot \alpha_{em} \cdot \int dz d^2\vec{k}\int \frac{d^2\vec{\kappa}V(\kappa)\alpha_s^2}{(\vec{\kappa}^2+\mu^2)^2}$$

$$\times\left[\frac{1-z}{z}\frac{I^{(a)}}{[\vec{k}^2+m^2+z(1-z)Q^2]^2}+\frac{z}{1-z}\frac{I^{(d)}}{[(\vec{k}+\vec{\kappa})^2+m^2+z(1-z)Q^2]^2}\right.$$
$$\left.+\frac{I^{(b)}+I^{(c)}}{[(\vec{k}+\vec{\kappa})^2+m^2+z(1-z)Q^2][\vec{k}^2+m^2+z(1-z)Q^2]}\right]. \qquad (2.21)$$

The short-hand notation α_s^2 should be in fact understood as

$$\alpha_s(\text{lower})\cdot\alpha_s(\text{upper})\equiv\alpha_s(\vec{\kappa}^2)\cdot\alpha_s(q^2)\,. \qquad (2.22)$$

with

$$q^2=\max[\vec{k}^2+m^2+z(1-z)Q^2,\vec{\kappa}^2]\,. \qquad (2.23)$$

We now calculate the integrands I which enter Eq.(2.21) $Sp\{...\}=2s^2\cdot I$. We will do this via light cone helicity amplitude technique. In the subsequent discussion we will use the following convention:

$$q'^{\mu}=q_+n_+^{\mu}$$

i.e., the light cone direction + is taken along the photon propagation.

A crutial point that justifies the usage of the helicity amplitude technique for all quarks lines inside the loop is that in the trace calculation all fermions can be treated *as on-mass shell*, thanks to the presence of $\hat{n}_-$ vertices. This property comes from the following arguments.

Note that every intermediate quark line in any diagram couples to at least one of the t-channel gluons. Algebraically, it means that every $\hat{k}+m$ stands near the factor $\hat{n}_-$. Let us apply the Sudakov decomposition to the γ matrix:

$$\gamma^{\mu}=\gamma_+n_+^{\mu}+\gamma_-n_-^{\mu}+\vec{\gamma}^{\mu};$$
$$\gamma_+=\hat{n}_-=\frac{1}{\sqrt{2}}(\gamma_0+\gamma_3)\,,\quad \gamma_-=\hat{n}_+=\frac{1}{\sqrt{2}}(\gamma_0-\gamma_3)\,.$$

Now decompose the propagator numerator of the constituent, to which this $\hat{n}_-$ leg couples,

$$\hat{k}+m=k_+\gamma_-+k_-\gamma_+-\vec{k}\vec{\gamma}+m\,, \qquad (2.24)$$

and rewrite it using notation of (4.9) and (4.11) as

$$\hat{k}+m=k_+\gamma_-+k_-^*\gamma_+-\vec{k}\vec{\gamma}+m+(k_--k_-^*)\gamma_+=\hat{k}^*+m+\frac{k^2-m^2}{2k_+}\gamma_+\,. \qquad (2.25)$$

In other words, we expressed the virtual quark propagator as the sum of an *on shell* quark propagator and an additional "instantaneous interaction" term. However, since $\hat{n}_-$ is inserted between two $(\hat{k}+m)$ factors, this item drops out due to the identity $\gamma_+\gamma_+=0$. The net result is that wherever $\hat{n}_-$ appears, both constituents can be treated on-mass-shell in the trace calculation, which completes the proof.

Having established that the fermion lines in the trace calculation can indeed be taken as if the quarks were real, we can now decompose the numerator of each ofthe quark lines as

$$\hat{k}+m\to\hat{k}^*+m=\sum_{\lambda}\bar{u}_{\lambda}u_{\lambda}\,, \qquad (2.26)$$

where spinors u_{λ} are for an on-mass shell fermion.

In the case of antiquark line the property derived above is valid as well. The only thing to remember here is that antiquark propagates upstream to the fermion arrow, so that

$$(-\hat{k}) + m = -\sum_{\lambda} \bar{v}_\lambda v_\lambda \,, \tag{2.27}$$

i.e., each antiquark propagator gives rise to factor -1.

The derivation is given in Appendix B in full detail and yields

$$\begin{aligned} ImA^T &= s\frac{32}{(2\pi)^2}\sum_i e_i^2 \cdot \alpha_{em} \cdot \int dz\, d^2\vec{k} \int \frac{d^2\vec{\kappa} V(\kappa)\alpha_S^2}{(\vec{\kappa}^2+\mu^2)^2} \\ &\times\Bigg\{ m^2 \left[\frac{1}{(\vec{k}+\vec{\kappa})^2 + m^2 + z(1-z)Q^2} - \frac{1}{\vec{k}^2 + m^2 + z(1-z)Q^2}\right]^2 \\ &\times + [z^2 + (1-z)^2] \left[\frac{\vec{k}+\vec{\kappa}}{(\vec{k}+\vec{\kappa})^2 + m^2 + z(1-z)Q^2} - \frac{\vec{k}}{\vec{k}^2 + m^2 + z(1-z)Q^2}\right]^2 \Bigg\} \end{aligned} \tag{2.28}$$

$$\begin{aligned} ImA^L &= s\frac{32}{(2\pi)^2}\sum_i e_i^2 \cdot \alpha_{em} \cdot \int dz\, d^2\vec{k} \int \frac{d^2\vec{\kappa} V(\kappa)\alpha_S^2}{(\vec{\kappa}^2+\mu^2)^2} \\ &\times 4z^2(1-z)^2Q^2 \left[\frac{1}{(\vec{k}+\vec{\kappa})^2 + m^2 + z(1-z)Q^2} - \frac{1}{\vec{k}^2 + m^2 + z(1-z)Q^2}\right]^2 \end{aligned} \tag{2.29}$$

2.4 Gluon density

It is obvious that Eqs.(2.28) and (2.29) are not directly related to the real experimental situation, for up to now, we assumed that the two exchanged gluons do not interact. Such interaction will definitely change the properties of the entire t-channel exchange, and in fact, as predicted by the BFKL equation, the resultant pomeron has rather little in common with the initial two perturbative gluons.

Since the BFKL evolution necessarily involves soft gluons (see below more on soft-to-hard diffusion), it does not allow for accurate perturbative calculations. It must be understood, however, that although we do not know what happens "inside the pomeron" on the way from proton to the quark-antiquark pair, we nevertheless know — and the knowlegde is based on the leading order BFKL analysis — that eventually the $q\bar{q}$ pair will interact with nothing else but two gluons. We underline that this conclusion does not require the gluons to be hard/ Rather, it relies on the fact that higher Fock states of the t-channel can be, to the leading $\log \frac{1}{x}$ approximation, absorbed in the two gluon state [20].

Thus, the only thing we need to know is the momentum distribution of the uppermost gluons, or, to put it exactly, the probability distribution to find a gluon with given light cone momentum fraction x_g and the transverse momentum $\vec{\kappa}$,

$$dn_g = \mathcal{F}(\vec{\kappa}, x_g)\frac{d\vec{\kappa}^2}{\vec{\kappa}^2}\frac{dx_g}{x_g}\,. \tag{2.30}$$

This distribution is called the *unintegrated (or differential) gluon structure function*, DGSF, or simply the *unintegrated gluon density.*

Since the differential gluon density is not calculable with pQCD, a reasonable way to proceed in our computation of the compton scattering amplitude further consists of finding the correspondence $V(\kappa) \leftrightarrow \mathcal{F}(\vec{\kappa}, x_g)$. Namely we will calculate the unintegrated gluon density *at the Born level*, $\mathcal{F}_{Born}$, in terms of $V(\kappa)$, and then postulate that the BFKL dynamics amounts to replacement $\mathcal{F}_{Born} \to \mathcal{F}$. This procedure will give us a unique prescription for how to correctly incorporate the unintegrated gluon density into the k_t-factorization calculations.

In order to provide a gentle introduction into the concept of the unintegarated parton densities, we start with the Fermi-Weizsäcker-Williams approximation in QED. We will find the expression for the unintegrated photon densities in the case of a single charged particle and charge neutral positronium and then translate the results to the case of color forces.

2.4.1 Differential density of gauge bosons: the QED primer

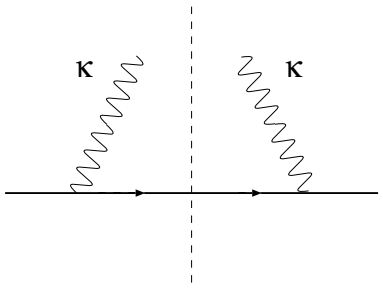

Figure 2.3: *The Fermi-Weizsäcker-Williams diagram for calculation of the flux of equivalent photons*

For this pedagogical introduction we recall the Fermi-Weizsäcker-Williams approximation in QED, which is the well-known precursor of the parton model (for the review see [21]). Here high energy reactions in the Coulomb field of a charged particle are treated as collisions with equivalent transversely polarized photons — partons of the charged particle, Fig.2.3. The familiar flux of comoving equivalent transverse soft photons carrying a light cone fraction $x_\gamma \ll 1$ of the momentum of a relativistic particle, let it be the electron, reads

$$dn_e^\gamma = \frac{\alpha_{em}}{\pi} \frac{\vec{\kappa}^2 d\vec{\kappa}^2}{(\vec{\kappa}^2 + \kappa_z^2)^2} \frac{dx_\gamma}{x_\gamma} \approx \frac{\alpha_{em}}{\pi} \frac{d\vec{\kappa}^2}{\vec{\kappa}^2} \frac{dx_\gamma}{x_\gamma}, \tag{2.31}$$

Here $\vec{\kappa}$ is photon transverse momentum and $\kappa_z = m_e x_\gamma$ is the photon longitudinal momentum in the electron Breit frame. The origin of $\vec{\kappa}^2$ in the numerator is in the current conservation, i.e., gauge invariance. Then the unintegrated photon structure function of the electron is by definition

$$\mathcal{F}_\gamma(x_\gamma, \vec{\kappa}^2) = \frac{\partial G_\gamma}{\partial \log \vec{\kappa}^2} = x_\gamma \frac{dn_e^\gamma}{dx_\gamma d \log \vec{\kappa}^2} = \frac{\alpha_{em}}{\pi} \left(\frac{\vec{\kappa}^2}{\vec{\kappa}^2 + \kappa_z^2} \right)^2. \tag{2.32}$$

2.4.2 Differential density of photons in a positronium

If the relativistic particle is a positronium, Fig. 2.4, destructive interference of electromagnetic fields of the electron and positron must be taken into account. Specifically, for soft photons with the wavelength $\lambda = \frac{1}{\kappa} \gg a_{\rm P}$, where $a_{\rm P}$ is the positronium Bohr radius, the electromagnetic

fields of an electron and positron cancel each other and the flux of photons vanishes, whereas for $\lambda \ll a_{\rm P}$ the flux of photons will be twice that for a single electron. The above properties are quantified by the formula

$$\mathcal{F}_\gamma^{\rm P}(x_\gamma, \vec{\kappa}^2) = N_c \frac{\alpha_{em}}{\pi} \left(\frac{\vec{\kappa}^2}{\vec{\kappa}^2 + \kappa_z^2} \right)^2 V(\kappa)\,, \tag{2.33}$$

where $N_c = 2$ is the number of charged particles in the positronium and corresponds to the Feynman diagrams of Figs. 2.4a and 2.4b. The vertex function $V(\kappa)$ is expressed in terms of the two-body form factor of the positronium,

$$V(\kappa) = 1 - F_2(\vec{\kappa}, -\vec{\kappa}) = 1 - \langle {\rm P}| \exp(i\vec{\kappa}(\boldsymbol{r}_- - \boldsymbol{r}_+))|{\rm P}\rangle\,, \tag{2.34}$$

where $\boldsymbol{r}_- - \boldsymbol{r}_+$ is the spatial separation of e^+ and e^- in the positronium. The two-body form factor $F_2(\vec{\kappa}, -\vec{\kappa})$ describes the destructive interference of electromagnetic fields of the electron and positron and corresponds to the Feynman diagrams of Figs. 2.4c and2.4d. It vanishes for large enough $\kappa \gtrsim a_{\rm P}^{-1}$, leaving us with $V(\kappa) = 1$, whereas for soft gluons one has

$$V(\kappa) \propto \vec{\kappa}^2 a_{\rm P}^2\,. \tag{2.35}$$

One can say that the law (2.35) is driven by electromagnetic gauge invariance, which guarantees that long-wave photons decouple from the charge neutral system.

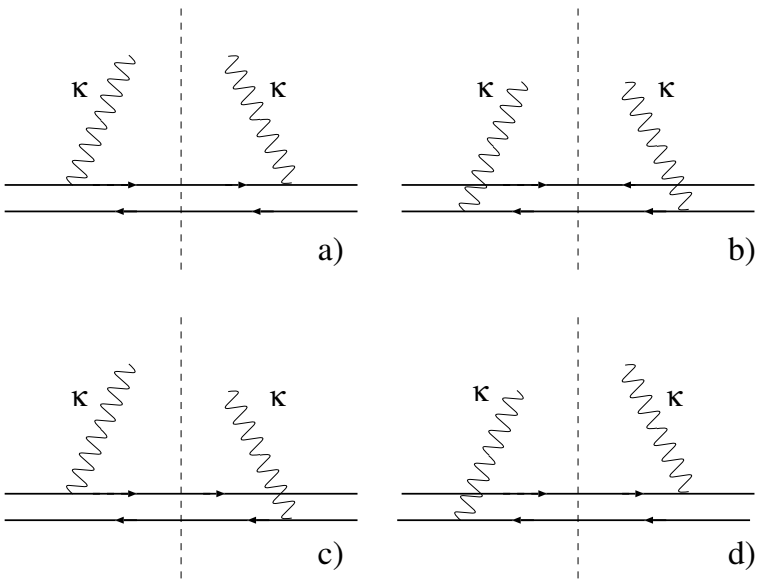

Figure 2.4: *The Fermi-Weizsäcker-Williams diagrams for calculation of the flux of equivalent photons in positronium.*

Finally, recall that the derivation of the differential flux of transverse polarized photons would also hold if the photons were massive vector bosons interacting with the conserved current, the only change being in the propagator. For instance, for the charge neutral source one finds

$$\mathcal{F}_V^{\rm P}(x_V, \vec{\kappa}^2) = N_c \frac{\alpha_{em}}{\pi} \left(\frac{\vec{\kappa}^2}{\vec{\kappa}^2 + m_V^2} \right)^2 V(\kappa)\,. \tag{2.36}$$

Recall that the massive vector fields are Yukawa-Debye screened, with the screening radius

$$R_c = \frac{1}{m_V}\,. \tag{2.37}$$

To lowest order in QED perturbation theory the two exchanged photons in figs.2.3, 2.4 do not interact and we shall often refer to (2.36) as the Born approximation for the differential vector boson structure function. One can regard (2.36) as a minimal model for soft $\vec{\kappa}$ behavior of the differential structure function for Yukawa-Debye screened vector bosons.

2.4.3 Differential gluon density in a proton

The expression for the Born level unintegrated gluon density in a color neutral proton can be obtained immediately by generalization of (2.33) and (2.36). The only extra thing one has to do is some color algebra, which leads to

$$\mathcal{F}_g^{(Born)} = C_F N_c \frac{\alpha_s(\vec{\kappa}^2)}{\pi} V(\kappa)\,. \tag{2.38}$$

Therefore, a prescription for how to include unintegrated gluon density is:

$$C_F N_c \frac{\alpha_s(\vec{\kappa}^2)}{\pi} V(\kappa) \equiv \mathcal{F}^{(Born)} \to \mathcal{F}\,. \tag{2.39}$$

Note that in this prescription one of the two strong coupling constants in (2.21) (the lower one) is absorbed into the definition of $\mathcal{F}$.

2.5 Final expressions

Bringing all pieces together, we obtain the answer for the total photoabsorption cross section:

$$\begin{aligned}\sigma_T(x,Q^2) &= \frac{\alpha_{em}}{\pi}\sum_i e_i^2 \int_0^1 dz \int d^2\vec{k} \int \frac{d^2\vec{\kappa}}{\vec{\kappa}^4}\alpha_s(q^2) \\ &\quad \times \mathcal{F}(x_g,\vec{\kappa}^2)\left[m_i^2\Phi_0^2 + [z^2+(1-z)^2]\vec{\Phi}_1^2\right]\,; \end{aligned} \tag{2.40}$$

$$\sigma_L(x,Q^2) = \frac{\alpha_{em}}{\pi}\sum_i e_i^2 \int_0^1 dz \int d^2\vec{k} \int \frac{d^2\vec{\kappa}}{\vec{\kappa}^4}\alpha_s(q^2)\cdot\mathcal{F}(x_g,\vec{\kappa}^2) 4Q^2z^2(1-z)^2\Phi_0^2\,, \tag{2.41}$$

where

$$\Phi_0 = \frac{1}{\vec{k}^2+\varepsilon^2} - \frac{1}{(\vec{k}-\vec{\kappa})^2+\varepsilon^2}\,; \quad \vec{\Phi}_1 = \frac{\vec{k}}{\vec{k}^2+\varepsilon^2} - \frac{\vec{k}-\vec{\kappa}}{(\vec{k}-\vec{\kappa})^2+\varepsilon^2}\,. \tag{2.42}$$

Here

$$\varepsilon^2 = z(1-z)Q^2 + m_f^2\,, \tag{2.43}$$

and the density of gluons enters at

$$x_g = \frac{Q^2+M_t^2}{W^2+Q^2} = x\left(1+\frac{M_t^2}{Q^2}\right)\,. \tag{2.44}$$

Here M_t is the transverse mass of the produced $q\bar{q}$ pair in the photon-gluon fusion $\gamma^* g \to q\bar{q}$:

$$M_t^2 = \frac{m_f^2 + \vec{k}^2}{1-z} + \frac{m_f^2 + (\vec{k}-\vec{\kappa})^2}{z}\,. \tag{2.45}$$

No restrictions on the transverse momentum in the $q\bar{q}$ loop, $\vec{k}$, and gluon momentum, $\vec{\kappa}$, are imposed in the above representations. The above-used BFKL scheme defines DGSF uniquely in terms of physical observables.

We note that equations obtained are for forward diagonal Compton scattering, but a similar representation in terms of the unintegrated gluons structure function holds also for the off-forward Compton scattering at finite momentum transfer $\mathbf{\Delta}$, and for off-diagonal Compton scattering when the virtualities of the initial and final state photons are different, $Q_f^2 \neq Q_i^2$, including the timelike photons and vector mesons, $Q_f^2 = -m_V^2$, in the final state.

The photoabsorption cross sections define the dimensionless structure functions

$$F_{T,L}(x,Q^2) = \frac{Q^2}{4\pi^2\alpha_{em}}\sigma_{T,L} \tag{2.46}$$

and $F_2 = F_T + F_L$, which admit the familiar pQCD parton model interpretation

$$F_T(x,Q^2) = \sum_{f=u,d,s,c,b,..} e_f^2[q_f(x,Q^2) + \bar{q}_f(x,Q^2)]\,, \tag{2.47}$$

where $q_f(x,Q^2)$, $\bar{q}_f(x,Q^2)$ are the integrated densities of quarks and antiquarks carrying the fraction x of the light cone momentum of the target and transverse momenta $\leq Q$.

2.6 The virtual Compton amplitude in the impact parameter space

A further deep insight into the Compton amplitude — and into the diffractive processes in general — can be gained by switching to the impact parameter (the transverse coordinate) representation. We will see that the answer will allow for a simple probabilistic form.

$$A = \int dz \int d^2\vec{r}\sigma(\vec{r})|\Psi_\gamma(z,\vec{r})|^2\,. \tag{2.48}$$

The quantity $\sigma(\vec{r})$ has the meaning of the dipole cross section, while the $\Psi_\gamma(z,\vec{r})$ represents the photon wave function.

In order to switch to the impact parameter space, we perform the 2-dimensional Fourier transform. We use the following equalities:

$$\begin{aligned}
\frac{1}{\vec{k}^2+\varepsilon^2} = \frac{1}{2\pi}\int d^2\vec{r}e^{i\vec{k}\vec{r}}f_0(r)\,; \quad &\Rightarrow \quad f_0(r) \equiv \int d^2\vec{k}\frac{e^{-i\vec{k}\vec{r}}}{\vec{k}^2\varepsilon^2} = K_0(\varepsilon r)\,; \\
\frac{\vec{k}}{\vec{k}^2+\varepsilon^2} = \frac{1}{2\pi}\int d^2\vec{r}e^{i\vec{k}\vec{r}}\vec{f}_1(\vec{r})\,; \quad &\Rightarrow \quad f_1(\vec{r}) \equiv \left(-i\frac{\partial}{\partial\vec{r}}\right)\int d^2\vec{k}\frac{e^{-i\vec{k}\vec{r}}}{\vec{k}^2\varepsilon^2} \\
&= \quad \left(-i\frac{\partial}{\partial\vec{r}}\right)K_0(\varepsilon r) = -i\varepsilon\frac{\vec{r}}{r}K_1(\varepsilon r)\,.
\end{aligned} \tag{2.49}$$

This leads to the representation

$$\begin{aligned}\Phi_0 &= \frac{1}{2\pi}\int d^2\vec{r}e^{i\vec{k}\vec{r}}K_0(\varepsilon r)\left(1-e^{i\vec{\kappa}\vec{r}}\right);\\ \vec{\Phi}_1 &= \frac{1}{2\pi}\int d^2\vec{r}e^{i\vec{k}\vec{r}}(-i\varepsilon)\frac{\vec{r}}{r}K_1(\varepsilon r)\left(1-e^{i\vec{\kappa}\vec{r}}\right).\end{aligned} \tag{2.50}$$

Let us now make the approximation that there is no other $\vec{k}$-dependence in the photoabsorption cross section. Then one immediately has

$$\begin{aligned}\int d^2\ \vec{k}\Phi_0\Phi_0^* &= \int d^2\vec{k}\frac{1}{4\pi^2}\int d^2\vec{r}_1 d^2\vec{r}_2\ e^{i\vec{k}\vec{r}_1-i\vec{k}\vec{r}_2}K_0(\varepsilon r_1)K_0(\varepsilon r_2)\left(1-e^{i\vec{\kappa}\vec{r}_1}\right)\left(1-e^{-i\vec{\kappa}\vec{r}_2}\right)\\ &= \int d^2\vec{r}\ K_0^2(\varepsilon r)\ 2[1-\cos(\vec{\kappa}\vec{r})].\end{aligned} \tag{2.51}$$

Substituting these expressions into photoproduction cross sections, one gets

$$\begin{aligned}\sigma_T(x,Q^2) &= \frac{\alpha_{em}}{\pi}\sum_i e_i^2\int_0^1 dz\int d^2\vec{r}\left[m_i^2K_0^2(\varepsilon r)+[z^2+(1-z)^2]\varepsilon^2K_1^2(\varepsilon r)\right]\\ &\times \int\frac{d^2\vec{\kappa}}{\vec{\kappa}^4}\alpha_s\mathcal{F}(x_g,\vec{\kappa}^2)\ 2[1-\cos(\vec{\kappa}\vec{r})];\\ \sigma_L(x,Q^2) &= \frac{\alpha_{em}}{\pi}\sum_i e_i^2\int_0^1 dz\int d^2\vec{r}\cdot 4Q^2z^2(1-z)^2\cdot K_0^2(\varepsilon r)\\ &\times \int\frac{d^2\vec{\kappa}}{\vec{\kappa}^4}\alpha_s\mathcal{F}(x_g,\vec{\kappa}^2)\ 2[1-\cos(\vec{\kappa}\vec{r})].\end{aligned} \tag{2.52}$$

2.6.1 Dipole cross section

The above results can put into the form (2.48) by breaking Eqs. (2.52) into some positively defined cross section and the square of the photon wave function. This is done in an unambiguous way by defining the *dipole cross section*.

Let us first consider the total quark-proton cross section,

$$\sigma_{qp}=\frac{2\pi}{3}\int\frac{d^2\vec{\kappa}}{\vec{\kappa}^4}\alpha_s(\vec{\kappa}^2)\mathcal{F}(x,\vec{\kappa}^2). \tag{2.53}$$

Note that this expression does not depend on the quark transverse momentum $\vec{k}$. This means that this cross section precisely corresponds not only to the plane wave, but also to any transverse wave packet. In particular, a localized state in the impact parameter space (that is, a quark with a fixed separation $\vec{\rho}_{qp}$ from the proton) would be described by the same formula.

Given this cross section, we can now ask for the interaction of a color dipole with the proton. In this, each extra gluon that is attached to the antiquark rather than to the quark gives rise to an extra phase factor $\exp(\pm i\vec{\kappa}\vec{r})$, as well as extra minus sign. These factors for the four diagrams then sum up to produce

$$1-e^{i\vec{\kappa}\vec{r}}-e^{-i\vec{\kappa}\vec{r}}+1=2[1-\cos(\vec{\kappa}\vec{r})].$$

The result for the dipole cross section is then

$$\begin{aligned}\sigma_{dip}(\vec{r}) &= \frac{2\pi}{3}\int\frac{d^2\vec{\kappa}}{\vec{\kappa}^4}\alpha_s\left(\max\left[\vec{\kappa}^2,\frac{A}{r^2}\right]\right)\mathcal{F}(x,\vec{\kappa}^2)2[1-\cos(\vec{\kappa}\vec{r})]\\ &= \frac{4\pi^2}{3}\int\frac{d\vec{\kappa}^2}{\vec{\kappa}^4}\alpha_s\left(\max\left[\vec{\kappa}^2,\frac{A}{r^2}\right]\right)\mathcal{F}(x,\vec{\kappa}^2)[1-J_0(\kappa r)].\end{aligned} \tag{2.54}$$

Note that, in contrast to (2.53), the argument of α_s contains now the effect of a possible screening from the complementary charge. Indeed, even when $\vec{\kappa}^2$ is small, the strong coupling constant does not rise rapidly, for such a rise requires the presence of soft gluon vertex correction loops, which are strongly suppressed by the color anti-charge of the antiquark.

Having defined the dipole color cross section, we can now return to the photoabsorption cross section and cast it into the form

$$\begin{aligned}
\sigma_T &= \int_0^1 dz \int d^2\vec{r}\; \sigma_{dip}(\vec{r}) \cdot |\Psi_\gamma^T|^2(z,\vec{r})\,, \quad \sigma_L = \int_0^1 dz \int d^2\vec{r}\; \sigma_{dip}(\vec{r}) \cdot |\Psi_\gamma^L|^2(z,\vec{r})\,; \\
|\Psi_\gamma^T(z,\vec{r})|^2 &= \frac{3\alpha_{em}}{\pi^2} \sum_i e_i^2 \left[m_i^2 K_0^2(\varepsilon r) + [z^2 + (1-z)^2] \varepsilon^2 K_1^2(\varepsilon r) \right] ; \\
|\Psi_\gamma^L(z,\vec{r})|^2 &= \frac{3\alpha_{em}}{\pi^2} \sum_i e_i^2 \; 4Q^2 z^2 (1-z)^2 K_0^2(\varepsilon r)\,. \qquad (2.55)
\end{aligned}$$

Note that this representation literally represents the probabilistic form (2.6) of the forward scattering amplitude.

Chapter 3

DGLAP vs. k_t factorization

The calculation of the forward Compton scattering amplitude conducted in the previous chapter within the framework of the k_t-factoriation approach can be used now to investigate the major similarities and the gross differences in comparison with the widely used DGLAP approach to the calculation of high energy reactions.

It turns out that in the double logarithmic regime — that is, when both $\log\frac{1}{x}$ and $\log Q^2$ are large, we might expect that both approaches are applicable and their predictions would asymptotically converge. We shall now demostrate that this is indeed the case, and we will also show what sort of phase space restrictions the DGLAP approach contains and what it leads to.

3.1 How DGLAP and k_t factorization approaches meet at high Q^2

Recall the familiar DGLAP equation [18] for scaling violations at small x,

$$\frac{dF_2(x,Q^2)}{d\log Q^2} = \sum_f e_f^2 \frac{\alpha_S(Q^2)}{2\pi}\int_x^1 dy[y^2+(1-y)^2]G\left(\frac{x}{y},Q^2\right) \approx \frac{\alpha_S(Q^2)}{3\pi}G(2x,Q^2)\sum_f e_f^2\,, \quad (3.1)$$

where, for the sake of simplicity, we consider only light flavors. Upon integration we find

$$F_2(x,Q^2) \approx \sum_f e_f^2 \int_{\mu^2}^{Q^2}\frac{d\overline{Q}^2}{\overline{Q}^2}\frac{\alpha_S(\overline{Q}^2)}{3\pi}G(2x,\overline{Q}^2)\,, \quad (3.2)$$

with μ^2 being the proper cut-off. In order to see the correspondence between the k_t-factorization and DGLAP factorization it is instructive to follow the derivation of (3.2) from the $\vec{\kappa}_\perp$-representation.

First, separate the $\vec{\kappa}^2$-integration into the DGLAP part of the gluon phase space, $\vec{\kappa}^2 \lesssim \overline{Q}^2 = \epsilon^2 + \vec{k}^2$, and the beyond-DGLAP region, $\vec{\kappa}^2 \gtrsim \overline{Q}^2$. One readily finds

$$\left(\frac{\vec{k}}{\vec{k}^2+\varepsilon^2} - \frac{\vec{k}-\vec{\kappa}}{(\vec{k}-\vec{\kappa})^2+\varepsilon^2}\right)^2 \to \begin{cases} \left(\frac{2z^2(1-z)^2Q^4}{\overline{Q}^8} - \frac{2z(1-z)Q^2}{\overline{Q}^6} + \frac{1}{\overline{Q}^4}\right)\vec{\kappa}^2 & \text{if} \quad \vec{\kappa}^2 \ll \overline{Q}^2 \\ \left(\frac{1}{\overline{Q}^2} - \frac{z(1-z)Q^2}{\overline{Q}^4}\right), & \text{if} \quad \vec{\kappa}^2 \gtrsim \overline{Q}^2 \end{cases} \quad (3.3)$$

Consider first the contribution from the DGLAP part of the phase space, $\vec{\kappa}^2 \lesssim \overline{Q}^2$. Notice that because of the factor $\vec{\kappa}^2$ in (3.3), the straightforward $\vec{\kappa}^2$ integration of the DGLAP component yields $G(x_g, \overline{Q}^2)$ and $\overline{Q}^2$ is precisely the pQCD hard scale for the gluonic transverse momentum scale:

$$\int_0^{\overline{Q}^2} \frac{d\vec{\kappa}^2}{\vec{\kappa}^4} \alpha_S(q^2) \mathcal{F}(x_g, \vec{\kappa}^2) \left(\frac{\vec{k}}{\vec{k}^2 + \varepsilon^2} - \frac{\vec{k} - \vec{\kappa}}{(\vec{k} - \vec{\kappa})^2 + \varepsilon^2} \right)^2$$
$$= \left(\frac{2z^2(1-z)^2 Q^4}{\overline{Q}^8} - \frac{2z(1-z)Q^2}{\overline{Q}^6} + \frac{1}{\overline{Q}^4} \right) \alpha_s(\overline{Q}^2) G(x_g, \overline{Q}^2) \tag{3.4}$$

The contribution from the beyond-DGLAP region of the phase space can be evaluated in terms of $\mathcal{F}(x_g, \overline{Q}^2)$ and the rescaling factor C_2:

$$\int_{\overline{Q}^2}^{\infty} \frac{d\vec{\kappa}^2}{\vec{\kappa}^4} \alpha_S(q^2) \mathcal{F}(x_g, \vec{\kappa}^2) \left(\frac{1}{\overline{Q}^2} - \frac{z(1-z)Q^2}{\overline{Q}^4} \right) = \left(\frac{1}{\overline{Q}^4} - \frac{z(1-z)Q^2}{\overline{Q}^6} \right) \alpha_s(\overline{Q}^2) \mathcal{F}(x_g, \overline{Q}^2) I(x_g, \overline{Q}^2)$$
$$= \left(\frac{2z^2(1-z)^2 Q^4}{\overline{Q}^8} - \frac{2z(1-z)Q^2}{\overline{Q}^6} + \frac{1}{\overline{Q}^4} \right) \alpha_s(\overline{Q}^2) \mathcal{F}(x_g, \overline{Q}^2) \log C_2(x_g, \overline{Q}^2, z) \,. \tag{3.5}$$

The latter form of (3.5) allows for convenient combination of (3.4) and (3.5) by rescaling the hard scale in the GSF

$$G(x_g, \overline{Q}^2) + \mathcal{F}(x_g, \overline{Q}^2) \log C_2(x_g, \overline{Q}^2, z) \approx G(x_g, C_2(x_g, \overline{Q}^2, z) \overline{Q}^2) \,. \tag{3.6}$$

Here the exact value of $I(x_g, \overline{Q}^2)$ depends on the rate of the $\vec{\kappa}^2$-rise of $\mathcal{F}(x_g, \vec{\kappa}^2)$. At small x_g and small-to-moderate $\overline{Q}^2$ one finds $I(x_g, \overline{Q}^2)$ substantially larger than 1 and $C_2(x_g, \overline{Q}^2, z) \gg 1$.

Now change from $d\vec{k}^2$ integration to $d\overline{Q}^2$ and again split the z, Q^2 integration into the DGLAP part of the phase space, $\overline{Q}^2 \ll \frac{1}{4}Q^2$, where either $z < \frac{\overline{Q}^2}{Q^2}$ or $1 - z < \frac{\overline{Q}^2}{Q^2}$, and the beyond-DGLAP region, $\overline{Q}^2 \gtrsim \frac{1}{4}Q^2$, where $0 < z < 1$. One finds

$$\int dz[z^2 + (1-z)^2] \left(\frac{2z^2(1-z)^2 Q^4}{\overline{Q}^8} - \frac{2z(1-z)Q^2}{\overline{Q}^6} + \frac{1}{\overline{Q}^4} \right)$$
$$= \begin{cases} \frac{4}{3\overline{Q}^2 Q^2}, & \text{if} \quad \overline{Q}^2 \ll \frac{1}{4}Q^2 \\ \left(2A_2 \frac{Q^4}{\overline{Q}^8} - 2A_1 \frac{Q^2}{\overline{Q}^6} + A_0 \frac{1}{\overline{Q}^4} \right), & \text{if} \quad \overline{Q}^2 \gtrsim \frac{1}{4}Q^2 \end{cases} , \tag{3.7}$$

where

$$A_m = \int_0^1 dz[z^2 + (1-z)^2] z^m (1-z)^m \,. \tag{3.8}$$

Let $\overline{C}_2$ be $C_2(x_g, \overline{Q}^2, z)$ at a mean point. Notice also that $M_t^2 \sim Q^2$, so that $x_g \sim 2x$. Then the contribution from the DGLAP phase space of $\overline{Q}^2$ can be cast in precisely the form (3.2):

$$F_2(x, Q^2)\Big|_{DGLAP} \approx \sum_f e_f^2 \int_0^{\frac{\overline{C}_2}{4}Q^2} \frac{d\overline{Q}^2}{\overline{Q}^2} \frac{\alpha_S(\overline{Q}^2)}{3\pi} G(2x, \overline{Q}^2) \,. \tag{3.9}$$

The beyond-DGLAP region of the phase space gives the extra contribution of the form

$$\Delta F_2(x,Q^2)\Big|_{non-DGLAP} \sim \sum_f e_f^2 \frac{\alpha_S(Q^2)}{3\pi} \int_{Q^2}^{\infty} \frac{d\overline{Q}^2}{\overline{Q}^2} \frac{Q^2}{\overline{Q}^2} G(2x,\overline{Q}^2)$$

$$\sim \sum_f e_f^2 \frac{\alpha_S(Q^2)}{3\pi} G(2x,Q^2)\,. \tag{3.10}$$

Eqs.(3.9) and (3.10) immediately reveal the phenomenological consequences of lifting the DGLAP restrictions in the transverse momenta integration. Indeed, the DGLAP approach respects the following strict inequalities

$$\vec{\kappa}^2 \ll \vec{k}^2 \quad \text{and} \quad \vec{k}^2 \ll Q^2\,. \tag{3.11}$$

As we just saw, removing the first limitation effectively shifted the upper limit in the $\overline{Q}^2$ integral to $\frac{\overline{C}_2}{4}Q^2 \neq Q^2$, while lifting the second constraint led to an additional, purely non-DGLAP contribution. Although both of these corrections lack one leading log-Q^2 factor, they are numerically substantial.

The above analysis suggests that the DGLAP and k_t-factorization schemes converge logarithmically at large Q^2. However, in order to reproduce the result (3.9) and (3.10) for the full phase space by the conventional DGLAP contribution (3.2) from the restricted phase space, (2.5) one has to ask for DGLAP gluon density $G_{pt}(x,Q^2)$ larger than the integrated GSF in the k_t-factorization scheme. The difference between the two gluon densities can be quite substantial in the domain of strong scaling violations.

3.2 The different evolution paths: soft-to-hard diffusion and vice versa

The above discussion of the contributions to the total cross section from the DGLAP and non-DGLAP parts of the phase space can conveniently be cast in the form of the Huygens principle. To the standard DGLAP leading logQ^2 (LLQ^2) approximation, one only considers the contribution from the restricted part of the available transverse phase space (2.5). The familiar Huygens principle for the homogeneous DGLAP LLQ^2 evaluation of parton densities in the x-Q^2 plane is illustrated in Fig. 3.1a. One starts with the boundary condition $p(x,Q_0^2)$ as a function of x at fixed Q_0^2. The evolution paths $(z,\tilde{Q}^2)$ for the calculation of $p(x,Q^2)$ shown in Fig. 3.1a are confined to a rectangle $x \leq z \leq 1$, $Q_0^2 \leq \tilde{Q}^2 \leq Q^2$. This evolution is unidirectional in the sense that there is no feedback on the x-dependence of $p(x,Q_1^2)$ from the x-dependence of $p(x,Q_2^2)$ at $Q_2^2 \geq Q_1^2$. In Fig. 3.1a we show some examples of evolution paths that are kinematically allowed but neglected in the DGLAP approximation. Starting with nearly flat or slowly rising $G(x,Q_0^2)$, one finds that the larger Q^2, the steeper the small-x rise of $G(x,Q^2)$.

At $x \ll 1$ the DGLAP contribution from the restricted transverse phase space (2.5) no longer dominates the multiparton production cross sections, the restriction (2.5) must be lifted and the contribution to the cross section from small $\vec{\kappa}_i^2$ and large $\vec{\kappa}_i^2 \gtrsim Q^2$ can no longer be neglected. The Huygens principle for the homogeneous BFKL evolution is illustrated in Fig. 3.1b. One starts with the boundary condition $\mathcal{F}(x_0,Q^2)$ as a function of Q^2 at fixed

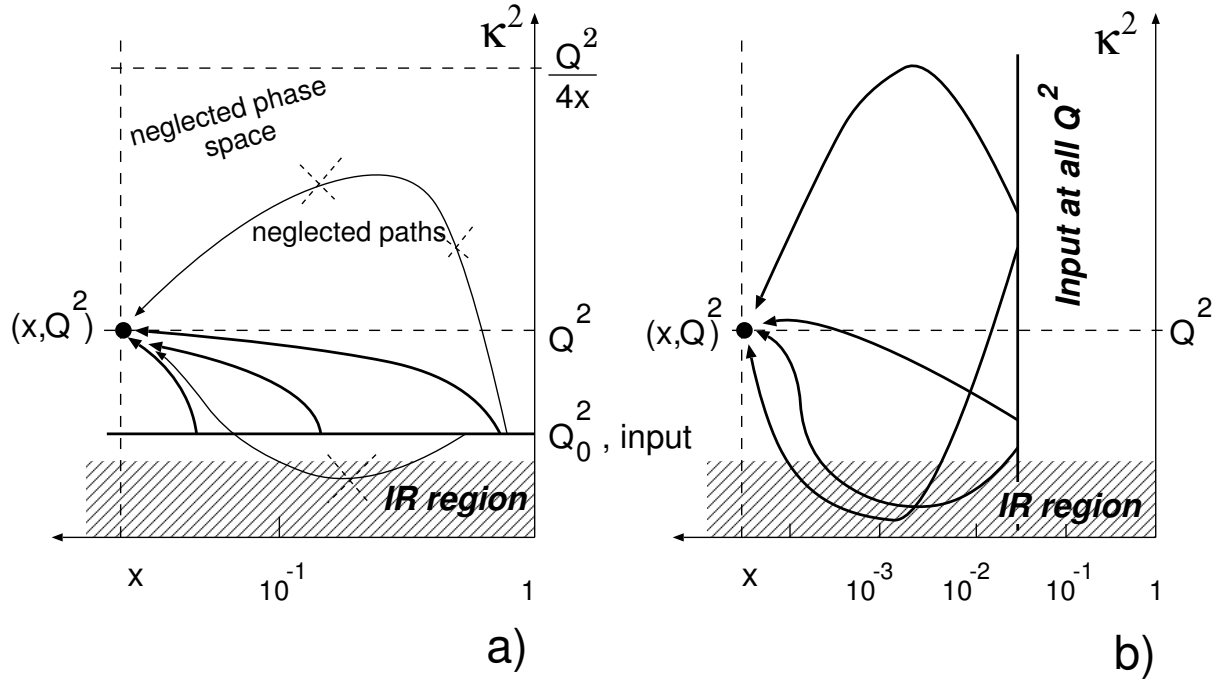

Figure 3.1: *The Huygens principle for Q^2, x evolution of DIS structure functions with* (a) *DGLAP restricted transverse phase space and* (b) *for the BFKL x evolution without restrictions on the transverse phase space and hard-to-soft & soft-to-hard diffusion.*

$x_0 \ll 1$. The evolution paths $(z, \tilde{Q}^2)$ for the calculation of $p(x, Q^2)$ are confined to a stripe $x \leq z \leq x_0$. In contrast to the unidirectional DGLAP evolution, one can say that under BFKL evolution the small-x behaviour of $p(x, Q^2)$ at large Q^2 is fed partly by the x-dependence of soft $p(x, Q^2)$ at larger x and vice-versa. The most dramatic consequence of this soft-to-hard and hard-to-soft diffusion, which can not be eliminated, is that at very small x the x-dependence of the gluon structure in the soft and hard regions will eventually be the same. The rate of such a hard-to-soft diffusion is evidently sensitive to the infrared regularization of pQCD; the model estimates show that in the HERA range of x it is very slow [22, 23].

Part II

Derivation of vector meson production amplitudes

Chapter 4

Description of a vector meson

In this chapter we first introduce the vector meson light cone wave function (LCWF) and show how it emerges in diagrammatic calculations. Then, describing S and D wave type vector particles, we give expressions for S and D wave vector meson spinorial structures, which we then prove by calculating the normalization condition for LCWF. Finally, we calculate $V \to e^+e^-$ decay constants to be used afterwards.

4.1 Bound states in QFT

While describing particle motion in non-relativistic Quantum Mechanics, one usually deals with a configuration space particle wave function, which is a good description because the number of particles is conserved. When one has a system of particles and shows that the wave function corresponding to their relative motion descreases at large relative distances at least exponentially, one can speak of a bound state.

In Quantum Field Theory (QFT) this approach needs an update, since the field function becomes an operator in Fock space. Besides, since a bound state always implies the presence of interaction, the projection of a physical bound state onto the Fock space of *free, non–interacting, plane-wave* state vectors has a rather complicated structure:

$$|V_{phys}\rangle = c_0|q\bar{q}\rangle + c_1|q\bar{q}g\rangle + c_2|q\bar{q}gg\rangle + c_3|q\bar{q}q\bar{q}\rangle + ... \tag{4.1}$$

We emphasize that in this decomposition, quarks and gluons are assumed free, i.e., *on-mass-shell*. The coefficients c_i can be called "wave functions" of the given projection of a physical vector meson, with $|c_i|^2$ being the probability of finding a vector meson in a given state.

The exact treatment of any reaction involving the vector meson must account for all terms in the above expansion. Demonstration of a method that would account for all these terms is, however, still an unresolved task, and currently one is limited to the term-by-term analysis of the vector meson reactions.

Given large number of papers devoted to the high-energy reactions involving vector mesons, and in particular, to the process of diffractive vector meson production in DIS, one might expect that the lowest Fock state in the above decomposition has already been thoroughly studied. It turns out, however, that it is not so, for in all early calculations the importance of the spin-angular coupling inside the vector meson and dramatic effects it entails were largely overlooked.

In this Chapter we fill this gap. We construct a full and exact theory of the vector meson stucture, provided the vector meson Fock space is saturated by the lowest $q\bar{q}$ state. Being only an approximation, this approach still is of vital importance to the whole field, for it results in a complete, self-consistent and self-contained spin-angular description of the vector meson. To our best knowlegde, our work represent the only satisfactory theory of spin structure of the vector meson.

4.2 LCWF and vertex factor

Let us now outline how a wave function of a bound state appears in the diagrammatic language.

In non-relativistic quantum mechanics, the two-particle bound state problem can be immediately reformulated as a problem for one particle of reduced mass μ, moving in the external potential. This reformulation allows one to split the wave function into two factors: the wave function of the motion of the composite particle as whole and the wave function corresponding to the internal motion of constituents. The former part factors out trivially, while the latter wave function obeys the following Schodinger equation

$$\left[\frac{\hat{p}^2}{2\mu} + V(r)\right]\psi(r) = E\psi(r)\,. \tag{4.2}$$

Since the wave function $\psi(r)$ and the interaction operator $V(r)$ exhibit good behavior at infinity, one can rewrite this equation in the momentum representation

$$\begin{aligned}
&\frac{p^2}{2\mu}\psi(p) + \frac{1}{(2\pi)^3}\int d^3k V(k)\psi(p-k) = E\psi(p)\,;\\
&\left(\frac{p^2}{m} - E\right)\psi(p) = -\frac{1}{(2\pi)^3}\int d^3k V(k)\psi(p-k)\,.
\end{aligned} \tag{4.3}$$

In this notation, this equation can be viewed as a homogeneous non-relativistic Bethe-Salpeter equation for the wave function $\psi(p)$ that describes the relative motion of constituents inside a composite particle.

Let us now introduce

$$\Gamma(p) \equiv \left(\frac{p^2}{m} - E\right)\psi(p) \tag{4.4}$$

Then Eq.(4.3) can be rewritten as

$$\Gamma(p) = -\frac{1}{(2\pi)^3}\int d^3k V(k)\frac{1}{\frac{(p-k)^2}{m} - E}\Gamma(p-k) \tag{4.5}$$

This equation has an absolutely straightforward diagrammatic interpretation (Fig.4.1). One sees that $\Gamma(p)$ stands for a bound-state $\to$ constituents transition vertex, with p being the relative momentum of the constituents. The actor $1/[\frac{(p-k)^2}{m} - E]$ describes propagation of the constituents and $V(k)$ stands for the interaction between constituents. Of course, the kinetic energy $p^2/2\mu \neq E$, the total energy, which is in fact negative, so no pole arises in the propagator.

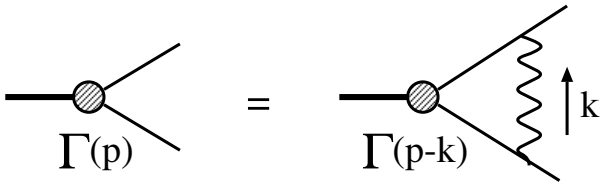

Figure 4.1: The diagrammatic interpretation of the integral equation for vertex function $\Gamma(p)$ (p is the relative constituents momentum).

In the relativistic case, i.e., in QFT, it is not clear *a priori* whether the whole picture that involves the wave function and the representation of the vector meson as free non-interacting constituents would work at all. Therefore, in our approach we will be aiming at introducing an appropriately defined wave function and demonstrating that hard processes involving vector mesons can be expressed in terms of expectation values of $q\bar{q}$ amplitudes between wave functions, i.e., we intend to treat a hard process in a probabilistic, quantum mechanics-like manner.

In the following we will show that this program succeeds. Namely we will introduce the *radial* wave function of the $q\bar{q}$ state of a vector meson as

$$\psi(q) \equiv \frac{\Gamma(q)}{M^2 - m_V^2}\,. \tag{4.6}$$

The angular dependence of the wave function will be treated separately, see Sect.4.4. Here $\Gamma(q)$ is the vertex factor, M^2 is the eigenvalue of the relativistic kinetic operator of the on-mass-shell $q\bar{q}$ state, and m_V^2 is the eigenvalue of the total relativisitic Hamiltonian, which is equal to the mass of the vector meson squared. Then, during an accurate and consistent analysis of a hard process Feynman diagrams, we will always make sure that wave function (4.6) automatically appears in calculations and the rest looks the same as if both fermions were on-mass-shell. If we see that fermion virtualities modify the results, or if different Fock states mix during hard interactions of the vector meson, it would signal the invalidity of the free particle parton language and consequenly the breakdown of the whole approach. This restriction must always be taken into account when obtaining and interpreting the parton model-based results.

4.3 Light cone formalism

The term "light cone approach" to high–energy process calculations can have different meanings. Some prefer to re-formulate the whole of QFT using light cone dynamics, introduce light cone quantization and derive light cone Feynman rules. For Light Cone Field Theory, see [24, 25]. One should keep in mind, however, that even within the usual QFT the light cone formalism can be freely used as a means to greatly simplify intermediate calculations. This is exactly the way we will use it.

It was noted long ago [26] that the calculation of a high-energy collision is simplied if one decomposes all momenta in terms of light cone n_+^μ, n_-^μ and transverse components, which we will always mark with the vector sign over a letter (so-called the Sudakov decomposition):

$$n_+^\mu = \frac{1}{\sqrt{2}}(1,\vec{0},1)\,; \quad n_-^\mu = \frac{1}{\sqrt{2}}(1,\vec{0},-1)\,; \quad (n_+n_-) = 1\,,\ (n_+n_+) = (n_-n_-) = 0$$

$$p^\mu = p_+ n_+^\mu + p_- n_-^\mu + \vec{p}^\mu\,; \quad p^2 = 2p_+p_- - \vec{p}^2\,. \tag{4.7}$$

Indeed, imagine two high energy particles colliding with momenta p^μ and q^μ, respectively, and equal masses m. Then one can choose such a frame of reference that in the Sudakov decomposition,

$$p^\mu = p_+ n_+^\mu + p_- n_-^\mu + \vec{p}^\mu\,,$$
$$q^\mu = q_+ n_+^\mu + q_- n_-^\mu + \vec{q}^\mu\,,$$

quantities p_- and q_+ are large ($p_-,\, q_+ \gg m$), while $p_+ = (\vec{p}^2 + m^2)/(2p_-)$ and $q_- = (\vec{q}^2 + m^2)/(2q_+)$ are small. The total energy squared of these two particles is, approximately,

$$s \equiv 2q_+p_-\,. \tag{4.8}$$

Note that our definition of s is somewhat different from the more familiar one $(p+q)^2$ by terms $\propto m^2, \vec{p}^2$. However, it is not of any importance for us, since in the course of the calculations we will keep track only of the highest power s contributions, i.e., everything will be calculated in the leading power of s approximation.

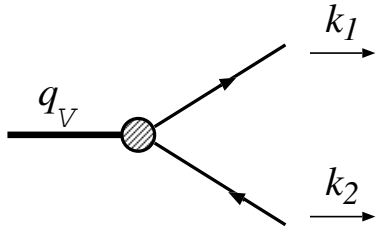

Figure 4.2: Kinematics of $V \to q\bar{q}$ vertex on the light cone. Vector meson momentum q_V is taken as incoming; constituents momenta are outgoing.

Let us now go further and examine the kinematics of a typical $q\bar{q}V$ vertex (Fig.4.2). The Sudakov decomposition of all momenta reads:

$$\begin{aligned} q_V^\mu &= q_{V+} n_+^\mu + q_{V-} n_-^\mu\,; \\ k_1^\mu &= k_{1+} n_+^\mu + k_{1-} n_-^\mu + \vec{k}^\mu = z q_{V+} n_+^\mu + y q_{V-} n_-^\mu + \vec{k}^\mu\,; \\ k_2^\mu &= k_{2+} n_+^\mu + k_{2-} n_-^\mu - \vec{k}^\mu = (1-z) q_{V+} n_+^\mu + (1-y) q_{V-} n_-^\mu - \vec{k}^\mu\,, \end{aligned} \tag{4.9}$$

so that

$$q_V^2 = 2q_{V+}q_{V-} = m_V^2\,; \quad k_1^\mu + k_2^\mu = q_V^\mu\,; \quad k_i^2 \neq m^2\,, \tag{4.10}$$

i.e., quarks can be off mass shell. Now let us introduce momenta k_i^* that would correspond to on-mass-shell fermions. The only component in k_i subject to modification is k_{i-}, or equivalently, the energy. Large k_{i+} components are insensitive to (reasonable) quark virtuality variations. So, to obtain the on-mass-shell momenta, one has to replace

$$k_{i-} = \frac{k_i^2 + \vec{k}^2}{2k_{i+}} \to k_{i-}^* = \frac{m^2 + \vec{k}^2}{2k_{i+}}\,. \tag{4.11}$$

Then the 4-vector

$$q^\mu = k_1^{*\mu} + k_2^{*\mu} \tag{4.12}$$

squared is equal to

$$M^2 = q^2 = 2q_+q_- = 2q_{V+}\left(k^*_{1-} + k^*_{2-}\right) = \frac{\vec{k}^2 + m^2}{z(1-z)}\,. \tag{4.13}$$

Once again we emphasize that the Feynman invariant mass (i.e., the total 4-momentum squared) of the virtual quark-antiquark pair is m_V^2. The quantity M^2 is the invariant mass of the free, non-interacting $q\bar{q}$ state (see 4.6). However it is precisely M, not m_V, that will govern the hard interaction of $q\bar{q}$ pair with gluons.

Finally, it is useful to introduce the relative momentum of free $q\bar{q}$ system:

$$2p_\mu = (k^*_1 - k^*_2)_\mu\,. \tag{4.14}$$

Trivial algebra then leads to

$$M^2 = 4m^2 + 4\mathbf{p}^2\,; \quad p^2 = -\mathbf{p}^2\,; \quad (pq) = 0\,, \tag{4.15}$$

where $\mathbf{p}$ is the relative 3-momentum in the $q\bar{q}$ pair rest frame. Its components are

$$\mathbf{p} = (\vec{p}, p_z)\,; \quad \vec{p} = \vec{k}\,; \quad p_z = \frac{1}{2}(2z-1)M\,. \tag{4.16}$$

4.4 Spin structure of a vector particle

Let us start with a well-known example of a deuteron, which is a non-relativistic analogy of a vector meson: they are both vector particles built up of two fermions. To have the correct (P-) parity, the proton and neutron must sit in the spin–triplet state, thus leaving us with two possible values of their angular momenta: $L = 0$ and 2.

In the conventional non-relativistic language one describes the spin-angular coupling by the Clebsh-Gordan technique. The non-relativistic Feynman diagram calculations can be best performed using an alternate approach. Here a deuteron, being a vector particle, is described by a 3-dimensional polarization vector $\mathbf{V}$. So, while calculating high energy processes involving $d \to pn$ transitions, one can use the following spin structure of deuteron-nucleon-nucleon vertex:

$$\phi_n^+\,\mathbf{\Gamma}\,\phi_p \cdot \mathbf{V}\,. \tag{4.17}$$

Since both nucleons can be treated on-mass-shell, only two terms enter Γ_i, which can be written as:

$$\phi_n^+\,\left[u(p)\sigma^i + w(p)(3p^ip^j - \delta^{ij}p^2)\sigma^j\right]\,\phi_p \cdot V^i \tag{4.18}$$

Here σ^i are Pauli matrices and $\mathbf{p}$ is the relative proton–neutron momentum. One immediately recognizes here spin structures corresponding to the pn pair sitting in S and D waves, respectively. In particular, squaring the above expression gives

$$\begin{aligned}
&(\mathbf{V}\mathbf{V}^*) \quad \text{for } |S|^2\\
&3(\mathbf{p}\mathbf{V})(\mathbf{p}\mathbf{V}^*) - (\mathbf{V}\mathbf{V}^*)\mathbf{p}^2 \quad \text{for } SD \text{ interference}\\
&3\mathbf{p}^2(\mathbf{p}\mathbf{V})(\mathbf{p}\mathbf{V}^*) + (\mathbf{V}\mathbf{V}^*)\mathbf{p}^4 \quad \text{for } |D|^2\,.
\end{aligned} \tag{4.19}$$

Now let us go relativistic and turn to vector mesons. The polarization state of a vector particle is described by a four-vector V_μ. Therefore, a general form of a $q\bar{q}V$ vertex has the form

$$\bar{u}'\Gamma_\mu u \cdot V_\mu \cdot \Gamma(p)\,,$$

where $\Gamma(p)$ is the familiar vertex factor. Up to now, it has been customary in the literature to choose the simplest form of the spinorial structure Γ_μ:

$$\bar{u}'\gamma_\mu u \cdot V_\mu \cdot \Gamma(p)\,. \tag{4.20}$$

One must admit, however, that (4.20) is simply an analogy of $q\bar{q}\gamma$ vertex and does not reflect the true internal structure of a vector meson. It is known [27] that the correct spinorial structure corresponding to pure the S wave $q\bar{q}$ state is

$$S_\mu = \gamma_\mu - \frac{2p_\mu}{M+2m} = \left(g_{\mu\nu} - \frac{2p_\mu p_\nu}{m(M+2m)}\right)\gamma_\nu \equiv \mathcal{S}_{\mu\nu}\gamma_\nu\,. \tag{4.21}$$

It is implied here that spinorial structures are inserted between *on-mass-shell spinors* in accordance with our principal guideline (see discussion in Sect.4.2).

Once S wave spinorial structure is established, the expression for D wave can be obtained by contracting S wave with the symmetric traceless tensor of rank two $3p_ip_j - \delta_{ij}\mathbf{p}^2$, rewritten in the Lorenz notation. To do so, one should replace

$$p_i \to p_\mu\,; \quad \delta_{ij} \to -g_{\mu\nu} + \frac{q_\mu q_\nu}{M^2}$$

(in the $q\bar{q}$ pair rest frame of reference $q_\mu = (M,\,0,\,0,\,0)$). However, since q_μ inserted between on-mass-shell spinors gives zero due to the Ward identity, one obtains the required tensor in the form $3p_\mu p_\nu + g_{\mu\nu}\mathbf{p}^2$. Its contraction with $\mathcal{S}_\mu$ yields

$$D_\mu = (3p_\mu p_\nu + g_{\mu\nu}\mathbf{p}^2)\cdot\mathcal{S}_{\nu\rho}\gamma_\rho = \mathbf{p}^2\gamma_\mu + (M+m)p_\mu = \left(\mathbf{p}^2 g_{\mu\nu} + \frac{M+m}{m}p_\mu p_\nu\right)\gamma_\nu \equiv \mathcal{D}_{\mu\nu}\gamma_\nu\,. \tag{4.22}$$

We will prove below that structures (4.21), (4.22) after being squared indeed reproduce (4.19); i.e., they correspond to pure S and D waves.

The quantities $\mathcal{S}_{\mu\nu}$ and $\mathcal{D}_{\mu\nu}$ used in (4.21), (4.22) have the meaning of S/D wave projectors, which will be used in all subsequent calculations. Namely all calculations will be at first performed for the naive $q\bar{q}V$ vertex (4.20) and then we will apply the projector technique to obtain expressions for S and D states.

4.5 Vector meson LCWF normalization

Before tackling the diffractive vector meson production process, we must first have a prescription for normalization of the vector meson wave function.

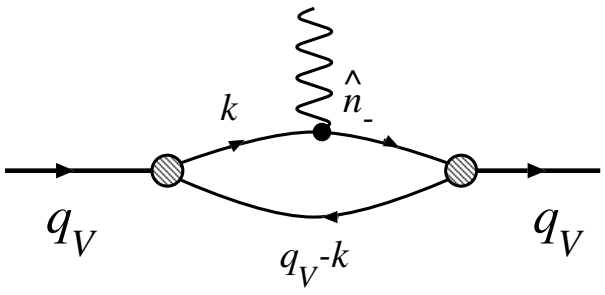

Figure 4.3: Diagram used for normalizing the vector meson LCWF. The amplitude of this diagram is set equal to $2q_+i$.

4.5.1 The naive $q\bar{q}V$ vertex

A natural way to normalize the wave function of a composite system is to set the amplitude given by the diagram in Fig.4.3 equal to $2q_+i$. Here the extra leg carries zero momentum but couples to the fermion line as $\gamma_\mu n_-^\mu$. Note that for a charged composite particle (e.g., a deuteron) this is precisely setting the electric form factor equal to unity in the soft photon limit.

As described above, we first treat the $q\bar{q}V$ vertex as $\bar{u}'\gamma_\mu u\cdot\Gamma(p)$. In this case the general expression for this amplitude is

$$A=\frac{(-1)}{(2\pi)^4}N_c\cdot\int d^4k\frac{Sp\{i\hat{V}_1\Gamma\cdot i(\hat{k}-\hat{q}_V+m)\cdot i\hat{V}_2^*\Gamma^*\cdot i(\hat{k}+m)\cdot i\hat{n}_-\cdot i(\hat{k}+m)\}}{[k^2-m^2+i\epsilon]\cdot[k^2-m^2+i\epsilon]\cdot[(k-q_V)^2-m^2+i\epsilon]}$$
$$=\frac{N_c}{(2\pi)^4}\cdot\int d^4k\frac{|\Gamma|^2Sp\{...\}}{[k^2-m^2+i\epsilon]^2[(k-q_V)^2-m^2+i\epsilon]}\,, \qquad (4.23)$$

where $N_c=3$ is a trivial color factor originating from the quark loop. We deliberately recognized V_1 and V_2 as distinct entities, just to make sure later that such a loop is diagonal in polarization states.

The first step is to rewrite this expression in terms of Sudakov's variables. As usual, one implements decomposition

$$k^\mu=zq_{V+}n_+^\mu+yq_{V-}n_-^\mu+\vec{k}^\mu\,;\quad q_V^2=2q_{V+}q_{V-}=m_V^2$$

and transforms

$$d^4k=\frac{1}{2}m_V^2d^2\vec{k}dydz\,.$$

Now we observe that the vertex functions Γ do not depend on y (and neither does the trace, as will be shown later), so we can immediately perform the integrations over y by means of the Cauchy theorem. Indeed, since the integral

$$\int_{-\infty}^{\infty}dy\frac{1}{[yzm_V^2-(\vec{k}^2+m^2)+i\epsilon]^2}\frac{1}{[(1-y)(1-z)m_V^2-(\vec{k}^2+m^2)+i\epsilon]}\,, \qquad (4.24)$$

is convergent and has good asymptotic behavior, one can close the integration contour in the most convenient way. To do so, one must find the position of all poles on the complex y plane:

$$y_{1,2}=\frac{\vec{k}^2+m^2}{zm_V^2}-\frac{i\epsilon}{zm_V^2};\quad y_3=1-\frac{\vec{k}^2+m^2}{(1-z)m_V^2}+\frac{i\epsilon}{(1-z)m_V^2}\,.$$

One sees that if $z<0$ or $z>1$, *all* poles lie on the same side of the real axis in the complex y plane, which leads to zero contribution. The contribution that survives comes from region $0<z<1$, which has, in fact, a simple physical meaning: all constituents must move in the same direction. In this region we close the integration contour in the upper half-plane and take the residue at $y=y_3$. Physically, this corresponds to putting the antiquark on-mass-shell. After this procedure, one gets for (4.24)

$$-\frac{2\pi i}{(1-z)m_V^2}\frac{1}{[yzm_V^2-(\vec{k}^2+m^2)+i\epsilon]^2}\Big|_{y=y_3}=-\frac{2\pi i}{(1-z)m_V^2}\frac{(1-z)^2}{[\vec{k}^2+m^2-z(1-z)m_V^2]^2}$$
$$=-\frac{2\pi i}{m_V^2}\frac{1}{z^2(1-z)}\frac{1}{[M^2-m_V^2]^2}\,.$$

One immediately recognizes here the same two-particle propagator as in (4.6). Therefore, the equation for the amplitude reads

$$A=i\frac{N_c}{(2\pi)^3}\cdot\int d^2\vec{k}\frac{dz}{z^2(1-z)}\cdot|\psi|^2\cdot\left(-\frac{1}{2}Sp\{...\}\right)\,. \tag{4.25}$$

We now turn to the trace calculations. As we found during the calculation of the forward Compton scattering amplitude, all the fermions can be treated in the trace calculations as if they were on-mass-shell. We will use this property in all subsequent calculations.

The easiest way to calculate the traces in our case is to do it covariantly, without involving further the Sudakov technique. Since quarks in the numerator can be as treated on-mass-shell, we first note that

$$(\hat{k}+m)\hat{n}_-(\hat{k}+m)=2(k^*n_-)(\hat{k}^*+m)\,,$$

so that

$$-\frac{1}{2}Sp\{...\}=-zq_+Sp\{\hat{V}_1(\hat{k}^*-\hat{q}+m)\hat{V}_2^*(\hat{k}^*+m)\}=-2zq_+\left[M^2(V_1V_2^*)+4(V_1p)(V_2^*p)\right]\,,$$

where p is the relative quark-antiquark momentum [see (4.15)]. Note that in the antiquark propagator we replaced $\hat{k}-\hat{q}_V\to\hat{k}^*-\hat{q}$, since the antiquark is now put on-mass-shell. Besides, we explicitly used here gauge condition $(qV)=0$, which means that polarization vectors must be written for the *on-mass-shell $q\bar{q}$ pair*, not the vector meson, — another important consequence of our approach. Substituting this into (4.25), one gets

$$1=\frac{N_c}{(2\pi)^3}\int d^2\vec{k}\frac{dz}{z(1-z)}|\psi|^2\left[-M^2(V_1V_2^*)-4(V_1p)(V_2^*p)\right]\,. \tag{4.26}$$

A prominent feature of this equation is the orthogonality of V_L and V_T polarization states — the necessary condition for any normalization prescription.

The next step is to realize that the integral can be cast in the form of $d^3\mathbf{p}$ integration by means of

$$\frac{dz}{z(1-z)}d^2\vec{k}=\frac{4}{M}dp_zd^2\vec{p}=\frac{4}{M}d^3\mathbf{p}\,.$$

Thus, the final expression for the normalization condition is

$$1=\frac{N_c}{(2\pi)^3}\int d^3\mathbf{p}\frac{4}{M}|\psi|^2[-M^2(V_1V_2^*)-4(V_1p)(V_2^*p)]\,. \tag{4.27}$$

We see that the expression being integrated is explicitly spherically non-symmetric, which is a manifestation of a certain D wave admixture. We now apply the projector technique to obtain results for S and D wave states.

4.5.2 Normalization for S wave vector meson

The correct expressions for pure S/D-type vertices can be readily obtained with the aid of the projector technique. Namely to obtain an expression for S wave, replace

$$V_\mu \to V_\nu \mathcal{S}_{\nu\mu}\,. \tag{4.28}$$

Such a replacement for V_1 leads to

$$-M^2(V_1V_2^*) - 4(V_1p)(V_2^*p) \Rightarrow -M^2(V_1V_2^*) - \frac{4M}{M+2m}(V_1p)(V_2^*p)$$

One then applies the same replacement to V_2^* to obtain

$$-M^2(V_1V_2^*) - \frac{4M}{M+2m}(V_1p)(V_2^*p) \Rightarrow -M^2(V_1V_2^*)\,.$$

The result for S wave states is

$$1 = \frac{N_c}{(2\pi)^3}\int d^3\mathbf{p}\; 4M|\psi^S(\mathbf{p}^2)|^2 \tag{4.29}$$

which is manifestly spherically symmetric.

4.5.3 Normalization for D wave vector meson

Results for D states are derived in the same way. The replacements $V_\mu^{(i)} \to V_\nu^{(i)}\mathcal{D}_{\nu\mu}\,,\ i=1,2$ lead to

$$-M^2\mathbf{p}^4(V_1V_2^*) + 3M^2\mathbf{p}^2(V_1p)(V_2^*p)\,. \tag{4.30}$$

After angular averaging,

$$\langle p_ip_j\rangle \to \frac{1}{3}\mathbf{p}^2\delta_{ij},$$

and one gets the normalization formula for D wave state:

$$1 = \frac{N_c}{(2\pi)^3}\int d^3\mathbf{p}\; 8M\mathbf{p}^4|\psi^D(\mathbf{p}^2)|^2 \tag{4.31}$$

Several remarks are in order. First, $S \to D$ state transitions are forbidden. Indeed, such an amplitude will be proportional to

$$-M^2[\mathbf{p}^2(V_1V_2^*) + 3(V_1p)(V_2^*p)]\,, \tag{4.32}$$

which vanishes after angular integration. We emphasize that the structure of results (4.29), (4.30), (4.32) is absolutely identical to Eq.(4.19). This fact can be viewed as the proof that spinorial structures (4.21), (4.22) indeed correspond to pure S and D wave states.

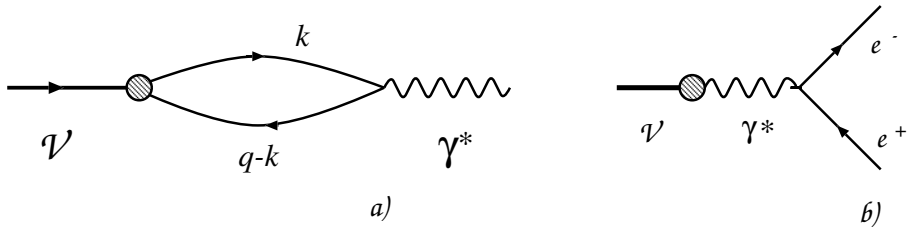

Figure 4.4: Normalizing LCWF to the $\Gamma(V \to e^+e^-)$ decay width: (a) the diagram for $V \to \gamma^*$ transition; (b) the diagram for $V \to e^+e^-$ decay.

4.6 Decay constant

An additional normalization condition consists in relating the vector meson wave function to the experimentally measurable physical quantity — $V \to e^+e^-$ decay width (Fig.4.4). The loop in Fig.4.4a describes transition $V \to \gamma^*$ and enters the amplitude of the decay $V \to e^+e^-$ (Fig.4.4b). Let us define the decay constant via

$$\mathcal{A} = i\langle 0|J^{em}_\mu|V\rangle = -if_V c_V \sqrt{4\pi\alpha} V_\mu \,. \tag{4.33}$$

So defined, f_V has dimension m^2. The quantity c_V reflects the flavor content of a vector meson (in the previous calculations it simply gave unity) and is equal to

$$c_V = \frac{1}{\sqrt{2}}, \frac{1}{3\sqrt{2}}, -\frac{1}{3}, \frac{2}{3} \tag{4.34}$$

for $\rho, \omega, \phi, J/\psi$ mesons, respectively.

Knowing that such a loop does not mix polarization states, we can multiply both sides of eq.(4.33) by V^* and get the expression

$$if_V = \frac{(-1)}{(2\pi)^4} N_c \cdot \int d^4k \frac{Sp\{i\hat{V}^* \cdot i(\hat{k}+m) \cdot i\hat{V}\Gamma \cdot i(\hat{k} - \hat{q}_V + m)\}}{(k^2 - m^2 + i\epsilon)\cdot((k-q_V)^2 - m^2 + i\epsilon)} \,. \tag{4.35}$$

Calculations similar to the above normalization condition derivation yield, for the naive type of vertex,

$$f_V = \frac{N_c}{(2\pi)^3} \cdot \int \frac{dz}{z(1-z)} d^2\vec{k}\ \psi_V[-M^2(VV^*) - 4(Vp)(V^*p)] \,. \tag{4.36}$$

Applying now the projector technique, one gets in the case of S states, after proper angular averaging,

$$f^{(S)} = \frac{N_c}{(2\pi)^3} \cdot \int d^3\mathbf{p}\ \psi_S \frac{8}{3}(M+m) \tag{4.37}$$

and, in the case of D states,

$$f^{(D)} = \frac{N_c}{(2\pi)^3} \cdot \int d^3\mathbf{p}\ \psi_D \frac{32}{3} \frac{\mathbf{p}^4}{M+2m} \,. \tag{4.38}$$

Finally, one can write down the expression for the decay width in terms of f_V:

$$\Gamma(V \to e^+e^-) = \frac{1}{32\pi^2 m_V^2} \cdot \frac{m_V}{2} 4\pi |A|^2 = \frac{4\pi\alpha^2}{3m_V^3} \cdot f_V^2 c_V^2 \,. \tag{4.39}$$

This formula can be used to extract the numerical value of f_V from experimental data.

4.7 Ansätze for LCWF

Later on we will be presenting numerical analyses of vector meson production cross sections, for which we will need some wave function Ansatz. Here we describe two forms of the wave function that will be exploited there. By no means should they be expected to accurately represent the true radial wave functions in a vector meson. Our Ansätze are pure guesses, based on non-relativistic quantum mechanical experience, of what the wave function *might* look like. Undoubtedly, such an approach involves a certain degree of ambiguity in the numerical results, and in our subsequent analysis we will study this ambiguity in detail.

4.7.1 Suppressed Coulomb wave functions

A first guess for the vector meson wave function, especially in the case of a heavy, non-relativistic meson, would be a Coulomb-like form, similar to the wave function of a positronium:

$$\psi(\mathbf{p}) \propto \frac{1}{(1+\mathbf{p}^2 a^2)^2}\,, \tag{4.40}$$

where a is a typical size of the meson.

However, such a hard wave function will not fit our course of calculations, since the expression for the decay constant will be ultra violet divergent. Furthermore, as we will see later, this hard wave function will lead to vector meson production amplitudes that do not saturate at scale $\mathbf{p}^2 \lesssim 1/a^2$, but that extend to $1/a^2 \ll \mathbf{p}^2 \lesssim Q^2$.

Thus, it appears that the hard wave function Ansatz leads to complications that do not seem to be resolvable within the lowest Fock state only. Therefore, starting from now, we will limit ourselves to the *soft wave function* Ansatz only, "soft wave function", meaning that all integrals of physically relevant amplitudes involving the wave function will be saturated by $\mathbf{p}^2 \lesssim 1/a^2$.

If we still prefer to have a Coulomb-like wave function, we can consider its slightly regularized form, which we will call the "suppressed Coulomb" wave function. In addition, in order to be able to conduct simple estimates, we will take as simple form as possible. So, in this ansatz the normalized wave functions read

$$\begin{aligned}
\psi_{1S}(\mathbf{p}^2) &= \frac{c_1}{\sqrt{M}}\frac{1}{(1+a_1^2\mathbf{p}^2)^2};\\
\psi_{2S}(\mathbf{p}^2) &= \frac{c_2}{\sqrt{M}}\frac{(\xi_{node}-a_2^2\mathbf{p}^2)}{(1+a_2^2\mathbf{p}^2)^3};\\
\psi_{D}(\mathbf{p}^2) &= \frac{c_D}{\sqrt{M}}\frac{1}{(1+a_D^2\mathbf{p}^2)^4}\,,
\end{aligned} \tag{4.41}$$

with normalization constants to be determined from Eqs.(4.29) and (4.31). Here parameters a_i are connected to the size of a bound system: in the coordinate representation $\psi_i \propto \exp(-r/a_i)$. For strict Coulomb functions one would have $a_D = 3a_2/2 = 3a_1 = R_{Bohr}$, where R_{Bohr} is the Bohr radius. However, this relation should be treated with care in the cases of $q\bar{q}$ quarkonia, where the quark-antiquark potential is quite complicated and therefore the a_i should rather be considered as free parameters. Value of ξ_{node} pinpoints the position of the node in the $2S$ radial wave function. For the pure Coulombic system $\xi_{node} = 1$, but in our case the exact

value of ξ_{node} should be obtained from the requirement of the orthogognality between $1S$ and $2S$ states, with a_1 and a_2 fixed from other requirements.

4.7.2 Oscillator type LCWF

By an oscillator-type wave function we mean

$$\psi(\mathbf{p}) \propto exp\left(-\frac{\mathbf{p}^2 a^2}{2}\right) ,$$

with a again being a typical size of the wave function. This wave function Ansatz corresponds to the case of a strong confinement. Although the approximately quadratic potential that leads to such a rapid descrease for $\mathbf{p}^2 > 1/a^2$ is not exactly what is suspected about the color-singlet static quark-antiquark potential (in the quenched approximation), these wave function still possess the main confinement-like properties.

In this ansatz one has

$$\begin{aligned}
\psi_{1S} &= c_1 \exp\left(-\frac{\mathbf{p}^2 a_1^2}{2}\right) ; \\
\psi_{2S} &= c_2 \left(\xi_{node} - \mathbf{p}^2 a_2^2\right) \exp\left(-\frac{\mathbf{p}^2 a_2^2}{2}\right) ; \\
\psi_D &= c_D \exp\left(-\frac{\mathbf{p}^2 a_D^2}{2}\right) .
\end{aligned} \tag{4.42}$$

Note again that for a purely oscillator potential one also has relation $a_D = a_2 = a_1$, which might not hold in our case, since the oscillator type potential is also a crude approximation of the true quark-antiquark interaction. The position of node ξ_{node} would be equal to $3/2$ for a pure oscillator model but, again in our case, its value could very well turn out to be different.

Chapter 5

Vector meson production amplitudes

5.1 Preliminary notes

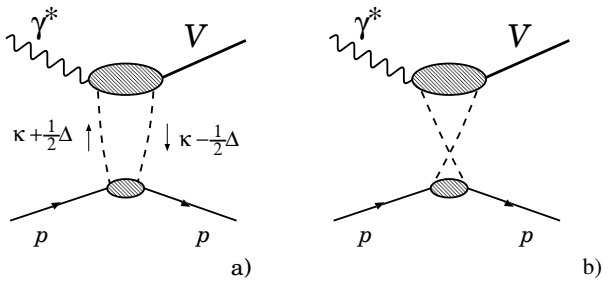

Figure 5.1: The QCD–inspired diagrams for $\gamma^* p \to Vp$ process with two gluon t–channel. Only Diagr.(a) contributes to the imaginary part of amplitudes.

Having set up the notation and defined and described a vector meson by itself, we are now ready to evaluate the full set of amplitudes of its off-forward virtual diffractive photoproduction.

In the pQCD-motivated approach to this process the pomeron exchange is viewed as a two-gluon exchange, as shown in Fig.5.1a. Using the scalarization procedure, we will split the diagram into two pieces and will treat each of them separately. The upper blob describes the pomeron-assisted transition of the virtual photon into a vector meson. In the perturbative QCD approach, which is legitimate here due to the presence of the relevant hard scale $\overline{Q}^2 = m_q^2 + z(1-z)Q^2$, the $q\bar{q}$ fluctuation of the virtual photon interacts with two hard gluons and then fuses to produce a vector meson. This interaction is described by four diagrams, given in Fig.5.2, with all possible two-gluons attachments to $q\bar{q}$ pair taken into account. All of them are equally important and needed for maintaining gauge–invariance and color transparency. The latter property means that in the case of very soft gluons the upper blob must yield zero, as the $q\bar{q}$ pair is colorless.

The lower part of the general diagram Fig.5.1a is, of course, not calculable in pQCD. The physically meaningful procedure is to relate it to the experimentally measurable gluon density. To do so, we will first calculate this lower blob in the Born approximation and then give a prescription for how to introduce the unintegrated gluon density. In the course of this

procedure we will neglect proton off-forwardness in the intermediate calculations and take it into account only at the very end, as a certain factor to the unintegrated gluon density.

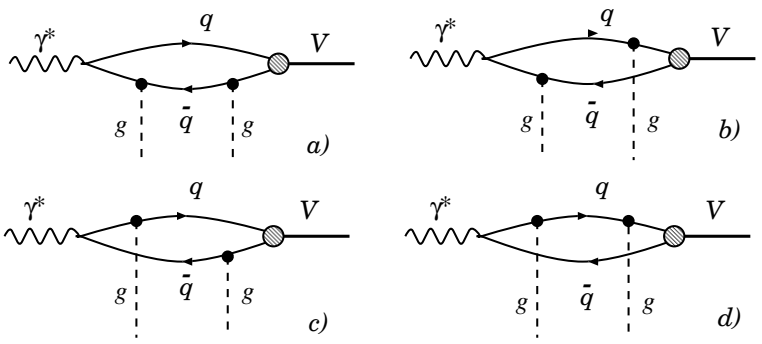

Figure 5.2: The content of the upper blob in Fig.5.1a in the pQCD approach. The true vector meson internal structure is approximated by the $q\bar{q}$ Fock state.

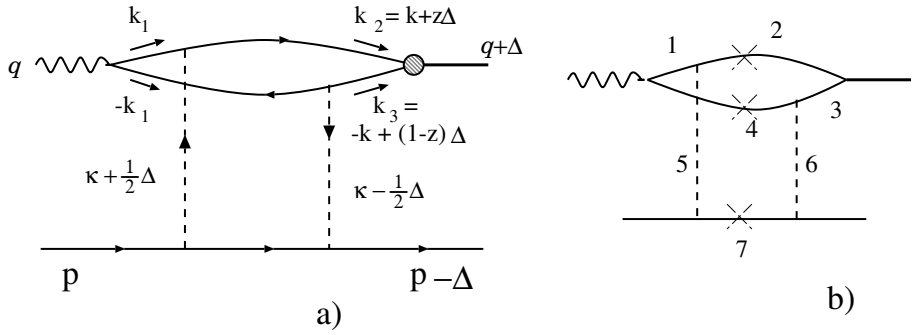

Figure 5.3: (a): A particularly useful convention of the loop momenta (only transverse components of quark momenta are shown). (b): the propagator notation used while calculating denominators. The crosses denote on-mass-shell particles.

5.2 Notation and helicity amplitudes

In our calculation we will use the following Sudakov decomposition (see also Fig.5.3a):

$$\begin{aligned} k_\mu &= y p_\mu{}' + z q_\mu{}' + \vec{k}_\mu \,; \\ \kappa_\mu &= \alpha p_\mu{}' + \beta q_\mu{}' + \vec{\kappa}_\mu \,; \\ \Delta_\mu &= \delta p_\mu{}' + \sigma q_\mu{}' + \vec{\Delta}_\mu \,. \end{aligned} \tag{5.1}$$

Here k and κ are momenta that circulate in the quark and gluon loops, respectively, and Δ is the momentum transfer. Vectors $p_\mu{}'$ and $q_\mu{}'$ denote the light-cone momenta: they are related to the proton and virtual photon momenta by

$$p_\mu = p_\mu{}' + \frac{m_p^2}{s} q_\mu{}'; \quad q_\mu = q_\mu{}' - x p_\mu{}'; \quad q'^2 = p'^2 = 0; \quad x = \frac{Q^2}{s} \ll 1; \quad s = 2(p'q') \,. \tag{5.2}$$

As it was mentioned in the Introduction, the condition $x \ll 1$ is necessary in order to speak about diffractive processes. The longitudinal momentum transfer can be readily found from kinematics (see Fig.5.1). In the higher power s terms it reads

$$m_p^2 = p^2 = (p-\Delta)^2 = m_p^2 - 2(p\Delta) + \Delta^2; \quad \Rightarrow \quad \sigma = -\frac{\vec{\Delta}^2}{s}\,;$$
$$m_V^2 = (q+\Delta)^2 = -Q^2 + 2(q\Delta) + \Delta^2 \quad \Rightarrow \quad \delta = x + \frac{m_V^2 + \vec{\Delta}^2}{s}\,. \tag{5.3}$$

The final vector meson momentum is given by

$$q_{V\mu} = q_\mu{}' + \frac{m_V^2 + \vec{\Delta}^2}{s} p_\mu{}' + \vec{\Delta}_\mu\,. \tag{5.4}$$

Finally, throughout the text, transverse momenta will be marked by the vector sign as $\vec{k}$ and 3-vectors will be written in bold characters.

There are several possible helicity amplitudes in the transition $\gamma^*_{\lambda_\gamma} \to V_{\lambda_V}$. First of all, both photon and vector meson can be transversely polarized. The polarization vectors are

$$e_{T\mu} = \vec{e}_\mu\,; \quad V_{T\mu} = \vec{V}_\mu + \frac{2(\vec{\Delta}\vec{V})}{s}(p'-q')_\mu\,. \tag{5.5}$$

Note that we took into account the fact that the vector meson momentum has finite transverse component $\vec{\Delta}$. The virtual photon can then have scalar polarization (which is often called longitudinal; we will use both terms) with polarization vector

$$e_{0\mu} = \frac{1}{Q}(q' + xp')_\mu\,. \tag{5.6}$$

Finally, the longitudinal polarization state of a vector meson is given by

$$V_{L\mu} = \frac{1}{M}\left(q_\mu{}' + \frac{\vec{\Delta}^2 - M^2}{s} p_\mu{}' + \vec{\Delta}_\mu\right)\,. \tag{5.7}$$

Note that, as we have already mentioned, in the self-consistent approach we must take the *running polarization vector* for the longitudinal polarization state. It depends on M, not m_V, which reflects the fact that in our approach we first calculate the production of an on-shell $q\bar{q}$ pair with (whose dynamics is governed by M) and then projects it onto the physical vector meson. We stress that this projection will automatically arise in the course of usual Feynman diagram evaluation.

Thus, there are 5 different amplitudes:

$$\begin{aligned} &L \to L \\ &T \to T \ (\lambda_\gamma = \lambda_V) \\ &T \to L \\ &L \to T \\ &T \to T \ (\lambda_\gamma = -\lambda_V) \end{aligned} \tag{5.8}$$

The first two are helicity-conserving amplitudes. They are dominant and almost insensitive to the momentum transfer $\vec{\Delta}$. The next two are single helicity flipping amplitudes. They are unavoidably proportional to $|\vec{\Delta}|$ in the combination $(\vec{e}\vec{\Delta})$ or $(\vec{V}^*\vec{\Delta})$ and would be vanishing for strictly forward scattering. Finally, the last amplitude corresponds to double helicity flip and will be proportional to $(\vec{e}\vec{\Delta})(\vec{V}^*\vec{\Delta})$.

5.3 The general amplitude

We will take the diagram of Fig.5.2c (also shown in Fig.5.3) as a generic diagram and perform a thorough analysis of it. It turns out that the other diagrams can — and will be — calculated in the same fashion.

The general expression for the amplitude given by Fig.5.2c reads:

$$
\begin{aligned}
iA = \int \frac{d^4k}{(2\pi)^4} \int \frac{d^4\kappa}{(2\pi)^4}\ \bar{u}'_p(-ig\gamma^{\nu'}t^{B'})i\frac{\hat{p}-\hat{\kappa}_1+m_p}{\left[(p-\kappa)^2-m_p^2+i\epsilon\right]}(-ig\gamma^{\mu'}t^{A'})u_p \\
\cdot(-i)\frac{g_{\mu\mu'}\delta_{AA'}}{\kappa_1^2-\mu^2+i\epsilon}\cdot(-i)\frac{g_{\nu\nu'}\delta_{BB'}}{\kappa_2^2-\mu^2+i\epsilon}\cdot c_V\cdot\Gamma^* \\
\cdot\frac{Sp\left\{ie\hat{e}\ i(\hat{k}_4+m)\ (-ig\gamma^{\nu}t^{B})\ i(\hat{k}_3+m)i\hat{V}^*\ i(\hat{k}_2+m)\ (-ig\gamma^{\mu}t^{A})\ i(\hat{k}_1+m)\right\}}{[k_1^2-m^2+i\epsilon]\,[k_2^2-m^2+i\epsilon]\,[k_3^2-m^2+i\epsilon]\,[k_4^2-m^2+i\epsilon]}
\end{aligned}
\tag{5.9}
$$

Here c_V is the same as in (4.34) and Γ is the familiar $q\bar{q}\to V$ vertex function. Note that we introduced "gluon mass" μ in gluon propagators to account for confinement at a phenomenological level.

Let's first calculate the numerator.

5.4 The color factor

If we consider strictly forward gluon scattering off a single quark, we have

$$
\frac{1}{N_c}Sp\{t^{B'}t^{A'}\}\cdot\delta_{AA'}\delta_{BB'}Sp\{t^Bt^A\}=\frac{1}{N_c}\frac{1}{2}\delta_{AB}\frac{1}{2}\delta_{AB}=\frac{1}{2}\frac{N_c^2-1}{2N_c}=\frac{1}{2}C_F=\frac{2}{3} \tag{5.10}
$$

However, we should take into account that quarks are sitting inside a colorless proton, whose color structure is

$$
\psi_{color}=\frac{1}{\sqrt{6}}\epsilon^{abc}q^aq^bq^c \tag{5.11}
$$

In this case there are two ways a pair of gluons can couple 3 quark lines (see Fig.5.4). In the first way, both gluons couple to the same quark. Since the quark momentum does not change after these two interactions, the nucleon stays in the same state: $\langle N|N\rangle=1$. In the second case gluon legs are attached to different quark lines, so that extra momentum κ circulates between quarks, which gives rise to the factor $\langle N|\exp(i\kappa r_1-i\kappa r_2)|N\rangle$, i.e. to the two-body form factor. Therefore, for the lower line, instead of

$$
\frac{1}{N_c}Sp\{t^Bt^A\}=\frac{1}{N_c}\frac{1}{2}\delta_{AB} \tag{5.12}
$$

one has

$$\begin{aligned}
&\frac{1}{6}\epsilon^{abc}\left(3\delta_{aa'}\delta_{bb'}t^A_{cc''}t^B_{c''c'}+6\delta_{aa'}t^A_{bb'}t^B_{cc'}\langle N|\exp(i\kappa r_1-i\kappa r_2)|N\rangle\right)\epsilon^{a'b'c'}\\
=\;& Sp\{t^At^B\}-Sp\{t^At^B\}\langle N|\exp(i\kappa r_1-i\kappa r_2)|N\rangle\\
=\;& \frac{1}{2}\delta_{AB}(1-\langle N|\exp(i\kappa r_1-i\kappa r_2)|N\rangle)\,. \qquad (5.13)
\end{aligned}$$

Note also that a similar calculation for N_c number of colors would yield the same result. Thus, the overall color factor is

$$\frac{1}{2}C_FN_cV(\kappa)=2V(\kappa)\equiv\frac{1}{2}C_FN_c(1-\langle N|\exp(i\kappa r_1-i\kappa r_2)|N\rangle). \qquad (5.14)$$

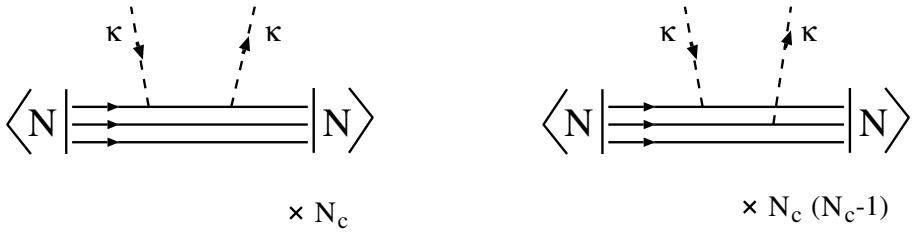

Figure 5.4: The ways two gluons can couple a colorless nucleon.

5.5 Scalarization of upper and lower parts

As is known, the highest power s contribution comes from so-called nonsense components of the gluon propagator (density matrix) decomposition:

$$g_{\mu\mu'}=\frac{2p'_\mu q'_{\mu'}}{s}+\frac{2p'_\mu q'_{\mu'}}{s}+g^\perp_{\mu\mu'}\;\approx\;\frac{2p'_\mu q'_{\mu'}}{s}\,. \qquad (5.15)$$

The lower (proton) line gives then

$$\bar u'(p)\cdot\hat q'(\hat p-\hat\kappa_1+m_p)\hat q'\cdot u(p-\Delta) \qquad (5.16)$$

To the highest power s order, it can be rewritten as

$$\bar u'_p\hat q'\hat p'\hat q'u_p\Big|_{forward}=\frac{1}{2}Sp\{\hat p'\hat q'\hat p'\hat q'\}=s^2\,. \qquad (5.17)$$

As we already mentioned, the effect of off-forwardness (skewedness) will be taken into account later. Combining all factors, one has for the numerator of Eq.(5.9)

$$\begin{aligned}
&(4\pi\alpha_s)^2\,\sqrt{4\pi\alpha_{em}}\;c_V\cdot\frac{1}{2}C_FN_cV(\kappa)\frac{4}{s^2}s^2\cdot Sp\left\{\hat e\;(\hat k_4+m)\;\hat q'\;(\hat k_3+m)\;\hat V^*\;(\hat k_2+m)\;\hat q'\;(\hat k_1+m)\right\}\\
=\;&(4\pi\alpha_s)^2\,\sqrt{4\pi\alpha_{em}}\;c_V\cdot 2C_FN_cV(\kappa)\cdot 2s^2\cdot I^{(c)}(\gamma^*\to V)\,. \qquad (5.18)
\end{aligned}$$

Note that we factored out $2s^2$ from the trace because it will appear later in all trace calculations. The resulting expression for amplitude (5.9) is then

$$A = \sqrt{4\pi\alpha_{em}}\, 4C_F N_c s^2\, c_V \cdot \int \frac{d^4k}{(2\pi)^4} \int \frac{d^4\kappa}{(2\pi)^4} \cdot \frac{(4\pi\alpha_s)^2 V(\kappa)}{\left[(p-\kappa_1)^2 - m_p^2 + i\epsilon\right] [\kappa_1^2 - \mu^2 + i\epsilon] [\kappa_2^2 - \mu^2 + i\epsilon]}$$
$$\cdot \frac{\Gamma^* I^{(c)}(\gamma^* \to V)}{[k_1^2 - m^2 + i\epsilon] [k_2^2 - m^2 + i\epsilon] [k_3^2 - m^2 + i\epsilon] [k_4^2 - m^2 + i\epsilon]} \tag{5.19}$$

One can immediately write similar expressions for the other three diagrams (Fig.5.2 a,b,d). Indeed, they will differ from Eq.(5.19) only by the last line: they will have different expressions for traces and propagator structures.

5.6 Denominator evaluation

We now turn to the calculation of denominators. As usual, we implement the Sudakov decomposition (5.1) and make use of the relation

$$d^4k = \frac{1}{2} s dy\, dz\, d^2\vec{k}\,.$$

Our procedure for evaluating the resulting integrals is motivated by the following arguments. We are interested only in the imaginary part of these diagrams. In fact, it can be shown that at the level of accuracy used here, the diagram in Fig.5.1a gives rise only to the imaginary part of the amplitude. The real part is given by Fig.5.1b and can be readily found from analyticity, so that here is no need for additional calculations. However it turns out small due to the smallness of the pomeron intercept, so we will neglect it in our subsequent calculations.

The imaginary part is calculated by setting three particles in the s-channel cut on-mass-shell, as is illustrated in Fig.5.3b. One way to do so is to apply the Cutkosky rules to modify our expression. Another, more straightforward way is to calculate three of the integrals (namely over α, β, y) via residues, which we do here.

The details of this calculations are given in Appendix A. Here we cite the result:

$$Im \int dy\, dz\, d\alpha\, d\beta\, \frac{\Gamma}{[\text{all propagators}]}$$
$$= \left(-\frac{\pi i}{s}\right)\left(-\frac{2\pi i}{s}\right)^2 \cdot \int \frac{dz}{z(1-z)} \psi_V(z,\vec{k}^2) \cdot \frac{1}{[\vec{k}_1^2 + m^2 + z(1-z)Q^2]} \frac{1}{(\vec{\kappa}^2+\mu^2)^2} \tag{5.20}$$

Here $\vec{k}_1$ is the transverse momentum flowing through photon vertex along the fermion line. Particularly, for diagram Fig.5.2c it is equal to $\vec{k}_1 = \vec{k} - (1-z)\vec{\Delta} - \vec{\kappa}_2$ (with the specific quark loop momentum choice given at Fig.(5.3a)).

Thus, the amplitude for this diagram has the form

$$A = \sqrt{4\pi\alpha_{em}}\, 4C_F N_c s^2\, c_V \cdot \frac{1}{2}s\, \frac{1}{2}s \cdot \left(-\frac{\pi i}{s}\right)\left(-\frac{2\pi i}{s}\right)^2 \cdot \frac{1}{(2\pi)^8}$$
$$\cdot \int \frac{dz}{z(1-z)} d^2\vec{k} \psi_V(z,\vec{k}^2) \int \frac{d^2\vec{\kappa} V(\kappa)}{(\vec{\kappa}^2+\mu^2)^2} (4\pi\alpha_s)^2 \cdot \frac{I^{(c)}}{[\vec{k}_1^2 + m^2 + z(1-z)Q^2]}\,. \tag{5.21}$$

After bringing all coefficients together, one gets

$$A^{(a)} = is\frac{C_F N_c c_V\sqrt{4\pi\alpha_{em}}}{64\pi^5}\cdot\int\frac{dz}{z(1-z)}d^2\vec{k}\psi_V(z,\vec{k}^2)\int\frac{d^2\vec{\kappa}V(\kappa)}{(\vec{\kappa}^2+\mu^2)^2}(4\pi\alpha_s)^2 \times\frac{I^{(c)}}{\vec{k}_1^2+m^2+z(1-z)Q^2}\,. \tag{5.22}$$

The other diagrams are calculated in the same way. The most important difference is that for each diagram we will have a propagator $1/[\vec{k}_1^2+m^2+z(1-z)Q^2]$ with its own definition of $\vec{k}_1$, the transverse momentum in photon vertex:

$$\begin{aligned}
&\text{a}\quad \vec{k}_{1a}=\vec{k}-(1-z)\vec{\Delta}=\vec{r}-\frac{1}{2}\vec{\Delta}\\
&\text{b}\quad \vec{k}_{1b}=\vec{k}-(1-z)\vec{\Delta}+\vec{\kappa}+\frac{1}{2}\vec{\Delta}=\vec{r}+\vec{\kappa}\\
&\text{c}\quad \vec{k}_{1c}=\vec{k}-(1-z)\vec{\Delta}-\vec{\kappa}+\frac{1}{2}\vec{\Delta}=\vec{r}-\vec{\kappa}\\
&\text{d}\quad \vec{k}_{1d}=\vec{k}+z\vec{\Delta}=\vec{r}+\frac{1}{2}\vec{\Delta}
\end{aligned} \tag{5.23}$$

Here $\vec{r}\equiv\vec{k}-(1-2z)\vec{\Delta}/2$. Thus, the whole expression for the imaginary part of the amplitude is

$$\begin{aligned}
A = {} & is\frac{C_F N_c c_V\sqrt{4\pi\alpha_{em}}}{64\pi^5}\cdot\int\frac{dz}{z(1-z)}d^2\vec{k}\psi_V(z,\vec{k}^2)\int\frac{d^2\vec{\kappa}V(\kappa)}{(\vec{\kappa}^2+\mu^2)^2}\,(4\pi\alpha_s)^2\\
&\times\left[\frac{1-z}{z}\frac{I^{(a)}}{\vec{k}_{1a}^2+m^2+z(1-z)Q^2}+\frac{I^{(b)}}{\vec{k}_{1b}^2+m^2+z(1-z)Q^2}\right.\\
&\left.+\frac{I^{(c)}}{\vec{k}_{1c}^2+m^2+z(1-z)Q^2}+\frac{z}{1-z}\frac{I^{(d)}}{\vec{k}_{1d}^2+m^2+z(1-z)Q^2}\right].
\end{aligned} \tag{5.24}$$

5.7 Off-forward gluon density

In Sect. 2.4 we discussed the forward unintegrated gluon density $\mathcal{F}(x_g,\vec{\kappa})$ and developed a prescription (see Eq.(2.39)) for how to introduce it into the k_t-factorization calculations. Being devised for forward scattering processes only, this gluon density bears a clear probabilistic sense, which is reflected in the word "density".

In the present case of vector meson production, the initial and final states are kinematically distinct, therefore the forward unintegrated gluon density in its pure form is not the relevant quantity; instead, the off-forward (or skewed) gluon structure function [28]

$$\mathcal{F}(x_1,x_2,\vec{\kappa},\vec{\Delta}) \tag{5.25}$$

should be used. It depends on the light cone momenta x_1 and x_2 carried by the first and the second gluon, on the transverse momentum $\vec{\kappa}$ inside the gluon loop, and on the total transverse momentum transfer $\vec{\Delta}$. At $x_1=x_2$ and $\vec{\Delta}=0$, the forward gluon structure function is recovered, which means that even the strictly forward vector meson production should be described by the off-forward gluon structure function.

The experimental determination of the off-forward gluon density might, in principle, be possible from accurate measurements of the off-forward virtual Compton scattering process, but the lack of such measurements makes this analysis infeasible in the nearest future. Thus, the original idea to involve in the vector meson calculations as little ambiguity as possible by determining the gluon content of the proton from other reactions does not work. One might, of course, expect that replacement

$$\mathcal{F}(x_1, x_2, \vec{\kappa}, \vec{\Delta}) \to \mathcal{F}\left(\frac{x_1 + x_2}{2}, \vec{\kappa}\right) \tag{5.26}$$

should be quite legitimate in kinematical regimes when $x_1 \approx x_2$, $\vec{\Delta} \ll \vec{\kappa}$, however such a regime obtains only in the photoproduction of light mesons and is severely violated as we go to higher Q^2 or higher m_V, so that such a replacement would be a poor option for most of the cases we study.

There is, however, way around, which allows us to reduce the unknown off-forward gluon distributions to the forward ones. As shown in [29], if the energy behavior of the gluon densities is describable by a simple Regge-type behavior

$$\mathcal{F} \propto \left(\frac{1}{x}\right)^{\lambda}, \tag{5.27}$$

then in the case $x_1 \gg x_2$ the off-forward unintegrated gluon structure functions can be related to the forward unintegrated gluon density according to

$$\mathcal{F}(x_1, x_2 \to 0, \vec{\kappa}, \vec{\Delta} \to 0) = R_g \cdot \mathcal{F}(x_1, \vec{\kappa}); \quad R_g = \frac{2^{2\lambda+3}}{\sqrt{\pi}} \frac{\Gamma(\lambda + \frac{5}{2})}{\Gamma(\lambda + 4)}. \tag{5.28}$$

Bearing this exact result in mind, one can hope that a similar relation will hold for gluon densities with a somewhat more complicated energy behavior — if the effective exponent λ is calculated in the vicinity of the kinematical point x_1, $\vec{\kappa}$.

Note that for the purposes of approximate numerical calculation correspondence (5.28) can be further simplified. Introduce an agrument shift $c(\lambda)$ such that

$$\mathcal{F}(x_1, 0, \vec{\kappa}, 0) \propto \frac{2^{2\lambda+3}}{\sqrt{\pi}} \frac{\Gamma(\lambda + \frac{5}{2})}{\Gamma(\lambda + 4)} \cdot \left(\frac{1}{x_1}\right)^{\lambda} = \left(\frac{1}{c(\lambda) x_1}\right)^{\lambda} \tag{5.29}$$

holds for all x_1. Simple arithmetics shows that $c(\lambda)$ changes from ≈ 0.435 at $\lambda = 0$ to 0.4 at $\lambda = 1$. Given this very flat dependence, we can approximate $c(\lambda)$ by a constant value 0.41 so that

$$\mathcal{F}(x_g, 0, \vec{\kappa}, 0) \approx \mathcal{F}(0.41 x_g, \vec{\kappa}). \tag{5.30}$$

This form will be used in our numerical calculations.

The effect of non-zero $\vec{\Delta}$ comes both from the pomeron-exchange and from the proton impact factor. Since pomeron singularity moves in complex j plane as $|t| = \vec{\Delta}^2$ changes, the value of the effective pomeron intercept will be affected by $\vec{\Delta}^2$, a customary representation of this effect (in the linear Regge trajectory approximation) being

$$\alpha_{I\!P}(\vec{\Delta}^2) = \alpha_{I\!P}(0) - b_{I\!P} \vec{\Delta}^2. \tag{5.31}$$

Although in our case the effective intercept of the gluon density is not an input number, but is generated dynamically, we still account for the above effect by multiplying the gluon density by the factor

$$\exp\left[-b_{I\!P}\vec{\Delta}^2\log(x_0/x)\right], \tag{5.32}$$

with $x_0 = 0.03$ and trajectory slope $b_{I\!P}$ taken to be different for hard ($x_{I\!P}^{hard} = 0.07$) and soft ($x_{I\!P}^{soft} = 0.15$) parts of the gluon density. Since the resulting contribution to the slope increases with energy growth, this effect is called the diffractive cone shrinkage.

The second — and the most significant effect of non-zero $\vec{\Delta}$ — comes from the proton impact factor. Effectively, it amounts to introduction of a proton form factor $F(\Delta^2)$, which would be equal to 1 at $\vec{\Delta}^2 = 0$ and would start significantly decreasing when $\vec{\Delta}^2$ grows larger than a certain scale $1/\Lambda_p^2$. In our numerical calculations we used the dipole form factor

$$F(\vec{\Delta}^2) = \left(\frac{1}{1+\vec{\Delta}^2/\Lambda_p^2}\right)^2 \tag{5.33}$$

with $\Lambda_p^2 = 1$ GeV^{-2}.

5.8 Final results for the naive vertex

Now, with the off-forward gluon structure function properly defined, the only things left to be calculated are integrands $I^i(\gamma \to V)$. For convenience, their calculation is also given in Appendix B. It turns out that the results can be written in the same way for all four diagrams via $\vec{k}_1$ given by (5.23); i.e., all quantities:

$$-\frac{1-z}{z}I^{(a)}, \quad I^{(b)}, \quad I^{(c)}, \quad -\frac{z}{1-z}I^{(d)}$$

can be written in a similar way:

$$\begin{array}{ll} T \to T & \left[(\vec{e}\vec{V}^*)(m^2+\vec{k}\vec{k}_1)+(\vec{V}^*\vec{k})(\vec{e}\vec{k}_1)(1-2z)^2-(\vec{e}\vec{k})(\vec{V}^*\vec{k}_1)\right] \\ L \to L & -4z^2(1-z)^2QM \\ T \to L & 2z(1-z)M(\vec{e}\vec{k}_1)(1-2z) \\ L \to T & -2z(1-z)Q(1-2z)(\vec{V}^*\vec{k}) \end{array}$$

We can, therefore, cast amplitude (5.24) in a compact form with the aid of functions $\vec{\Phi}_1$ and Φ_2:

$$\Phi_2 = -\frac{1}{(\vec{r}+\vec{\kappa})^2+\overline{Q}^2} - \frac{1}{(\vec{r}-\vec{\kappa})^2+\overline{Q}^2} + \frac{1}{(\vec{r}+\vec{\Delta}/2)^2+\overline{Q}^2} + \frac{1}{(\vec{r}-\vec{\Delta}/2)^2+\overline{Q}^2}; \tag{5.34}$$

$$\vec{\Phi}_1 = -\frac{\vec{r}+\vec{\kappa}}{(\vec{r}+\vec{\kappa})^2+\overline{Q}^2} - \frac{\vec{r}-\vec{\kappa}}{(\vec{r}-\vec{\kappa})^2+\overline{Q}^2} + \frac{\vec{r}+\vec{\Delta}/2}{(\vec{r}+\vec{\Delta}/2)^2+\overline{Q}^2} + \frac{\vec{r}-\vec{\Delta}/2}{(\vec{r}-\vec{\Delta}/2)^2+\overline{Q}^2}. \tag{5.35}$$

With these functions, for the naive $q\bar{q}V$ vertex the whole expression in square brackets in (5.24) with sign minus (which we denote here as $I_{\lambda_\gamma\lambda_V}$) has the form:

$$\begin{aligned} I_{LL} &= -4QMz^2(1-z)^2\Phi_2\,; \\ I_{TT} &= (\vec{e}\vec{V}^*)[m^2\Phi_2 + (\vec{k}\vec{\Phi}_1)] + (1-2z)^2(\vec{k}\vec{V}^*)(\vec{e}\vec{\Phi}_1) - (\vec{e}\vec{k})(\vec{V}^*\vec{\Phi}_1)\,; \\ I_{TL} &= 2Mz(1-z)(1-2z)(\vec{e}\vec{\Phi}_1)\,; \\ I_{LT} &= -2Qz(1-z)(1-2z)(V\vec{k})\Phi_2\,. \end{aligned} \tag{5.36}$$

Replacing $V(\kappa)$ by the unintegrated gluon density according to (2.39) and using the approximation for the off-forward gluon density (5.30), we obtain the final expressions for a general amplitude of reaction $\gamma^*_{\lambda_\gamma} \to V_{\lambda_V}$ in the naive vertex:

$$\boxed{\begin{aligned} A(x,Q^2,\vec{\Delta}) = -is\frac{c_V\sqrt{4\pi\alpha_{em}}}{4\pi^2}\int_0^1\frac{dz}{z(1-z)}\int d^2\vec{k}\psi(z,\vec{k}) \\ \int\frac{d^2\vec{\kappa}}{\vec{\kappa}^4}\alpha_S\mathcal{F}(x,\vec{\kappa},\vec{\Delta})\cdot I(\gamma^*\to V)\,, \end{aligned}} \tag{5.37}$$

5.9 Final results for S and D wave amplitudes

Now we can use projector technique to obtain results for S/D wave states.

$$V_\mu \to V_\nu\mathcal{S}_{\nu\mu}\,; \quad \mathcal{S}_{\mu\nu} = g_{\mu\nu} - \frac{2p_\mu p_\nu}{m(M+2m)} \;\Rightarrow\; I^S = I + \frac{2(\mathbf{Vp})}{m(M+2m)}p_\mu\otimes\gamma_\mu\,; \tag{5.38}$$

$$V_\mu \to V_\nu\mathcal{D}_{\nu\mu}\,; \quad \mathcal{D}_{\mu\nu} = \mathbf{p}^2 g_{\mu\nu} + \frac{(M+m)p_\mu p_\nu}{m} \;\Rightarrow\; I^D = I\mathbf{p}^2 - \frac{(M+m)(\mathbf{Vp})}{m}p_\mu\otimes\gamma_\mu\,;$$

Note that $(\mathbf{Vp})$ is 3D scalar product. While contracting, we encounter terms proportional to $p_\mu\otimes\gamma_\mu$ which should be understood as

$$p_\mu\otimes\gamma_\mu = I_{V_T}\{\vec{V}\to\vec{p}\} + I_{V_L}\{1\equiv V_z\to p_z\equiv\frac{1}{2}(2z-1)M\}. \tag{5.39}$$

The result of this substitution reads:
for e_T:

$$\begin{aligned} &I_{T\to T}\{\vec{V}\to\vec{p}\} + I_{T\to L}\{1\equiv V_z\to p_z\equiv\frac{1}{2}(2z-1)M\} \\ &= m^2\left[(\vec{e}\vec{k})\Phi_2 - (\vec{e}\vec{\Phi}_1)(1-2z)^2\right] \end{aligned} \tag{5.40}$$

for e_0:

$$\begin{aligned} &I_{L\to T}\{\vec{V}\to\vec{p}\} + I_{L\to L}\{1\equiv V_z\to p_z\equiv\frac{1}{2}(2z-1)M\} \\ &= -2Qz(1-z)(2z-1)m^2\Phi_2 \end{aligned} \tag{5.41}$$

Thus, the resulting integrands for S wave type mesons are

$$
\begin{aligned}
I^S_{L\to L} &= -4QMz^2(1-z)^2\left[1+\frac{(1-2z)^2}{4z(1-z)}\frac{2m}{M+2m}\right]\Phi_2\,;\\
I^S_{T\to T} &= (\vec{e}\vec{V}^*)[m^2\Phi_2+(\vec{k}\vec{\Phi}_1)]+(1-2z)^2(\vec{k}\vec{V}^*)(\vec{e}\vec{\Phi}_1)\frac{M}{M+2m}\\
&\quad -(\vec{e}\vec{k})(\vec{V}^*\vec{\Phi}_1)+\frac{2m}{M+2m}(\vec{k}\vec{e})(\vec{k}\vec{V}^*)\Phi_2\,;\\
I^S_{T\to L} &= 2Mz(1-z)(1-2z)(\vec{e}\vec{\Phi}_1)\left[1+\frac{(1-2z)^2}{4z(1-z)}\frac{2m}{M+2m}\right]-\frac{Mm}{M+2m}(1-2z)(\vec{e}\vec{k})\Phi_2\,;\\
I^S_{L\to T} &= -2Qz(1-z)(1-2z)(\vec{V}^*\vec{k})\frac{M}{M+2m}\Phi_2\,.
\end{aligned}
\tag{5.42}
$$

and for D wave type mesons are

$$
\begin{aligned}
I^D_{L\to L} &= -QMz(1-z)\left(\vec{k}^2-\frac{4m}{M}p_z^2\right)\Phi_2\,;\\
I^D_{T\to T} &= (\vec{e}\vec{V}^*)\mathbf{p^2}[m^2\Phi_2+(\vec{k}\vec{\Phi}_1)]+(1-2z)^2(\mathbf{p}^2+m^2+Mm)(\vec{k}\vec{V}^*)(\vec{e}\vec{\Phi}_1)\\
&\quad -\mathbf{p}^2(\vec{e}\vec{k})(\vec{V}^*\vec{\Phi}_1)-m(M+m)(\vec{k}\vec{e})(\vec{k}\vec{V}^*)\Phi_2\,;\\
I^D_{T\to L} &= \frac{1}{2}M(1-2z)\left[(\vec{e}\vec{\Phi}_1)\left(\vec{k}^2-\frac{4m}{M}p_z^2\right)+m(M+m)(\vec{e}\vec{k})\Phi_2\right]\,;\\
I^D_{L\to T} &= -2Qz(1-z)(1-2z)(\vec{V}^*\vec{k})(\mathbf{p}^2+m^2+Mm)\Phi_2\,.
\end{aligned}
\tag{5.43}
$$

Equations (5.42) and (5.43), together with expression (5.37), constitute the ultimate sets of all helicity amplitudes. They give explicit forms for the vector meson production amplitudes within the leading-log-approximation used in this work.

Chapter 6

Analysis for heavy quarkonia

The general answers (5.42), (5.43) are, of course, incomprehensible at a quick glance. Therefore, a further analysis is needed to grasp the most vivid features of the results and to disentangle s-channel helicity-conserving and double helicity-flip amplitudes.

Since in the heavy vector mesons quarks can be treated non-relativistically, further simplifications in analytical formulas (5.42), (5.43) are possible due to the presence of an additional small parameter $\mathbf{p}^2/m^2$.

In what follows we will first perform the twist expansion and then relate simplified amplitudes to the decay constants (4.37), (4.38). We will then analyze twist hierarchy of the amplitudes and compare results for S vs. D states. Although we perform this analysis for heavy mesons, we wish to stress that all qualitative features (S vs. D difference, Q^2 dependence, etc.) will hold for light quarkonia as well.

6.1 Twist expansion

Here we shall expand the amplitudes (or, to be more exact, the quantities $\vec{\Phi}_1$ and Φ_2 (5.34), (5.35)) in inverse powers of the hard scale $\overline{Q}^2$ — the twist — and then perform azimuthal angular averaging over ϕ_κ.

Expanding Φ_2 in twists in the main logarithmic region

$$\mu^2, \vec{\Delta}^2, \vec{k}^2 \ll \vec{\kappa}^2 \ll \overline{Q}^2 \,, \tag{6.1}$$

one observes that twist–1 terms cancel, so one has to retain twist–2 and twist–3 terms proportional $\vec{\kappa}^2$:

$$\Phi_2 = \frac{2\vec{\kappa}^2}{\overline{Q}^4} - \frac{8\vec{\kappa}^2\vec{r}^2}{\overline{Q}^6} \tag{6.2}$$

The analogous decomposition for $\vec{\Phi}_1$ reads

$$\vec{\Phi}_1 = \frac{4\vec{r}\vec{\kappa}^2}{\overline{Q}^4} - \frac{12\vec{r}\vec{\kappa}^2 r^2}{\overline{Q}^6} - \frac{\vec{\Delta}(\vec{r}\vec{\Delta})}{\overline{Q}^4} \tag{6.3}$$

Note that the last term does not contain $\vec{\kappa}^2$. However, one must track it because it will be important in double helicity-flip amplitudes.

6.2 Twist expansion for S wave type mesons

With the aid of this decomposition one obtains for amplitude $L \to L$

$$I^S_{L\to L} = -4QMz^2(1-z)^2\frac{2\vec{\kappa}^2}{\overline{Q}^4}\left[1+\frac{(1-2z)^2}{4z(1-z)}\frac{2m}{M+2m}\right]; \tag{6.4}$$

for amplitude $T \to T$

$$\begin{aligned} I^S_{T\to T} &= (\vec{e}\vec{V}^*)\left[m^2\frac{2\vec{\kappa}^2}{\overline{Q}^4}+\frac{4\vec{\kappa}^2}{\overline{Q}^4}\vec{k}^2\right] + \frac{2m}{M+2m}\cdot\frac{1}{2}\vec{k}^2(\vec{e}\vec{V}^*)\frac{2\vec{\kappa}^2}{\overline{Q}^4} \\ &+\left[(1-2z)^2\frac{M}{M+2m}-1\right]\left[\vec{k}^2(\vec{e}\vec{V}^*)\frac{2\vec{\kappa}^2}{\overline{Q}^4}-\frac{\vec{k}^2}{2\overline{Q}^4}(\vec{e}\vec{\Delta})(\vec{V}^*\vec{\Delta})\left(1+\frac{6\vec{\kappa}^2(1-2z)^2}{\overline{Q}^2}\right)\right]. \end{aligned} \tag{6.5}$$

This amplitude is naturally split into s–channel helicity-conserving and double helicity-flip parts:

$$\begin{aligned} I^S_{T\to T}(\lambda_\gamma=\lambda_V) &= (\vec{e}\vec{V}^*)\frac{2\vec{\kappa}^2}{\overline{Q}^4}\left[m^2+2\vec{k}^2(z^2+(1-z)^2)+\frac{m}{M+2m}\vec{k}^2(1-2(1-2z)^2)\right]; \\ I^S_{T\to T}(\lambda_\gamma=-\lambda_V) &= 4z(1-z)(\vec{e}\vec{\Delta})(\vec{V}^*\vec{\Delta})\frac{\vec{k}^2}{2\overline{Q}^4}\left(1+\frac{6\vec{\kappa}^2(1-2z)^2}{\overline{Q}^2}\right)\left[1+\frac{(1-2z)^2}{4z(1-z)}\frac{2m}{M+2m}\right]. \end{aligned}$$

Finally, single spin flip amplitudes are

$$\begin{aligned} I^S_{T\to L} &= -2Mz(1-z)(1-2z)^2\frac{2\vec{\kappa}^2}{\overline{Q}^4}(\vec{e}\vec{\Delta})\left[1+\frac{(1-2z)^2}{4z(1-z)}\frac{2m}{M+2m}\right]; \\ I^S_{L\to T} &= -2Qz(1-z)(1-2z)^2\frac{2\vec{\kappa}^2}{\overline{Q}^4}(\vec{V}^*\vec{\Delta})\frac{2\vec{k}^2}{\overline{Q}^2}\frac{M}{M+2m}. \end{aligned} \tag{6.6}$$

6.3 Twist expansion for D–type vector mesons

Here we will need to track higher–twist terms. It will turn out later that leading contributions vanish, so that twist–3 terms will be crucial for our results. For amplitude $L \to L$ one has

$$I^D_{L\to L} = -QMz(1-z)\left(\vec{k}^2-\frac{4m}{M}p_z^2\right)\cdot\frac{2\vec{\kappa}^2}{\overline{Q}^4}\left(1-\frac{4\vec{k}^2}{\overline{Q}^2}\right). \tag{6.7}$$

For amplitude $T \to T$, one obtains

$$\begin{aligned} I^D_{T\to T} &= (\vec{e}\vec{V}^*)\mathbf{p}^2\left[m^2\frac{2\vec{\kappa}^2}{\overline{Q}^4}\left(1-\frac{4\vec{k}^2}{\overline{Q}^2}\right)+\frac{2\vec{\kappa}^2}{\overline{Q}^4}2\vec{k}^2\right] \\ &+\left[-4z(1-z)\mathbf{p}^2+(1-2z)^2m(M+m)\right]\left\{\frac{2\vec{\kappa}^2}{\overline{Q}^4}\vec{k}^2(\vec{e}\vec{V}^*)-\frac{\vec{k}^2}{2\overline{Q}^4}(\vec{e}\vec{\Delta})(\vec{V}^*\vec{\Delta})\left[1+\frac{6\vec{\kappa}^2(1-2z)^2}{\overline{Q}^2}\right]\right\} \\ &-m(M+m)\frac{1}{2}\vec{k}^2(\vec{e}\vec{V}^*)\frac{2\vec{\kappa}^2}{\overline{Q}^4}\left(1-\frac{4\vec{k}^2}{\overline{Q}^2}\right). \end{aligned} \tag{6.8}$$

Note that we kept track of all terms $\propto |p|^4$. Again, one can separate out s-channel helicity-conserving and double helicity-flip parts:

$$\begin{aligned} I^D_{T\to T}(\lambda_\gamma=\lambda_V) &= (\vec{e}\vec{V}^*)\frac{\vec{\kappa}^2}{\overline{Q}^4}\left[2\mathbf{p}^2\left(m^2+2\vec{k}^2-4\vec{k}^2\frac{m^2}{\overline{Q}^2}\right)-m(M+m)\vec{k}^2\left(1-\frac{4\vec{k}^2}{\overline{Q}^2}\right)\right. \\ &\quad \left.-2\vec{k}^2\left(\vec{k}^2-\frac{4m}{M}p_z^2\right)\right] \\ I^D_{T\to T}(\lambda_\gamma=-\lambda_V) &= \left(\vec{k}^2-\frac{4m}{M}p_z^2\right)(\vec{e}\vec{\Delta})(\vec{V}^*\vec{\Delta})\frac{\vec{k}^2}{2\overline{Q}^4}\left(1+\frac{6\vec{\kappa}^2(1-2z)^2}{\overline{Q}^2}\right) \end{aligned} \tag{6.9}$$

Finally, single helicity-flip amplitudes are

$$\begin{aligned} I^D_{T\to L} &= \frac{1}{2}M(1-2z)\left[\frac{-2(1-2z)(\vec{e}\vec{\Delta})\vec{\kappa}^2}{\overline{Q}^4}\left(\vec{k}^2-\frac{4m}{M}p_z^2\right)+m(M+m)\frac{4\vec{\kappa}^2\vec{k}^2}{\overline{Q}^6}(1-2z)(\vec{e}\vec{\Delta})\right] \\ &= -\frac{\vec{\kappa}^2}{\overline{Q}^4}(1-2z)^2M(\vec{e}\vec{\Delta})\left[\vec{k}^2-\frac{4m}{M}p_z^2-m(M+m)\frac{2\vec{k}^2}{\overline{Q}^2}\right]; \\ I^D_{L\to T} &= -8Qz(1-z)(1-2z)^2(\mathbf{p}^2+m^2+mM)\frac{\vec{\kappa}^2}{\overline{Q}^6}\vec{k}^2(\vec{V}^*\vec{\Delta}). \end{aligned} \tag{6.10}$$

6.4 Final results for S wave mesons

In order to grasp the major features of various S and D wave amplitudes, further simplifications can be achieved if one neglects spherically non-symmetric arguments of α_s and gluon density. First we rewrite the general expression (5.37) in the more convenient form:

$$A(x,Q^2,\vec{\Delta})=-is\frac{c_V\sqrt{4\pi\alpha_{em}}}{4\pi^2}\int d^3\mathbf{p}\frac{4}{M}\psi(\mathbf{p}^2)\int\frac{d^2\vec{\kappa}}{\kappa^4}\alpha_S\mathcal{F}\cdot I(\gamma^*\to V). \tag{6.11}$$

In this expression everything except for integrands $I(\gamma^*\to V)$ is spherically symmetric, thus making it possible to perform angular averaging over $\Omega_{\mathbf{p}}$ in these integrands.

6.4.1 S wave: $\Omega_{\mathbf{p}}$ averaging

Here all the calculations are fairly straightforward. In the non-relativistic case one can everywhere put $z\to 1/2\,; M=2m=m_V$. The resultant integrands are:

$$
\begin{aligned}
I^S(L\to L) &= -\frac{8QM}{(Q^2+M^2)^2}\vec{\kappa}^2 \\
I^S(T\to T;\lambda_\gamma=\lambda_V) &= \frac{8M^2}{(Q^2+M^2)^2}\vec{\kappa}^2 \\
I^S(T\to T;\lambda_\gamma=-\lambda_V) &= \frac{16}{3}\frac{(\vec{e}\vec{\Delta})(\vec{V}^*\vec{\Delta})}{(Q^2+M^2)^2}\left[1+\frac{96}{5}\frac{\vec{\kappa}^2\mathbf{p}^2}{M^2(Q^2+M^2)}\right] \\
I^S(T\to L) &= -\frac{64}{3}\frac{M(\vec{e}\vec{\Delta})}{(Q^2+M^2)^2}\frac{\mathbf{p}^2}{M^2}\vec{\kappa}^2 \\
I^S(L\to T) &= -\frac{512}{15}\frac{Q(\vec{V}^*\vec{\Delta})}{(Q^2+M^2)^2}\frac{\mathbf{p}^4}{M^2(Q^2+M^2)}\vec{\kappa}^2
\end{aligned}
\qquad (6.12)
$$

Note several things: since the accurate $1S$ wave differs from the naive γ_μ spinorial structure only by relativistic corrections, one would obtain the same results in the case of naive $q\bar{q}V$ vertex. The only difference would be an extra factor 2 for the $L\to T$ amplitude, which is a higher-twist amplitude, anyway.

Thus, the only thing left is integration over $|\mathbf{p}|$. Note that these amplitudes are naturally expressed in terms of decay constants. Indeed, in the extreme non-relativistic case the expression (4.37) becomes

$$
f^{(S)}=\frac{3m_V}{2\pi^3}\int d^3\mathbf{p}\;\psi_S \quad\Rightarrow\quad \int d^3\mathbf{p}\;\psi_S=\frac{2\pi^3}{3m_V}f^{(S)} \qquad (6.13)
$$

6.4.2 S wave: the differential cross section for $L\to L$

Here we would like to digress and, for the sake of logical completeness, show how one obtains the final result for the differential cross section using the example of the $L\to L$ amplitude. If needed, the same can be done for the other amplitudes.

One has:

$$
\begin{aligned}
&\int d^3\mathbf{p}\;\psi_S\frac{4}{m_V}\frac{-8Qm_V}{(Q^2+m_V^2)^2}\cdot\pi\int^{\overline{Q}^2}\frac{d\vec{\kappa}^2}{\vec{\kappa}^2}\frac{\partial G(x,\vec{\kappa}^2)}{\partial\log\vec{\kappa}^2}\alpha_s(\vec{\kappa}^2)\exp(-\frac{1}{2}B_{3I\!P}\vec{\Delta}^2) \\
&=-\frac{32\pi Q}{(Q^2+m_V^2)^2}G(x,\overline{Q}_0^2)\alpha_s(\overline{Q}_0^2)\exp(-\frac{1}{2}B_{3I\!P}\vec{\Delta}^2)\int d^3\mathbf{p}\;\psi_S \\
&=-\frac{32\pi Q}{(Q^2+m_V^2)^2}\exp(-\frac{1}{2}B_{3I\!P}\vec{\Delta}^2)G(x,\overline{Q}_0^2)\alpha_s(\overline{Q}_0^2)\frac{2\pi^3}{3m_V}f_V\,.
\end{aligned}
$$

Using this result, we transform (6.11) into

$$
\begin{aligned}
A &= is\frac{f_V c_V\sqrt{4\pi\alpha_{em}}}{4\pi^2}\cdot\frac{64\pi^4}{3}\frac{Q}{m_V}\frac{G\cdot\alpha_s}{(Q^2+m_V^2)^2} \\
&= is\frac{16\pi^2}{3}\frac{Q}{m_V}\cdot c_V f_V\cdot\sqrt{4\pi\alpha_{em}}\frac{G\cdot\alpha_s\exp(-\frac{1}{2}B_{3I\!P}\vec{\Delta}^2)}{(Q^2+m_V^2)^2}\,.
\end{aligned}
$$

The expression for the differential cross section reads ($t \equiv \vec{\Delta}^2$):

$$\begin{aligned}\frac{d\sigma}{dt} &= \frac{1}{16\pi s^2}|A|^2 \\ &= \frac{16\pi^3}{9}\frac{Q^2}{m_V^2}\cdot(c_V f_V)^2 4\pi\alpha_{em}\cdot\frac{G^2\alpha_s^2\exp(-B_{3\mathbb{P}}t)}{(Q^2+m_V^2)^4}\,.\end{aligned}$$

Finally, one can express this cross section through $\Gamma(V\to e^+e^-)$ (see (4.39)):

$$\boxed{\frac{d\sigma}{dt} = \frac{16\pi^3}{3\alpha_{em}}Q^2 m_V\cdot\Gamma(V\to e^+e^-)\cdot\frac{G^2\alpha_s^2\exp(-B_{3\mathbb{P}}t)}{(Q^2+m_V^2)^4}\,.} \tag{6.14}$$

6.4.3 S wave: the other amplitudes

$T\to T, \lambda_\gamma = \lambda_V$:

In the non-relativistic case, this amplitude is readily obtained from the above formulas after $Q\to m_V$ replacement in the numerator of the amplitude [see (6.12)]. This means in particular that in this limit

$$R^{(S)} \equiv \left(\frac{A_{LL}}{A_{TT}}\right)^2 = \frac{Q^2}{m_V^2}\,. \tag{6.15}$$

$T\to T, \lambda_\gamma = -\lambda_V$:

This amplitude is very interesting because of the competition of two very different terms — soft and hard scale contributions. Indeed, integration over the gluon loop gives

$$A \propto \frac{G(x,\mu^2)}{\mu^2} + \frac{96}{5}\frac{G(x,\overline{Q}^2)\mathbf{p}^2}{M^2(Q^2+M^2)}\,. \tag{6.16}$$

We see that the soft contribution turns out to be of leading twist, while the pQCD contribution is of higher twist. This observation was first made in [6] for the naive type of $q\bar{q}V$ vertex; here we see that it also holds for more accurate S and D wave vector mesons.

$T\to L$ **and** $L\to T$

In the case of heavy quarkonia these single spin-flip amplitudes are suppressed by non-relativistic factors. Besides, the amplitude $L\to T$ is of twist 3, which is another source of suppression. Their ratios to $A(T\to T)\equiv A(T\to T;\lambda_\gamma=\lambda_V^*)$ read

$$\frac{A(T\to L)}{A(T\to T)} = -\frac{8}{3}\frac{(\vec{e}\vec{\Delta})}{m_V}\cdot w_2\,; \quad \frac{A(L\to T)}{A(T\to T)} = -\frac{64}{15}\frac{Q(\vec{V}^*\vec{\Delta})}{Q^2+m_V^2}\cdot w_4\,. \tag{6.17}$$

The model-dependent quantities w_2 and w_4 are defined via

$$w_2 = \frac{1}{m_V^2}\frac{\int d^3\mathbf{p}\ \mathbf{p}^2\ \psi_S}{\int d^3\mathbf{p}\ \psi_S}\,; \quad w_4 = \frac{1}{m_V^4}\frac{\int d^3\mathbf{p}\ \mathbf{p}^4\ \psi_S}{\int d^3\mathbf{p}\ \psi_S}\,. \tag{6.18}$$

Within the oscillator Ansatz (4.42) their values are

$$w_2 = \frac{3}{2}\frac{1}{(m_V R)^2}\,; \quad w_4 = \frac{15}{4}\frac{1}{(m_V R)^4}\,. \tag{6.19}$$

6.5 Final results for the D wave

This case is much subtler. It turns out that the leading terms in integrands $I^{(D)}$, proportional to $m^2|p|^2$, cancel out after angular averaging, so that many new terms, including higher twist terms come into play. This cancellation is, in fact, quite understandable. Indeed, in the very beginning we showed that vertex $\bar{u}'\gamma_\mu u$ contains both S and D waves, with D wave probability being suppressed for heavy quarks due to their non-relativistic motion. This means in particular that the *photon* couples to $q\bar{q}$ pairs sitting either in the S or D state. However, at the other end of the quark loop, we have a vector meson in pure D wave. Therefore, the largest items in $\langle\gamma_{S+D}|...|V_D\rangle$ cancel out due to S–D orthogonality.

6.5.1 D wave: $\Omega_{\mathbf{p}}$ averaging for the $L \to L$ amplitude

If we limited ourselves only to the leading $\mathbf{p}^2/m^2$ terms, we would get

$$\int d\Omega_{\mathbf{p}} \left(\vec{k}^2 - \frac{4m}{M}p_z^2\right) = 4\pi \cdot \left(\frac{2}{3}\mathbf{p}^2 - 2\cdot\frac{1}{3}\mathbf{p}^2\right) = 0\,,$$

which is the manifestation of S–D orthogonality. Thus, we see that $\mathbf{p}^2/m^2$ terms vanish after angular averaging. Therefore, one has to be extremely careful here and must take into account all possible sources of $\mathbf{p}^4/m^4$ terms. To do so, one has to perform the following averaging:

$$\left\langle 4z(1-z)\cdot\frac{1}{\overline{Q}^4}\cdot\left(\vec{k}^2 - \frac{4m}{M}p_z^2\right)\cdot\left(1 - \frac{4\vec{k}^2}{\overline{Q}^2}\right)\right\rangle\,. \tag{6.20}$$

Before performing the averaging, let us make a list of useful formulas :

$$\begin{aligned}
&\langle\vec{k}^2\rangle = \frac{2}{3}\mathbf{p}^2 \quad \langle p_z^2\rangle = \frac{1}{3}\mathbf{p}^2\\
&\langle\vec{k}^2\vec{k}^2\rangle = \frac{8}{15}\mathbf{p}^4 \quad \langle\vec{k}^2 p_z^2\rangle = \frac{2}{15}\mathbf{p}^4 \quad \langle p_z^2 p_z^2\rangle = \frac{3}{15}\mathbf{p}^4
\end{aligned} \tag{6.21}$$

Finally, remember that $p_z^2 = \frac{1}{4}(1-2z)^2M^2$.

One has to perform the following averaging

$$\left\langle 4z(1-z)\cdot\frac{1}{\overline{Q}^4}\cdot\left(\vec{k}^2 - \frac{4m}{M}p_z^2\right)\cdot\left(1 - \frac{4\vec{k}^2}{\overline{Q}^2}\right)\right\rangle \tag{6.22}$$

Note that all factors should be carefully examined; all four contribute to the final answer. Decomposing $\overline{Q}^2$

$$\overline{Q}^2 = m^2 + z(1-z)Q^2 = m^2 + \frac{1}{4}Q^2 - \frac{1}{4}(1-2z)^2Q^2 \equiv \overline{Q}_0^2 - \frac{p_z^2}{M^2}Q^2\,, \tag{6.23}$$

with $\overline{Q}_0^2 = m^2 + Q^2/4$, one gets

$$\frac{1}{\overline{Q}^4} = \frac{1}{\overline{Q}_0^4}\left(1 + 2\frac{p_z^2}{M^2}\frac{Q^2}{\overline{Q}_0^2}\right)\,. \tag{6.24}$$

Omitting $\overline{Q}_0^{-4}$, one has

$$\left\langle \left(1-\frac{4p_z^2}{M^2}\right)\cdot\left(1+2\frac{p_z^2}{M^2}\frac{Q^2}{\overline{Q}_0^2}\right)\cdot\left(\vec{k}^2-\frac{4m}{M}p_z^2\right)\cdot\left(1-\frac{4\vec{k}^2}{\overline{Q}_0^2}\right)\right\rangle \tag{6.25}$$

With the aid of (6.11), one obtains

$$\begin{aligned}
&\left\langle \vec{k}^2-\frac{4m}{M}p_z^2\right\rangle-\frac{4}{M^2}\left\langle \vec{k}^2p_z^2-2p_z^2p_z^2\right\rangle+2\frac{Q^2}{M^2\overline{Q}_0^2}\left\langle \vec{k}^2p_z^2-2p_z^2p_z^2\right\rangle-\frac{4}{\overline{Q}_0^2}\left\langle \vec{k}^2\vec{k}^2-2p_z^2\vec{k}^2\right\rangle\\
=&\left(\frac{2}{3}\mathbf{p}^2-\frac{4m}{3M}\mathbf{p}^2\right)-\frac{4}{M^2}\mathbf{p}^4\left(\frac{2}{15}-\frac{6}{15}\right)+2\frac{Q^2}{M^2\overline{Q}_0^2}\mathbf{p}^4\left(\frac{2}{15}-\frac{6}{15}\right)-\frac{4}{\overline{Q}_0^2}\mathbf{p}^4\left(\frac{8}{15}-\frac{4}{15}\right)\\
=&\frac{2}{3}\mathbf{p}^2\frac{4\mathbf{p}^2}{M+2m}+\frac{16\mathbf{p}^4}{15M^2}-\frac{8Q^2\mathbf{p}^4}{15M^2\overline{Q}_0^2}-\frac{16\mathbf{p}^4}{15\overline{Q}_0^2}\\
=&\frac{4\mathbf{p}^4}{3M^2}\left(1+\frac{4}{5}-\frac{8}{5}\frac{Q^2}{Q^2+M^2}-\frac{16}{5}\frac{M^2}{Q^2+M^2}\right)\\
=&\frac{4\mathbf{p}^4}{15M^2}\left(1-8\frac{M^2}{Q^2+M^2}\right)
\end{aligned}\tag{6.26}$$

One can now — again — express the integral over quark loop through the decay constant (see (4.38)):

$$\int d^3\mathbf{p}\ \mathbf{p}^4\ \psi_D \Rightarrow f^{(D)}\cdot\frac{\pi^3 m_V}{2}\,. \tag{6.27}$$

to give

$$-\frac{64\pi^4}{15}\ \frac{Q}{m_V}\ \frac{G\cdot\alpha_s\cdot\exp(-\frac{1}{2}B_{3I\!P}\vec{\Delta}^2)}{(Q^2+m_V^2)^2}\cdot f^{(D)}\cdot\left(1-8\frac{m_V^2}{Q^2+m_V^2}\right)\,. \tag{6.28}$$

Comparison with $L\to L$ amplitude reveals that

$$\boxed{\frac{A_{LL}^D}{A_{LL}^S}=\frac{1}{5}\left(1-8\frac{m_V^2}{Q^2+m_V^2}\right)\cdot\frac{f^{(D)}}{f^{(S)}}\,.} \tag{6.29}$$

6.5.2 D wave: the other amplitudes

For the helicity-conserving amplitude one has to repeat the same averaging procedure. The calculation proceeds as follows:

$$\begin{aligned}
&\left\langle\left(1+2\frac{p_z^2}{M^2}\frac{Q^2}{\overline{Q}_0^2}\right)\cdot\left[2\mathbf{p}^2\left(m^2+2\vec{k}^2-4\vec{k}^2\frac{m^2}{\overline{Q}^2}\right)-m(M+m)\vec{k}^2\left(1-\frac{4\vec{k}^2}{\overline{Q}^2}\right)-2\vec{k}^2\left(\vec{k}^2-\frac{4m}{M}p_z^2\right)\right]\right\rangle\\
&=2m^2\mathbf{p}^2-\frac{2}{3}m(M+m)\mathbf{p}^2+2\frac{p_z^2}{M^2}\frac{Q^2}{\overline{Q}_0^2}\left(\frac{1}{2}M^2\frac{1}{3}-3M^2\frac{2}{15}\right)+\frac{8}{3}\mathbf{p}^4-\frac{8}{15}\mathbf{p}^4+\frac{m^2}{\overline{Q}_0^2}\mathbf{p}^4\frac{16}{15}\\
&=-\frac{2}{3}\mathbf{p}^4-\frac{8}{15}\mathbf{p}^4+\frac{8}{3}\mathbf{p}^4+\frac{16}{15}\frac{M^2}{M^2+Q^2}\mathbf{p}^4+\frac{8}{15}\frac{Q^2}{M^2+Q^2}\mathbf{p}^4\\
&=2\mathbf{p}^4\left(1+\frac{4}{15}\frac{M^2}{M^2+Q^2}\right)\,.
\end{aligned}\tag{6.30}$$

The result can be written as

$$\frac{A^D_{LL}}{A^D_{TT}} = \frac{1}{15}\frac{1-8\dfrac{m_V^2}{Q^2+m_V^2}}{1+\dfrac{4}{15}\dfrac{m_V^2}{Q^2+m_V^2}}\,. \tag{6.31}$$

In the case of the double helicity-flip amplitude we again have contributions from soft and hard scales with the same hierarchy of twists, namely

$$A \propto \frac{G(x,\mu^2)}{\mu^2} - \frac{96}{7}\frac{G(x,\overline{Q}^2)\mathbf{p}^2}{M^2(Q^2+M^2)} \tag{6.32}$$

so we again see the soft domination in the double helicity-flip amplitude.

In the case of single spin-flip amplitudes, no dangerous calcellations among leading terms arise. Before giving a list of amplitudes, we wish to emphasize that in the case of D wave mesons there are no non-relativistic suppression factors like w_2 and w_4 defined in (6.18). This means that, for moderate momentum transfers, helicity non-conserving amplitudes are crutial in the case of D wave mesons.

6.6 S wave vs. D wave comparison

We would like to present our final results in a form that stresses the remarkable differences between S wave and D wave amplitudes. Below we give a table of the ratios

$$\rho_{ij} \equiv \frac{A^D(i\to j)}{A^S(i\to j)}\frac{f^{(S)}}{f^{(D)}} \tag{6.33}$$

for helicity-conserving and single spin-flip amplitudes. Double spin-flip amplitudes are not given due to the presence of incalculable non-perturbative contributions.

$$\begin{aligned}
\rho_{LL} &= \frac{1}{5}\left(1-8\frac{m_V^2}{Q^2+m_V^2}\right)\\
\rho_{TT} &= 3\left(1+\frac{4}{15}\frac{m_V^2}{Q^2+m_V^2}\right)\\
\rho_{TL} &= -\frac{3}{5}\frac{1}{w_2}\left(1+3\frac{m_V^2}{Q^2+m_V^2}\right)\\
\rho_{LT} &= \frac{9}{8}\frac{1}{w_4}
\end{aligned} \tag{6.34}$$

Here we note several things: First, the abnormally large higher twist contributions to D wave amplitudes are seen here as terms $\propto m_V^2/(Q^2+m_V^2)$. They even force the opposite sign of the $L\to L$ amplitude in the moderate Q^2 domain. Second, we see highly non-trivial — and even non-monotonic — Q^2 dependence of the $(A_{LL}/A_{TT})^2$ ratio, which will lead to the presence of a dip in experimentally measured σ_L/σ_T for D wave meson production. Finally, we must stress that in the case of D wave mesons there is no non-relativistic suppression for single spin-flip amplitudes, as there was in S wave mesons. This leads us to the conclusion that s-channel helicity is strongly violated in the case of D wave meson production.

Part III

Numerical analysis

Chapter 7

Determination of the unintegrated gluon structure function of the proton: DGD2000 analysis

The familiar objects from the Gribov-Lipatov-Dokshitzer-Altarelli-Parisi (DGLAP) evolution description of deep inelastic scattering are quark, antiquark and gluon distribution functions $q_i(x,Q^2), \bar{q}_i(x,Q^2)$, and $g(x,Q^2)$. (Hereafter x, Q^2 are the standard DIS variables.) At small x they describe the integral flux of partons with the light cone momentum x in units of the target momentum and transverse momentum squared $\leq Q^2$ and form the basis of the highly sophisticated description of hard scattering processes in terms of collinear partons [18]. On the other hand, at very small x, the object of the Balitskii-Fadin-Kuraev-Lipatov evolution equation is the differential gluon structure function (DGSF) of the target [19, 30],

$$\mathcal{F}(x,Q^2) = \frac{\partial G(x,Q^2)}{\partial \log Q^2}\,, \tag{7.1}$$

with $G(x,Q^2) \equiv xg(x,Q^2)$. (Evidently the related unintegrated distributions can be defined also for charged partons.) For instance, it is precisely DGSF of the target proton that emerges in the familiar color dipole picture of inclusive DIS at small x [31, 32, 33] and diffractive DIS into dijets [34]. Another familiar example is the QCD calculation of helicity amplitudes of diffractive DIS into continuum [35, 36] and production of vector mesons [37, 38]. DGSF's are custom-tailored for QCD treatment of hard processes, where one needs to keep track of the transverse momentum of gluons neglected in the standard collinear approximation [39, 40, 41, 42].

In the past two decades, DGLAP phenomenology of DIS has become a big industry and several groups — notably GRV [43], CTEQ [44] & MRS [45] and others [46] — keep continuously incorporating new experimental data and providing the high energy community with updates of the parton distribution functions supplemented with the interpolation routines that facilitate practical applications. On the other hand, there are several pertinent issues — the onset of the purely perturbative QCD treatment of DIS and the impact of soft mechanisms of photoabsorption on the proton structure function in the region of large Q^2 standing highest on the list — that cannot be answered within the DGLAP approach because DGLAP evolution is obviously hampered at moderate to small Q^2. The related issue is to what extent the soft mechanisms of photoabsorption can bias the Q^2 dependence of the proton structure

function and, consequently, the determination of the gluon density from scaling violations. We recall here the recent dispute [47] over the applicability of the DGLAP analysis at $Q^2 \lesssim$ 2–4 GeV^2 triggered by the so-called Caldwell's plot [48]. Arguably, the $\vec{\kappa}$-factorization formalism of DGSF, in which the interesting observables are expanded in interactions of gluons of transverse momentum $\vec{\kappa}$ changing from soft to hard, is better suited to explore the issue of soft-hard interface. Last but not least, neglecting the transverse momentum $\vec{\kappa}$ of gluons is a questionable approximation in evaluation of production cross sections of jets or hadrons with large transverse momentum. It is distressing, then, that convenient, ready-to-use, parameterizations of DGSF are not yet available in the literature.

Here we perform a simple phenomenological determination of the DGSF at small x based on the 1978 Baltskii-Lipatov (BL) scheme [30], in which the DGSF is directly related to the physical observable — the proton structure function $F_{2p}(x,Q^2)$. In the early 1990's the BL scheme was extended to other observables and dubbed $\vec{\kappa}$-factorization [49]; it is also closely related to the color dipole factorization in the color dipole BFKL approach [31, 32, 33]. Our interest is in producing a ready-to-use Ansatz for $\mathcal{F}(x,\vec{\kappa}^2)$ so that we take advantage of large body of the early work on color dipole BFKL factorization [32, 50, 51] and follow a very pragmatic strategy first applied in [35, 36]: (i) for hard gluons with large $\vec{\kappa}$ we make as much use as possible of the existing DGLAP parameterizations of $G(x,\vec{\kappa}^2)$; (ii) for the extrapolation of hard gluon densities to small $\vec{\kappa}^2$ we use an Ansatz [34] which correctly describes the color gauge invariance constraints on radiation of soft gluons by color singlet targets; (iii) as suggested by color dipole phenomenology, we supplement the density of gluons with small $\vec{\kappa}^2$ with a non-perturbative soft component; (iv) as suggested by the soft-hard diffusion inherent in the BFKL evolution, we allow for propagation of the predominantly hard-interaction driven small-x rise of DGSF into the soft region, invoking plausible soft-to-hard interpolations. The last two components of DGSF are parameterized following modern wisdom on the infrared freezing of the QCD coupling and short propagation radius of perturbative gluons. Having specified the infrared regularization, we can apply the resulting $\mathcal{F}(x,\vec{\kappa}^2)$ to evaluation of the photoabsorption cross section in the whole range of small to large Q^2.

7.1 The Ansatz for the differential gluon structure function

The major insight into parameterization of the DGSF comes from early experience with color dipole phenomenology of small-x DIS. In the color dipole approach, which is closely related to $\vec{\kappa}$-factorization, the principal quantity is the total interaction cross section of the $q\bar{q}$ color dipole $\boldsymbol{r}$ with the proton target [32, 52, 53],

$$\sigma(x,r) = \frac{\pi^2 r^2}{3} \int \frac{d\vec{\kappa}^2}{\vec{\kappa}^2} \frac{4[1-J_0(\kappa r)]}{(\kappa r)^2} \alpha_S \left(\max\{\vec{\kappa}^2, \frac{A}{r^2}\} \right) \mathcal{F}(x,\vec{\kappa}^2) \,, \tag{7.2}$$

which, for very small color dipoles, can be approximated by

$$\sigma(x,r) = \frac{\pi^2 r^2}{3} \alpha_S \left(\frac{A}{r^2} \right) G\left(x, \frac{A}{r^2} \right) \,, \tag{7.3}$$

where $A \approx 10$ comes from properties of the Bessel function $J_0(z)$. The phenomenological properties of the dipole cross section are well understood; for extraction of $\sigma(x,r)$ from the

experimental data see [20, 54]. The known dipole size dependence of $\sigma(x,r)$ serves as a constraint on the possible $\vec{\kappa}^2$ dependence of $\mathcal{F}(x,\vec{\kappa}^2)$.

As we argued in section 3.2, DGLAP fits are likely to overestimate $\mathcal{F}_{hard}(x,\vec{\kappa}^2)$ at moderate $\vec{\kappa}^2$. Still, approximation (7.3) does a good job when the hardness A/r^2 is very large, and at large Q^2 we can arguably approximate the DGSF by the direct differentiation of available fits (e.g., GRV, CTEQ, MRS) to the integrated gluon structure function $G_{pt}(x,Q^2)$:

$$\mathcal{F}_{pt}(x,\vec{\kappa}^2) \approx \frac{\partial G_{pt}(x,\vec{\kappa}^2)}{\partial \log \vec{\kappa}^2}\,. \tag{7.4}$$

Hereafter the subscript pt serves as a reminder that these gluon distributions were obtained from the pQCD evolution analyses of the proton structure function and cross sections of related hard processes.

The available DGLAP fits are only applicable at $\vec{\kappa}^2 \geq Q_c^2$, (see table 1 for the values of Q_c^2); in the extrapolation to soft region $\vec{\kappa}^2 \leq Q_c^2$ we are bound to an educated guess. To this end, recall that perturbative gluons are confined and do not propagate to large distances; recent fits [55] to the lattice QCD data suggest Yukawa-Debye screening of perturbative color fields with propagation/screening radius $R_c \approx 0.27fm$. Incidentally, precisely this value of R_c for Yukawa-screened color fields has been used since 1994 in the very successful color dipole phenomenology of small-x DIS [50, 51]. Furthermore, an important finding of [51] is a good quantitative description of the rising component of the proton structure function starting with the Yukawa-screened perturbative two-gluon exchange as a boundary condition for the color dipole BFKL evolution.

The above suggests that the $\vec{\kappa}^2$ dependence of perturbative hard $\mathcal{F}_{hard}(x,\vec{\kappa}^2)$ in the soft region $\vec{\kappa}^2 \leq Q_c^2$ is similar to the Yukawa-screened flux of photons in the positron, cf. eq. (2.33), with α_{em} replaced by the running strong coupling of quarks $C_F\alpha_S(\vec{\kappa}^2)$ and with factor N_c instead of 2 for leptons in the positronium, (for the early discussion see [34]),

$$\mathcal{F}_{pt}^{(B)}(\vec{\kappa}^2) = C_F N_c \frac{\alpha_s(\vec{\kappa}^2)}{\pi}\left(\frac{\vec{\kappa}^2}{\vec{\kappa}^2+\mu_{pt}^2}\right)^2 V_N(\vec{\kappa})\,. \tag{7.5}$$

Here $\mu_{pt} = \frac{1}{R_c} = 0.75$ GeV is the inverse Yukawa screening radius and must not be interpreted as a gluon mass; more sophisticated forms of screening can well be considered. Following [50, 51, 56, 22], we impose also the infrared freezing of strong coupling: $\alpha_S(\vec{\kappa}^2) \leq 0.82$. Recently the concept of freezing coupling has become very popular; for a review see [57].

The vertex function $V_N(\vec{\kappa})$ describes the decoupling of soft gluons, $\vec{\kappa} \ll \frac{1}{R_p}$, from the color neutral proton and has the same structure as in eq. (2.34). In the nonrelativistic oscillator model for the nucleon one can relate the two-quark form factor of the nucleon to the single-quark form factor,

$$F_2(\vec{\kappa},-\vec{\kappa}) = F_1\left(\frac{2N_c}{N_c-1}\vec{\kappa}^2\right)\,. \tag{7.6}$$

To the extent that $R_c^2 \ll R_p^2$ the detailed functional form of $F_2(\vec{\kappa},-\vec{\kappa})$ is not crucial. The simple relation (7.6) will be used also for a more realistic dipole approximation,

$$F_1(\vec{\kappa}^2) = \frac{1}{(1+\frac{\vec{\kappa}^2}{\Lambda^2})^2}\,. \tag{7.7}$$

The gluon probed radius of the proton and the charge radius of the proton can be somewhat different and $\Lambda \sim 1$ GeV must be regarded as a free parameter. Anticipating the forthcoming discussion of the diffraction slope in vector meson production we put $\Lambda = 1$ GeV.

As discussed above, the hard-to-soft diffusion makes the DGSF rise at small x even in the soft region. We model this hard-to-soft diffusion by matching the $\vec{\kappa}^2$ dependence (7.5) to the DGLAP fit $\mathcal{F}_{pt}(x, Q_c^2)$ at the soft-hard interface Q_c^2 and by assigning to $\mathcal{F}_{hard}(x, \vec{\kappa}^2)$ in the region of $\vec{\kappa}^2 \leq Q_c^2$ the $\vec{\kappa}^2$ dependence of the Born term (7.5) and the x-dependence as shown by the DGLAP fit $\mathcal{F}_{pt}(x, Q_c^2)$, i.e.,

$$\mathcal{F}_{hard}(x, \vec{\kappa}^2) = \mathcal{F}_{pt}^{(B)}(\vec{\kappa}^2) \frac{\mathcal{F}_{pt}(x, Q_c^2)}{\mathcal{F}_{pt}^{(B)}(Q_c^2)} \theta(Q_c^2 - \vec{\kappa}^2) + \mathcal{F}_{pt}(x, \vec{\kappa}^2) \theta(\vec{\kappa}^2 - Q_c^2) \,. \tag{7.8}$$

Because the accepted propagation radius — $R_c \sim 0.3$ fm — for perturbative gluons is short compared to a typical range of the strong interaction, the dipole cross section (7.2) evaluated with the DGSF (7.8) would miss an interaction strength in the soft region for large color dipoles. In Refs. [50, 51] this missing strength for large dipoles has been modeled by the non-perturbative, soft mechanism with energy-independent dipole cross section, whose specific form [50, 38] has been driven by early analysis [56] of the non-perturbative two-gluon exchange and tested against the diffractive vector meson production data [38]. More recently, several closely related models for $\sigma_{\rm soft}(r)$ have appeared in the literature. (See, for example, models for dipole-dipole scattering via polarization of non-perturbative QCD vacuum [58] and the model of soft-hard two-component pomeron [59]). In the spirit of eq. (7.4) one can parameterize interaction of large color dipoles in terms of the genuinely soft, non-perturbative component of DGSF. The principal point about this non-perturbative component of DGSF is that it must not be subjected to pQCD evolution. Thus, the arguments about the hard-to-soft diffusion-driven rise of perturbative DGSF even at small $\vec{\kappa}^2$ do not apply to the non-perturbative DGSF and we take it to be energy-independent,

$$\mathcal{F}_{soft}^{(B)}(x, \vec{\kappa}^2) = a_{soft} C_F N_c \frac{\alpha_s(\vec{\kappa}^2)}{\pi} \left(\frac{\vec{\kappa}^2}{\vec{\kappa}^2 + \mu_{soft}^2} \right)^2 V_N(\vec{\kappa}) \,, \tag{7.9}$$

where $\mu_{soft}^2 \ll \mu_{pt}^2$. Furthermore, it is natural that the soft component of DGSF decreases in the perturbative domain of $\vec{\kappa}^2 \gtrsim \mu_{pt}^2$ faster than the perturbative Born term (7.5), which is achieved by the extrapolation of the form suggested in [35, 36],

$$\mathcal{F}(x, \vec{\kappa}^2) = \mathcal{F}_{soft}^{(B)}(x, \vec{\kappa}^2) \frac{\kappa_s^2}{\vec{\kappa}^2 + \kappa_s^2} + \mathcal{F}_{hard}(x, \vec{\kappa}^2) \frac{\vec{\kappa}^2}{\vec{\kappa}^2 + \kappa_h^2} \,, \tag{7.10}$$

with $\kappa_s \sim \mu_{pt}$.

The described Ansatz for DGSF must be regarded as a poor man's approximation. The separation of small-$\vec{\kappa}^2$ DGSF into the genuine non-perturbative component and small-$\vec{\kappa}^2$ tail of the hard perturbative DGSF is not unique. Specifically, we attributed to the latter the same small-x rise as in the DGLAP fits at Q_c^2, although one cannot exclude the possibility that the hard DGSF has a small x-independent component. The issues of soft-hard separation and whether or not the non-perturbative component of DGSF enters different observables in a universal manner must be addressed in dynamical models for infrared regularization of perturbative QCD and the non-perturbative QCD vacuum, and only can be answered by

confronting such models with experiment. We recall that in the conventional DGLAP analysis the effect of soft gluons is reabsorbed into the input gluon distributions.

The $\vec{\kappa}$-factorization formulas (2.40) and (2.41) correspond to the full phase space extension of the leading-order (LO) DGLAP approach at small x. For this reason our Ansätze for $\mathcal{F}_{hard}(x,Q^2)$ will be based on LO DGLAP fits to the gluon structure function of the proton $G_{pt}(x,Q^2)$. We consider the GRV98LO [43], CTEQ4L, version 4.6 [44] and MRS LO 1998 [45] parameterizations. We refer to our Anzätze for DGSF based on those LO DGLAP input as D-GRV, D-CTEQ and D-MRS parameterizations, respectively.

Our formulas (2.40), (2.41) describe the sea component of the proton structure function. Arguably these LL$\frac{1}{x}$ formulas are applicable at $x \lesssim x_0 = 1 \div 3 \cdot 10^{-2}$. At large Q^2 the experimentally attainable values of x are not so small. In order to give a crude idea of finite-energy effects at moderately small x, we stretch our fits to $x \gtrsim x_0$, multiplying the above Ansatz for DGSF by the purely phenomenological factor $(1-x)^5$, motivated by the familiar large-x behaviour of DGLAP parameterizations of the gluon structure function of the proton. We also add to the sea components (2.40), (2.41) the contribution from DIS on valence quarks, borrowing the parameterizations from the respective GRV, CTEQ and MRS fits. The latter are only available for $Q^2 \geq Q_c^2$. At $x \lesssim 10^{-2}$ this valence contribution is small and fades away rapidly with decreasing x[51].

7.2 The parameters of DGSF for different DGLAP inputs

Our goal is to obtain a small-x DGSF in the whole range of $\vec{\kappa}^2$ by adjusting the relevant parameters to the experimental data on small-x $F_{2p}(x,Q^2)$ in the whole available region of Q^2, as well as the real photoabsorption cross section. The theoretical calculation of these observables is based on Eqs. (2.40), (2.41), (7.10).

The parameters that we did not adjust but borrowed from early work in the color dipole picture are $R_c = 0.27$ fm (i.e., $\mu_{pt} = 0.75$ GeV), and the frozen value of the LO QCD coupling with $\Lambda_{QCD} = 0.2$ GeV:

$$\alpha_S(Q^2) = \min\left\{0.82, \frac{4\pi}{\beta_0 \log\frac{Q^2}{\Lambda^2_{QCD}}}\right\} . \tag{7.11}$$

We recall that the GRV, MRS and CTEQ fits to GSF start the DGLAP evolution at quite a different soft-to-hard interface Q_c^2 and diverge markedly, especially at moderate and small $\vec{\kappa}^2$. The value of Q_c^2 is also borrowed from these fits and is not a free parameter.

The adjustable parameters are μ_{soft}, a_{soft}, $m_{u,d}$, $\vec{\kappa}_s^2$ and $\vec{\kappa}_h^2$. (For the heavier quark masses we take $m_s = m_{u,d} + 0.15$GeV and $m_c = 1.5$ GeV.) Both $m_{u,d}$ and μ_{soft} then have clear physical meaning and we have certain insight into their variation range from the early work on color dipole phenomenology of DIS.

The rôle of these parameters is as follows. The quark mass $m_{u,d}$ defines the transverse size of the $q\bar{q} = u\bar{u}, d\bar{d}$ Fock state of the real photon, whose natural scale is the size of the ρ-meson. Evidently, roughly equal values of $F_{2p}(x,Q^2)$ can be obtained for somewhat smaller $\mathcal{F}(x,Q^2)$ at the expense of taking smaller $m_{u,d}$, i.e., larger size of the photon, and vise versa. Therefore, although the quark mass does not explicitly enter the parameterization for $\mathcal{F}(x,\vec{\kappa}^2)$,

the preferred value of $m_{u,d}$ could have been correlated with the DGLAP input. We find that it is sufficient to take the universal $m_{u,d} = 0.22$ GeV.

The μ_{soft}^{-2} defines the soft scale in which the non-perturbative glue is confined, and controls the r-dependence of, and in conjunction with a_{soft} sets the scale for, the dipole cross section for large size $q\bar{q}$ dipoles in the photon. We find that it is sufficient to take the universal $a_{soft} = 2$ and $\kappa_s^2 = 3$ GeV^2 for the parameter of suppression of the hard tale of non-perturturbative soft glue.

The magnitude of the dipole cross section at large and moderately small dipole size depends also on the soft-to-hard interpolation of DGSF, which is sensitive to DGLAP inputs for perturbative component $G_{pt}(x, Q^2)$. This difference of DGLAP inputs can be corrected for by adjusting μ_{soft}^2 and the hard-to-soft interface parameter $\vec{\kappa}_h^2$. The slight rise of $\vec{\kappa}_h^2$ helps to suppress somewhat too strong x-dependence of the soft tale of the perturbative glue. The specific parameterizations for $\vec{\kappa}_h^2$ depend on the DGLAP input and are presented in table 1. Only $\vec{\kappa}_h^2$ and μ_{soft} varied from one DGLAP input to another. The soft components of the D-GRV and D-CTEQ parameterizations turn out identical. The eye-ball fits are sufficient for the purposes of the present exploratory study. The parameters found are similar to those used in [35, 36] where the focus has been on the description of diffractive DIS.

Table 1. The parameters of differential gluon structure function for different DGLAP inputs.

	D-GRV	D-MRS	D-CTEQ
LO DGLAP input	GRV98LO [43]	MRS-LO-1998 [45]	CTEQ4L(v.4.6) [44]
Q_c^2, GeV^2	0.895	1.37	3.26
κ_h^2, GeV^2	$\left(1 + 0.0018 \log^4 \frac{1}{x}\right)^{1/2}$	$\left(1 + 0.038 \log^2 \frac{1}{x}\right)^{1/2}$	$\left(1 + 0.047 \log^2 \frac{1}{x}\right)^{1/2}$
μ_{soft}, GeV	0.1	0.07	0.1

One minor problem encountered in numerical differentiation of all three parameterizations for $G_{pt}(x, Q^2)$ was the seesaw $\vec{\kappa}^2$-behavior of the resulting DGSF (7.4), which was an artifact of the grid interpolation routines. Although this seesaw behavior of DGSF would be smoothed out in integral observables such as $G(x, Q^2)$ or $F_{2p}(x, Q^2)$, we still preferred to remove the unphysical seesaw cusps and have a smooth DGSF. This was achieved by calculating DGSF from (7.4) at the center of each interval of the Q^2-grid and further interpolating the results between these points. By integrating the $\mathcal{F}_{pt}(x, Q^2)$ smoothed in this way one recovers the input $G_{pt}(x, Q^2)$. The values of Q_c^2 cited in Table 1 corresponds to centers of the first bin of the corresponding Q^2-grid.

7.3 The description of the proton structure function $F_{2p}(x, Q^2)$

We focus on the sea-dominated leading $\log\frac{1}{x}$ region of $x < 10^{-2}$. The practical calculation of the proton structure function involves the two running arguments of DGSF: x_g and $\vec{\kappa}^2$. We recall that in the standard collinear DGLAP approximation one has $\vec{\kappa}^2 \ll \vec{k}^2 \ll Q^2$ and $x_g \approx 2x$, [see eq. (3.1)]. Within the $\vec{\kappa}$-factorization approach one finds that the dominant contribution to $F_{2p}(x, Q^2)$ comes from $M_t^2 \sim Q^2$, with little contribution from $M_t^2 \gtrsim Q^2$. Because at small x_g the x_g dependence of $\mathcal{F}(x_g, Q^2)$ is rather steep, we take into account the

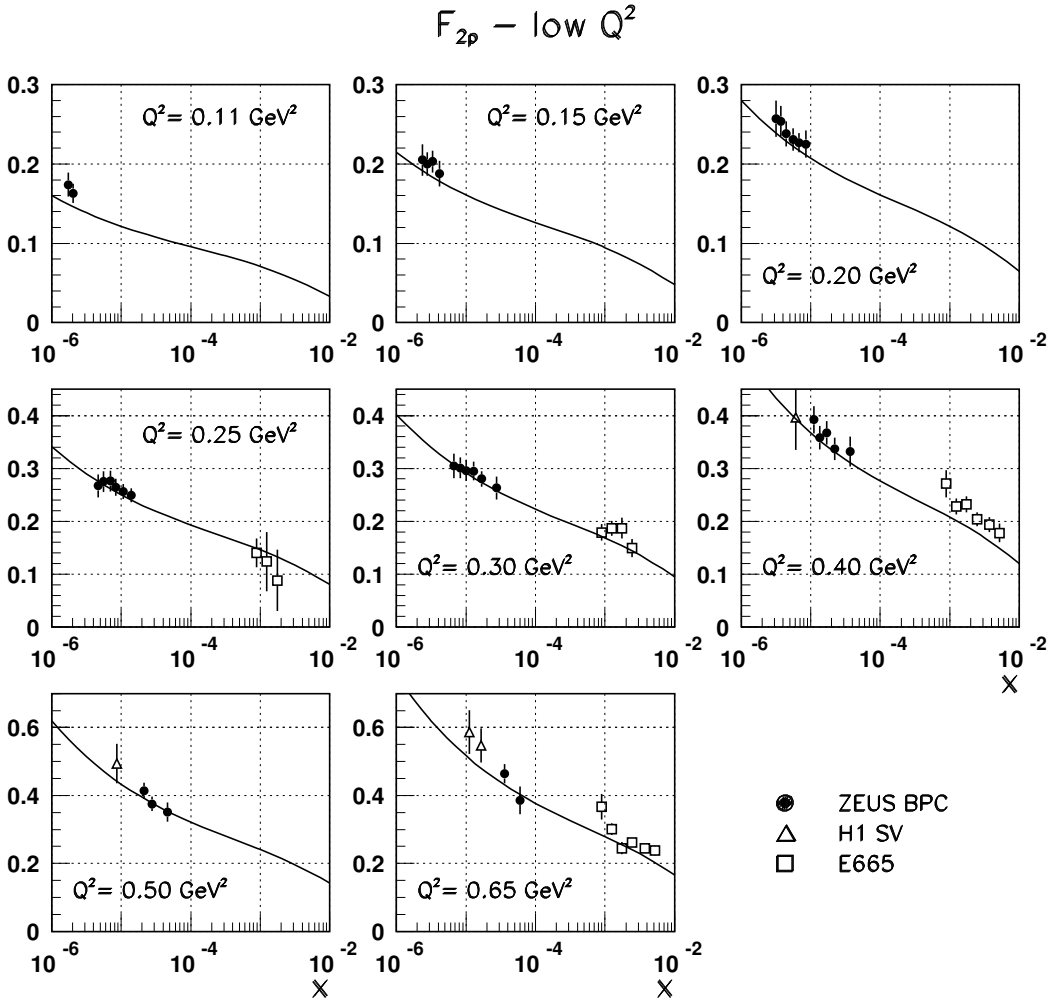

Figure 7.1: *The $\vec{\kappa}$-factorization description of the experimental data on $F_{2p}(x,Q^2)$ in the low Q^2 region; black circles are ZEUS BPC data [62], open triangles denote H1 shifted vertex (SV) data [64], open squares are E665 data [65]. Solid line represents $\vec{\kappa}$-factorization results for the D-GRV parameterization of the differential gluon structure function $\mathcal{F}(x,\vec{\kappa}^2)$.*

$x_g - x$ relationship (2.44). Anticipating the results on effective intercepts, we notice that for all practical purposes one can neglect the impact of $\vec{\kappa}$ on the relation (2.44), which simplifies greatly the numerical analysis. Indeed, the x_g dependence of $\mathcal{F}(x_g,\vec{\kappa}^2)$ is important only at large $\vec{\kappa}^2$, that is, in the region that can contribute to $F_{2p}(x,Q^2)$ only at large Q^2. But the larger Q^2, the better holds the DGLAP ordering $\vec{\kappa}^2 \ll k^2, Q^2$. On the other side, at small-to-moderate Q^2, the DGLAP the ordering breaks down, however the x_g dependence of $\mathcal{F}(x_g,\vec{\kappa}^2)$ is weak here.

Obviously, achieving a good agreement from small-to-moderate to large Q^2 is a nontrivial

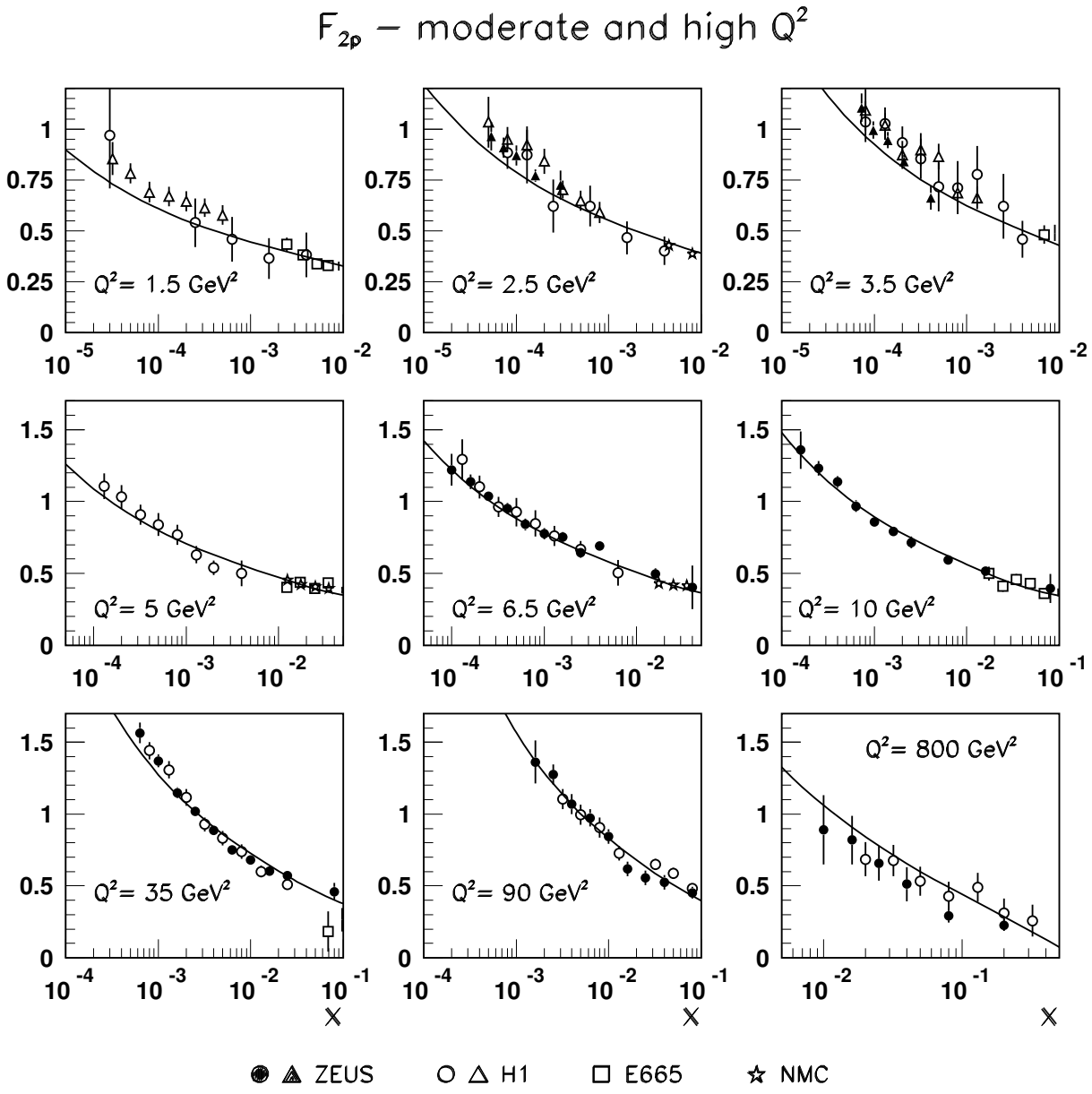

Figure 7.2: *The $\vec{\kappa}$-factorization description of the experimental data on $F_{2p}(x,Q^2)$ in the moderate and high Q^2 region; black circles and triangles are ZEUS data [60], [61], open circles and triangles show H1 data [63], [64], open squares are E665 data [65], stars refer to NMC results [66]. Solid line represents $\vec{\kappa}$-factorization results for the D-GRV parameterization of the differential gluon structure function $\mathcal{F}(x,\vec{\kappa}^2)$.*

task, because strong modification of the soft contribution to $\mathcal{F}(x,\vec{\kappa}^2)$ is unavoidably echoed in the integrated gluon SF throughout the whole range of Q^2 and affects the calculated structure function from small-to-moderate to large Q^2.

The quality of description of the experimental data on the small-x proton structure function achieved is illustrated by figs. 7.1, 7.2. The data shown include recent HERA data (ZEUS [60], ZEUS shifted vertex [61], ZEUS BPC [62], H1 [63], H1 shifted vertex [64]), FNAL E665 experiment [65] and the CERN NMC experiment [66]. When plotting the E665 and NMC

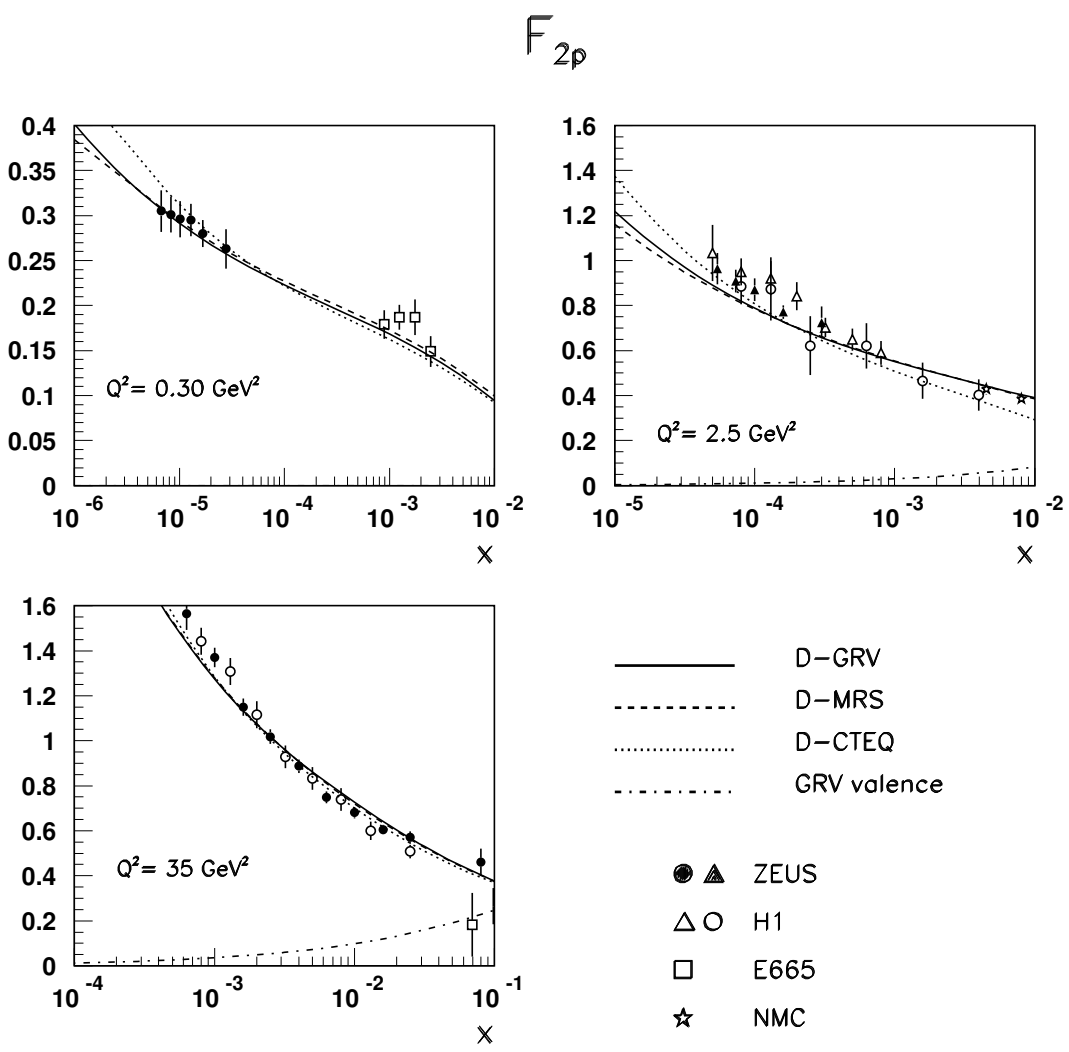

Figure 7.3: *A comparison of the $\vec{\kappa}$-factorization description of the experimental data on $F_{2p}(x,Q^2)$ for several values of Q^2 with the D-GRV, D-CTEQ and D-MRS parameterizations of the differential gluon structure function $\mathcal{F}(x,\vec{\kappa}^2)$. The contribution to $F_{2p}(x,Q^2)$ from DIS off valence quarks is shown separately for larger Q^2.*

data, we took the liberty of shifting the data points from the reported values of Q^2 to the closest Q^2 boxes for which the HERA data were available. For $Q^2 < Q_c^2 = 0.9$ GeV^2 the parameterizations for valence distributions are not available and our curves show only the sea component of $F_{2p}(x,Q^2)$; at larger Q^2 the valence component is included.

For $x < 10^{-2}$ the accuracy of our D-GRV description of the proton structure function is commensurate with that of the accuracy of standard LO GRV fits. In order not to cram the figures with nearly overlapping curves, we show the results for the D-GRV parameterization. The situation with D-CTEQ and D-MRS is very similar, as is seen in Fig. 7.3, where we show on a larger scale simultaneously the results based on the D-GRV, D-CTEQ and D-MRS DGSFs for several selected values of Q^2. Here, at large Q^2, we show separately the contribution from valence quarks. The difference between the results for $F_{2p}(x,Q^2)$ for different DGLAP inputs is marginal for all practical purposes, see also a comparison of the results for $\sigma^{\gamma p}$ for different DGLAP inputs in Fig. 7.4.

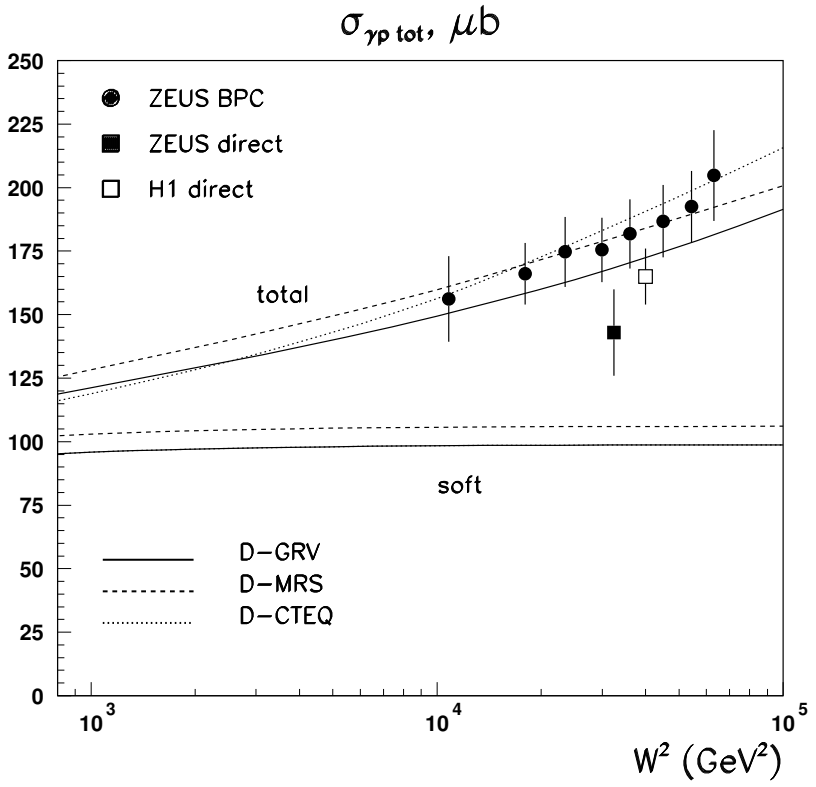

Figure 7.4: *A comparison of the $\vec{\kappa}$-factorization description of the experimental data on real photoabsorption cross section based on the D-GRV, D-CTEQ and D-MRS parameterizations of the differential gluon structure function $\mathcal{F}(x,\vec{\kappa}^2)$. The squares show the experimental data from 1992-93 direct measurements, the bullets are the results of extrapolation of virtual photoabsorption to $Q^2 = 0$ ([62] and references therein). The soft component of photoabsorption cross section is shown separately.*

7.4 Real photoabsorption cross section $\sigma^{\gamma p}$

In the limiting case of $Q^2 = 0$, the relevant observable is the real photoabsorption cross section $\sigma^{\gamma p}$. Although the Bjorken variable is meaningless at very small Q^2, the gluon variable x_g remains well defined at $Q^2 = 0$, [see Eq. (2.44)]. In Fig. 7.4 we present our results alongside the results of the direct measurements of $\sigma^{\gamma p}$ and the results of extrapolation of virtual photoabsorption cross sections to $Q^2 = 0$. For a summary of the experimental data see Ref. [62]. The soft contribution to the cross section is shown separately. We recall that our parameterizations for $\mathcal{F}(x,\vec{\kappa}^2)$ give identical soft cross sections for the GRV and CTEQ inputs (Table 1). The barely visible decrease of $\sigma^{\gamma p}_{soft}$ towards small W is a manifestation of $\propto (1-x)^5$ large-x behaviour of gluon densities. The extension to lower energies requires introduction of the secondary reggeon exchanges which goes beyond the subject of this study.

We emphasize that we reproduce well the observed magnitude and pattern of the energy dependence of $\sigma^{\gamma p}$ in an approach with a manifestly energy-independent soft contribution to

the total cross section. In this scenario the energy dependence of $\sigma^{\gamma p}$ is entirely due to the x_g-dependent hard component $\mathcal{F}_{hard}(x_g, Q^2)$ and, as such, this rise of the total cross section for a soft reaction can be regarded as driven entirely by very substantial hard-to-soft diffusion. Such a scenario has repeatedly been discussed earlier [50, 51, 67]. Time and time again we shall see similar effects of hard-to-soft diffusion and vice-versa. Notice that hard-to-soft diffusion is a straightforward consequence of the full phase space calculation of partonic cross sections and we do not see any possibility for decoupling of the hard gluon contribution from the total cross sections of any soft interaction, whose generic example is the real photoabsorption.

Chapter 8

Properties of differential gluon structure function

8.1 DGSF in the momentum space

8.1.1 Soft/hard decomposition of DGSF

We now focus on the x and $\vec{\kappa}^2$ behavior of the so-determined DGSF starting for reference with the D-GRV parameterization. The same pattern holds for DGSF based on CTEQ and MRS DGLAP inputs (see below). In Figs. 8.1 and 8.2 we plot the differential gluon density $\mathcal{F}(x_g, Q^2)$, while in Fig. 8.3 we show the integrated gluon density

$$G_D(x, Q^2) = \int_0^{Q^2} \frac{d\vec{\kappa}^2}{\vec{\kappa}^2} \mathcal{F}(x, \vec{\kappa}^2)\,. \tag{8.1}$$

Here the subscript D is a reminder that the integrated $G_D(x, Q^2)$ is derived from DGSF. As such, it must not be confused with the DGLAP parameterizations $G_{pt}(x, Q^2)$ denoted with the subscript pt.

Figs. 8.1 and 8.2 illustrate the interplay at various x of the non-perturbative soft component of DGSF and perturbative hard contribution supplemented with the continuation into $\vec{\kappa}^2 \leq Q_c^2$ described above. The soft and hard contributions are shown by dashed and dotted lines, respectively; their sum is given by solid line.

Apart from the large-x suppression factor $(1-x)^5$, our non-perturbative soft component does not depend on x. At moderate x ($\sim 10^{-2}$), it dominates the soft region of $\vec{\kappa}^2 \lesssim 1 \div 2$ GeV^2; the hard component takes over at higher $\vec{\kappa}^2$. The soft-hard crossover point is close to μ_{pt}^2, but because of the hard-to-soft diffusion it moves with decreasing x to a gradually smaller $\vec{\kappa}^2$.

In this determination of DGSF we focus on the ready-to-use parameterizations; the dynamical evolution properties of the this DGSF will be addressed elsewhere. Concerning the relation between DGSF and the observable proton structure function, the early work by Kwiecinski et al. [68] is close in spirit to ours, the difference being in a treatment of the non-perturbative soft component and subjecting DGSF to unified BFKL/DGLAP evolution. In Fig. 8.2 we present DGSF taken from the plots in [68]; the agreement with our results is good, which indicates a consistency of our purely phenomenological parameterizations of DGSF with general expectations from the BFKL dynamics.

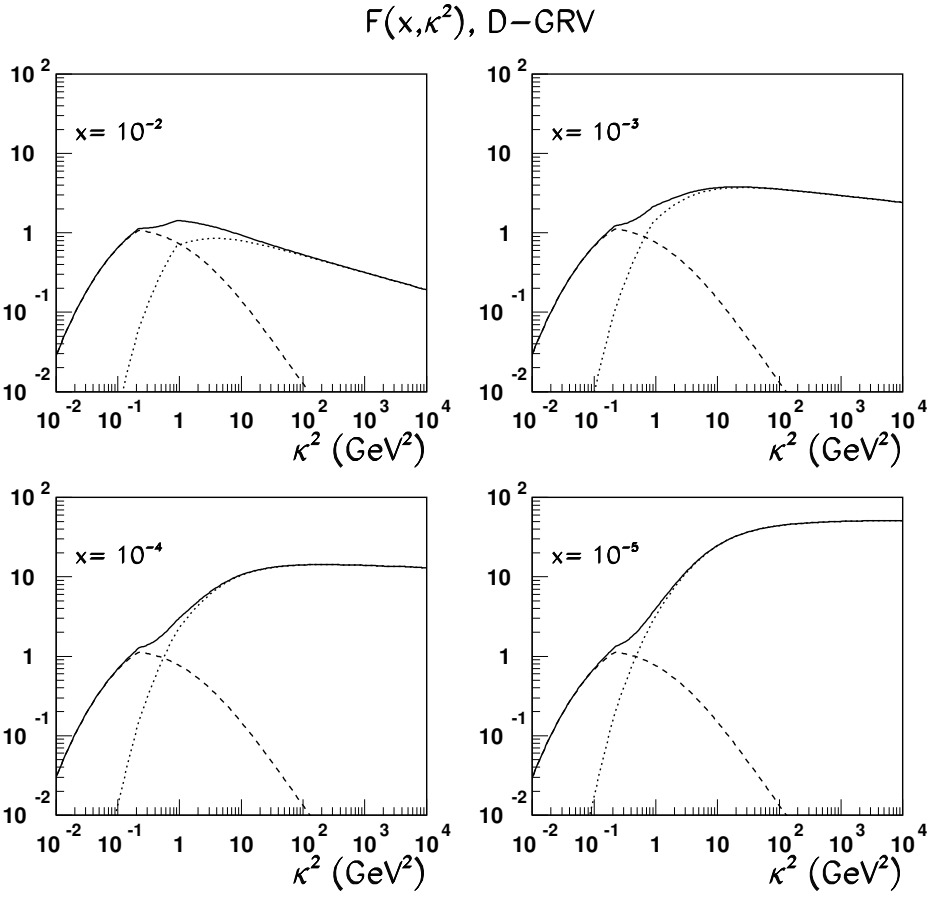

Figure 8.1: *D-GRV differential gluon structure function $\mathcal{F}(x,\vec{\kappa}^2)$ as a function of $\vec{\kappa}^2$ at several values of x. Dashed and dotted lines represent the soft and hard components; the total unintegrated gluon density is shown by the solid line*

8.1.2 Soft/hard decomposition of the integrated gluon structure function

The rôle of the soft component is further illustrated by Fig. 8.3, where we show the integrated gluon density (8.1) and its soft and hard components $G_{soft}(x,Q^2)$ and $G_{hard}(x,Q^2)$, respectively. The soft contribution $G_{soft}(x,Q^2)$ is a dominant feature of the integrated gluon density $G_D(x,Q^2)$ for $Q^2 \lesssim 1$ GeV^2. It builds up rapidly with Q^2 and receives the major contribution from the region $\vec{\kappa}^2 \sim 0.3 \div 0.5$ GeV^2. Our Ansatz for $\mathcal{F}_{soft}(x,\vec{\kappa}^2)$ is such that it starts decreasing already at $\vec{\kappa}^2 \sim 0.2$ GeV^2 and vanishes rapidly beyond $\vec{\kappa}^2 \gtrsim \kappa^2_{soft}$. The residual rise of the soft gluon density beyond $Q^2 \sim 0.5$ GeV^2 is still substantial: $G_{soft}(x,Q^2)$ rises by about the factor two before it flattens at large Q^2. We emphasize that $G_{soft}(Q^2)$ being finite at large Q^2 is quite natural — a decrease of $G_{soft}(Q^2)$ at large Q^2 is only possible if $\mathcal{F}_{soft}(Q^2)$ becomes negative at large Q^2, which does not seem to be a viable option.

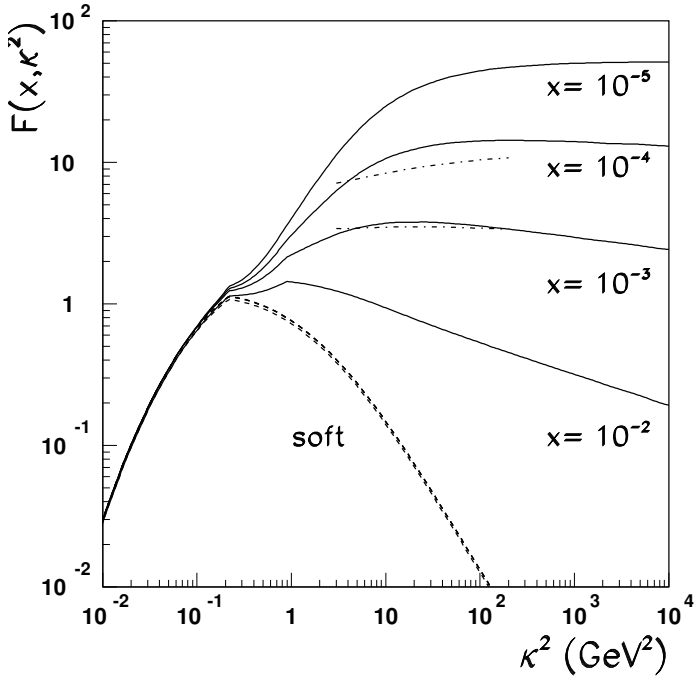

Figure 8.2: *The same as in Fig. 8.1 but overlaid onto one graph for illustration of the x-dependence of $\mathcal{F}(x,\vec{\kappa}^2)$. The dashed lines shows the soft component $\mathcal{F}_{soft}(x,\vec{\kappa}^2)$ and its slight variation with x due to the finite-x factor $(1-x)^5$. The dot-dashed curves show the Kwiecinski et al. [68] results for DGSF from a $\vec{\kappa}$-factorization phenomenology of $F_{2p}(x,Q^2)$ based on the solution of the unified BFKL/DGLAP equation.*

At moderately small x ($\sim 10^{-2}$) the scaling violations are still weak and the soft contribution $G_{soft}(x,Q^2)$ remains a substantial part — about one half — of integrated GSF $G_D(x,Q^2)$ *at all* Q^2. At very small x ($\lesssim 10^{-3}$) the scaling violations in the gluon structure function are strong and $G_{hard}(x,Q^2) \gg G_{soft}(x,Q^2)$ starting from $Q^2 \sim$ 1-2 GeV^2.

8.1.3 Soft/hard decomposition of the proton structure function $F_2(x,Q^2)$

Eqs. (2.40), (2.41) define the soft/hard decomposition of the proton structure function. In Fig. 8.4 we show $F_{2p}^{hard}(x,Q^2)$ and $F_{2p}^{soft}(x,Q^2)$ as a function of Q^2 for two representative values of x. Notice how the significance of the soft component as a function of Q^2 rises as one moves from fully differential $\mathcal{F}(x,Q^2)$ to the integrated $G_D(x,Q^2)$ to the doubly integrated $F_{2p}^{soft}(x,Q^2)$. At a moderately small x ($\sim 10^{-3}$), the soft contribution is a dominant part of $F_{2p}(x,Q^2)$, although the rapidly rising hard component $F_{2p}^{hard}(x,Q^2)$ gradually takes over at smaller x.

Notice that not only does $F_{2p}^{soft}(x,Q^2)$ not vanish at large Q^2, but it rises slowly with Q^2

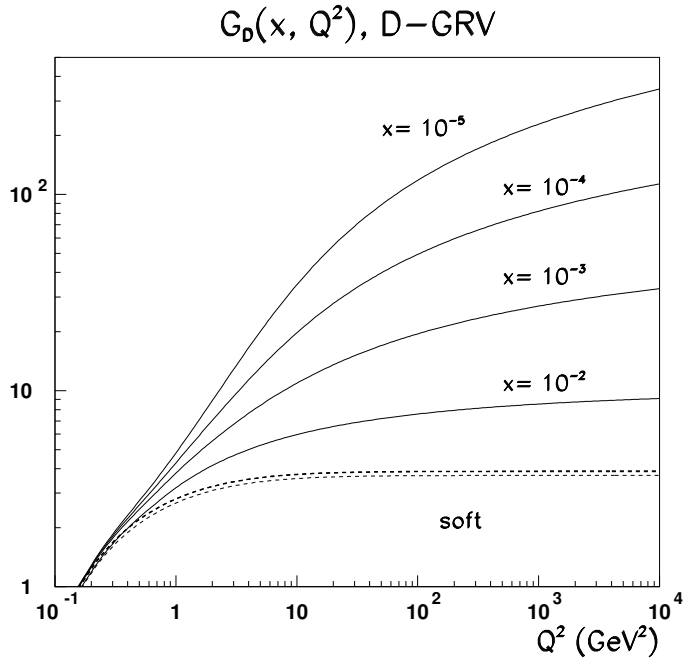

Figure 8.3: *The same as Fig. 8.1 but for the integrated gluon structure function $G_D(x, Q^2)$ as given by the D-GRV parameterization of the differential gluon structure function $\mathcal{F}(x, \vec{\kappa}^2)$ (for discussion see Section 6.2.*

as

$$F_{2p}^{soft}(x, Q^2) \sim \sum e_f^2 \frac{4G_{soft}(Q^2)}{3\beta_0} \log \frac{1}{\alpha_S(Q^2)} \,. \tag{8.2}$$

Again, the decrease of $F_{2p}^{soft}(x, Q^2)$ with Q^2 would only be possible at the expense of unphysical negative-valued $G_{soft}(Q^2)$ at large Q^2.

8.2 DGSF in the x-space: effective intercepts and hard-to-soft diffusion

It is instructive to look at the change of the x-dependence from the differential gluon structure function $\mathcal{F}(x, \vec{\kappa}^2)$ to the integrated gluon structure function $G_D(x, Q^2)$ and, further, to the proton structure function $F_{2p}(x, Q^2)$. It is customary to parameterize the x-dependence of various structure functions by the effective intercept. For instance, the effective intercept τ_{eff} for differential gluon structure function is defined by the parameterization

$$\mathcal{F}(x, \vec{\kappa}^2) \propto \left(\frac{1}{x}\right)^{\tau_{eff}(\vec{\kappa}^2)} \,. \tag{8.3}$$

One can define the related intercepts τ_{hard} for the hard component $\mathcal{F}_{hard}(x, \vec{\kappa}^2)$. Notice that in our Ansatz $\tau_{soft} \equiv 0$.

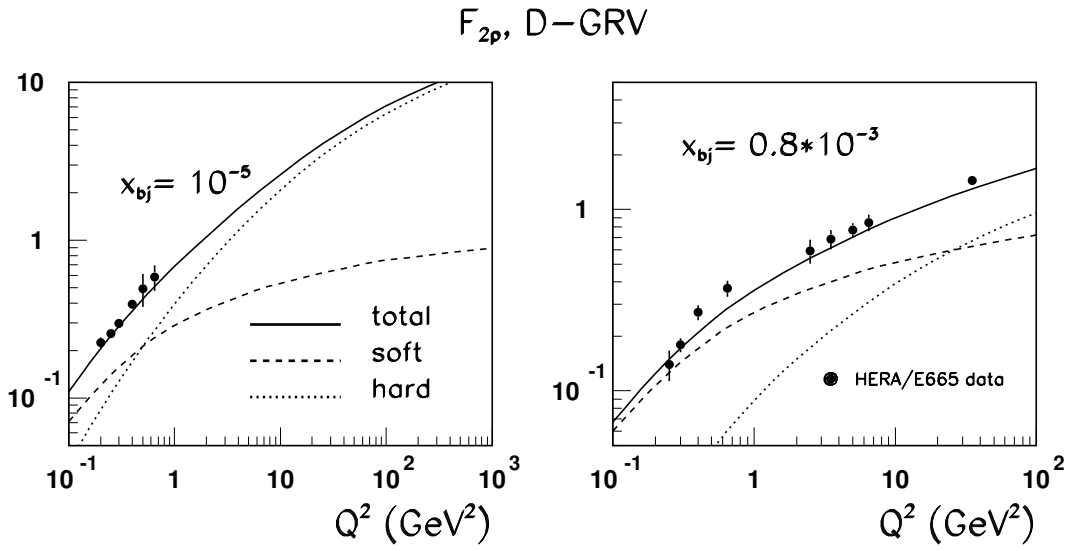

Figure 8.4: *The soft-hard decomposition of $\vec{\kappa}$-factorization results for the proton structure function $F_{2p}(x,Q^2)$ evaluated with the D-GRV parameterization of the differential gluon structure function $\mathcal{F}(x,\vec{\kappa}^2)$.*

The power law (8.3) is only a crude approximation to the actual x-dependence of DGSF and the effective intercept τ_{eff} will evidently depend on the range of x fitted. To be more definitive, for the purposes of the present discussion we define the effective intercept as

$$\tau_{eff}(\vec{\kappa}^2) = \frac{\log[\mathcal{F}(x_2,\vec{\kappa}^2)/\mathcal{F}(x_1,\vec{\kappa}^2)]}{\log(x_1/x_2)}\,, \tag{8.4}$$

taking $x_2 = 10^{-5}$ and $x_1 = 10^{-3}$. The effective intercept $\tau_{hard}(\vec{\kappa}^2)$ is defined by (8.4) in terms of $\mathcal{F}_{hard}(x,\vec{\kappa}^2)$.

One can define the related intercepts $\lambda_{eff}, \lambda_{hard}$ for the integrated gluon structure function $G_D(x,Q^2)$:

$$G_D(x,Q^2) \propto \left(\frac{1}{x}\right)^{\lambda_{eff}(Q^2)}\,. \tag{8.5}$$

In the case of $F_{2p}(x,Q^2)$ we define the intercept $\Delta(Q^2)$ in terms of the variable $\overline{x}$ defined as

$$\bar{x} = \frac{Q^2+M_V^2}{W^2+Q^2} \sim x_g\,, \tag{8.6}$$

where M_V is the mass of the ground state vector meson in the flavor channel considered. Such a replacement allows one to treat the range $Q^2 \lesssim 1$ GeV^2 on equal footing, where the formally defined Bjorken variable x can no longer be interpreted as a light cone momentum carried by charged partons. For the purposes of the direct comparison with $\tau(Q^2)$ and $\lambda(Q^2)$, and

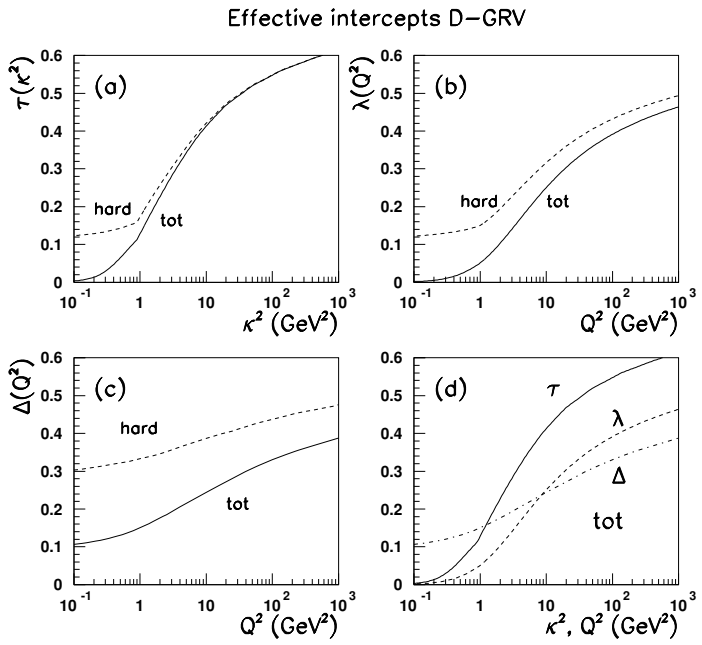

Figure 8.5: *Effective intercepts for total and hard components of (a) the differential gluon structure function $\mathcal{F}(x,Q^2)$, (b) the integrated gluon structure function $G_D(x,Q^2)$ and (c) the proton structure function $F_{2p}(x,Q^2)$ evaluated with the D-GRV parameterization of the differential gluon structure function $\mathcal{F}(x,\vec{\kappa}^2)$. In graph (d) we compare the effective intercepts $\tau_{eff}(Q^2), \lambda_{eff}(Q^2)$ and $\Delta_{eff}(Q^2)$ for $\mathcal{F}(x,Q^2)$, $G_D(x,Q^2)$ and $F_{2p}(x,Q^2)$, respectively.*

in order to avoid biases caused by the valence structure function, here we focus on intercepts $\Delta_{eff}, \Delta_{hard}$ for the sea component of the proton structure function $F_{2p}^{sea}(x,Q^2)$:

$$F_{2p}^{sea}(x,Q^2) \propto \left(\frac{1}{x}\right)^{\Delta_{eff}(Q^2)} . \tag{8.7}$$

The results for the effective intercepts are shown in figs. 8.5, 8.6 and 8.7.

In our simplified hard-to-soft extrapolation of $\mathcal{F}_{hard}(x,Q^2)$ we attribute to $\mathcal{F}_{hard}(x,Q^2)$ at $Q^2 \leq Q_c^2$ the same x-dependence as at $Q^2 = Q_c^2$ modulo to slight modifications for the x-dependence of $\vec{\kappa}_h^2$. This gives the cusp in $\tau_{hard}(Q^2)$ at $Q^2 = Q_c^2$, i.e., the first derivative of $\tau_{hard}(Q^2)$ is discontinuous at $Q^2 = Q_c^2$.

A comparison of Fig. 8.2 with Fig. 8.3 and further with Fig. 8.4 shows clearly that only in DGSF $\mathcal{F}(x,Q^2)$ is the effect of the soft component concentrated at small Q^2. In integrated $G_D(x,Q^2)$, and especially in the proton structure function $F_{2p}(x,Q^2)$, the impact of the soft component extends to much larger Q^2. The larger the soft contribution, the stronger is the reduction of τ_{eff} from τ_{hard} and so forth, as evident from Fig. 8.5a to 8.5b to 8.5c. See also Figs. 8.6 and 8.7.

The change of effective intercepts from differential $\mathcal{F}(x,Q^2)$ to integrated $G_D(x,Q^2)$ is straightforward; the principal effect is that $\lambda_{hard}(Q^2) < \tau_{hard}(Q^2)$ and $\lambda_{eff}(Q^2) < \tau_{eff}(Q^2)$, which reflects the growing importance of soft component in $G_D(x,Q^2)$. The change of effective

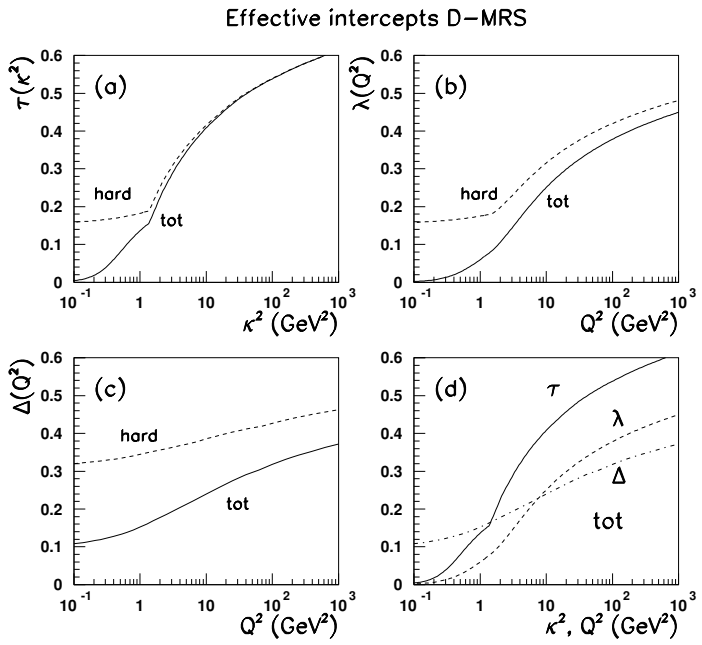

Figure 8.6: *Effective intercepts for total and hard components of (a)the differential gluon structure function $\mathcal{F}(x,Q^2)$, (b) the integrated gluon structure function $G_D(x,Q^2)$ and (c) the proton structure function $F_{2p}(x,Q^2)$ evaluated with the D-MRS parameterization of the differential gluon structure function $\mathcal{F}(x,\vec{\kappa}^2)$. In graph (d) we compare the effective intercepts $\tau_{eff}(Q^2), \lambda_{eff}(Q^2)$ and $\Delta_{eff}(Q^2)$ for $\mathcal{F}(x,Q^2)$, $G_D(x,Q^2)$ and $F_{2p}(x,Q^2)$, respectively.*

intercepts from $\mathcal{F}(x,Q^2)$ and $G_D(x,Q^2)$ to $F_{2p}(x,Q^2)$ is less trivial and exhibits two dramatic consequences of the hard-to-soft and soft-to-hard diffusion. If the standard DGLAP contribution (3.2) were all, then the change from the intercept $\lambda(Q^2)$ for integrated gluon density to the intercept $\Delta(Q^2)$ for the proton structure function $F_{2p}(x,Q^2)$ would be similar to the change from $\tau(Q^2)$ to $\lambda(Q^2)$; i.e., the effective intercept $\Delta_{eff}(Q^2)$ would have been close to zero for $Q^2 \lesssim 1$ GeV^2. However, by virtue of the hard-to-soft diffusion phenomenon inherent to the $\vec{\kappa}$-factorization, $F_{2p}(x,Q^2)$ receives a contribution from gluons with $\vec{\kappa}^2 > Q^2$, which enhances substantially $\Delta_{hard}(Q^2)$ and $\Delta_{eff}(Q^2)$. The net result is that at small to moderately large Q^2 we find $\Delta_{hard}(Q^2) > \lambda_{hard}(Q^2)$ and $\Delta_{eff}(Q^2) > \lambda_{eff}(Q^2)$. As we emphasized above, the rise of the real photoabsorption cross section is precisely of the same origin.

The second effect is a dramatic flattening of the effective hard intercept $\Delta_{hard}(Q^2)$ over the whole range of Q^2. For all three DGLAP inputs $\Delta_{hard}(Q^2)$ flattens at approximately the same Δ_{hard} (≈ 0.4).

The set of Figs. 8.5–8.7 also shows that the systematics of intercepts in the hard region of $Q^2 > Q_c^2$ is nearly identical for all the three DGLAP inputs. In the soft region we have a slight inequality $\tau_{hard}(\vec{\kappa}^2)|_{D-MRS} > \tau_{hard}(\vec{\kappa}^2)|_{D-GRV}$, which can be readily attributed to a slight inequality $Q_c^2(MRS) > Q_c^2(GRV)$. In the case of CTEQ4L(v.4.6) input the value of $Q_c^2(CTEQ)$ is substantially larger than $Q_c^2(MRS)$, $Q_c^2(GRV)$. In the range $Q_c^2(MRS)$, $Q_c^2(GRV) < \vec{\kappa}^2 < Q_c^2(CTEQ)$, the effective intercept $\tau_{hard}(\vec{\kappa}^2)$ rises steeply with

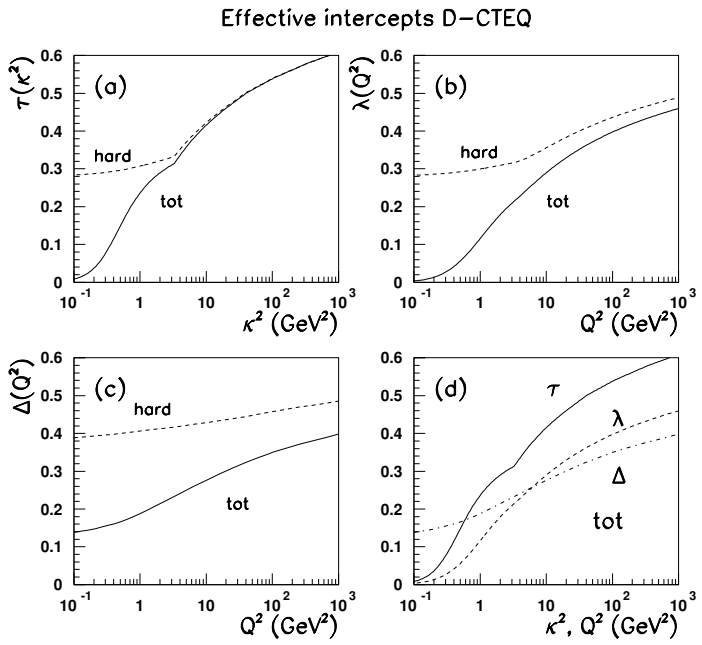

Figure 8.7: *Effective intercepts for total and hard components of (a) the differential gluon structure function $\mathcal{F}(x,Q^2)$, (b) the integrated gluon structure function $G_D(x,Q^2)$ and (c) the proton structure function $F_{2p}(x,Q^2)$ evaluated with the D-CTEQ parameterization of the differential gluon structure function $\mathcal{F}(x,\vec{\kappa}^2)$. In graph (d) we compare the effective intercepts $\tau_{eff}(Q^2), \lambda_{eff}(Q^2)$ and $\Delta_{eff}(Q^2)$ for $\mathcal{F}(x,Q^2)$, $G_D(x,Q^2)$ and $F_{2p}(x,Q^2)$, respectively.*

$\vec{\kappa}^2$. This explains why in the soft region $\tau_{hard}(\vec{\kappa}^2)|_{CTEQ}$ is significantly larger than for the D-GRV and D-MRS parameterizations. The difference among intercepts for the three parameterizations decreases gradually from differential $\mathcal{F}(x,\vec{\kappa}^2)$ to integrated $G_D(x,Q^2)$ gluon density to the proton structure function $F_{2p}(x,Q^2)$.

Finally, in Fig. 8.8 we compare our results for $\Delta_{eff}(Q^2)$ with the recent experimental data from the ZEUS collaboration [61]. Since in the experimental fit the range of $x = [x_{max}, x_{min}]$ varies from point to point, we mimicked the experimental procedure in our evaluation of Δ_{eff} from Eq. (8.11) by taking $\overline{x}_2 = x_{max}$ and $\overline{x}_1 = x_{min}$. This explains the somewhat irregular Q^2-dependence. The experimental data include both sea and valence components. At $Q^2 > Q_c^2(GRV) = 0.9$ GeV^2 we included the valence component of the structure function, taking the GRV98LO parameterization. For CTEQ4L(v.4.6) and MRS-LO-1998, the values of Q_c^2 are substantially larger. The valence component is, however, a small correction and we took the liberty of extracting the valence contribution $F_{2p}^{val}(x,Q^2)$ from GRV fits for $Q_c^2(GRV) < Q^2 < Q_c^2(MRS), Q_c^2(CTEQ)$. The overall agreement with experiment is good. Differences among the three parameterizations is marginal and can, of course, be traced back to Figs. 8.5–8.7.

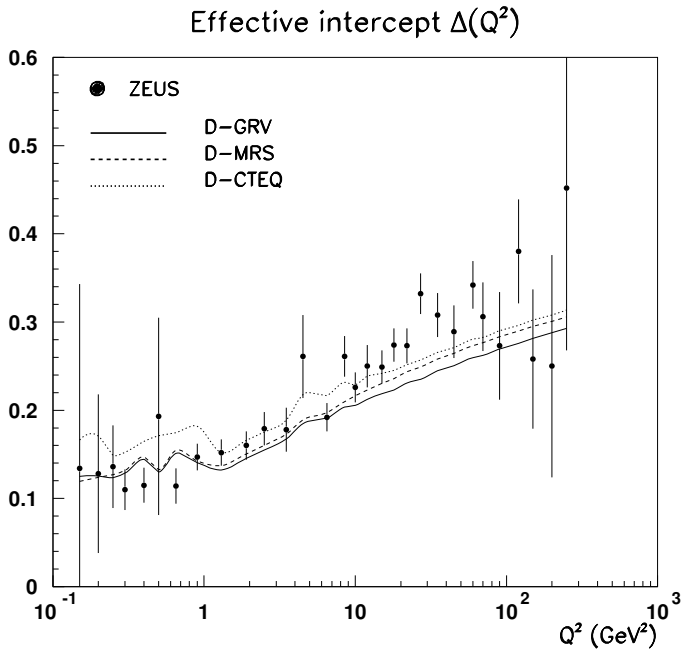

Figure 8.8: *Effective intercepts $\Delta(Q^2)$ of the proton structure function $F_{2p}(x,Q^2)$ in the HERA domain evaluated for the D-GRV, D-MRS and D-CTEQ parameterizations for the differential gluon structure function $\mathcal{F}(x,\vec{\kappa}^2)$; the experimental data points are from ZEUS [61]*

8.3 How the gluon densities of $\vec{\kappa}$-factorization differ from DGLAP gluon densities

It is instructive also to compare our results for the integrated GSF (8.1) with the conventional DGLAP fit $G_{pt}(x,Q^2)$. In Fig. 8.9 we present such a comparison between our integrated D-GRV distribution (the solid curves) and the GRV98LO distribution (the dashed curves). As was anticipated in section 3.2, at very large Q^2 the two gluon distributions converge. We also anticipated that at small x and moderate Q^2 the DGLAP gluon structure functions $G_{pt}(x,Q^2)$ are substantially larger than the result of integration of DGSF (see Eq. (8.1)). At $x = 10^{-5}$ they differ by as much as a factor 3 over a broad range of $Q^2 \lesssim 100$ GeV^2. The difference between the integrated DGSF and the DGLAP fit decreases gradually at large x, and is marginal at $x = 10^{-2}$.

Recall the substantial divergence of the GRV, MRS and CTEQ gluons structure functions of the DGLAP approximation $G_{pt}(x,Q^2)$ at small and moderate Q^2. Contrary to that, the $\vec{\kappa}$-factorization D-GRV, D-CTEQ and D-MRS gluon structure functions $G_D(x,Q^2)$ are nearly identical. We demonstrate this property in Fig. 8.10 where we show integrated $G_D(x,Q^2)$ and their DGLAP counterparts $G_{pt}(x,Q^2)$ for the three parameterizations at two typical values of x. Because of an essentially unified treatment of the region $\vec{\kappa}^2 \leq Q_c^2$ and strong constraint on DGSF in this region from the experimental data at small Q^2, such a convergence of D-GRV, D-CTEQ and D-MRS DGSFs is not unexpected.

One can also compare the effective intercepts for our integrated GSF $G_D(x,Q^2)$ with those

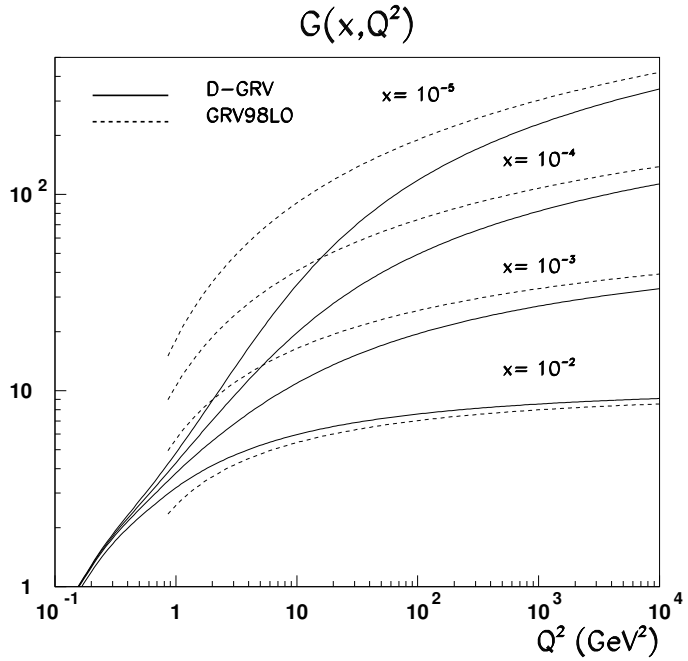

Figure 8.9: *Comparison of our results for integrated gluon density $G_D(x,Q^2)$ evaluated with the D-GRV parameterization of the differential gluon structure function $\mathcal{F}(x,\vec{\kappa}^2)$ with the GRV98L0 DGLAP input parameterization $G_{pt}(x,Q^2)$.*

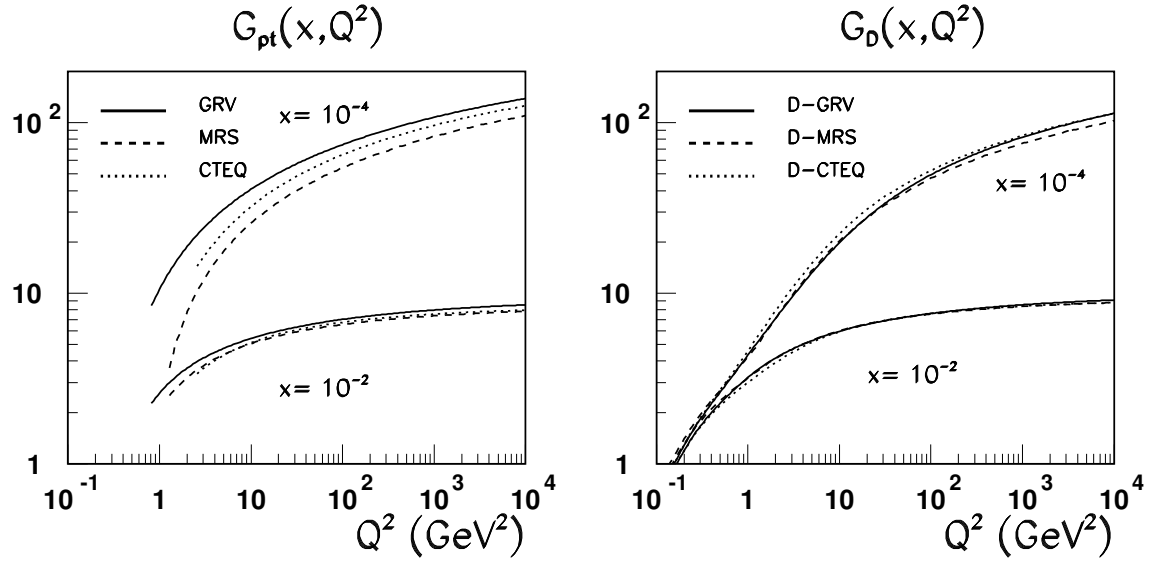

Figure 8.10: *Comparison of the divergence of GRV98L0, CTEQ4L(v.4.6) and MRS-LO-1998 gluon structure functions $G_{pt}(x,Q^2)$ in the left box with the divergence of our integrated gluon structure functions $G_D(x,Q^2)$ evaluated for the D-GRV, D-CTEQ and D-MRS parameterizations for differential gluon structure function $\mathcal{F}(x,Q^2)$ at two typical values of x*

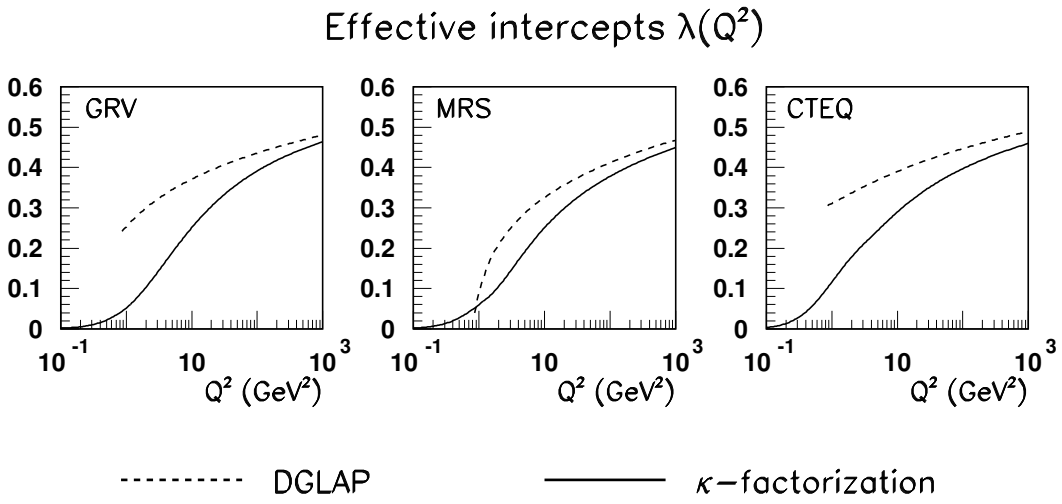

Figure 8.11: *Comparison of the intercept $\lambda_{eff}^{(pt)}(Q^2)$ of the x-dependence of the GRV98L0, CTEQ4L(v.4.6) and MRS-LO-1998 gluon structure functions $G_{pt}(x,Q^2)$ with their counterpart $\lambda_{eff}(Q^2)$ for integrated $G_D(x,Q^2)$ evaluated with D-GRV, D-CTEQ and D-MRS parameterizations for differential gluon structure function $\mathcal{F}(x,Q^2)$.*

obtained from DGLAP gluon distributions $G_{pt}(x,Q^2)$. Fig. 8.11 shows large differences of $\lambda_{eff}^{(pt)}(Q^2)$ from one DGLAP input to another. At the same time, this divergence of different DGLAP input parameterizations is washed out to a large extent in the $\vec{\kappa}$-factorization description of physical observables (see also (8.8)).

8.4 How different observables probe the DGSF

The issue we address in this section is how different observables map the $\vec{\kappa}^2$-dependence of $\mathcal{F}(x_g,\vec{\kappa}^2)$. We expand on the qualitative discussion in section 3.2 and corroborate it with numerical analysis following the discussion in [52]. We start with the two closely related quantities — the longitudinal structure function $F_L(x,Q^2)$ and scaling violations $\partial F_2(x,Q^2)/\partial \log Q^2$ — and proceed to $F_{2p}(x,Q^2)$ and the charm structure function of the proton $F_{2p}^{c\bar{c}}(x,Q^2)$. This mapping is best studied if in (2.40) and (2.41) we integrate first over $\vec{k}$ and z. In order to focus on the $\vec{\kappa}^2$ dependence we prefer presenting different observables in terms of $\mathcal{F}(2x,\vec{\kappa}^2)$ and $G_D(2x,\vec{\kappa}^2)$,

$$F_L(x,Q^2) = \frac{\alpha_S(Q^2)}{3\pi}\sum e_f^2 \int \frac{d\vec{\kappa}^2}{\vec{\kappa}^2}\Theta_L^{(f\bar{f})}(Q^2,\vec{\kappa}^2)\mathcal{F}(2x,\vec{\kappa}^2)\,, \tag{8.8}$$

$$\frac{\partial F_2(x,Q^2)}{\partial \log Q^2} = \frac{\alpha_S(Q^2)}{3\pi}\sum e_f^2 \int \frac{d\vec{\kappa}^2}{\vec{\kappa}^2}\Theta_2^{(f\bar{f})}(Q^2,\vec{\kappa}^2)\mathcal{F}(2x,\vec{\kappa}^2)\,. \tag{8.9}$$

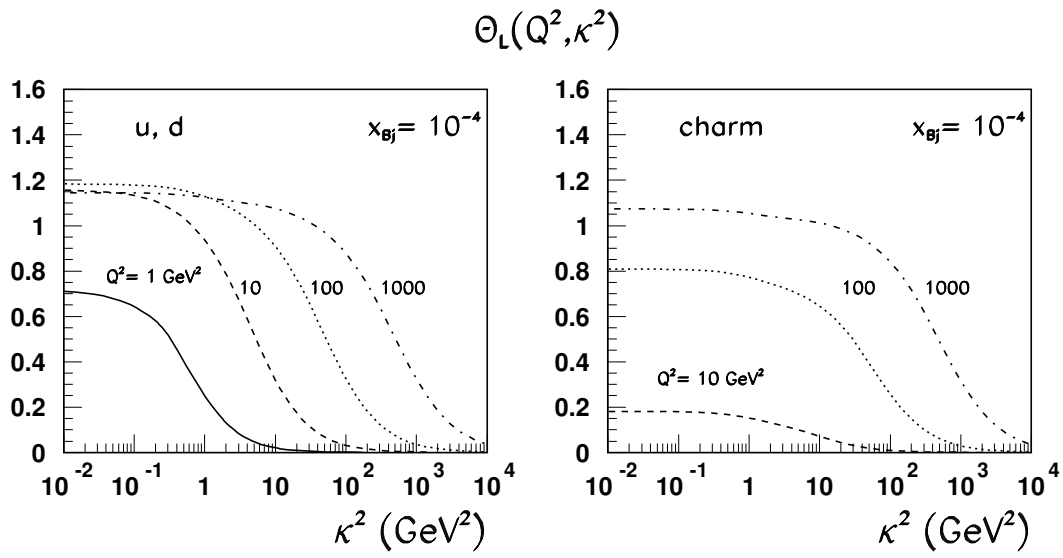

Figure 8.12: *The weight function Θ_L for mapping of the differential gluon structure function $\mathcal{F}(x,\vec{\kappa}^2)$ as a function of $\vec{\kappa}^2$ for several values of Q^2. We show separately the results for light flavors, u, d, and c.*

In the numerical calculation of $F_L(x,Q^2)$ starting from Eq. (2.41) we have x_g and $\vec{\kappa}^2$ as the two running arguments of $\mathcal{F}(x_g,\vec{\kappa}^2)$. As discussed above, the mean value of x_g is close to $2x$, but the exact relation depends on $\vec{\kappa}^2$. The $\vec{k}, z$ integration amounts to averaging of $\mathcal{F}(x_g,\vec{\kappa}^2)$ over certain range of x_g. The result of this averaging is for the most part controlled by the effective intercept $\tau_{eff}(\vec{\kappa}^2)$:

$$\langle \mathcal{F}(x_g,\vec{\kappa}^2)\rangle = \left\langle \mathcal{F}(2x,\vec{\kappa}^2)\left(\frac{2x}{x_g}\right)^{\tau_{eff}(\vec{\kappa}^2)}\right\rangle = r(\vec{\kappa}^2)\mathcal{F}(2x,\vec{\kappa}^2)\,. \tag{8.10}$$

Because the derivative of $\tau_{eff}(\vec{\kappa}^2)$ changes rapidly around $\vec{\kappa}^2 = Q_c^2$, the rescaling factor $r(\vec{\kappa}^2)$ also has a rapid variation of the derivative at $\vec{\kappa}^2 = Q_c^2$, which in due turn generates the rapid change of derivatives of $\Theta_{L,2}^{(f\bar{f})}(Q^2,\vec{\kappa}^2)$ around $\vec{\kappa}^2 = Q_c^2$. As far as the mapping of differential $\mathcal{F}(2x,\vec{\kappa}^2)$ is concerned, this is an entirely marginal effect. However, if we look at the mapping of the integrated gluon structure function $G_D(x,Q^2)$, which is derived from (8.8) and (8.9) by integration by parts,

$$F_L(x,Q^2) = -\frac{\alpha_S(Q^2)}{3\pi}\sum e_f^2 \int \frac{d\vec{\kappa}^2}{\vec{\kappa}^2}\frac{\partial\Theta_L^{(f\bar{f})}(Q^2,\vec{\kappa}^2)}{\partial\log\vec{\kappa}^2}G_D(2x,\vec{\kappa}^2)\,, \tag{8.11}$$

$$\frac{\partial F_2(x,Q^2)}{\partial\log Q^2} = -\frac{\alpha_S(Q^2)}{3\pi}\sum e_f^2 \int \frac{d\vec{\kappa}^2}{\vec{\kappa}^2}\frac{\partial\Theta_2^{(f\bar{f})}(Q^2,\vec{\kappa}^2)}{\partial\log\vec{\kappa}^2}G_D(2x,\vec{\kappa}^2)\,, \tag{8.12}$$

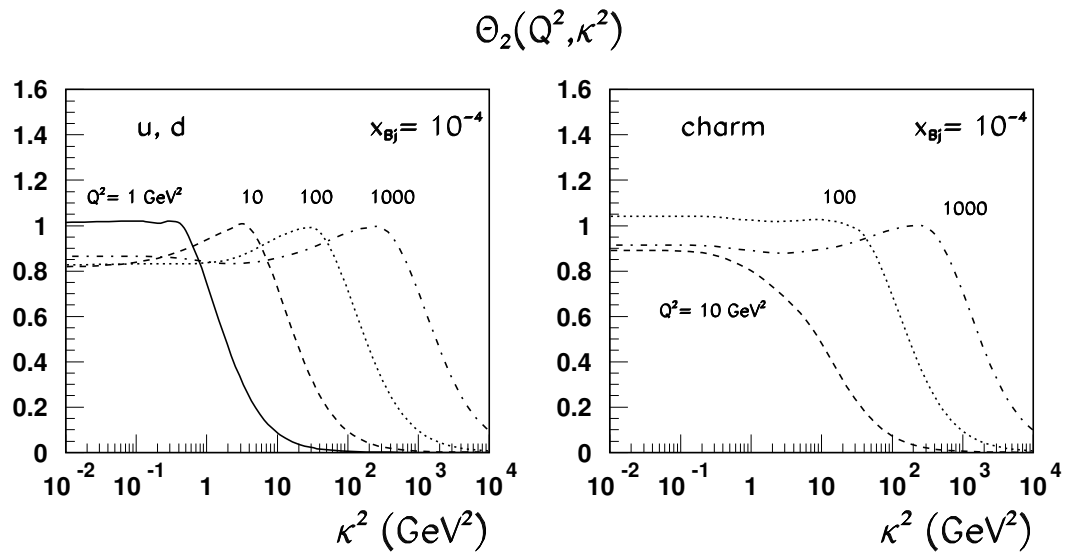

Figure 8.13: *The weight function Θ_2 for mapping of the differential gluons structure function $\mathcal{F}(x,\vec{\kappa}^2)$ as a function of $\vec{\kappa}^2$ for several values of Q^2. We show separately the results for light flavors, u, d, and c.*

then the weight functions $\partial\Theta_{2,L}^{(f\bar{f})}(Q^2,\vec{\kappa}^2)/\partial\log\vec{\kappa}^2$ will exhibit a slightly irregular behaviour around $\vec{\kappa}^2 = Q_c^2$. Evidently, such an irregularity appears in any region of fast variation of $\tau_{eff}(\vec{\kappa}^2)$; in our simplified model it is somewhat amplified by the cusp-like $\vec{\kappa}^2$ dependence of $\tau_{eff}(\vec{\kappa}^2)$.

Finally, starting from (8.12), one obtains a useful representation for how the proton structure function $F_{2p}(x,Q^2)$ maps the integrated gluon structure function:

$$F_{2p}(x,Q^2) = -\int_0^{Q^2}\frac{dq^2}{q^2}\frac{\alpha_S(q^2)}{3\pi}\sum e_f^2\int\frac{d\vec{\kappa}^2}{\vec{\kappa}^2}\frac{\partial\Theta_2^{(f\bar{f})}(q^2,\vec{\kappa}^2)}{\partial\log\vec{\kappa}^2}G_D(2x,\vec{\kappa}^2)$$
$$= \frac{1}{3\pi}\sum e_f^2\int\frac{d\vec{\kappa}^2}{\vec{\kappa}^2}W_2^{(f\bar{f})}(Q^2,\vec{\kappa}^2)\alpha_S(\vec{\kappa}^2)G_D(2x,\vec{\kappa}^2) \qquad (8.13)$$

In Figs. 8.12 and 8.13 we show the weight functions Θ_L and Θ_2. Evidently, for light flavours and very large Q^2 they can be approximated by step-functions

$$\Theta_{L,2}^{(f\bar{f})}(Q^2,k^2) \sim \theta(C_{L,2}Q^2 - \vec{\kappa}^2)\,, \qquad (8.14)$$

where the scale factors $C_L \sim \frac{1}{2}$ and $C_2 \sim 2$ can be readily read from Figures (for the related discussion see [52]). Note that the value $C_2 \sim 2$ corresponds to $\bar{C}_2 \sim 8$ introduced in Section 3.2. Recall that the development of the plateau-like behaviour of Θ_L and Θ_2 which extends to $\vec{\kappa}^2 \sim Q^2$ signals the onset of the leading $\log Q^2$ approximation. For large Q^2 in the approximation (8.14) the $\vec{\kappa}^2$ integration can be carried out explicitly and $F_L(x,Q^2) \propto G_D(2x, C_L Q^2)$. Similarly, $\partial F_2(x,Q^2)/\partial\log Q^2 \propto G_D(2x, C_2 Q^2)$ (cf. Eq. (3.6)).

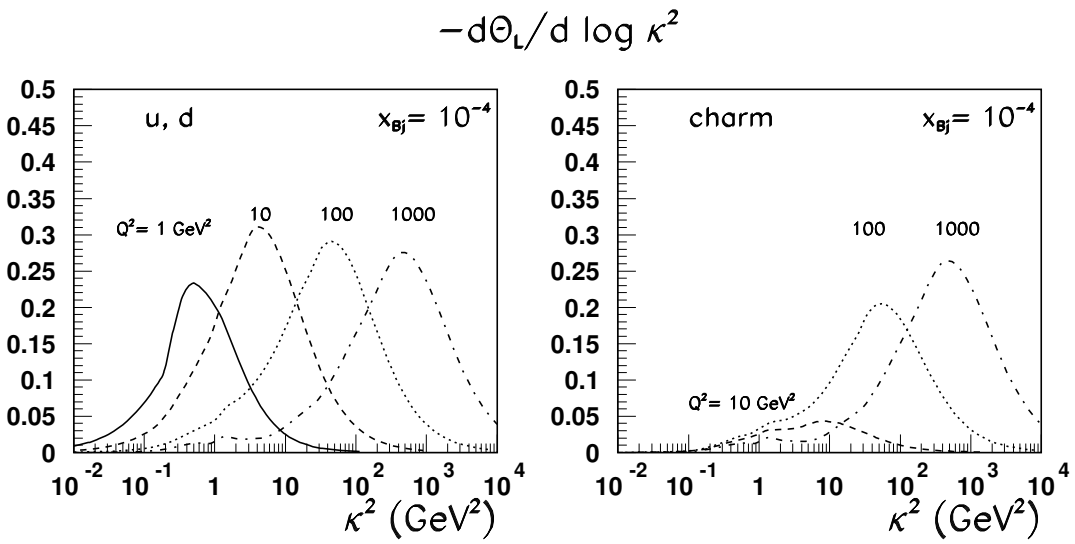

Figure 8.14: *The weight function $-\partial\Theta_L/\partial\log(\vec{\kappa}^2)$ for mapping of the integrated gluon structure function $G_D(x,\vec{\kappa}^2)$ as a function of $\vec{\kappa}^2$ for several values of Q^2. We show separately the results for light flavors and charm.*

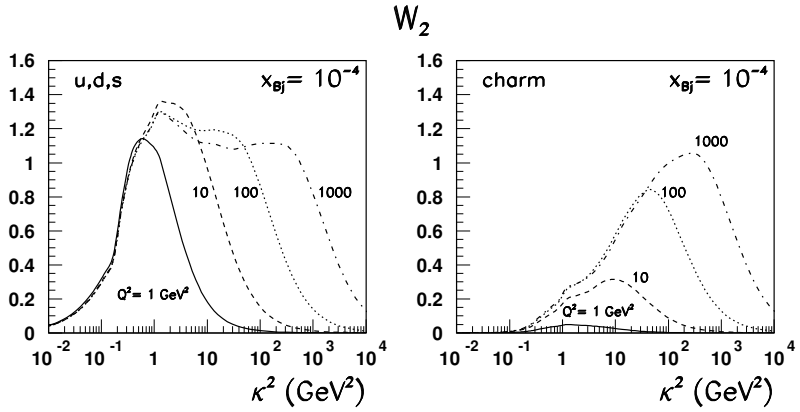

Figure 8.15: *The weight function W_2 for mapping of the integrated gluon structure function $G_D(x,\vec{\kappa}^2)$ as a function of $\vec{\kappa}^2$ for several values of Q^2. We show separately the results for light flavors and charm*

A still better picture of how F_L and scaling violations map the integrated GSF is given by Figs. 8.14 and 8.15, where we show results for $-\partial\Theta(f\bar{f})_L/\partial\log\vec{\kappa}^2$ and $W_2^{(f\bar{f})}$. The first quantity is sharply peaked at $\vec{\kappa}^2 \sim C_L Q^2$; the second quantity develops a plateau at large Q^2.

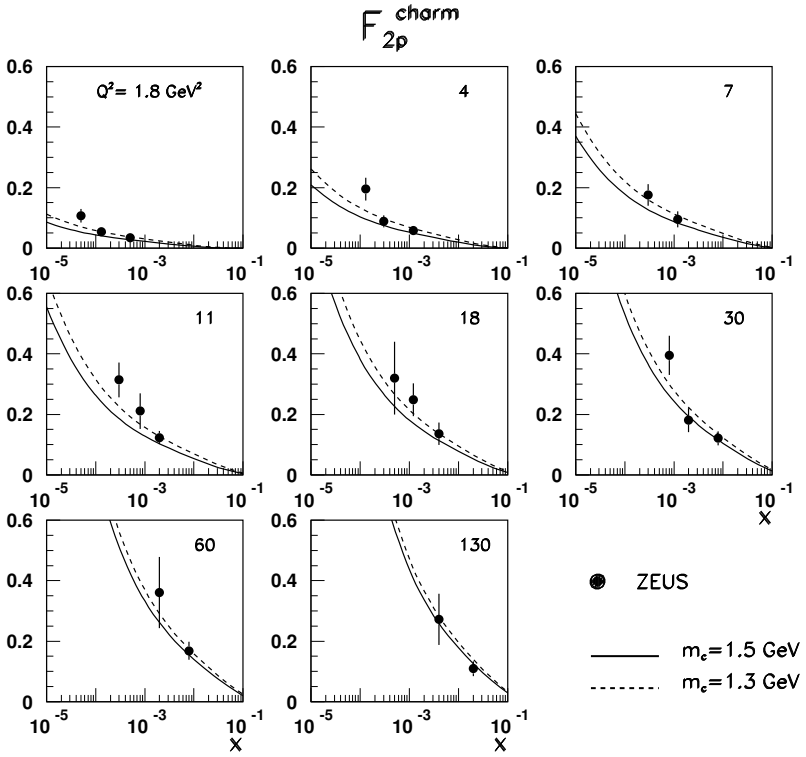

Figure 8.16: *A comparison of the experimental data from ZEUS [69] on the charm structure function of the proton with $\vec{\kappa}$-factorization results for $F_2^{c\bar{c}}(x,Q^2)$ based on the D-GRV parameterization of the differential gluon structure function $\mathcal{F}(x,Q^2)$.*

As can easily be seen, scaling violations receive a substantial contribution from the beyond-DGLAP region, $\vec{\kappa}^2 > Q^2$.

Because of the heavy mass, the case of the charm structure function $F_{2p}^{c\bar{c}}(x,Q^2)$ is somewhat special. Figs. 8.14 and 8.15 show weak sensitivity of $F_{2p}^{c\bar{c}}(x,Q^2)$ to the soft component of $\mathcal{F}(x,\vec{\kappa}^2)$, which has an obvious origin: long-wavelength soft gluons with $\kappa \lesssim m_c$ decouple from the color neutral $c\bar{c}$ Fock state of the photon, which has a small transverse size $\left(\lesssim \frac{1}{m_c}\right)$. Our results for $F_{2p}^{c\bar{c}}(x,Q^2)$ are shown in Fig. 8.16; the agreement with the recent precision experimental data from ZEUS [69] is good.

Chapter 9

Improved determination of the differential glue in proton: DGD2002 analysis

During the last two years new high-accuracy measurements of the structure function F_{2p} in the expanded parameter space were presented by ZEUS [70], [71] and H1 [72]. In the light of our analysis, the most important improvement was extension into the low-x region (down to $x = 6.7 \cdot 10^{-7}$ [70]) and $2 \div 3\%$ accurate determination of F_{2p} in the small-Q^2 (0.25 GeV^2 $< Q^2 <$ 0.65 GeV^2) and relatively small-x ($10^{-5} < x < 10^{-3}$) region. Even a brief comparison of k_t-factorization predictions for F_{2p} in this region based on the DGSF from the previous section showed a systematic several-sigma deviation from experimental points. The second problem with the old differential DGSF was that we did not quite match the experimentally measured exponent of F_{2p} rise towards high $1/x$. As our analysis showed (see Fig. 8.8), the predicted intercept was $1 \div 2\sigma$ lower for $Q^2 > 10$ GeV^2.

Thus, not being able to claim that we reproduce the F_{2p} data well enough with the old DGSF, we re-extracted the differential gluon structure function. This time the eye ball fits were not acceptable, and therefore a χ^2-minimization procedure was carried out. This chapter presents the results of this reevaluation.

9.1 Fitting procedure and parameters of DGSF

Our goal is a determination of small-x DGSF in the whole range of $\vec{\kappa}^2$ by adjusting the relevant parameters to the experimental data on small-x $F_{2p}(x, Q^2)$ in the whole available region of Q^2. The k_t-factorization predictions for F_{2p} were calculated at $N = 191$ points in (x, Q^2) space and compared to the experimentally values measured at HERA. These points include all data available currently for low-Q^2 region ($Q^2 < 1$ GeV^2), as well as all data points for several higher values of Q^2, namely $Q^2 = 1.5$, 2.5, 2.7, 3.5, 4.5, 5.0, 6.5, 10 and 35 GeV^2. The χ^2 was calculated according to

$$\chi^2 = \sum_{i=1}^{N} \frac{(F_{2p}^{theor.} - F_{2p}^{exp.})^2}{\sigma_{stat}^2 + \sigma_{syst}^2}. \tag{9.1}$$

The parameters that we did not adjust but borrowed from early work in the color dipole picture are $R_c = 0.27$ fm, i.e., $\mu_{pt} = 0.75$ GeV, and the frozen value of the LO QCD coupling

with $\Lambda_{QCD} = 0.2$ GeV (7.11). Our previous analysis showed that the parametrizations D-GRV, D-MRS, and D-CTEQ (that is, DGSF based on GRV, MRS, and CTEQ fits to integrated gluons) were very close to one another throughout the whole x, $\vec{\kappa}^2$ space. Simply stated, no matter from what particular DGLAP parametrization we start, we arrive at virtually the same shape of the differential gluon structure function. To this end we used only GRV98LO fits, since they are available for the widest range of x and Q^2 values.

The adjustable parameters are μ_{soft}, a_{soft}, $m_{u,d}$, $\vec{\kappa}_s^2$ and $\vec{\kappa}_h^2$ (for the heavier quark masses we take $m_s = m_{u,d} + 0.15$GeV and $m_c = 1.5$ GeV). Both $m_{u,d}$ and μ_{soft} have clear physical meaning and we have certain insight into their variation range from the early work on color dipole phenomenology of DIS. The rôle of these parameters is as follows. The quark mass $m_{u,d}$ defines the transverse size of the $q\bar{q} = u\bar{u}, d\bar{d}$ Fock state of the real photon, whose natural scale is the size of the ρ-meson. Evidently, roughly equal values of $F_{2p}(x, Q^2)$ can be obtained for somewhat smaller $\mathcal{F}(x, Q^2)$ at the expense of taking smaller $m_{u,d}$ and vice-versa. Therefore, although the quark mass does not explicitly enter the parameterization for $\mathcal{F}(x, \vec{\kappa}^2)$, the preferred value of $m_{u,d}$ could have been correlated with the DGLAP input. We find that it is sufficient to take $m_{u,d} = 0.21$ GeV, which is slightly lower than 0.22 GeV, used before.

Parameter μ_{soft}^{-2} defines the soft scale in which the non-perturbative glue is confined, and controls the r-dependence of, and in conjunction with a_{soft} sets the scale for, the dipole cross section for large size $q\bar{q}$ dipoles in the photon. We find that it is sufficient to take $\mu_{soft} = 0.1$ GeV and $\kappa_s^2 = 1$ GeV^2 everywhere.

The magnitude of the dipole cross section at large and moderately small dipole size depends also on the soft-to-hard interpolation of DGSF, which is sensitive to DGLAP inputs for perturbative component $G_{pt}(x, Q^2)$. This difference of DGLAP inputs can be corrected for by adjusting the hard-to-soft interface parameter $\vec{\kappa}_h^2$. The slight rise of $\vec{\kappa}_h^2$ helps to suppress somewhat too strong x-dependence of the soft tale of the perturbative glue. The specific parameterizations for $\vec{\kappa}_h^2$ depend on the DGLAP input and are presented in Table 2. Only $\vec{\kappa}_h^2$ and μ_{soft} varied from one DGLAP input to another.

In order to be able to assess the uncertainty in the determination of DGSF, we performed several χ^2 minimization procedures using slightly different sets of free parameters. The resulting parameters of the fits are shown in Table 2; below we comment on each fit in detail.

Fit 1

When obtaining Fit 1, we adjusted values of a_{soft}, the transition point Q_c^2 in (7.8), the functional form of $\kappa_h^2 = \kappa_h^2(x)$, which we took as a first order polynomial $a + b\log(1/x)$, and the power ζ of the high-x suppression factor $(1-x)^\zeta$.

The resulting value of ζ turned out uncomfortably large ($\zeta \approx 11$). Numerically, such a strong suppression serves as a remedy against somewhat too slow x-behavior of F_{2p} as we approach $x \sim 10^{-2}$ from the low-x side. Although rather artificial, this suppression factor does not invalidate our approach, since the exact behavior of the glue in the limit $x \to 1$ lies far beyond the scope of the present approach. Still, we would like to note the alarming tendency that, even with this factor, a large contribution to the overall χ^2 comes precisely from the region we wanted to correct ($10^{-3} < x < 10^{-2}$). This might be an indication that our understanding of this region is far from perfect. More analysis is needed to settle this issue.

Fit 2

In Fit 2 we opened up another degree of freedom; namely we allowed for shifting in the second argument of $G(x,Q^2)$. As early analyses showed, the best k_t-factorization to DGLAP correspondence would be

$$\mathcal{F}(x,\vec{\kappa}^2) \leftrightarrow \left.\frac{\partial G(x,Q^2)}{\partial \log Q^2}\right|_{Q^2=C\kappa^2} . \tag{9.2}$$

The early analysis gave $C \approx 2$, but in our approach we treated C as free parameter.

We started from Fit 1 and let the χ^2 slide to its minimum as we freed parameter C. We expected $C > 1$ at the minimum point. Indeed, our predictions with Fit 1 for the high-Q^2 region suffered from too-high values at high x and too-low values at very small x. As early analysis indicated, when we shift the $\vec{\kappa}^2$ scale according to (9.2) we make the unintegrated gluon density increase for $x < 10^{-3}$ and decrease at higher values of x. We expect this tendency to survive the multiple integration procedure and to echo in the proton structure F_{2p}.

The minimization procedure gave $C \approx 1.1$ with slight adjustment of other parameters (see Table 2 for details).

Fit 3

In the region of very hard gluons both Fit 1 and Fit 2 rely on the leading order DGLAP parametrizations of $G(x,Q^2)$. Although it is desirable that the integrated gluon structure function $G_D(x,Q^2)$ based on our parametrizations approaches in the double logarithmic limit the conventional gluon density obtained from DGLAP evolution, there is certainly no requirement that our fits be built on these DGLAP fits. One should only make sure that at $\log(1/x) \gg 1$ and $\log(Q^2/\Lambda^2_{QCD}) \gg 1$ behavior of our fits is compatible with the corresponding behavior of the DGLAP fits.

The properties of the DGLAP-evolved gluon density in this limit is well understood. Since the anomalous dimension of gluons is higher than that of the sea quarks, the secondary gluons in this limit tend to be radiated from gluons as well. The evolution of the integrated gluon density $G(x,Q^2) = xg(x,Q^2)$ separates out and is governed by

$$\frac{\partial G(x,Q^2)}{\partial \log Q^2} = \frac{\alpha_s(Q^2)}{2\pi}\int_x^1 dz G\left(\frac{x}{z},Q^2\right) P_{GG}(z)\,, \tag{9.3}$$

with the splitting function

$$P_{GG}(z) = 2N_c\left[z(1-z) + \frac{z}{(1-z)_+} + \frac{1-z}{z}\right] + \frac{11}{6}N_c\delta(1-z)\,. \tag{9.4}$$

The Regge-type behavior

$$G(x,Q^2) = f(Q^2)\cdot\left(\frac{1}{x}\right)^{\Delta} \tag{9.5}$$

with constant Δ is compatible with the DGLAP equations and leads to

$$\begin{aligned}\frac{d\log f(Q^2)}{ds} &= 4N_c\int_x^1 dz\, z^{\Delta}\left[z(1-z) + \frac{z}{(1-z)_+} + \frac{1-z}{z} + \delta(1-z)\frac{11}{12}\right] \\ &= 4N_c\left[\frac{1}{\Delta} - \frac{1}{\Delta+1} + \frac{1}{\Delta+2} - \frac{1}{\Delta+3} + \frac{11}{12} + \mathcal{C} + \psi(\Delta+2)\right] \\ &\equiv \delta\,. \end{aligned} \tag{9.6}$$

Here

$$s = \log\left[\frac{\log\left(Q^2/\Lambda^2_{QCD}\right)}{\log\left(Q^2_0/\Lambda^2_{QCD}\right)}\right] \tag{9.7}$$

and $\mathcal{C}$ and ψ are the Euler constant and the digamma function, respectively. One immediately gets the solution for the integrated gluon structure function

$$G(x,Q^2) \propto \left[\log\left(\frac{Q^2}{\Lambda^2_{QCD}}\right)\right]^{\delta} \cdot \left(\frac{1}{x}\right)^{\Delta}, \tag{9.8}$$

which leads to the DGSF of the form

$$\mathcal{F}(x,\vec{\kappa}^2) \propto \left[\log\left(\frac{\vec{\kappa}^2}{\Lambda^2_{QCD}}\right)\right]^{\delta-1} \cdot \left(\frac{1}{x}\right)^{\Delta}. \tag{9.9}$$

This analysis inspires us to search for a parametrization of $\mathcal{F}_{pt}$ that would be power-like both in $\log\left(\vec{\kappa}^2/\Lambda^2_{QCD}\right)$ and $\log(1/x)$ in the double logarithmic regime.

The functional form of $\mathcal{F}_{pt}$ that Fit 3 is based on is

$$\mathcal{F}_{pt}(x,\vec{\kappa}^2)|_{Fit3} = 0.245 \cdot \left[\log\left(\frac{\vec{\kappa}^2}{\Lambda_{QCD}}\right)\right]^{0.34-6\sqrt{x}} \cdot \left(\frac{1}{x}\right)^{0.4}. \tag{9.10}$$

Table 2. The parameters of DGD2002 fits to differential gluon densities.

	Fit 1	Fit 2	Fit 3
hard input	GRV98LO	GRV98LO	Eq.(9.10)
$\vec{\kappa}^2$-shift		$C = 1.1$	
Q^2_c, GeV^2	1.45	1.45	1.4
a_{soft}	2.66	2.63	2.6
κ^2_h, GeV^2	$0.4 + 0.245 \log\frac{1}{x}$	$0.38 + 0.245 \log\frac{1}{x}$	$0.31 \log\frac{1}{x}$
total χ^2	257	245	226

9.2 The properties of the gluon structure function

In Fig. 9.1 we plotted the three fits to the differential gluon structure functions obtained above vs. $\vec{\kappa}^2$ at several values of x. One observes there a number of interesting features.

First, the three curves display rather similar behavior at very small x, but at x as high as 10^{-2} the difference among them throughout the region $\vec{\kappa}^2 > 1$ GeV^2 is quite sizable. Still, all of these parametrizations of DGSF do provide a reasonably accurate description of F_{2p}. Thus we conclude that modern experimental data on F_{2p} do not place severe restrictions on the shape of differential glue at not-very-small x (say, $x \gtrsim 10^{-3}$).

The second feature of the curves presented is their salient two-peak shape. The technical origin of this clear separation of the soft and hard exchange mechanisms is, of course, the very abrupt extrapolation of soft gluons into the hard region and vice-versa, generated by high powers ζ. This might seem artificial, but as we described, such abrupt extrapolation seemed necessary in order to obtain the correct behavior of effective intercept of F_{2p} and therefore

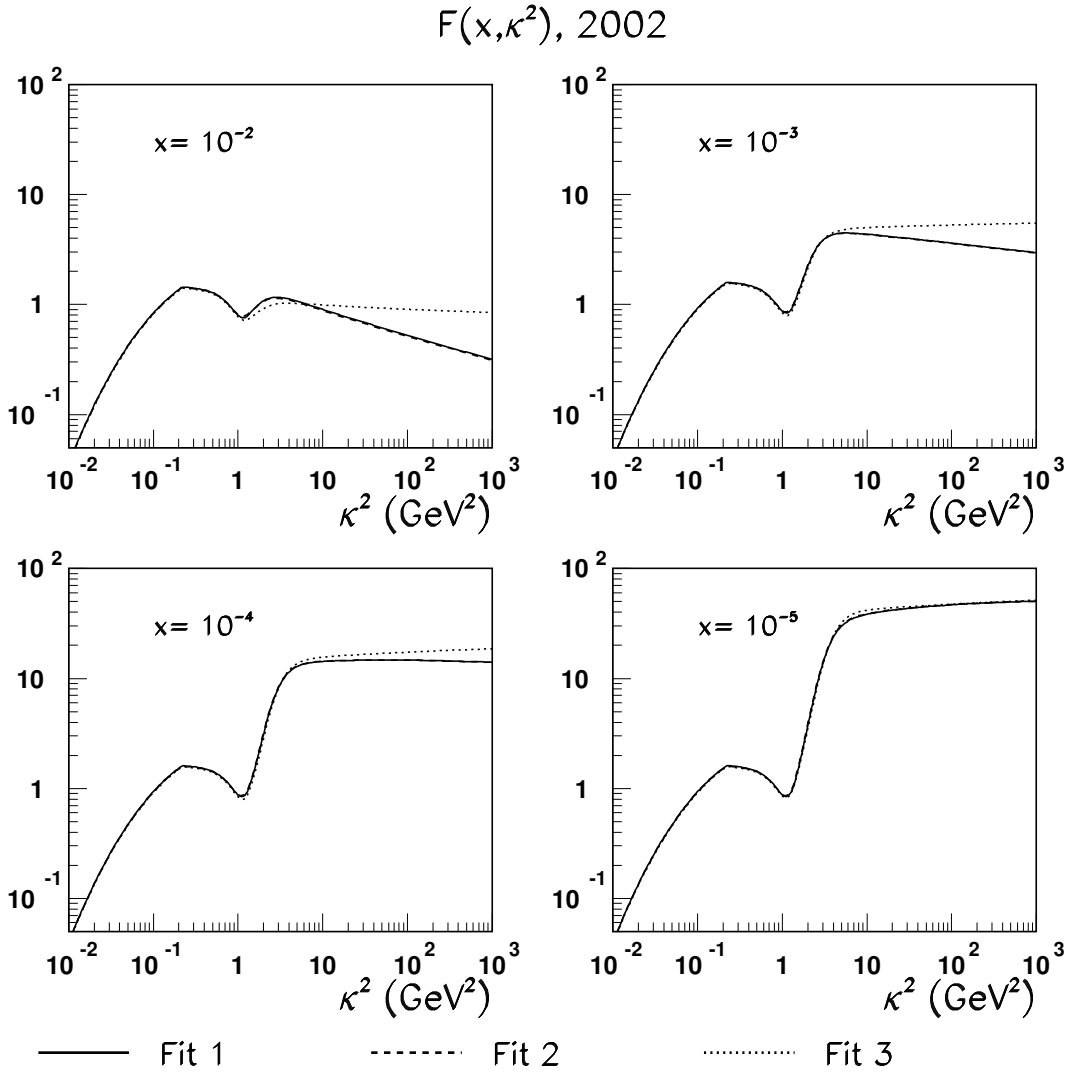

Figure 9.1: *Differential gluon structure function as function of κ^2: DGD2002 analysis*

it was quite essential for getting a better χ^2. Thus, we inclined to think that such clear separation of the soft and hard mechanisms is indeed preferred by experiment.

The integrated gluon structure function is shown in Figs. 9.2. A similar observation, although in a subdued form, can be made. At $x = 10^{-2} \div 10^{-3}$ one can notice some departure among the curves, which die out as we shift towards lower and lower x. As we go to smaller x, we observe a plateau around $\vec{\kappa}^2 \sim 1 \div 3$ GeV^2, which originates from the two-peak shape of $\mathcal{F}(x, \vec{\kappa}^2)$ and becomes more and more prominent.

Note also that at small x and very large Q^2 all three $G_D(x, Q^2)$ curves, including Fit 3 with the simple-formula parameterization of $\mathcal{F}_{hard}$, approach each other.

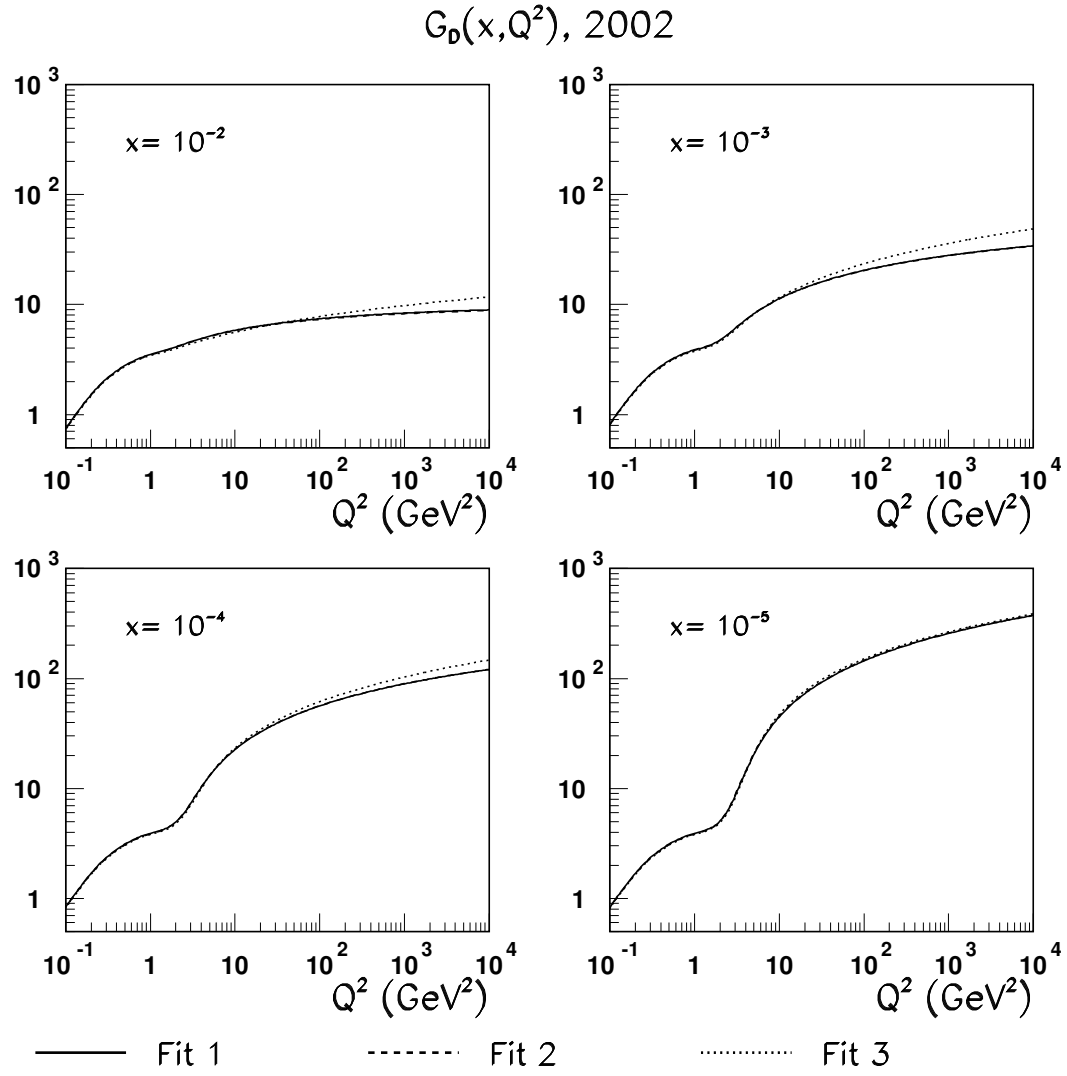

Figure 9.2: *Integrated gluon structure function as function of Q^2: DGD2002 analysis*

9.3 The observables

9.3.1 Structure function F_{2p} and its derivatives

Since the overall behavior of structure function $F_{2p}(x, Q^2)$ was the quantity we tried to fit, one can expect a very good description of the data. Indeed, as Figs. 9.3 and 9.4 show, our calculations for F_{2p} based on all three DGSF fits go almost directly through the experimental points. This trend is somewhat spoiled beyond the region of fitting, namely for $x > 0.01$, but still we do not run into any severe discrepancy even here. Note also that throughout the fitting region all three curves differ by less than 5%.

Fig. 9.5 illustrates the improvement in the description of the structure function F_{2p} by the k_t-factorization calculations as we switch from old DGD2000 parametrizations of DGSF to

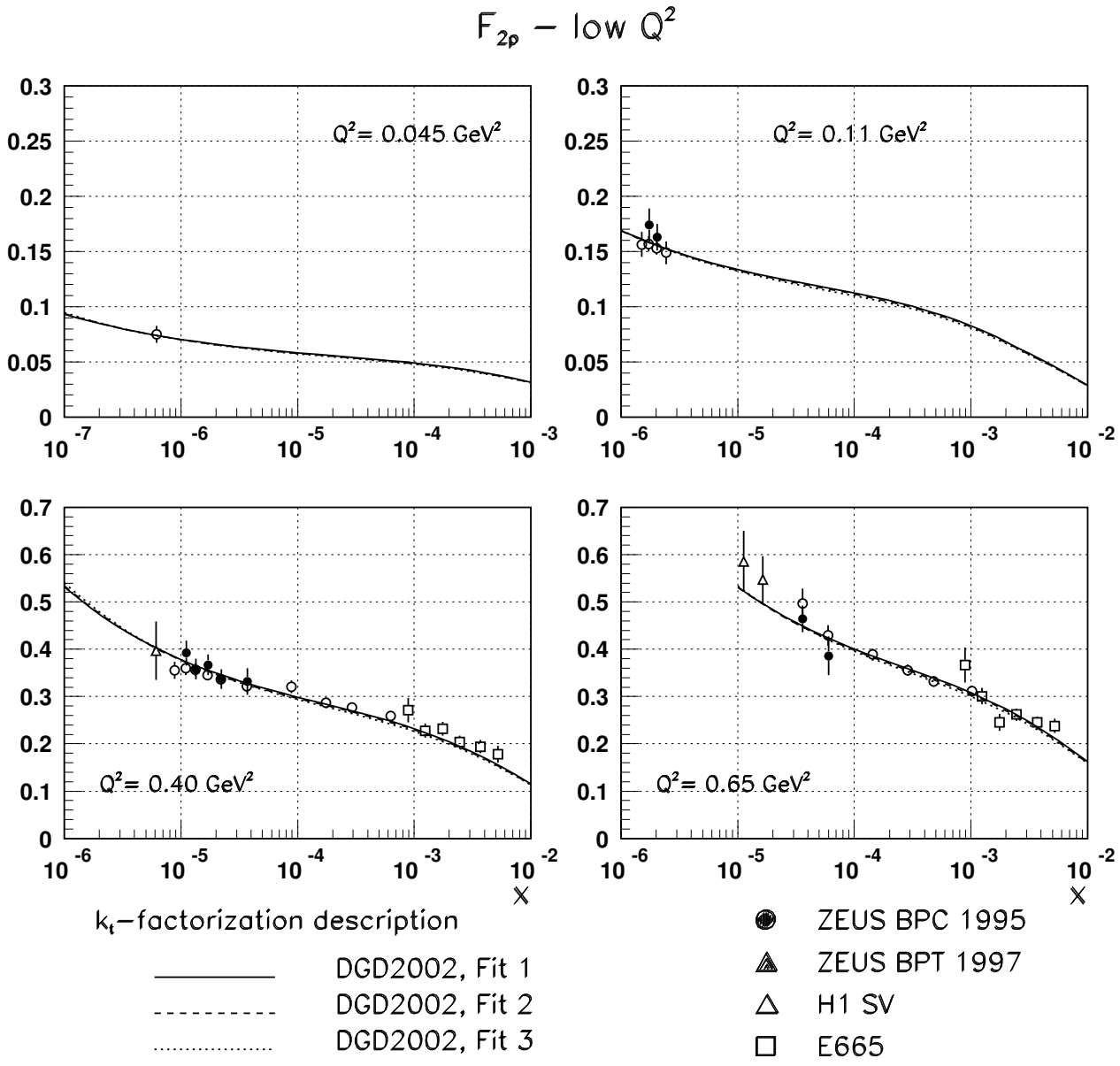

Figure 9.3: *The k_t-factorization results for the structure function $F_{2p}(x, Q^2)$ in the small Q^2 region*

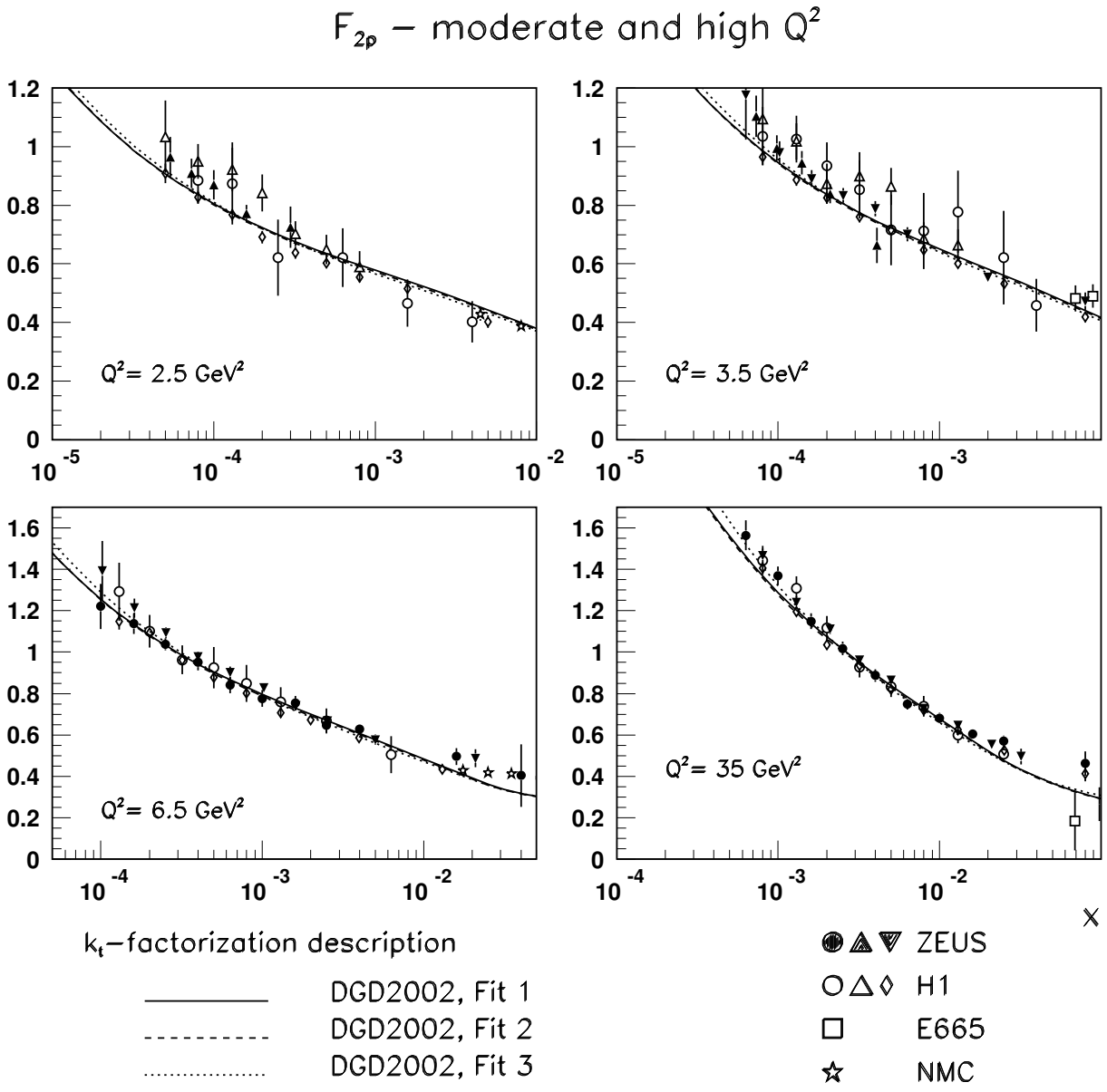

Figure 9.4: *The k_t-factorization results for the structure function $F_{2p}(x, Q^2)$ in the moderate and high Q^2 region*

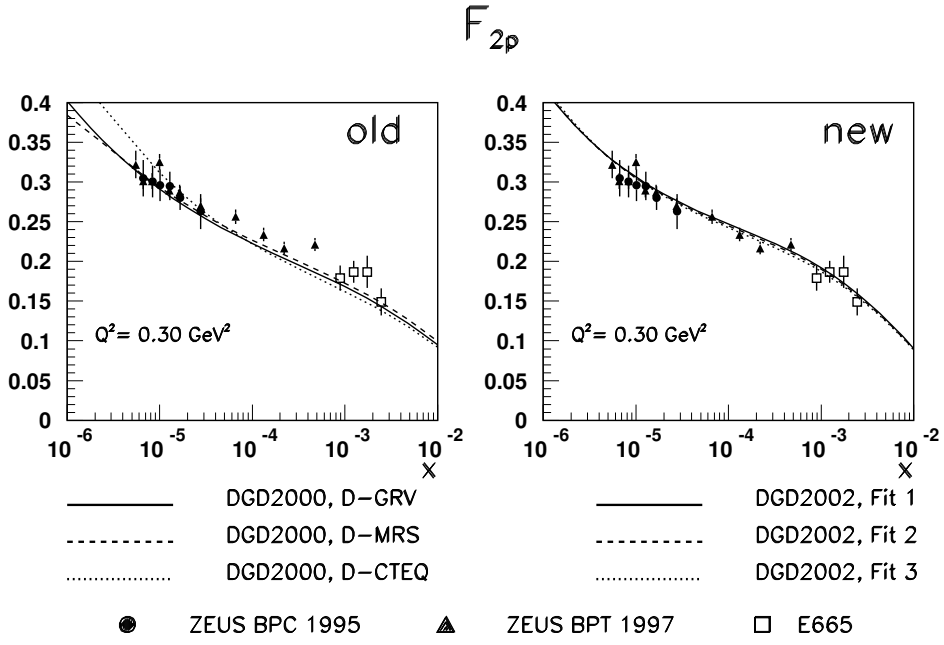

Figure 9.5: *The improvement of the k_t-factorization predictions for the structure function F_{2p} based on DGD2000 (left panel) and DGD2002 (right panel) parametrizations of the differential gluon structure function*

the new DGD2002 fits. The curves now go through very constraining new data points and therefore have less tendency to depart from each other outside the fitting range.

Fig. 9.6 shows the effective intercept of structure function F_{2p} in the moderate Q^2 domain, together with recent H1 data [73]. The intercepts were calculated according to

$$\Delta(Q^2) = \frac{\log[F_{2p}(x_1, Q^2)/F_{2p}(x_2, Q^2)]}{\log(x_2/x_1)}. \tag{9.11}$$

For each differential gluon density fit we plotted here two curves: the upper one, corresponding to the effective intercept taken between $x_1 = 10^{-5}$ and $x_2 = 10^{-4}$, and the lower one for $x_1 = 10^{-4}$ and $x_2 = 10^{-3}$. Significant deviation between the two curves indicates the fact that the power-like law

$$F_{2p}(x, Q^2) \propto \left(\frac{1}{x}\right)^{\lambda(Q^2)} \tag{9.12}$$

is only a very crude approximation.

The agreement with the data is reasonable, especially when one takes into account that at lower Q^2 one should compare the data with the upper curves and at higher Q^2 the data should be compared with the lower curves. This is due to the experimental procedure used by H1 to determine the intercepts: at smaller Q^2 the value of the intercept comes from data points in the range $x \in (10^{-5}, 10^{-3})$, while at higher Q^2 only $x \sim 10^{-3} \div 10^{-2}$ were available.

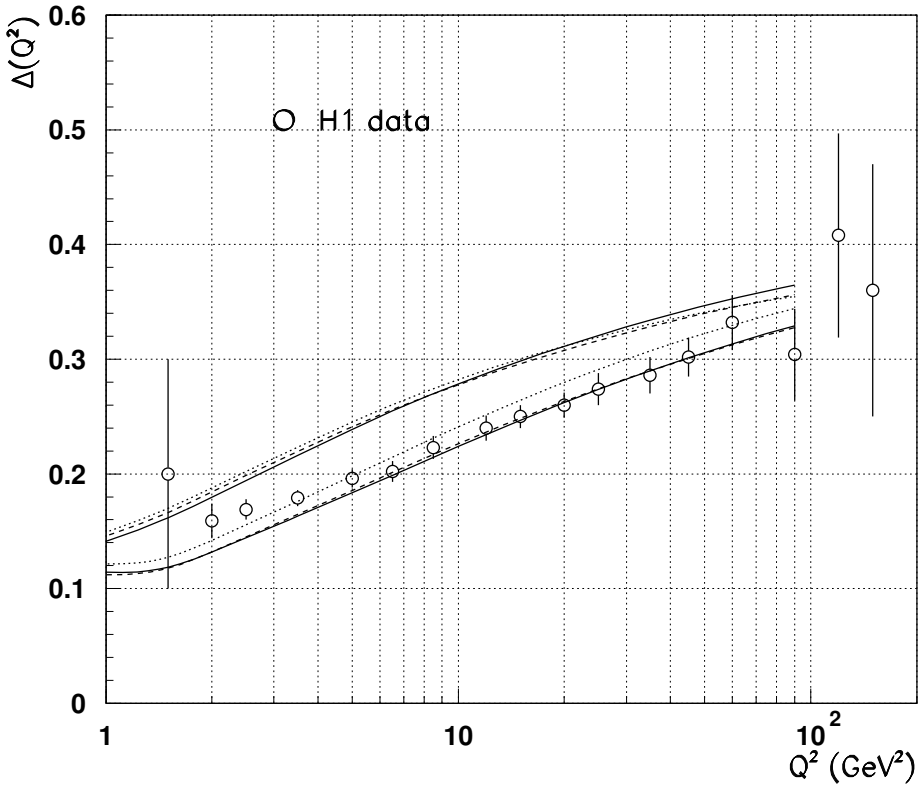

Figure 9.6: *The k_t-factorization predictions for the effective intercepts of the structure function F_{2p} in the moderate Q^2 region confronted with H1 data (solid circles)*

9.3.2 Structure function F_L

In 1999 H1 published improved data on the determination of the structure function $F_L(x, Q^2)$. We show them in Fig. 9.7, together with our predictions. The general agreement can be seen, but since the data are not very constraining, little futher information can be extracted from this plot.

9.3.3 Real photoabsorption cross section

Finally, in Fig. 9.8, we show experimental data for real photoabsorption cross section $\sigma_{\gamma p}$, together with our predictions.

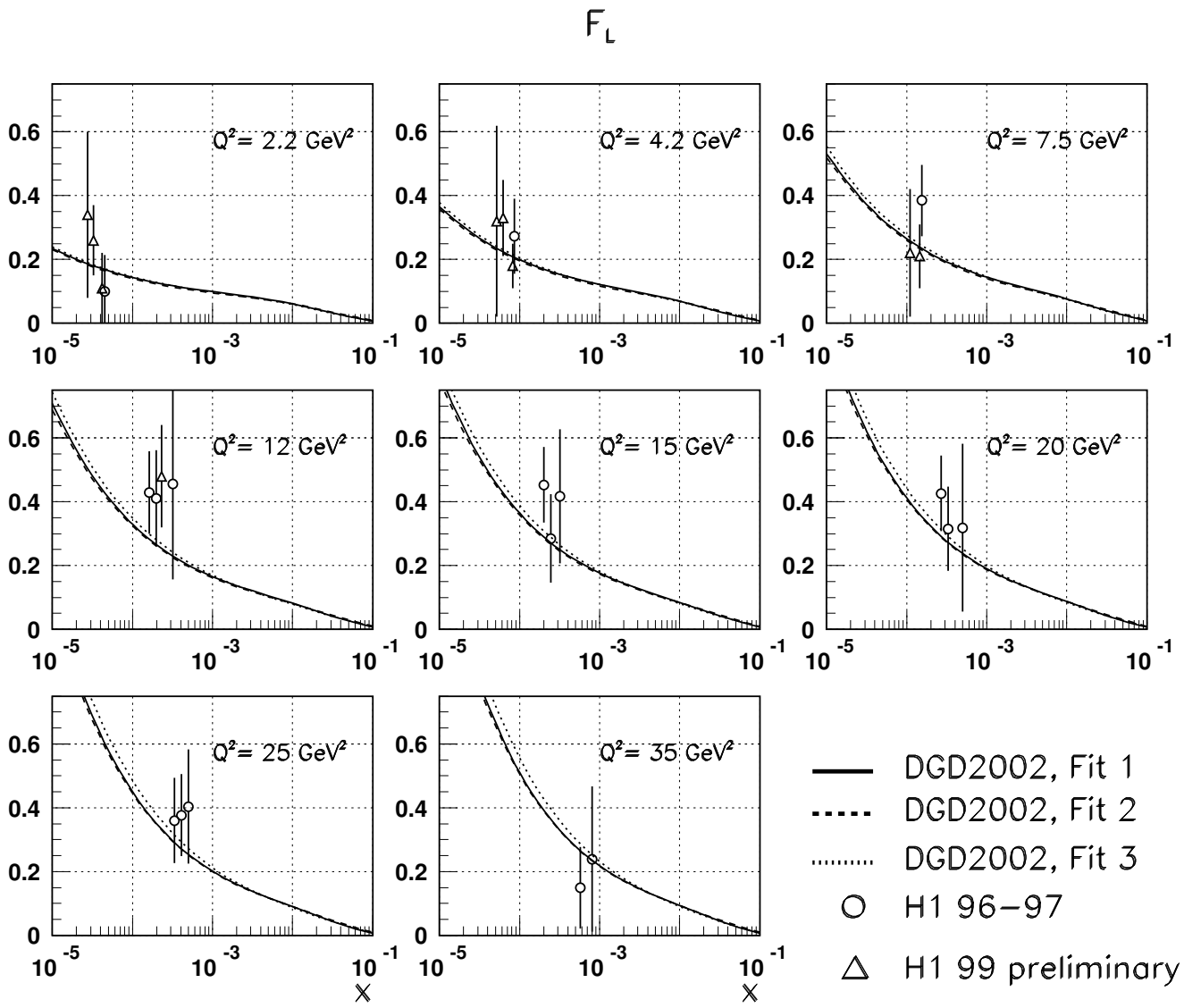

Figure 9.7: *The longitudinal structure function F_L of the proton in the moderate Q^2 region*

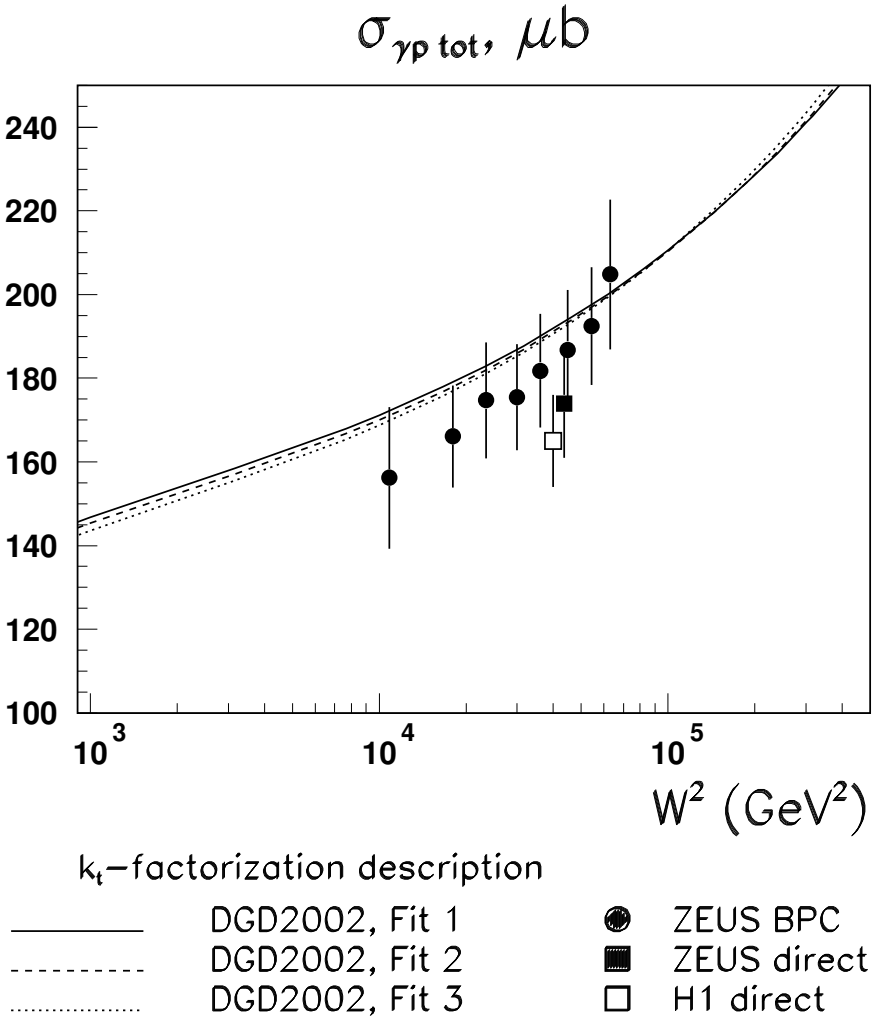

Figure 9.8: *The predictions of the real photoabsorption cross section as function of total energy based on DGD2002 parametrization*

Chapter 10

Numerical analysis of vector meson producton

10.1 $1S$ states: a brief look

10.1.1 Absolute values of cross sections and scaling phenomenon

An overview of the experimental results on vector meson production together with our predictions is given by Fig. 10.1. Here we plotted the experimentally measured values of ρ meson cross sections for photoproduction (H1 [74] and ZEUS [75]) and electroproduction (H1 [76] and ZEUS [77]), ϕ meson electroproduction cross sections (H1 [78] and ZEUS [79], [80]), J/ψ photoproduction (H1 [81]) and electroproduction cross sections (H1 [82] and ZEUS [77], [83]), and $\Upsilon(1S)$ photoproduction cross sections (H1 [81] and ZEUS [84]). All experimental data points are either taken at $W = 75$ GeV or are extrapolated to this energy. Whenever possible, we used the energy dependence measured experimentally in the corresponding papers. In the case of Υ meson photoproduction no reliable data on energy dependence are available, so we used a power law, $\sigma(\Upsilon) \propto W^{\delta}$ with $\delta = 1.75$, which comes from our calculations.

In the case of ϕ, J/ψ and Υ mesons, the cross sections were multiplied by appropriate flavor factors in order to remove trivial sensitivity of the cross sections to the mean-square charge $\langle e_i^2 \rangle$ of the quark content in a vector meson.

As suggested by the twist expansion analysis, the total production cross sections should exhibit an approximate scaling in the variable $\overline{Q}^2$. Indeed, as Fig. 10.1 shows, the experimental data for various vector mesons do possess such a scaling property: data points for ρ, ϕ, and J/ψ taken at the same values of $\overline{Q}^2$ almost coincide. It is worth noting that the scaling phenomenon takes place even at small $\overline{Q}^2$. Note that the k_t-factorization predictions also exhibit approximate scaling phenomenon.

10.1.2 The energy and $|t|$-dependence

The remarkable scaling in the variable $\overline{Q}^2$ is observed not only in the magnitude of the production cross sections, but also in the patterns of energy dependence and $|t|$-dependence.

The energy dependence of the vector meson production cross sections is compatible within

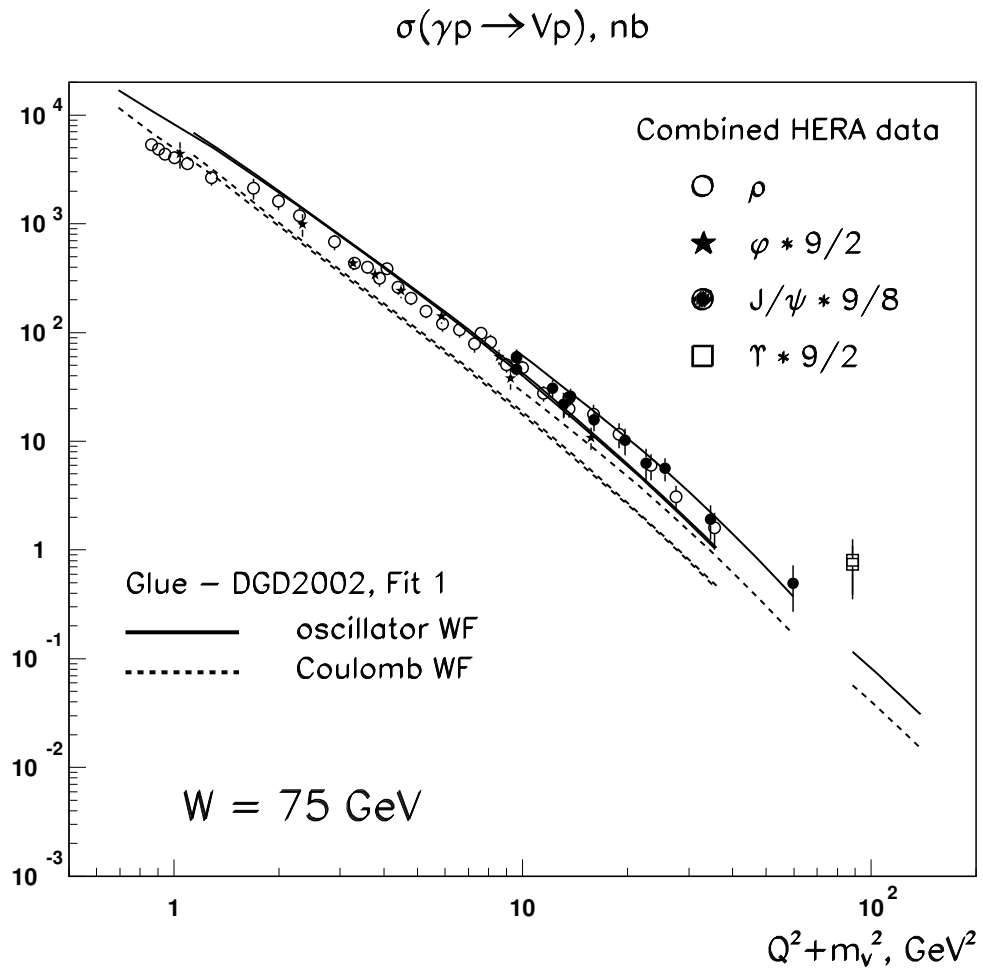

Figure 10.1: *The total cross section of diffraction electroproduction of various vector mesons against the scaling variable $Q^2 + m_V^2$. Results are scaled according to flavor content to equilibrate the electric charges of different flavours. The k_t-factorization predictions based on oscillator (solid lines) and suppressed Coulomb (dashed lines) are also shown. All calculations are performed for $W = 75$ GeV; the experimental points are either taken in this energy range or consistently extrapolated to this energy.*

experimental errors with the power-like Regge-type growth:

$$\sigma \propto W^{\delta}\,; \quad \delta = 4[\alpha_{I\!P} - 1]\,. \tag{10.1}$$

The latter equality reflects the assumption that the energy behavior comes from the gluon content of the proton, which is usually linked to the pomeron intercept $\alpha_{I\!P}$ at $|t| = 0$.

The t-dependence of the differential cross section $d\sigma/d|t|$ can be approximated for $|t| \lesssim 0.5$ GeV^2 by a simple exponential law,

$$\frac{d\sigma}{d|t|} \propto e^{-B|t|}\,. \tag{10.2}$$

The magnitude of the slope parameter B shows how "fragile" the proton and the produced meson are.

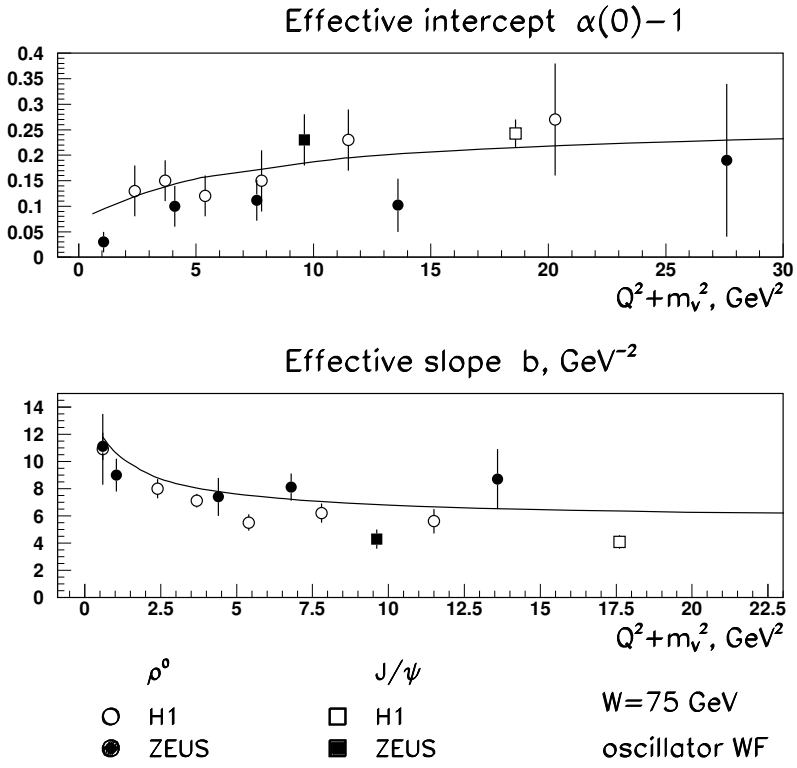

Figure 10.2: *The effective intercepts (upper panel) and effective slopes(lower panel) of the vector meson production cross sections vs. the scaling variable $Q^2 + m_V^2$. The data points represent ρ meson and J/ψ meson results. The curves are the k_t-factorization calculations for the ρ meson with the oscillator wave function.*

Both quantities — the intercept and the slope — do exhibit Q^2 dependence, but again via the scaling variable $\overline{Q}^2$. Fig. 10.2 shows a plot from [16], where the k_t-factorization predictions for these quantities are compared with the experimental available results. Although the agreement is not perfect, the tendency is caught by the k_t-factorization calculations. Below we will give more detailed investigation of both quantities.

10.1.3 The level of accuracy

Before proceeding further we should have a clear idea of what level of accuracy one can expect from the k_t-factorization predictions. There is a number of quantities that can be a source of uncertainty in the final answers. We discuss them below.

The gluon density

The gluon content of the proton is an intrinsically non-perturbative quantity, and therefore it is not calculable within the k_t-factorization approach. Our extensive analysis of the structure function F_{2p} led us to an accurate determination of the differential gluon density $\mathcal{F}(x,\vec{\kappa}^2)$ in the proton. The k_t-factorization results for various physical observables based on different fits to $\mathcal{F}(x,\vec{\kappa}^2)$ differ from each other at the level of several percent.

As we discussed above, the vector meson production amplitudes are related not to the diagonal quantity $\mathcal{F}(x,\vec{\kappa}^2)$, but to the off-diagonal (skewed) gluon distribution $\mathcal{F}(x_1,x_2,\vec{\kappa},\vec{\Delta})$. The situation can be partially cured by linking the skewed gluon distribution to the diagonal one by means of the Shuvaev formula (5.28) or its simplified version (5.30). Since such a linking is strictly valid only when x_1 or x_2 vanishes, and therefore it is a good approximation in the cases $Q^2 \gg m_V^2$ and $Q^2 \ll m_V^2$.

If $Q^2 \approx m_V^2$, this linking is not well justified and the whole procedure introduces an uncertainty. In order to test the magnitude of the uncertainty associated with the skewness of the gluon density we performed an additional check; namely we calculated the ρ meson cross sections at low Q^2 using strictly forward and simplified off-forward (5.30) Ansätze for the gluon structure function. We found that at $Q^2 = 0$ using forward instead of non-forward (the latter is the default option for all calculations here) reduced the cross section by a factor of 1.07. Obviously, the smallness of this factor originates from low average value of the energy growth exponent λ.

Thus, the inaccuracy introduced at low Q^2 by the forward/off-forward Ansatz for gluon density is no more than 10%.

The wave function

With the gluon density being brought under reasonable control, the only major uncalculable piece of the pie is vector meson wave function. As described above, we focus on the soft wave function; in particular, we used the oscillator and "suppressed Coulomb" wave function Ansätze. Being virtually the two limiting cases of what the radial part of the wave function can look like, they represent fairly well the region of uncertainty introduced by a specific choice of the wave function.

As can be seen from the above figures, the calculations based on the oscillator wave function Ansatz are roughtly twice as large as those obtained with the suppressed Coulomb wave function.

The width of vector meson

In our calculations we treated the produced vector mesons as particles with negligible width. This is not the case for the ρ meson, whose width is about 1/5 of its mass. Usually, the incorporation of a finite width of a produced particle is conducted via effective "smearing" of the results (which depend on the mass of the particle produced) over a certain mass interval. If the cross sections calculated for a given mass happen to have a convex dependence on mass (which is precisely the case in ρ meson production), then such a smearing will lower the values of the cross sections. Thus, from very general arguments, we can expect such a smearing in our case as well. Roughly, it should amount to a decrease of the cross sections by factor of $(1+\Gamma_\rho/m_\rho) \approx 1.2$.

A more accurate calculation of this effect is a non-trivial task. The problem is that in our treatment of the vector meson production we *never* refer to the vector meson mass. We deal only with the effective invariant mass of the $q\bar{q}$ pair. Therefore accurate calculation of the smearing effect requires solution of conceptually non-trivial problems.

The limits of k_t-factorization approach

Finally, the very approach we use has limited domain of applicability. In particular, it would be fallacious to extend our calculations to the high Q^2-region. A rough criterion for the border of the applicability domain can be given by $Q^2_{max} \sim \sqrt{W^2\mu^2_{soft}}$, which is about 50 GeV^2 for the HERA energy range. Above this values the logarithms $\log(Q^2/\mu^2_{soft})$ will be more important than $\log(1/x)$ and one can expect that k_t-factorization will underestimate observed cross sections.

10.2 The ρ meson production

In this section we provide a detailed description of the k_t-factorization predictions for ρ meson production. Note that throughout this chapter we treat the physical ρ meson as a pure $1S$ state. Whether this is indeed realized in nature, and what changes if S/D wave mixing occurs, will be discussed in Chapter 11.

Whenever experimental data available we compare them with our results.

10.2.1 Q^2 dependence

The Q^2-dependence of the ρ meson production cross section is shown in Fig. 10.3. One sees that as we slide to higher values of Q^2 the cross section drops sharply. Although for the major part of the Q^2 region shown the experimental data points fall roughly between the oscillator and Coulomb wave function predictions, two separate regions of discrepancy are easily visible.

Low Q^2 region

The first problematic point is the low-Q^2 region. As we come from moderate Q^2 down to $Q^2 = 1$ GeV^2 and below, our predictions — if compared to the experimental points — tend to climb too high.

The first thought would be to suspect that our predictions rise too steeply as $Q^2 \to 0$. An accurate analysis shows, however, that this suspicion misses the point. In fact, the $Q^2 \to 0$ behavior of our predictions is perfectly compatible with experimentally observed tendencies. This rather unexpected fact is illustrated by Figs. 10.4 and 10.5.

In Fig. 10.4 we zoom in on the region $Q^2 < 1$ GeV^2, where the available experimental data include ZEUS 95 BPC [77], ZEUS 94 photoproducton [75] and H1 photoproduction [74] measurements. The k_t-factorization prediction based on the oscillator wave function (which seems to be a more reasonable choice for the ρ mesons than the Coulomb WF) and on DGD2002, Fit 3 are shown with solid line. The k_t predictions overshoot the data throughout the whole region shown here. However, when simply divided by 2, the predictions pass exactly through all the data points (dotted curve in Fig. 10.4), including the photoproduction point.

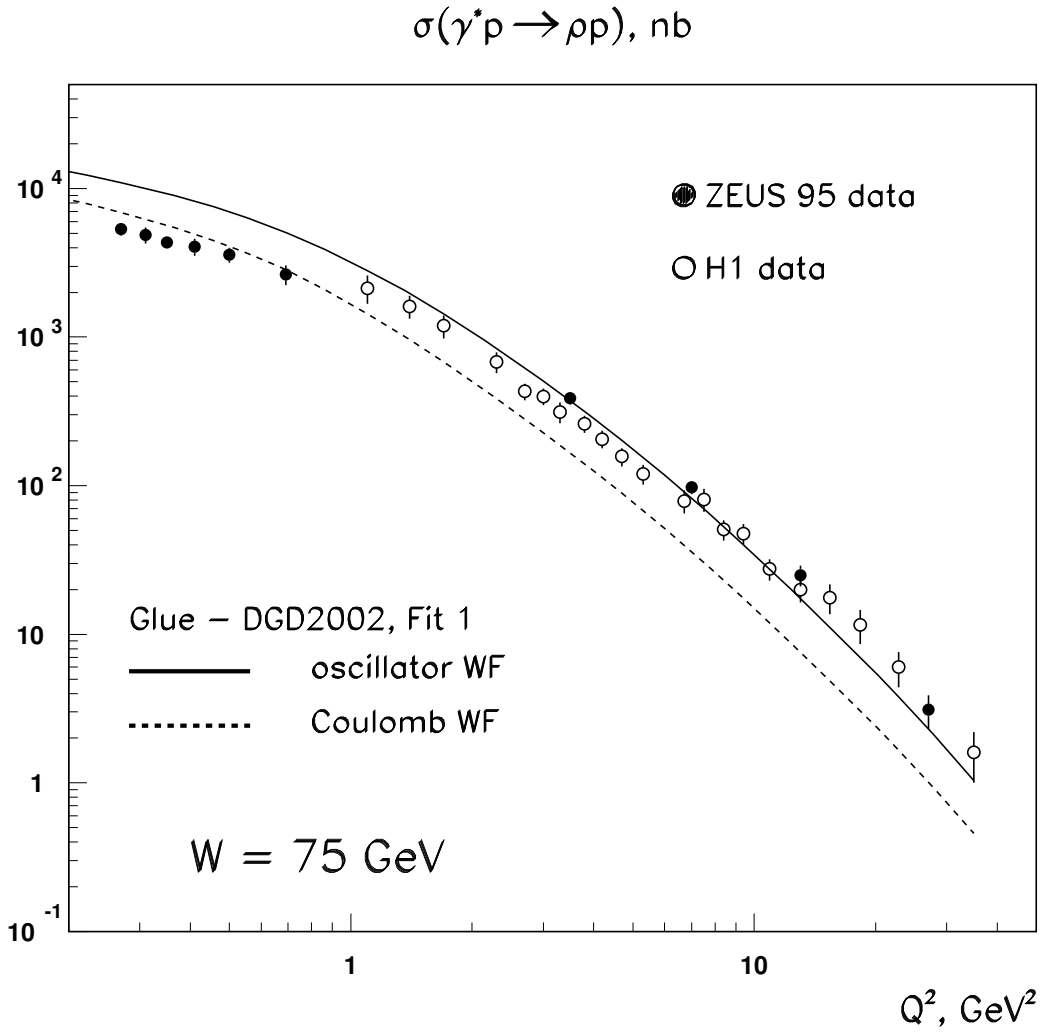

Figure 10.3: *Total cross section of the diffractive ρ meson production as a function of Q^2. The k_t-factorization predictions based on oscillator (solid lines) and suppressed Coulomb (dashed lines) wave functions are also shown. All calculations were performed for $W = 75$ GeV using DGD2002, Fit 1.*

Alternatively, one can try parameterizing the cross sections at low Q^2 by a simple formula:

$$\sigma(Q^2) \propto \frac{1 + R(Q^2)}{(Q^2 + m_{eff}^2)^n}; \quad R(Q^2) \equiv \frac{\sigma_L(Q^2)}{\sigma_T(Q^2)}, \tag{10.3}$$

which is equivalent to

$$\sigma_T(Q^2) \propto \frac{1}{(Q^2 + m_{eff}^2)^n}. \tag{10.4}$$

In order to find parameters m_{eff}^2, n that reproduce the low-Q^2 behavior of our predictions, we

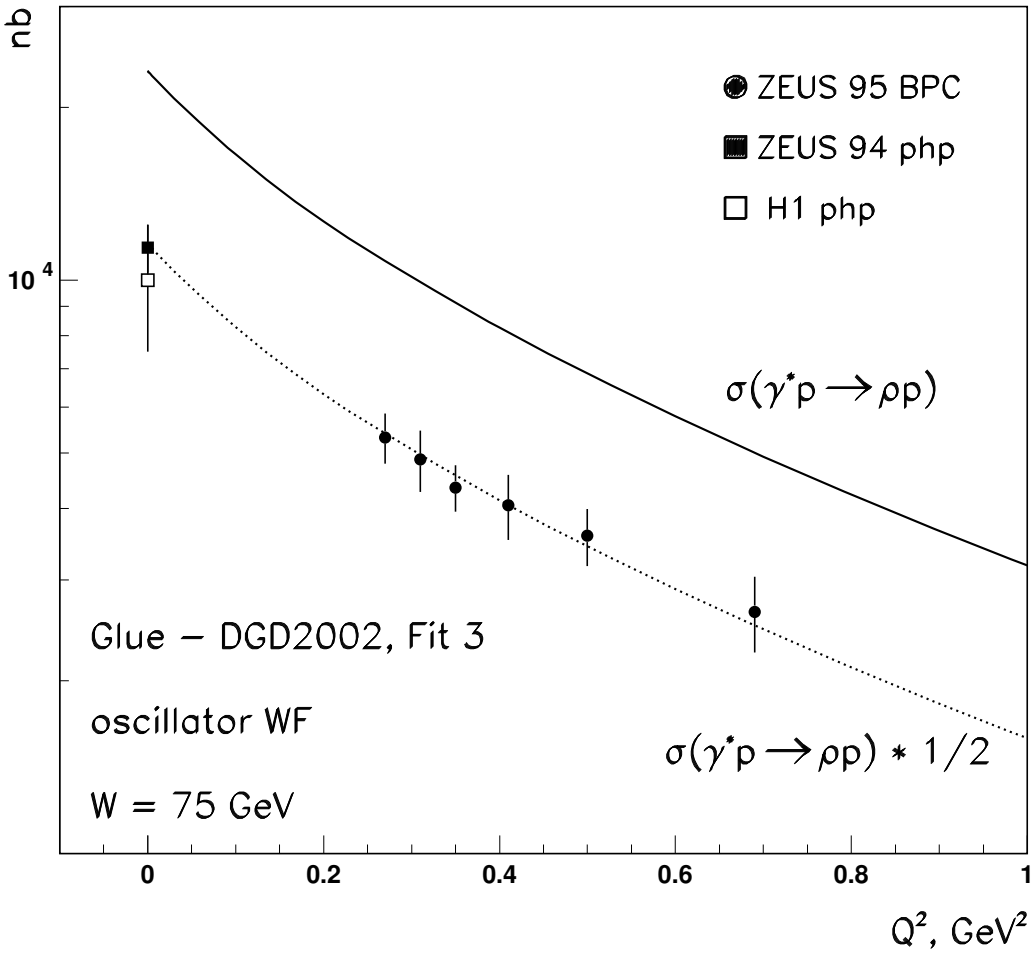

Figure 10.4: *Total cross section of the diffractive ρ meson production as a function of Q^2 in the small-Q^2 region. The solid curve represents the k_t-factorization predictions; dashed line shows the same prediction divided by two.*

plotted in Fig. (10.5) the quantity

$$\mathcal{R} = \frac{\log[\sigma_T(Q^2=0)/\sigma_T(Q^2)]}{\log(1+Q^2/m_{eff}^2)} \tag{10.5}$$

against $\xi \equiv 1 + Q^2/m_{eff}^2$. If Eq.(10.4) holds, this quantity should be equal to n for all values of ξ. We see that when $m_{eff}^2 \approx 0.4$ GeV^2, $\mathcal{R}$ has the flattest shape vs. ξ and is ≈ 2.

This result is in perfect agreement with low-Q^2 analysis of the ZEUS BPC data [77]; when

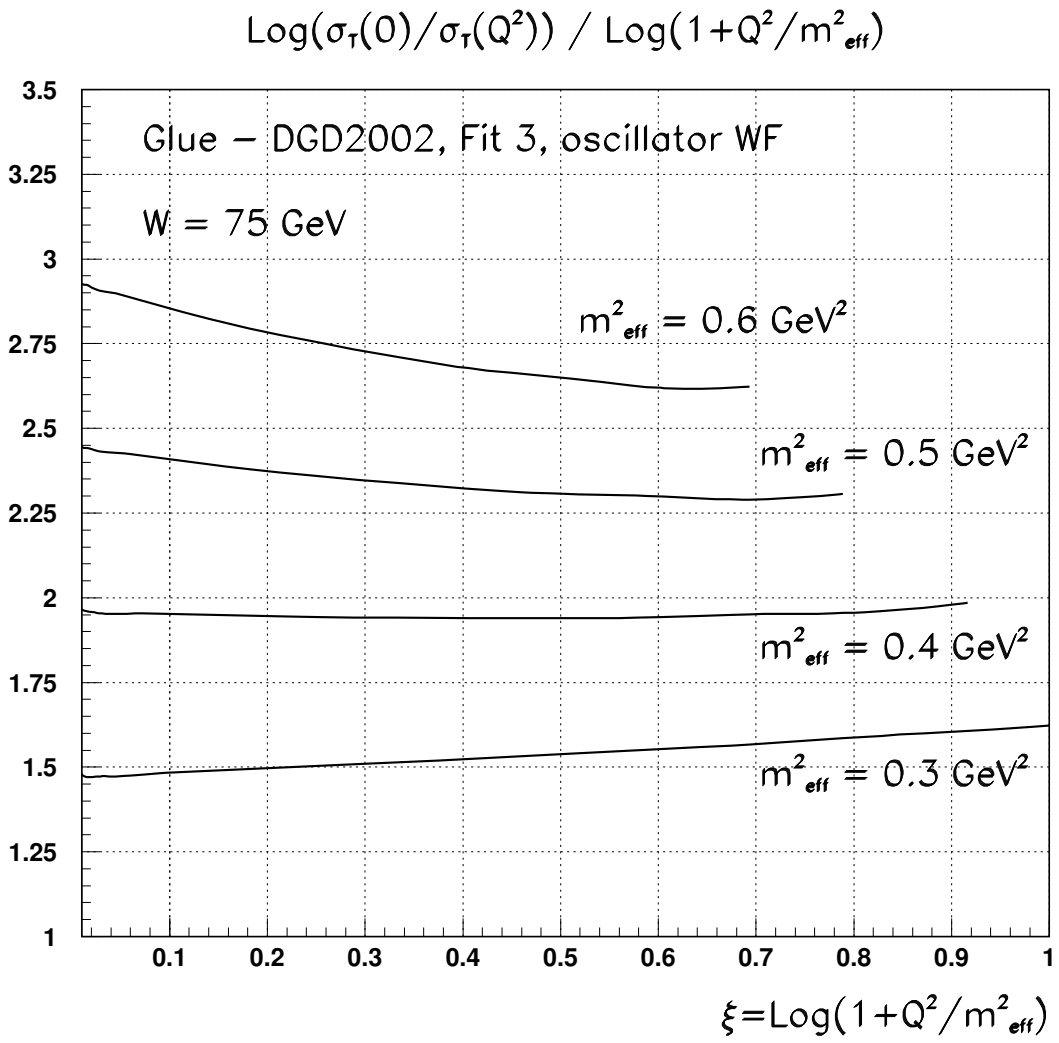

Figure 10.5: *The effective $Q^2 + m^2_{eff}$ exponent of the transverse ρ meson production cross section in the low-Q^2 region as a function of $\xi = 1 + Q^2/m^2_{eff}$ at various values of m_{eff}*

fitted by the formula

$$\sigma(Q^2) \propto \frac{1 + R(Q^2)}{(Q^2 + m^2_{eff}(exp))^2}\,, \tag{10.6}$$

the data yield

$$m_{eff}(exp) = 0.66 \pm 0.11 \text{ GeV}\,,$$

in the excellent agreement with our $m_{eff} \approx 0.6 \div 0.65$ GeV. Note that although in our analysis power n was a free parameter, it turned out close to 2.

Three conclusions can be drawn from this analysis.

First, we showed that, although there is a sizable (by factor of 2) departure of *the magnitude* the k_t factorization predictions from the experimentally measured cross sections, the *shape*

of low-Q^2 behavior is perfectly reproduced by the calculations based on the oscillator wave function.

Second, this analysis demonstrates that the value $m_{eff} \approx 0.65$ GeV is dynamically generated. Indeed, the light quark mass used in our approach was pre-fixed by the gluon structure function analysis at the level $m_q = 0.21$ GeV. Still, $m^2_{eff} > 4m^2_q$, which means that approximately one-half of m^2_{eff} comes from quark momentum. The exact proportion depends, of course, on the particular choice of the vector meson wave function. It still remains to be foudn out whether or not such a successful description of the low-Q^2 behavior of the cross section by means of the oscillator wave function is accidental.

Third, the above means that the actual region where our predictions and the experimental data really mismatch is not the low-Q^2, but rather moderate-Q^2 region, $Q^2 \approx 1$ GeV^2.

High Q^2 region

The second region where our predictions tend to depart from the data is that for high Q^2 region ($Q^2 \gtrsim 5 \div 10$ GeV^2). If the cross section is (locally) fitted by the power-like fall-off

$$\sigma(Q^2) \propto \frac{1}{(Q^2 + m_\rho^2)^n}, \tag{10.7}$$

then this discrepancy can be expressed numerically in terms of the effective Q^2 exponent n. The experimental determination of this exponent resulted in the following: The ZEUS 95 data [77] with $Q^2 > 5$ GeV^2 are consistent with fit (10.7) with energy independent n_{exp}, whose avegare value is found to be 2.32 ± 0.10. The more copious H1 data sample [76] taken at $W = 75$ GeV results in $n_{exp} = 2.24 \pm 0.09$, which is in agreement with ZEUS fit.

The k_t factorization predictions for this exponent is shown in Fig. 10.6. Here we plotted the local analog of the exponent n_{exp}, i.e., the quantity

$$n\left(Q^2 = \sqrt{Q_1^2\, Q_2^2}\right) = \frac{\log[\sigma(Q_1^2)/\sigma(Q_2^2)]}{\log[(Q_2^2 + m_\rho^2)/(Q_1^2 + m_\rho^2)]}. \tag{10.8}$$

Again, if fit (10.7) holds, n should be independent of Q^2.

Graphs in Fig. 10.6 show that this is not the case. At intermediate Q^2, n starts already from about 2.5, then grows as Q^2 increases, and for $Q^2 > 20$ GeV^2 it is even higher than 3.0.

Although standing in constrast with fits to experimental data, such a Q^2 growth of $n(Q^2)$ is still firmly grounded theoretically. Qualitatively, this can be understood from the analysis of the leading $\log Q^2$ result. At fixed W^2 and high enough Q^2, the Q^2 dependence of the cross section comes from

$$\sigma(Q^2) \propto \frac{1 + R(Q^2)}{(Q^2 + m_\rho^2)^4} \cdot \left[G\left(c\frac{Q^2}{W^2}, Q^2/4\right)\right]^2, \tag{10.9}$$

where $c \approx 0.41$ comes from the approximate representation of the off-forward gluon distribution (5.30). The Q^2 dependence of the slope B and of the running coupling α_s is not essential for our point.

The non-trivial Q^2 behavior arises from the integrated gluon structure function. In Fig. 10.7, left panel, we show its Q^2 behavior at $W = 75$ GeV. The origin of the peaked shape is obvious: at moderate Q^2 the integrated glue grows due to the sharp explicit Q^2 dependence (that is,

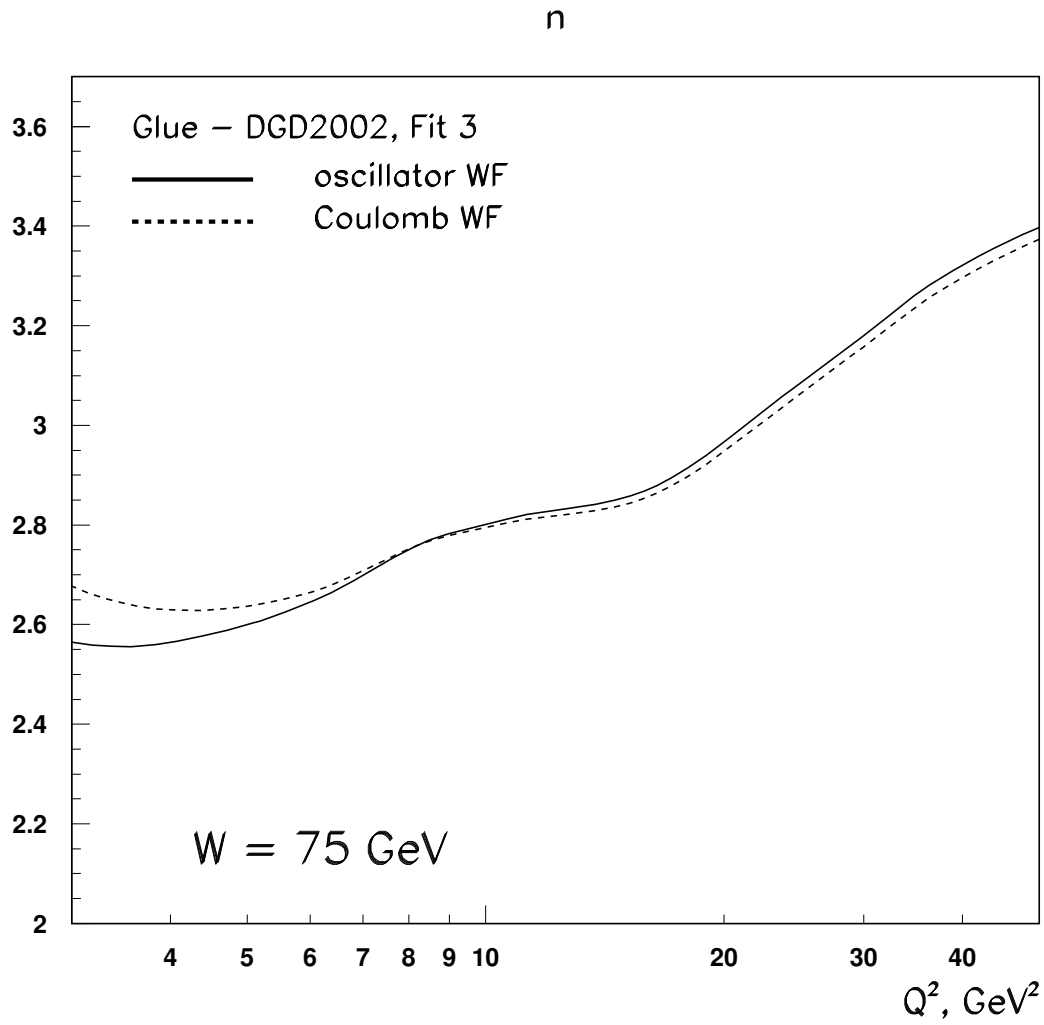

Figure 10.6: *Effective $Q^2 + m^2_{eff}$ exponent of the total ρ meson production cross section in the high-Q^2 region as a function of Q^2. The solid and dashed curves represent calculations for oscillator and suppressed Coulomb wave functions respectively*

due to large values of the unintegrated gluon density $F(x, \vec{\kappa}^2)$), while for larger Q^2 the effect of decreasing x_{eff} overpowers and leads to the decreasing of G as Q^2 grows further.

On the right panel of Fig. 10.7 we show the local Q^2 exponent n_G of the gluon density (the gluon density contribution to the local Q^2 exponent n is equal to $2n_G$),

$$n_G\left(Q^2 = \sqrt{Q_1^2\, Q_2^2}\right) = \frac{\log[G(Q_1^2)/G(Q_2^2)]}{\log[(Q_2^2 + m_\rho^2)/(Q_1^2 + m_\rho^2)]}\,. \tag{10.10}$$

One sees that at moderate Q^2, when G is stil rising, it damps the Q^2 fall, but when $Q^2 \gtrsim 10$ GeV^2, gluon density starts decreasing on its own. This is precisely the reason why at higher

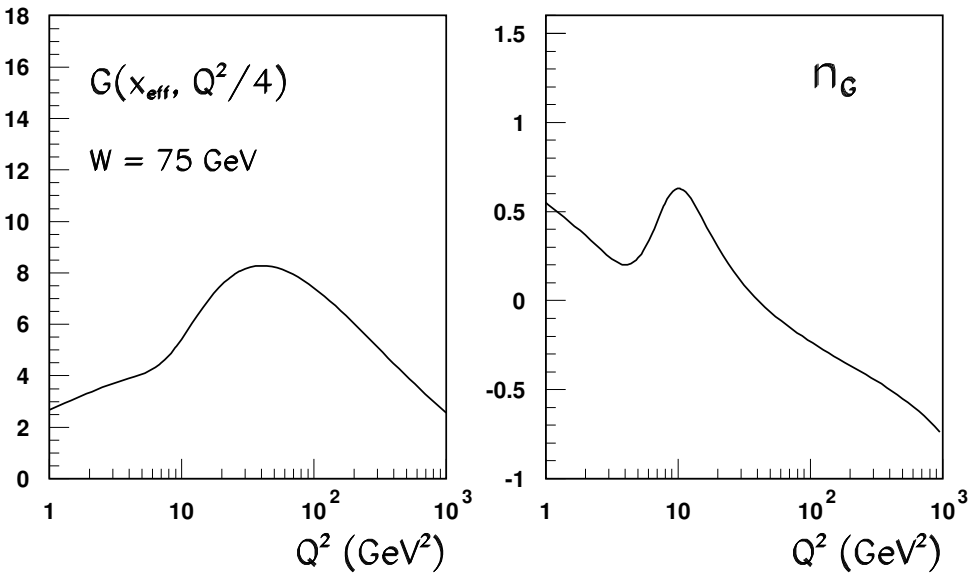

Figure 10.7: *(Right panel) The Q^2 behavior of the integrated gluon density $G(0.41Q^2/W^2, Q^2/4)$ at fixed value of $W = 75$ GeV obtained by integration of the DGD2002 Fit 1; (left panel) The effective Q^2 exponent of this integrated gluon density.*

Q^2 the Q^2 exponent n (Fig. 10.6) grows.

The arguments that justify such a behavior seem to be universal and, to this end, it is surprising why the experimental data do not exhibit such a behavior.

10.2.2 $\sigma_L - \sigma_T$ decomposition

An important insight into the Q^2 behavior of the ρ meson production cross sections comes from the separate analysis of $\sigma_L(Q^2)$ and $\sigma_T(Q^2)$; that is, the proportion of the ρ meson production rates cause by transverse and longitudinal photons.

Fig. 10.8 represents the results for these cross sections within the k_t-factorization approach compared with experimental data [85].

One sees that at high Q^2 we do provide a reasonably good description of the σ_L, but our σ_T curves sink significantly deeper as Q^2 grows. Thus, it is too steep Q^2-falloff of σ_T that causes departure of our curves from the data.

If analyzed in terms of power-like fits

$$\sigma_T(Q^2) \propto (Q^2 + m_\rho^2)^{-n_T}\,; \quad \sigma_L(Q^2) \propto (Q^2 + m_\rho^2)^{-n_L}\,, \tag{10.11}$$

the experimental data yield [85]

$$n_T(exp) = 2.47 \pm 0.03\,. \tag{10.12}$$

We found no explicit expermental results for n_L, but clearly it should be even less than n_T.

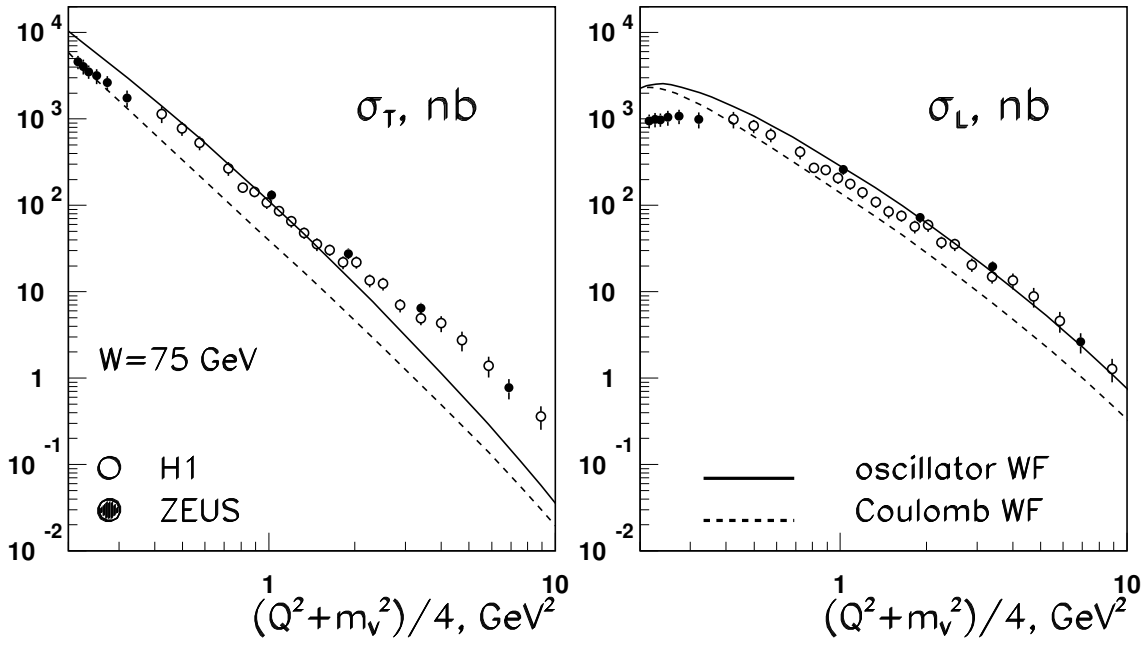

Figure 10.8: *Experimental data on transverse σ_T and longitudinal σ_L cross sections of ρ meson production compared with the k_t-factorization approach.*

The k_t-factorization predictions for the local values of n_L and n_T, defined similarly to (10.8), are shown in Fig. 10.9. At higher Q^2, n_L and n_T grow to 3 and 4, respectively, the latter standing in stark contast to the data.

Fig. 10.10 depicts the ratio

$$R(Q^2) = \frac{\sigma_L(\gamma^* p \to \rho p)}{\sigma_T(\gamma^* p \to \rho p)}, \tag{10.13}$$

experimental points taken from [76]. The glaring disagreement at higher Q^2 is, of course, caused by overly suppressed σ_T that our calculations predict. Evidently, if we found a way to increase σ_T the ratio $R(Q^2)$ would be automatically cured.

10.2.3 Energy dependence

The growth of the vector meson production cross sections is a well-established fact. It is linked basically to the energy growth of the pomeron exchange, and therefore fitting the cross sections to the energy power law

$$\sigma(W) \propto W^\delta \tag{10.14}$$

seems a natural way to quantitize the energy growth.

Fig. 10.11 shows the experimental data on energy rise exponent δ from ZEUS [77] and H1 [76], together with the k_t-factorization predictions based on oscillator and Coulomb wave function. Since the true W-dependence of the cross sections can deviate from simple power law (10.14), the exponent δ can depend on W as well. At lower Q^2 the upper pair of curves

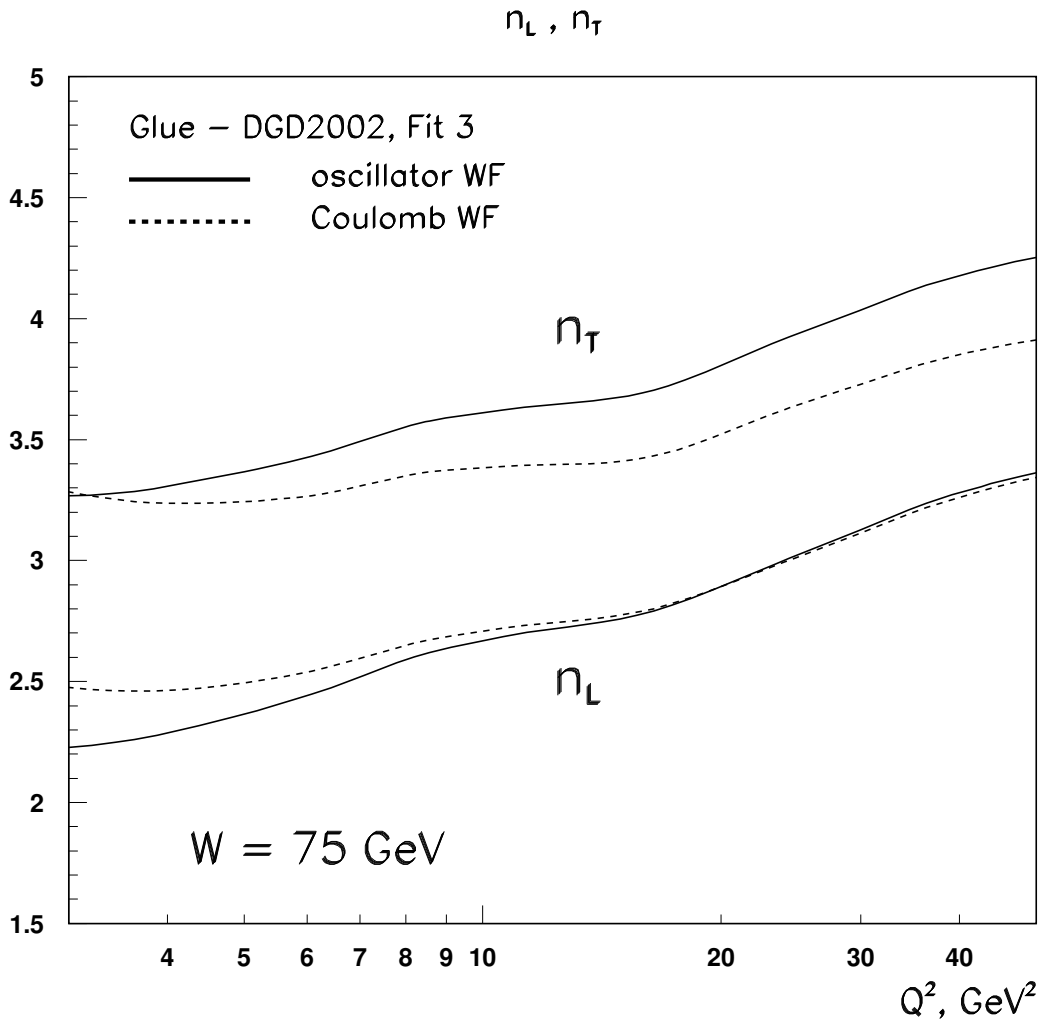

Figure 10.9: *The effective Q^2 exponents shown separately for σ_L and σ_T as functions of Q^2. Solid and dashed lines correspond to oscillator and suppressed Coulomb wave functions respectively*

corresponds to δ calculated between 50 and 75 GeV, while the lower pair corresponds to the energy range between 110 and 150 GeV.

One sees that the agreement is rather good, although the tendency that our curves are slightly higher than the (ZEUS) data is noticeable. However, due to still significant experimental errors, it is too early to draw any more definite conclusions.

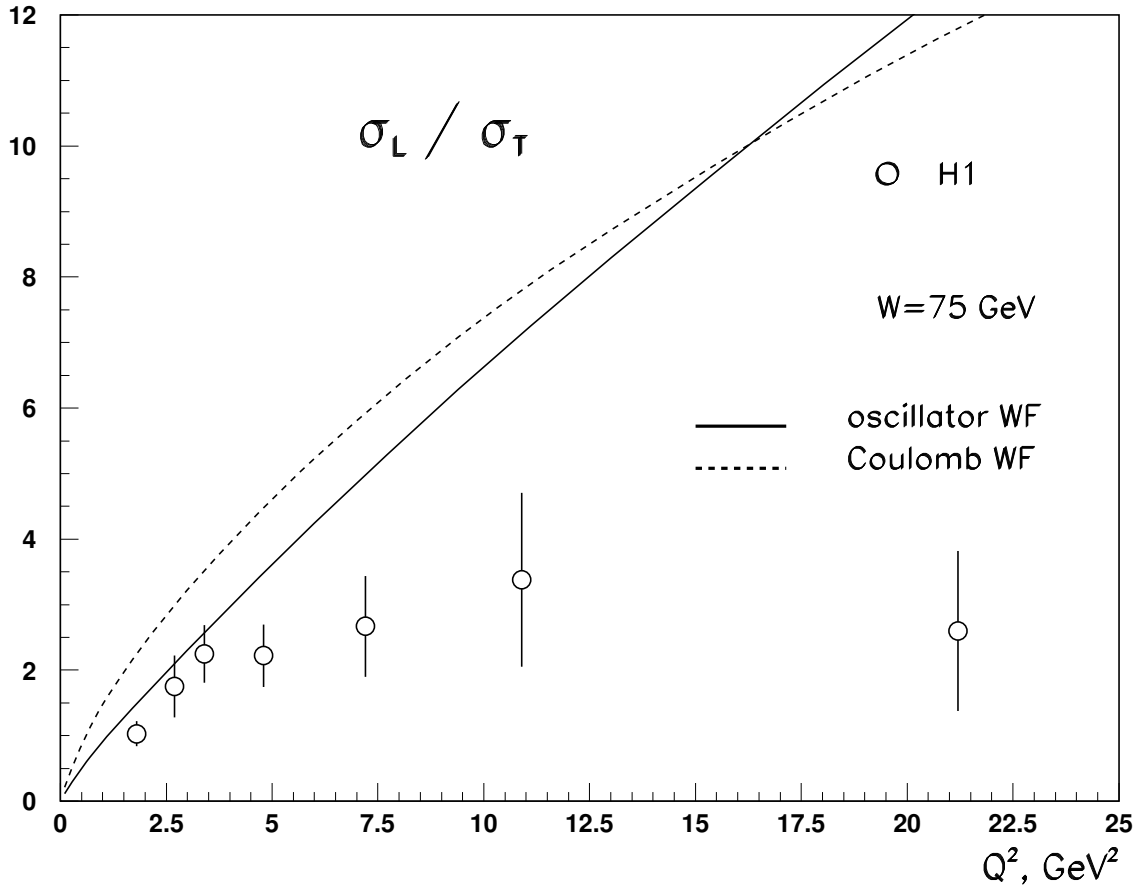

Figure 10.10: *Ratio $R = \sigma_L/\sigma_T$ as a function of Q^2 for ρ meson as a function of Q^2. Solid and dashed lines correspond to oscillator and suppressed Coulomb wave functions, respectively*

10.2.4 t-dependence

The analysis of t-dependence of the differential cross sections within a perturbative framework has an ambiguous status. On one side, if we deal with the proton in final state, this dependence is governed largely by the intrinsically non-perturbative (multiparticle) form factor of the proton. Therefore, in order to have a plausible t-dependence, we have to introduce a certain "educated guess". On the other hand, our gluon density analysis already uses this form factor, and therefore places some contraints on it. Finally, as the analysis suggests, at low t, within diffraction cone, several other mechanisms modify the t dependence of the proton form factor. If one parametrizes the differential cross sections at low t ($t < 0.5$ GeV^2) by an exponential law with slope parameter b,

$$\frac{d\sigma}{d|t|} \propto e^{-b|t|}, \tag{10.15}$$

one finds that various sources of t-dependence can be treated in terms of contributions to the overall slope b approximately additively.

In principle there can be three sources of the non-zero contributions to the slope: the

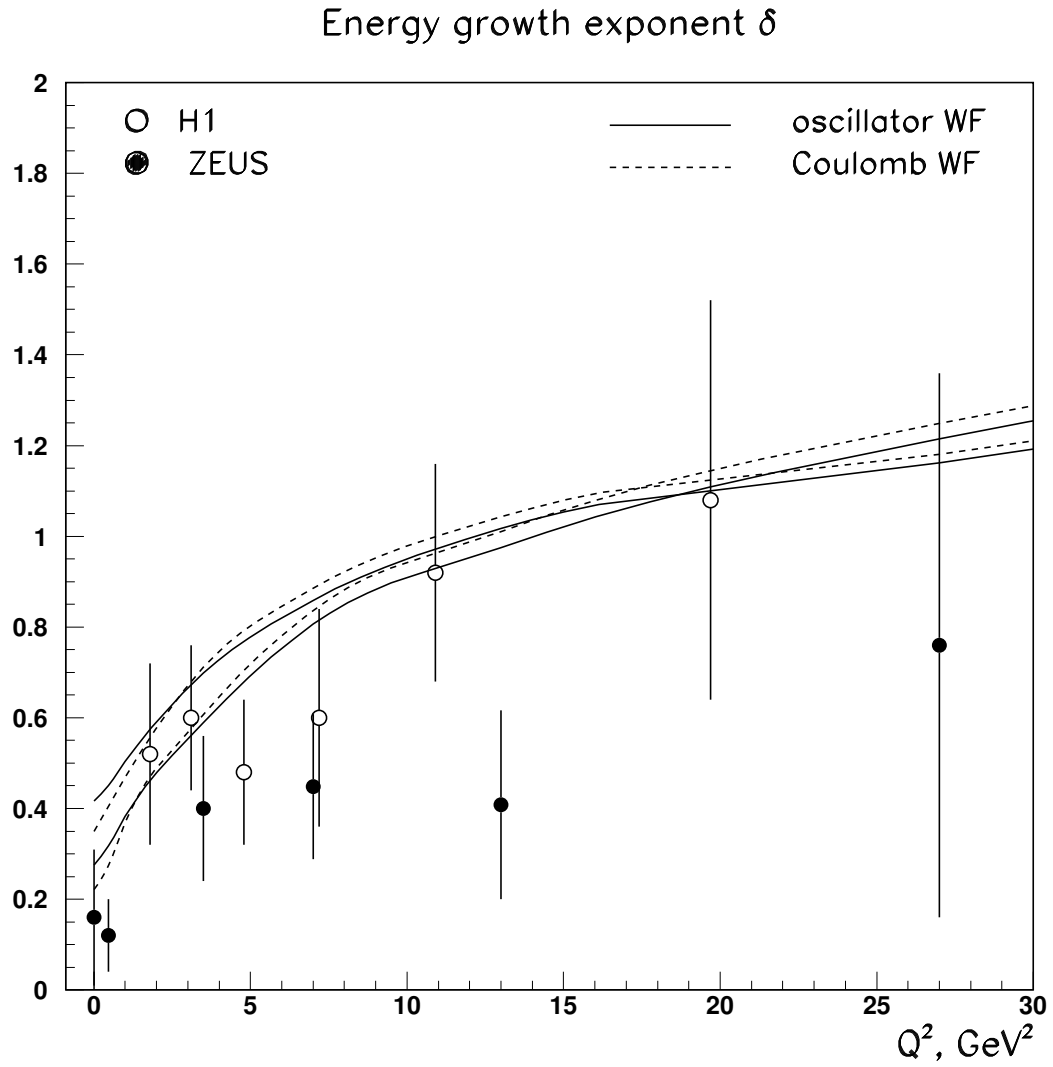

Figure 10.11: *Effective exponents δ of energy growth for the ρ meson production cross sections. Solid and dashed lines correspond to oscillator and suppressed Coulomb wave functions, respectively. The upper pair of curves (at low Q^2) corresponds to δ calculated between 50 and 75 GeV, while the lower pair is the result for δ calculated between 110 and 150 GeV.*

proton transition, the $\gamma^* \to V$ transition, and the exchange (the pomeron propagation):

$$b = b_{p\to p} + b_{exch.} + b_{\gamma^*\to V} \,. \tag{10.16}$$

The first term appears in our calculations explicitly as an effective slope of the energy- and $\vec{\kappa}^2$-independent dipole form factor,

$$F(\vec{\Delta}^2) = \frac{1}{\left(1+\vec{\Delta}^2/\Lambda^2\right)^2}; \quad \Lambda = 1 \text{ GeV}; \quad \to \quad b_{p\to p} = 4 \text{ GeV}^{-2} \,. \tag{10.17}$$

The second term is also introduced explicitly. It is responsible for the shrinkage of the diffractive cone with energy growth. The third term appears from the accurate QCD treatment of the $\gamma^* \to V$ transition. It possesses a characteristic $1/(Q^2 + m_V^2)$ shape, which leads to the scaling phenomenon mentioned earlier.

Due to the above blend of uncalculable soft and perturbative hard contributions, the k_t-factorization approach should not be expected to yield first-principles predictions for the absolute value of the slope parameter. Nevertheless, one can ask whether or not some kinematic dependencies observed can be efficiently accomodated within our approach.

In principle, one can invoke several definitions of the effective slope parameter, however there is no siginficant difference among them. Below, in Table 3, we compare results for three definitions of the effective slope:

$$b(\text{def.1}) = -\frac{d\log(d\sigma/d|t|)}{d|t|}\bigg|_{|t|=0}; \quad b(\text{def.2}) = \frac{1}{\sigma}\frac{d\sigma}{d|t|}\bigg|_{|t|=0}; \quad b(\text{def.3}) = \frac{1}{\langle|t|\rangle} = \frac{\int d\sigma}{\int |t| d\sigma}, \tag{10.18}$$

calculated at several Q^2 points.

Table 3. Various possible definitions of the effective slope and their values obtained from k_t-factorization calculations at three characteristic values of Q^2.

Q^2, GeV^2	b(def.1)	b(def.2)	b(def.3)
0	14.0	13.1	11.4
2.2	10.2	9.6	8.7
27	6.7	6.3	6.3

In Fig. 10.12 we present our results for the slope parameter of the ρ meson production cross section. The results for our calculations give somewhat too high values of the slope than the experimentally measured numbers (ZEUS [77] and H1 [76]), but nevertheless they exhibit the right Q^2 dependence.

It is interesting to note that the slopes for σ_L and σ_T differ slightly (see Fig. 10.13). Note also that at small Q^2 the calculations based on the Coulomb wave function give larger slopes.

Fig. 10.14 shows a typical pattern of the $|t|$-dependence of the differential cross sections in the region of small-to-moderate t ($0 < |t| < 1.5$ GeV^2). The oscillator wave function was used everywhere in this figure. One sees that initial approximately exponential decrease of the differential cross section flattens at higher $|t|$ as the process leaves the diffractive peak.

10.2.5 Helicity amplitudes

Our analysis explicitly takes into account all possible helicity amplitudes $\gamma^*(\lambda_\gamma) \to V(\lambda_V)$, with $\lambda_\gamma, \lambda_V = 0, \pm 1$. Since the pomeron exchange does not distiguish left from right, only five independent helicity amplitudes survive.

Fig. 10.15 shows the absolute values of the five helicity amplitudes plotted against the momentum transfer squared $|t|$. Within diffraction cone one sees the characteristic behavior of all the amplitudes. In the region of moderate $|t|$ one can observe diffractive dips, whose location changes from one amplitude to the other. As we did not focus on large t, we cannot be sure that the dips are located exactly where we predicted. Nevertheless, this picture shows the general pattern of the t-behavior of the helicity amplitudes.

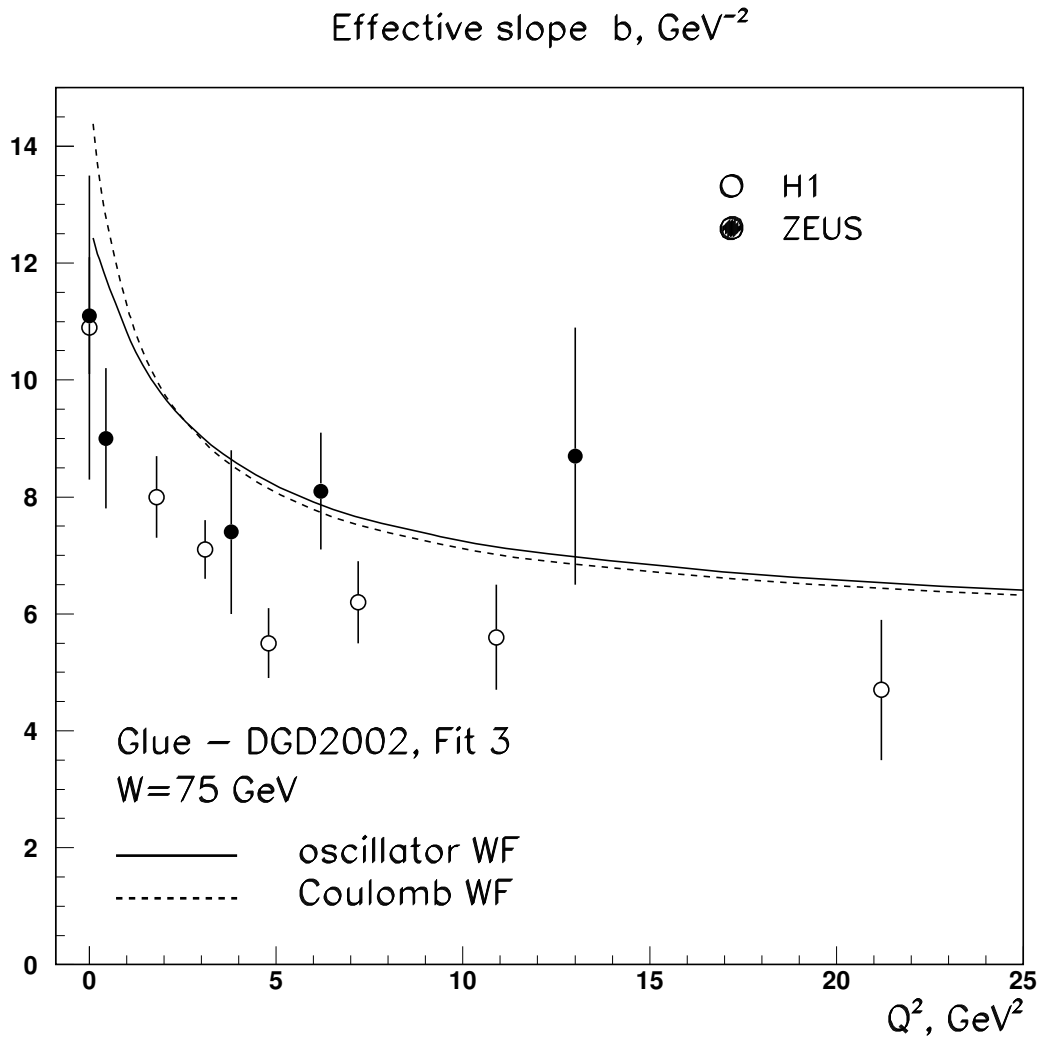

Figure 10.12: *Effective slopes b of the ρ meson differential cross section within the diffraction cone as functions of Q^2. Solid and dashed lines correspond to the oscillator and suppressed Coulomb wave functions, respectively.*

It is clear that the presence of helicity flip amplitudes leads to the breaking of the s-channel helicity conservation. It is therefore interesting to ask what the magnitudes of the helicity-flip amplitudes are.

Fig. 10.16 gives the answer to this question. Here we show ratios of the helicity-flip to helicity-non-flip amplitudes

$$\frac{|A(\gamma_T \to V_{-T})|}{|A(\gamma_T \to V_T)|}; \quad \frac{|A(\gamma_T \to V_L)|}{|A(\gamma_0 \to V_L)|}; \quad \frac{|A(\gamma_0 \to V_T)|}{|A(\gamma_0 \to V_L)|}, \tag{10.19}$$

and whenever possible compare k_t-factorization predictions to the avaliable experimental data, as taken from [85].

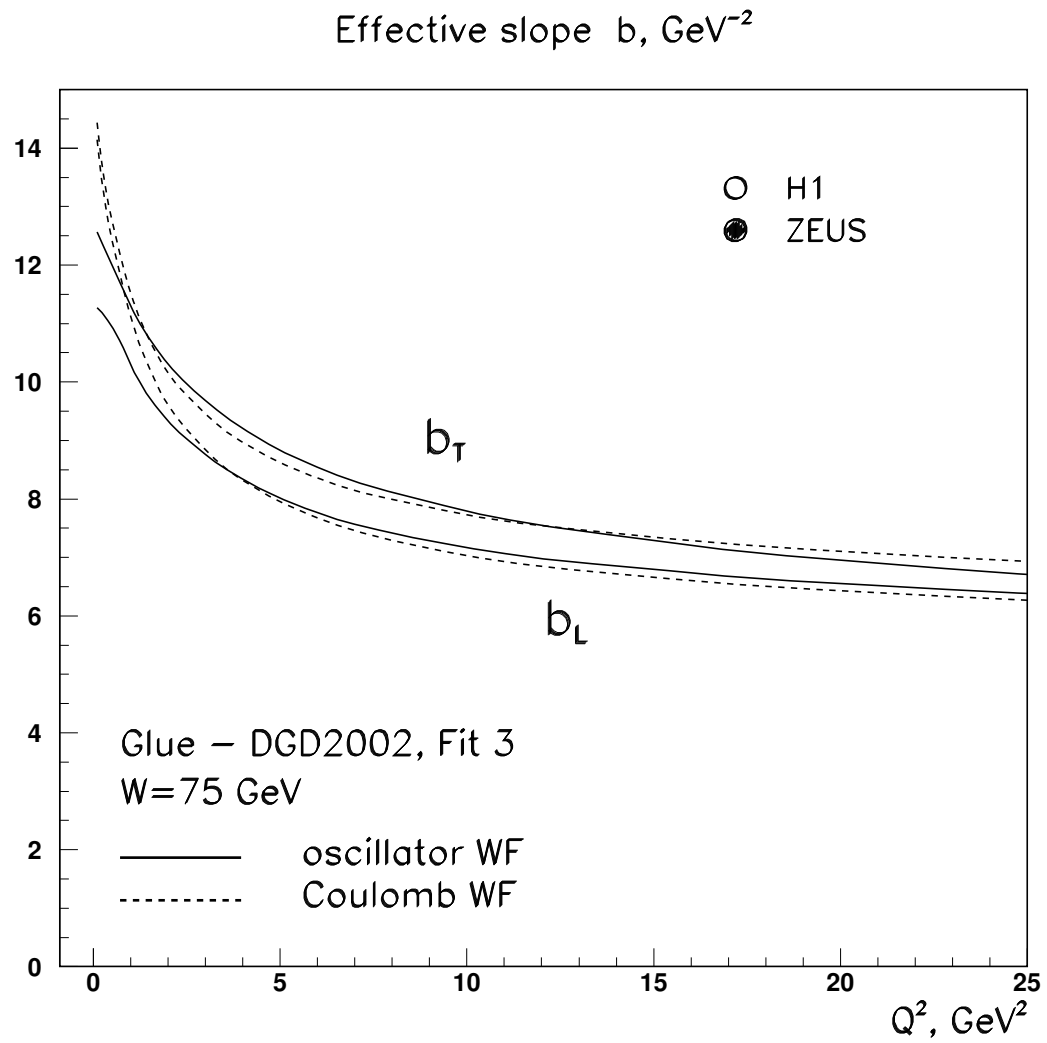

Figure 10.13: *Effective slopes b_L and b_t of the ρ meson longitudinal and transverse differential cross sections within the diffraction cone as functions of Q^2. Solid and dashed lines correspond to the oscillator and suppressed Coulomb wave functions, respectively.*

Finally, we made predictions for all the spin density matrix elements for ρ meson production and compared them with H1 [76] and ZEUS [86] data. Results are shown in Fig. 10.17.

10.3 ϕ mesons

The production of ϕ mesons has much similarity to ρ meson production. Therefore we will not provide as detailed a discussion of the predictions as we did for the ρ meson, but will rather show our predictions for the quantities that have been measured experimentally for the ϕ mesons.

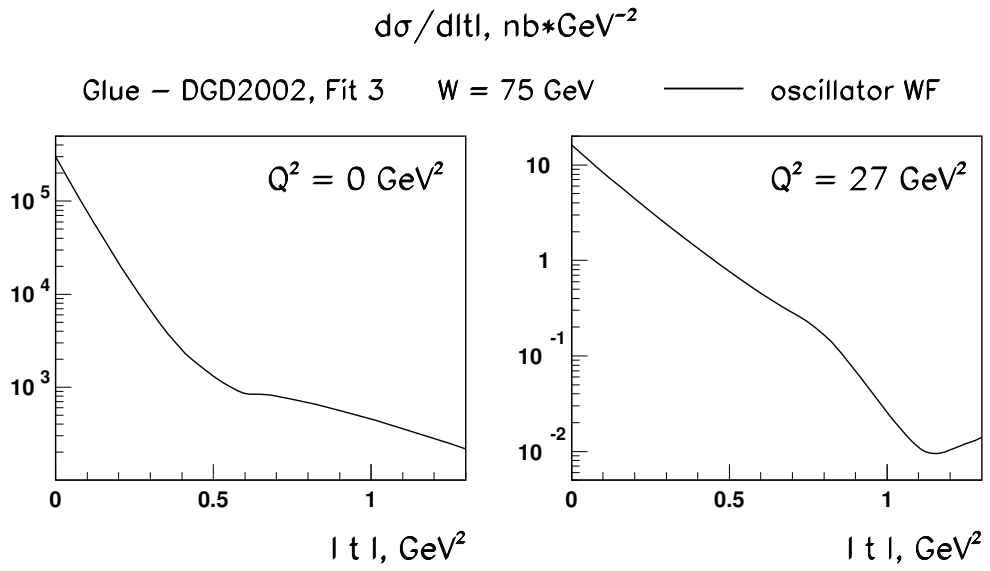

Figure 10.14: *The transverse momentum squared dependence of the differential ρ meson production cross sections at two characteristic values of Q^2.*

Fig. 10.18 shows the total cross sections of diffractive ϕ meson production as a function of Q^2 data taken from H1 [78] and ZEUS [79], [80]. Remembering the scaling phenomenon of the vector meson production cross sections, we should expect a picture similar to what happens in the ρ meson case. Indeed, we see in this figure a reasonably good description of the data for moderate Q^2, and a slight overshooting of our predictions as we move towards small Q^2.

It is interesting to compare ρ meson and ϕ meson production cross sections taken at equal Q^2. Fig. 10.19 shows our predictions for the ratio $\sigma(\gamma^* p \to \phi p)/\sigma(\gamma^* p \to \rho p)$ together with the experimental data. If the scaling phenomenon holds, at higher Q^2 the ratio is expected to approach constant value of 2/9, and such a tendency to do so is indeed visible at the figure. However, at smaller Q^2 the ratio goes down. This behavior should be expected, for at smaller Q^2 the ratio can be approximated by

$$\frac{\sigma(\gamma^* p \to \phi p)}{\sigma(\gamma^* p \to \rho p)} \propto \left(\frac{Q^2 + m^2_{\rho eff}}{Q^2 + m^2_{\phi eff}} \right)^2 , \tag{10.20}$$

with $m_{\rho eff} < m_{\phi eff}$.

One sees that our predictions for this ratio agree with the data very well. Moreover, note the remarkable coincidence of the results based on the oscillator and Coulomb wave functions. The reason for that is, of course, the fact that we study here not absolute values of cross sections, but their ratios. This removes a significant part of the ambiguity present in this or that specific choice of the wave function and reveals the features of the k_t-factorization approach in its pure form.

Finally, Fig. 10.20 shows the experimental results for the ϕ meson density matrix measurement by H1 [78]. Our predictions agree well with the data.

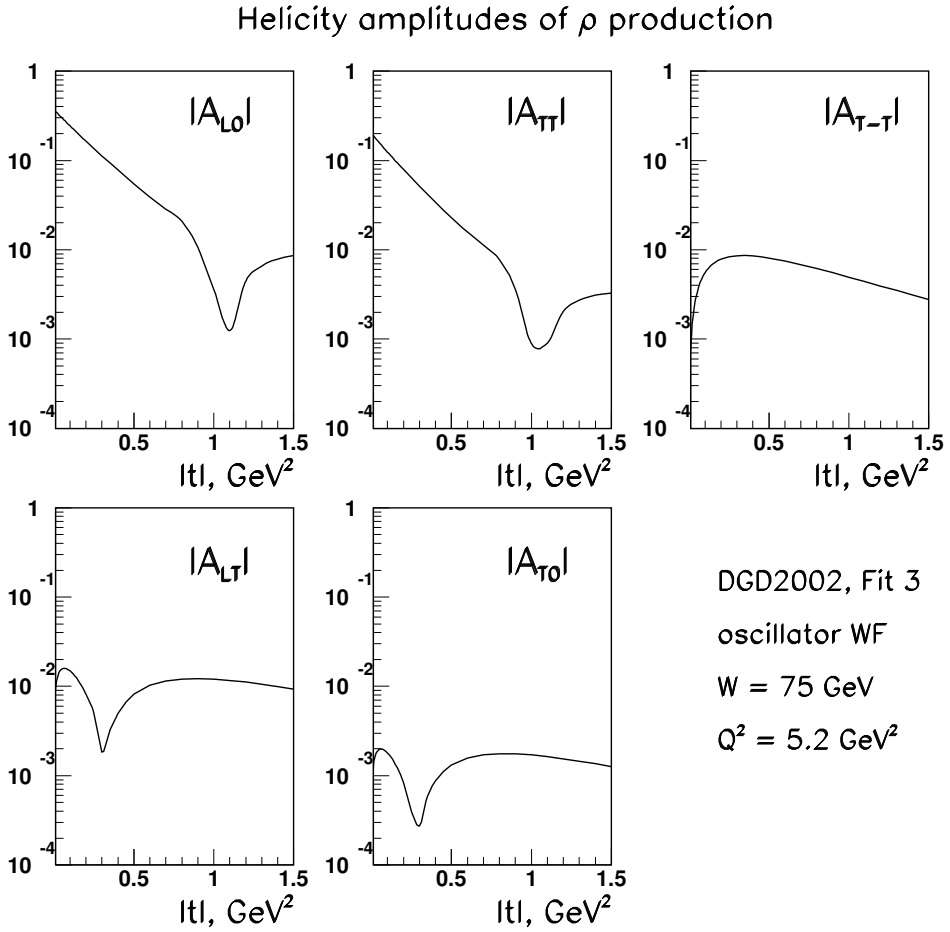

Figure 10.15: *The transverse momentum squared dependence of the five helicity amplitudes for ρ meson production at $Q^2 = 5.2\ GeV^2$.*

10.4 J/ψ and Υ mesons

Fig. 10.21 shows the k_t-factorization predictions for the total cross sections for J/ψ meson electroproduction as a function of Q^2 compared with available data from H1 [81], [82] and ZEUS [77], [83]. A reasonable agreement throughout the whole Q^2 range is seen.

The photoproduction cross sections versus total energy W of the γp collision are shown at Fig. 10.22. One can see again that the k_t-factorization calculations give predictions within accuracy of roughly a factor of 2, uncertainty coming from the meson wave function. Still, the experimental data fit between the two curves.

Fig. 10.23 shows the $\sigma_L - \sigma_T$ decomposition of the J/ψ meson production cross sections taken from [85]. An agreement at a similar level of accuracy is observed as well. The ratio $R(Q^2) = \sigma_L/\sigma_T$ is shown in Fig. 10.24. The data are taken from ZEUS and H1.

The energy dependence of the $\Upsilon(1s)$ meson photoproduction is shown in Fig. 10.25. One observes that the experimental points soar about 10 times higher than both curves. The origin

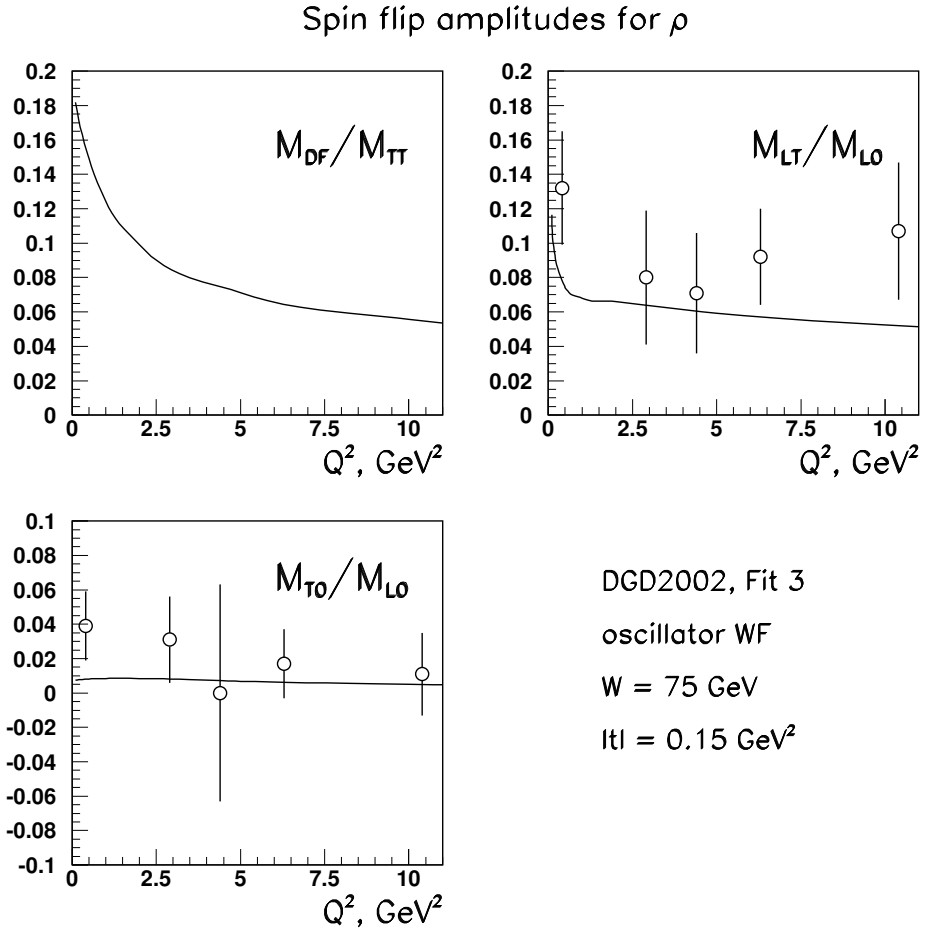

Figure 10.16: *The Q^2 dependence of the spin-flip to non-spin-flip amplitudes in the ρ meson production compared with the combined HERA data.*

of this discrepancy is not clear. While the k_t-factorization predictions for the Υ production cross sections follow the scaling behavior in Fig. 10.1, the Υ photoproduction data do not comply with this tendency. It should be noted also that a similar behavior is observed for other processes: that is, the production rates for Υ seems to be higher than expected.

10.5 Production of excited states

In this section we will give some of the most prominent features in the reaction of diffractive production of $2S$ and D-wave vector mesons.

In Fig. 10.26 we show the ratios of the excited-to-ground state production cross sections

$$r(2S/1S) = \frac{\sigma(\gamma p \to V(2S)p)}{\sigma(\gamma p \to V(1S)p)}; \quad r(D/1S) = \frac{\sigma(\gamma p \to V(D)p)}{\sigma(\gamma p \to V(1S)p)}. \tag{10.21}$$

for the ρ system and for charmonium.

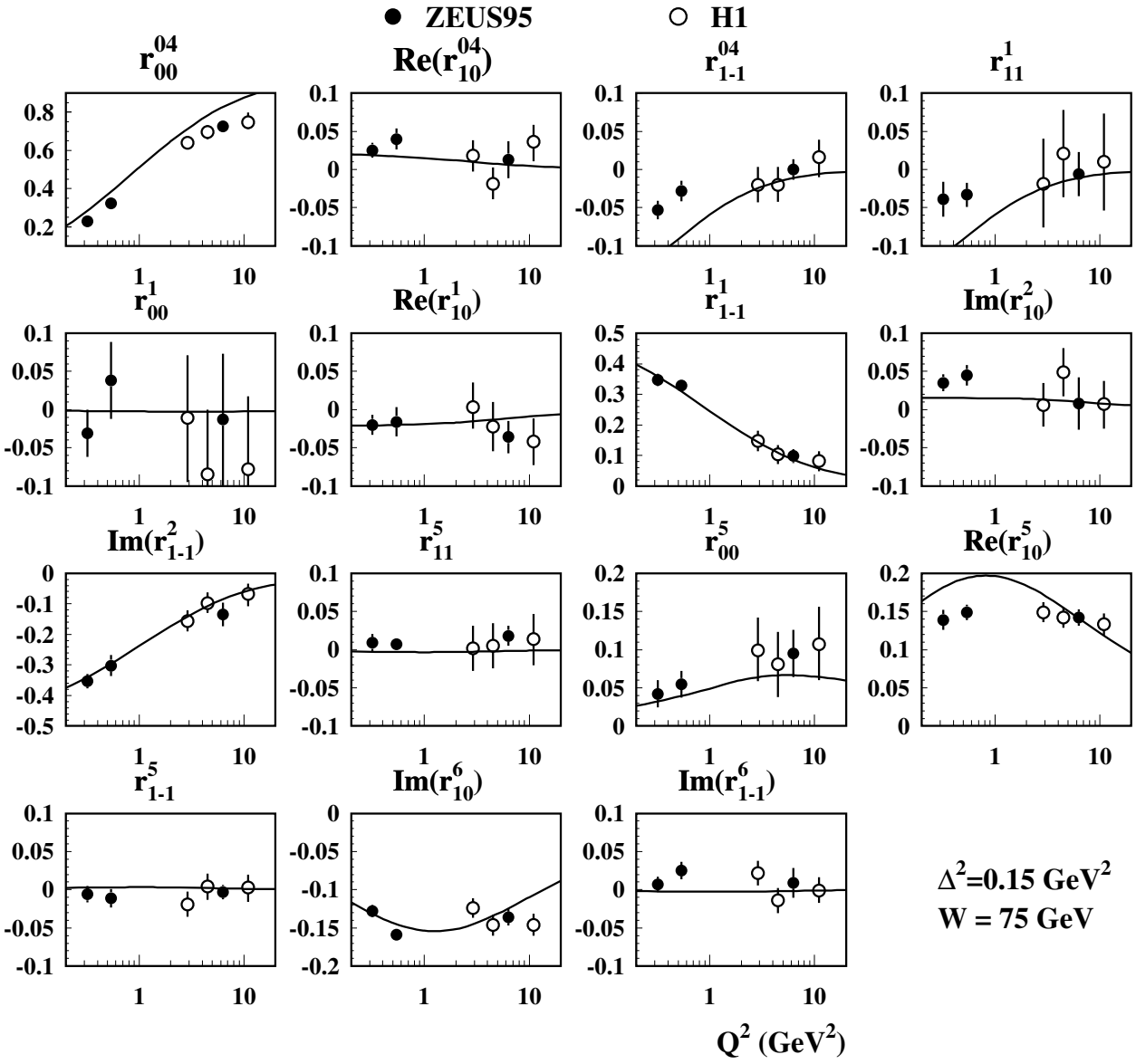

Figure 10.17: *Experimental data on spin density matrix for ρ meson production as function of Q^2 compared with k_t-factorization predictions based on the oscillator wave function.*

A brief look reveals that, although the production rate both of $2S$ and of D-wave states are suppressed with respect to ground state, a radically different Q^2 behavior of the suppression factors $r(2S/1S)$ and $r(D/1S)$ is observed. This difference is due to the distinctly different nature of suppression in these two cases.

The suppression for $2S$ state production comes from the much-discussed node effect of the $2S$ state wave function. Indeed, if one looks at the $2S$ production amplitude in the impact parameter space, then one sees the product of two factors: the photon wave function multiplied by dipole cross section $\Psi_\gamma \cdot \sigma_{dip}$ and the radial wave function of the produced meson. At low

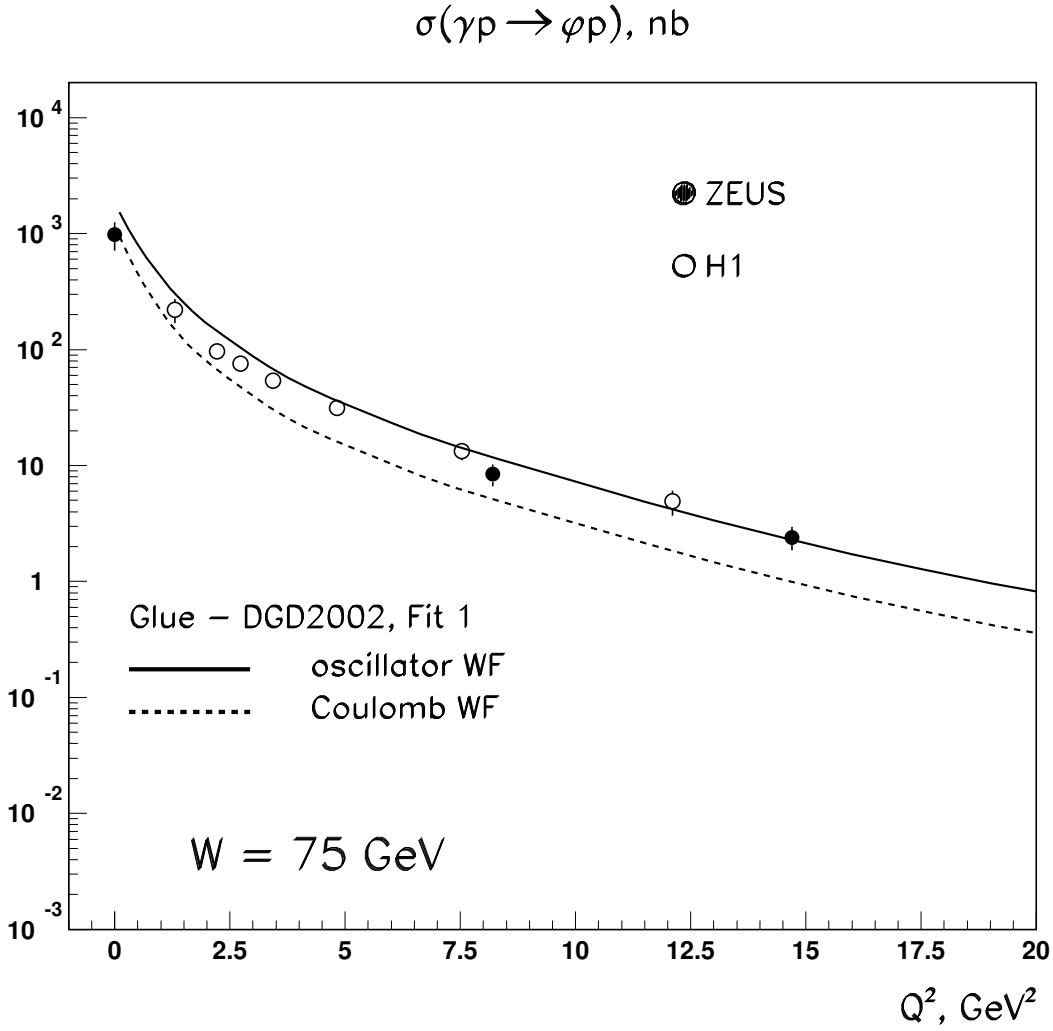

Figure 10.18: *Total cross section of the diffractive ϕ meson production as a function of Q^2. The k_t-factorization predictions based on oscillator (solid lines) and suppressed Coulomb (dashed lines) wave functions are also shown. All calculation are performed for $W = 75$ GeV using DGD2002, Fit 1.*

Q^2, $\Psi_\gamma \cdot \sigma_{dip}$ is a wide function, peaked at a hadronic scale, which is precisely where the node of the vector meson wave function is located. This results in significant calcellation between contributions from impact parameter regions smaller and higher than the node position. At higher Q^2 the photon wave function shrinks, and the peak of $\Psi_\gamma \cdot \sigma_{dip}$ shifts toward smaller r — that is, away from the node. Thus, the effect of calcellation vanishes.

As for the D wave meson suppression, it arises from the angular part of the integrals. In fact, if the initial photon were built only of the S wave $q\bar{q}$ pair, then, due to ortogonality between pure S and D waves, there would be no D wave vector mesons at all. However, the

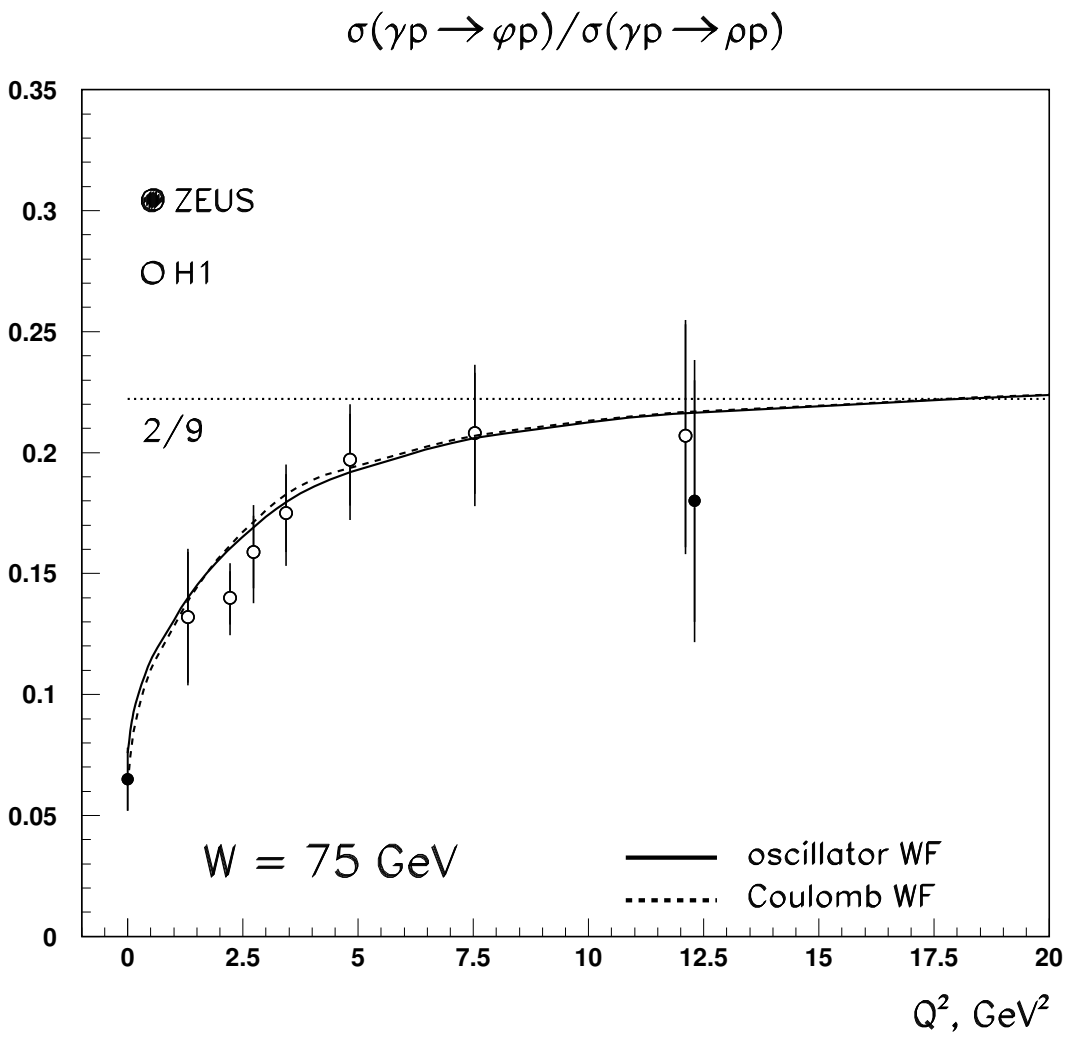

Figure 10.19: *Ratio of ϕ meson to ρ meson total production cross sections as function Q^2. Solid and dashed lines correspond to oscillator and suppressed Coulomb wave functions, respectively.*

spinorial structure of the photon coupling to the quark line does not correspond to the pure S wave, but contains an admixture of D wave as well. This D wave part leads to the D wave meson producton and, since it is rather small, the cross sections turn out to be suppressed as well.

The situation is basically the same both in the ρ system and in charmonium. The major difference is the energy scale of the node effect suppression, which can be directly related to the mass of the corresponding meson.

In the case of charmonium the k_t-factorization predictions are compared with the available H1 data on $\psi(2s)$ production [87], [88]. A good agreement is seen.

As vividly illustrated by Fig. 10.26, a mere measurement of the production cross section

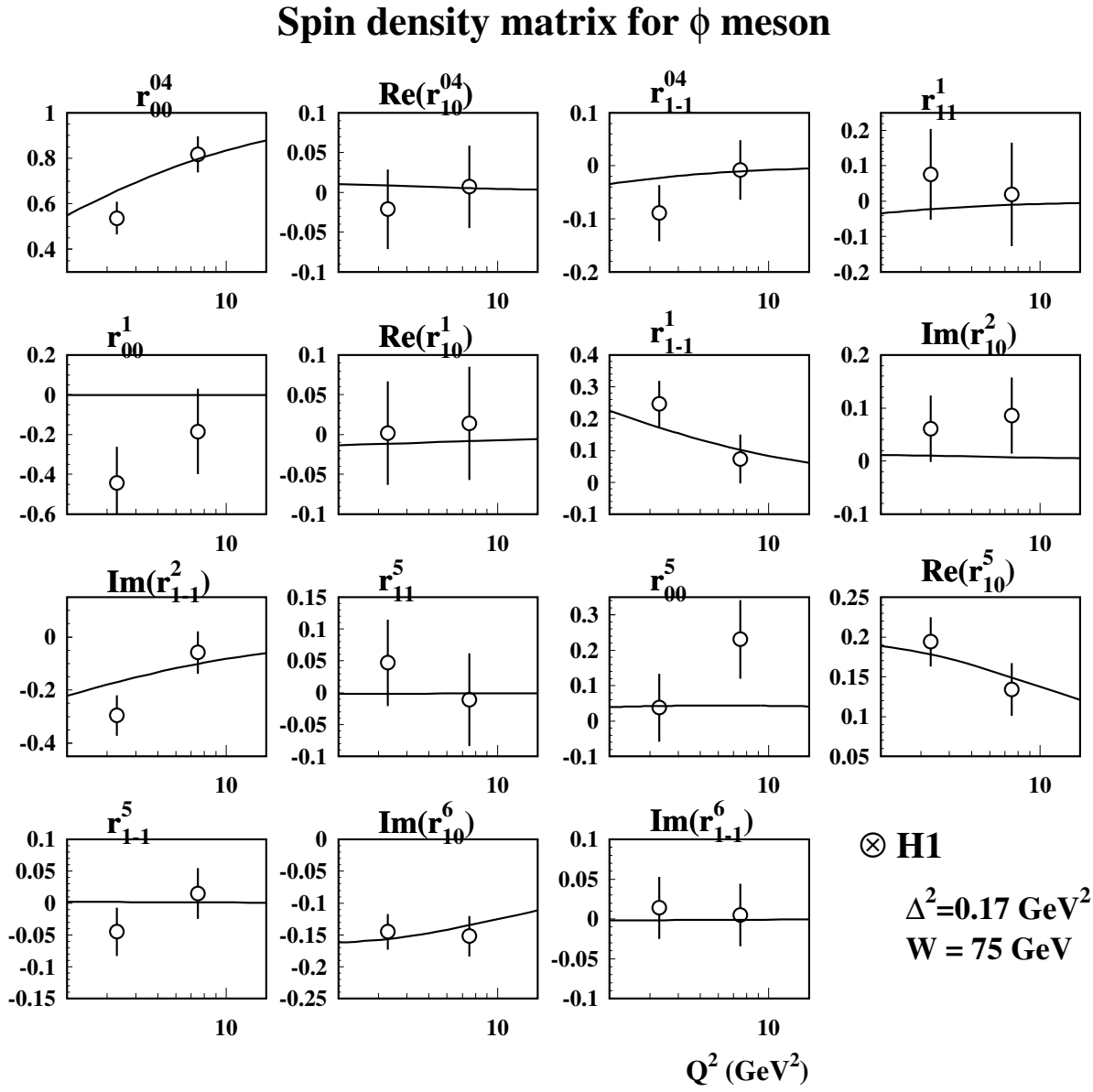

Figure 10.20: *Experimental data on spin density matrix for the ϕ meson production as functions of Q^2, compared with k_t-factorization predictions based on the oscillator wave function.*

for high-lying states in the ρ spectrum (such as $\rho'(1450)$ and $\rho'(1700)$) at high Q^2 might be enough to get some insight into the spin-angular structure of these states. However, even more dramatic distinction between S and D wave states is offered by the $R_V = \sigma_L(V)/\sigma_T(V)$ measurements.

Fig. 10.27 shows ratios $R(1S)$, $R(2S)$, and $R(D)$ for the ρ system. We see that at higher Q^2 the following hierarchy exists:

$$R(1S) \gg R(2S) \gg R(D)\,, \tag{10.22}$$

with about one order of magnitude difference between the $1S$ and D wave production rates. At smaller Q^2, $R(2S)$ exhibits very characteristic spectacular wiggles. Starting from zero at

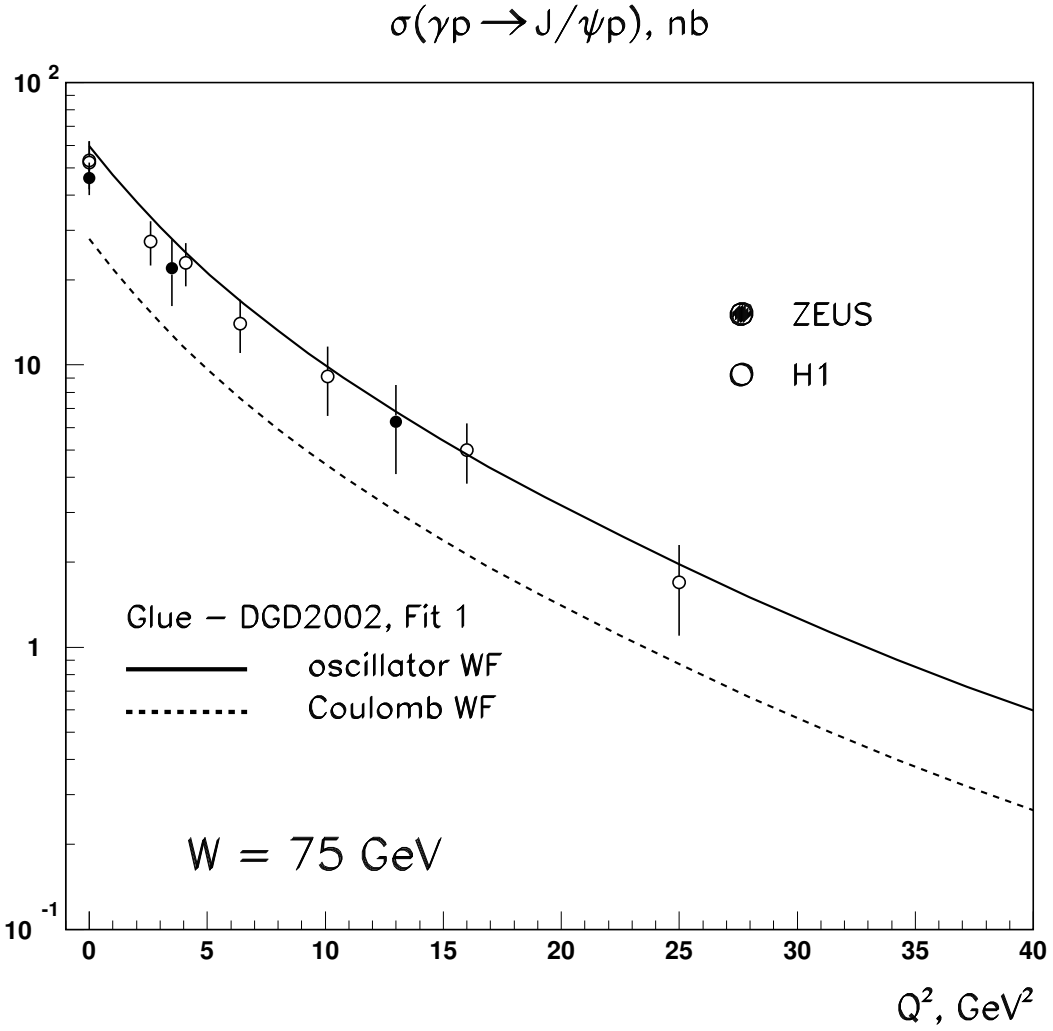

Figure 10.21: *Total cross section of diffractive J/ψ meson production as a function of Q^2. The k_t-factorization predictions based on oscillator (solid lines) and suppressed Coulomb (dashed lines) wave functions are also shown. All calculations were performed for $W = 75$ GeV using DGD2002, Fit 1.*

$Q^2 = 0$, it springs to a local maximum of ≈ 0.6 at $Q^2 \approx 0.1$ GeV^2, then rapidly drops, and then rises again. This behavior is the manifestation of the node effect as well. Indeed, since the structure of the transverse and longitudinal photons is not identical, the strongest cancellation takes places at different Q^2 values in these two cases. In particular, the curve suggests that as start from $Q^2 = 0$ and we slide along Q^2 scale, the strongest cancellation occurs in σ_T earlier than in σ_L.

A word of caution should be offered now: The exact position of the node in the $2S$ state wave function cannot be predicted accurately and depends on the particular Ansatz for the

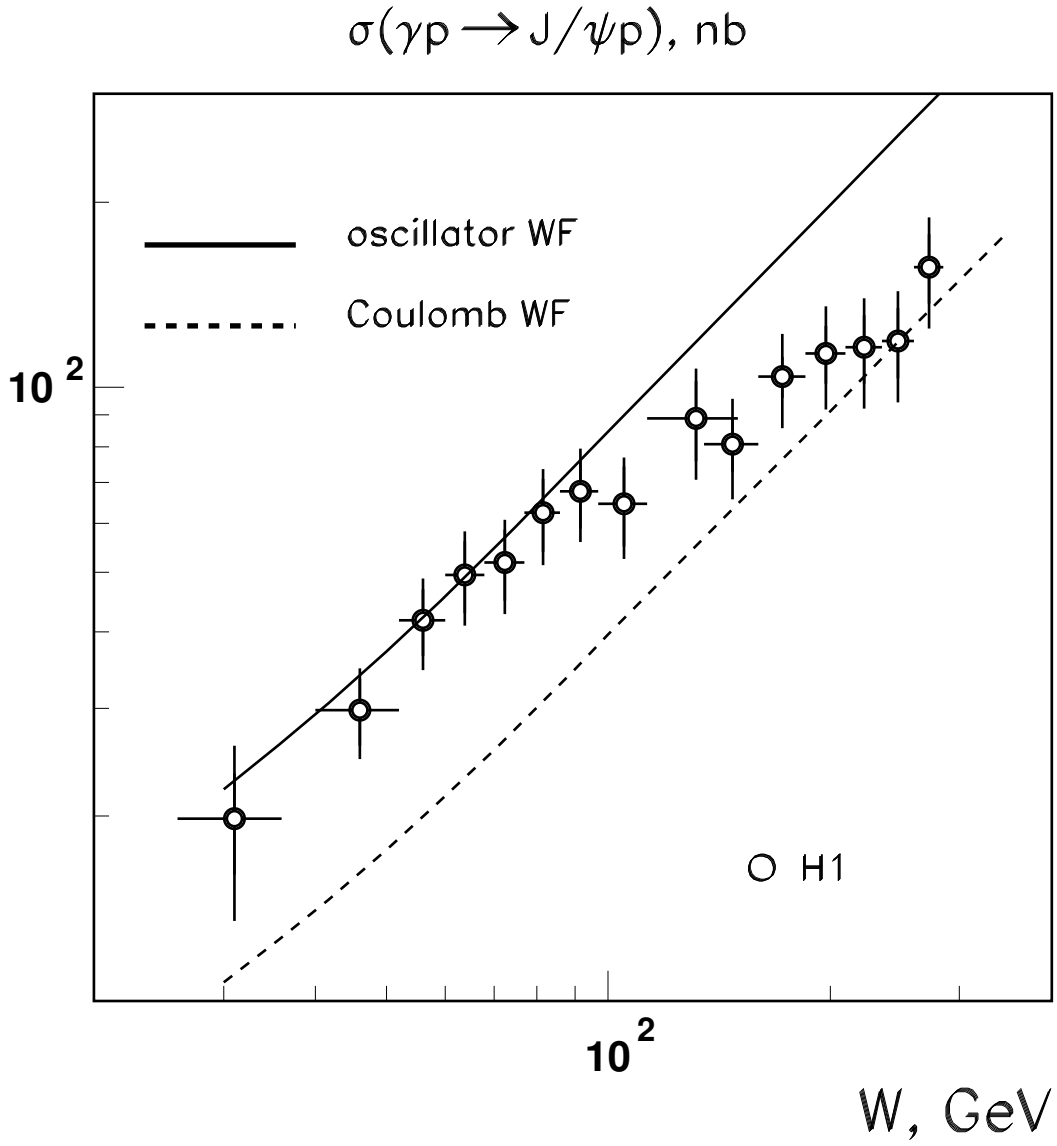

Figure 10.22: *The energy dependence of the total J/ψ meson photoproduction cross section. The k_t-factorization predictions based on oscillator (solid lines) and suppressed Coulomb (dashed lines) wave functions are also shown. All calculations were performed for $W = 75$ GeV using DGD2002, Fit 1.*

wave function chosen. This means that the wiggly shape of $R(2S)$ in Fig. 10.27 — with positions and the values of local extrema — should not be regarded as accurate predictions. In fact, one cannot even be sure that the non-monotonic Q^2 behavior of $R(2S)$ actually takes place. This curve simply illustrates what kind of effect can be expected. The specific profile of this curve is not, of course, predictable, as long as we rely on simple vector meson wave functions.

An immediate conclusion from this is that we have found an observable that is extremely sensitive to the minute details of the vector meson wave function — a powerful tool that would

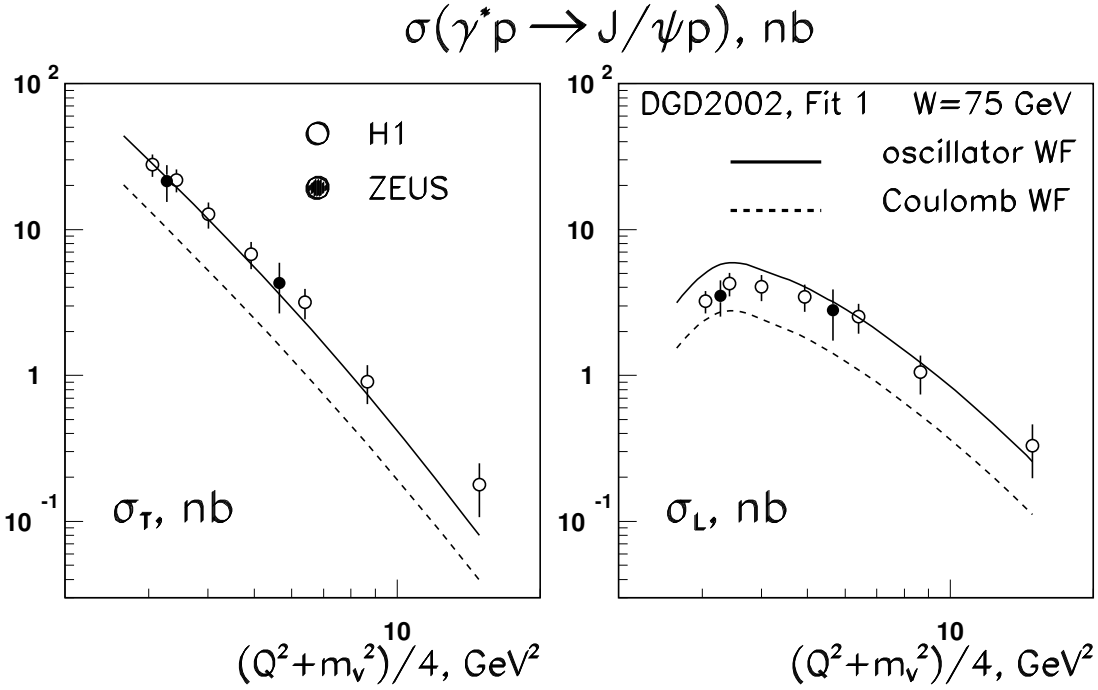

Figure 10.23: *Decomposition of the J/ψ production cross sections in σ_L and σ_T.*

help distinguish between various models of the vector meson structure.

The t-dependence of the $2S$ state production also shows remarkable features originating from the node effect. Fig. 10.28 shows how the t-profile of the differential cross section changes over a narrow Q^2 region. The strongest cancellation, due to the node effect, takes place at $Q^2 = 0\,, |t| = 0$. When we increase $|t|$ or Q^2 the strength of the cancellation diminishes and the differential cross section grows.

Finally, in Fig. 10.29 we show the spin-angular density matrix for the $1S$, $2S$, and D states in the ρ system. A dramatic difference among the Q^2 profiles in both the SCHC and SCHNC matrix elements is seen. Note that some of the matrix elements are even of opposite sign for S and D wave states.

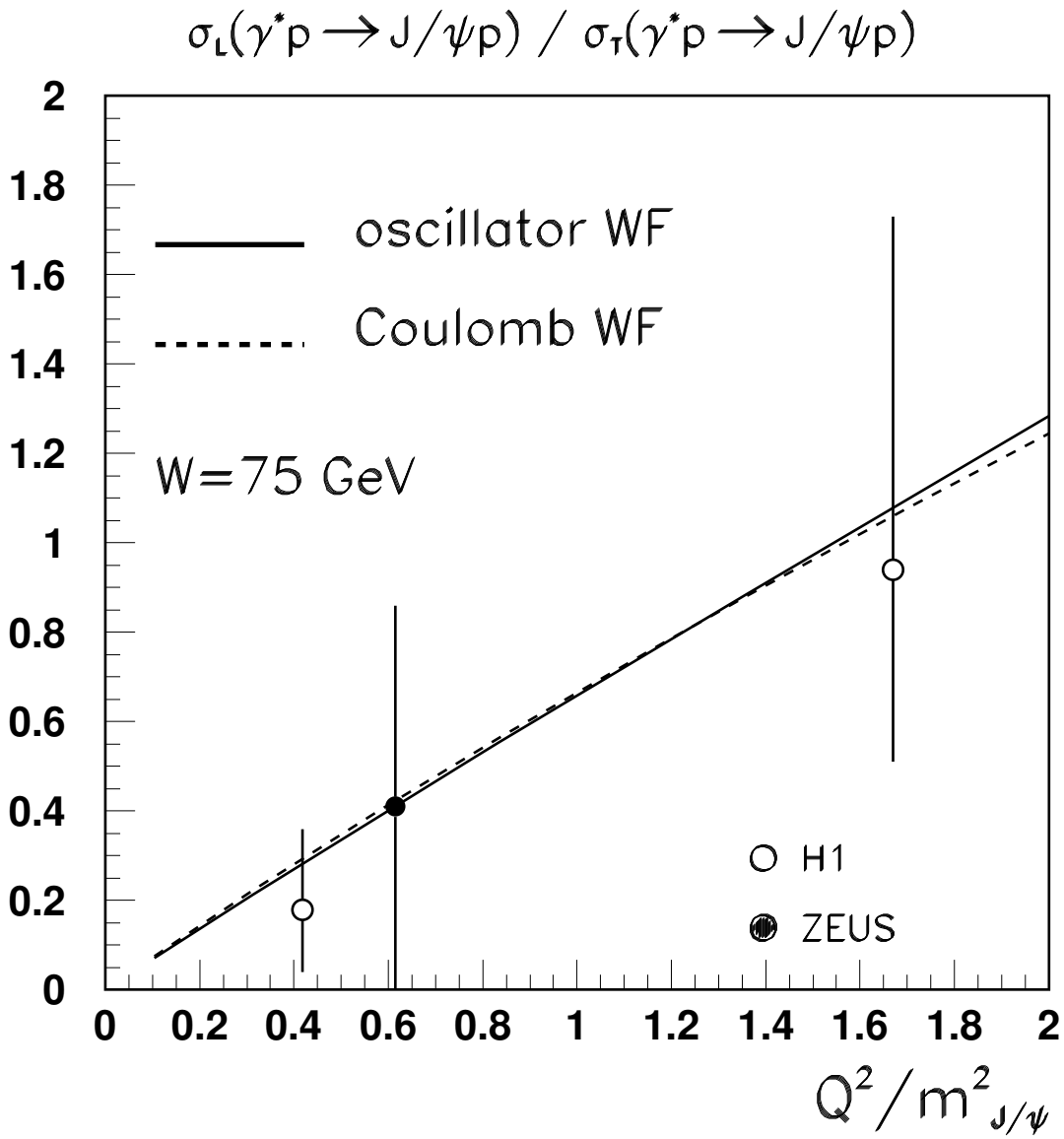

Figure 10.24: *The ratio $R = \sigma_L/\sigma_T$ as a function of Q^2 for J/ψ meson production as a function of Q^2. Solid and dashed lines correspond to oscillator and suppressed Coulomb wave functions, respectively.*

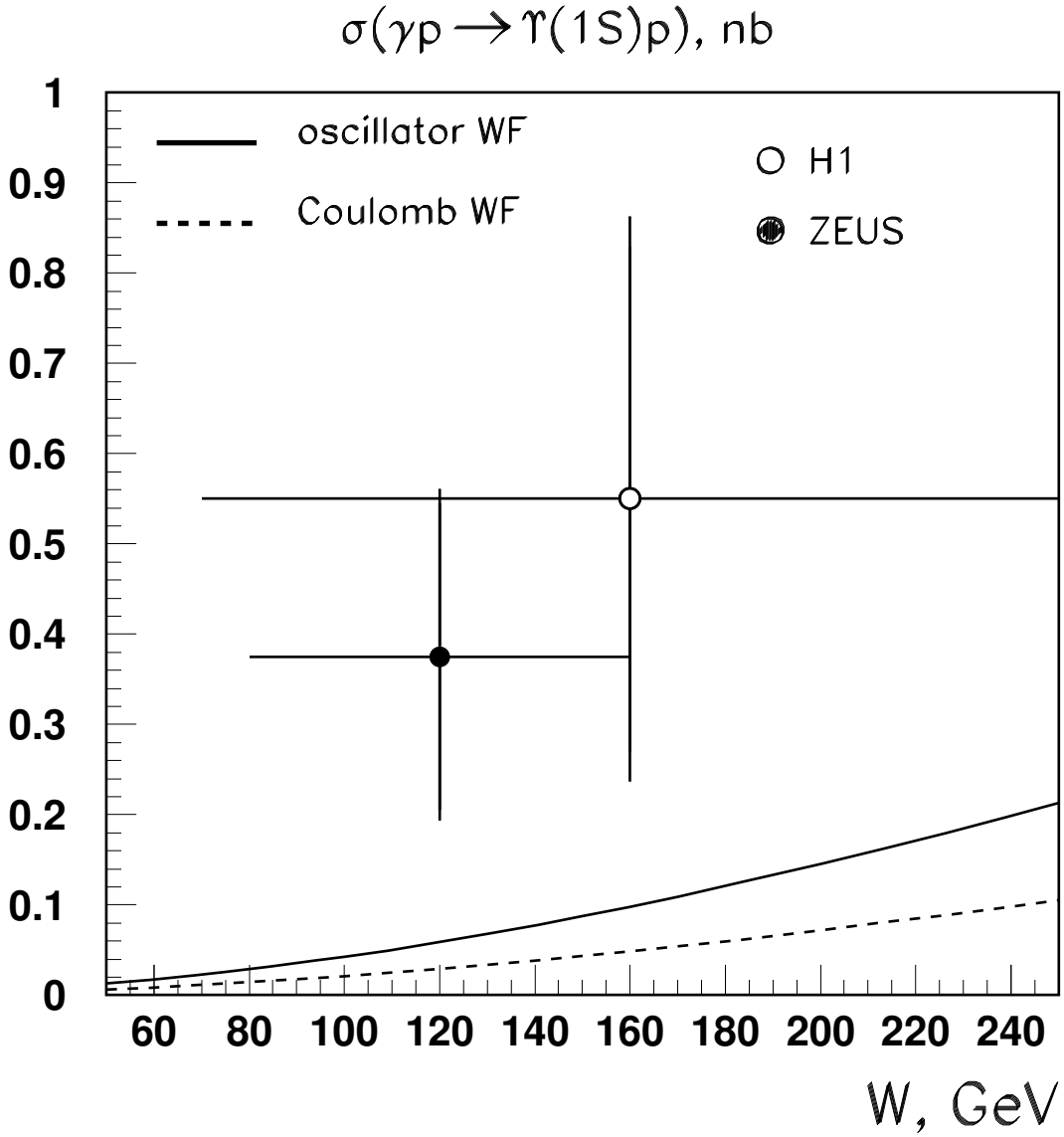

Figure 10.25: *The energy dependence of the total $\Upsilon(1S)$ meson photoproduction cross section. The k_t-factorization predictions based on oscillator (solid lines) and suppressed Coulomb (dashed lines) wave functions are also shown. All calculations were performed for $W = 75$ GeV using DGD2002, Fit 1.*

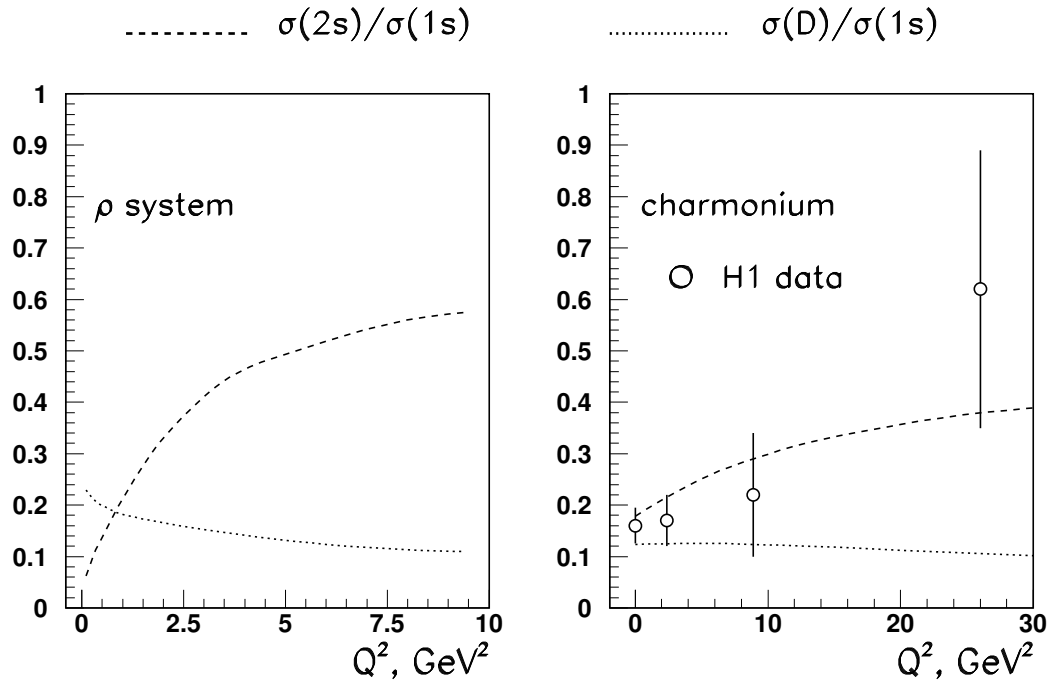

Figure 10.26: *The Q^2 behavior of the ratio of excited to ground state vector meson production cross sections for ρ and charmonium systems. Dashed and dotted lines represent $\sigma(2S)/\sigma(1S)$ and $\sigma(D)/\sigma(1S)$ ratios, respectively. In all calculations, the oscillator wave function was used.*

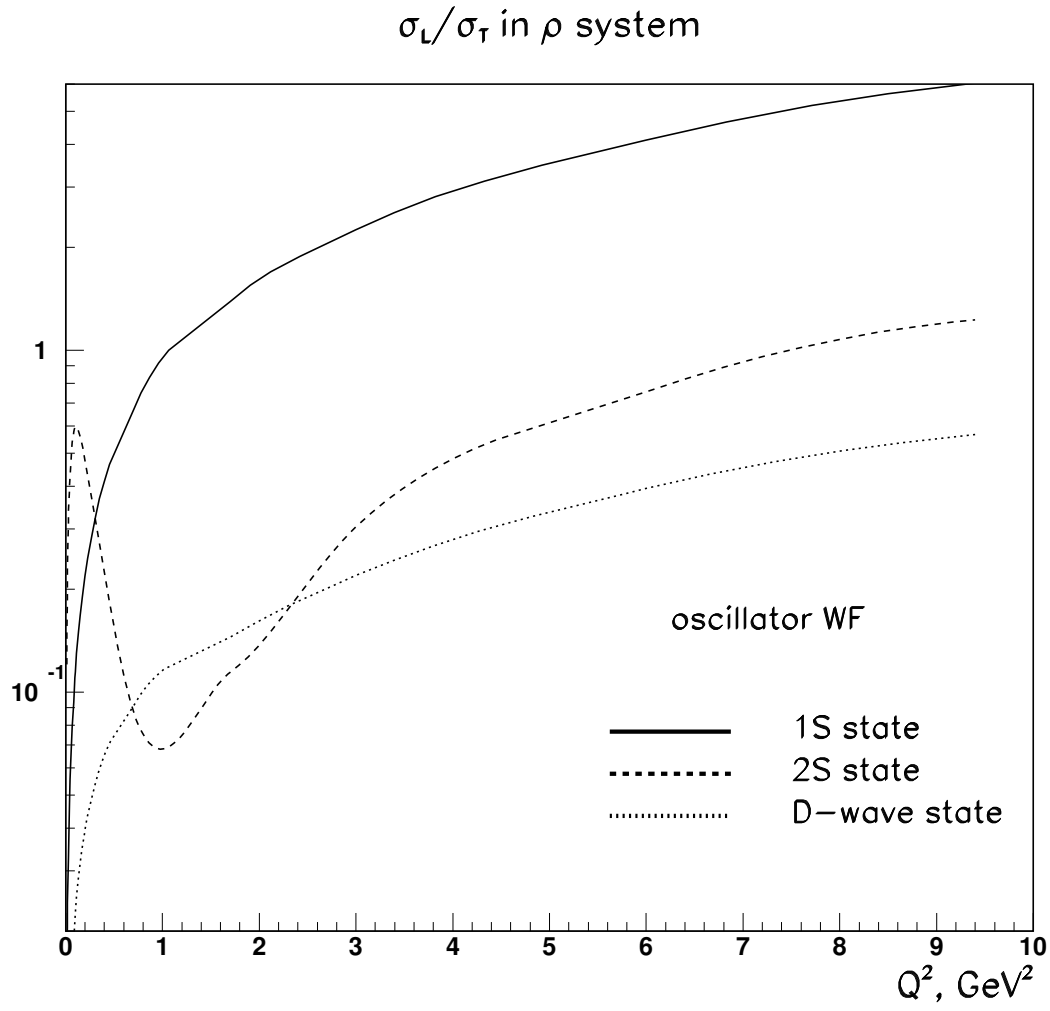

Figure 10.27: *The Q^2 behavior of the σ_L/σ_T ratio for $1S$ (solid line), $2S$ (dashed line) and D wave (dotted line) states in the ρ system. In all calculations, the oscillator wave function was used.*

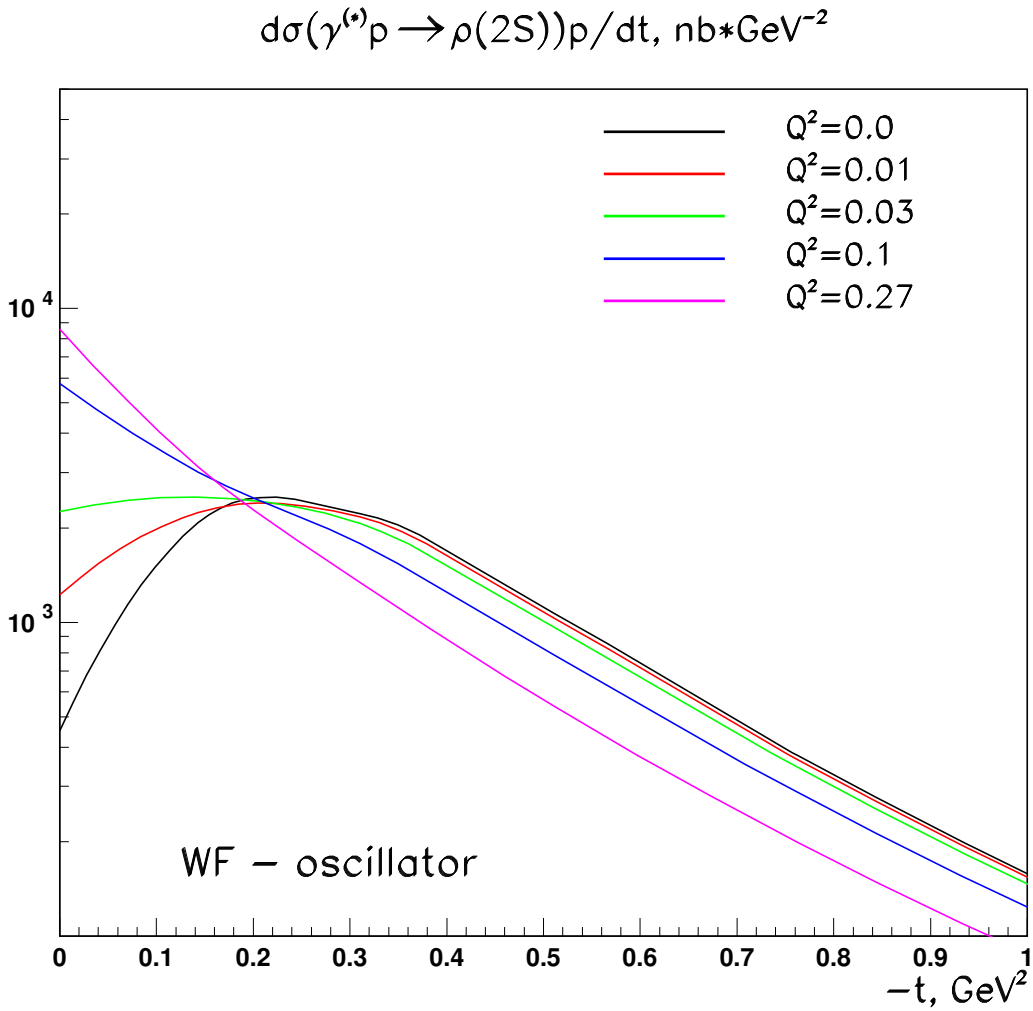

Figure 10.28: *Strong forward dip for 2S state in ρ system: the change in t profile of the differential cross section within a narrow Q^2 region.*

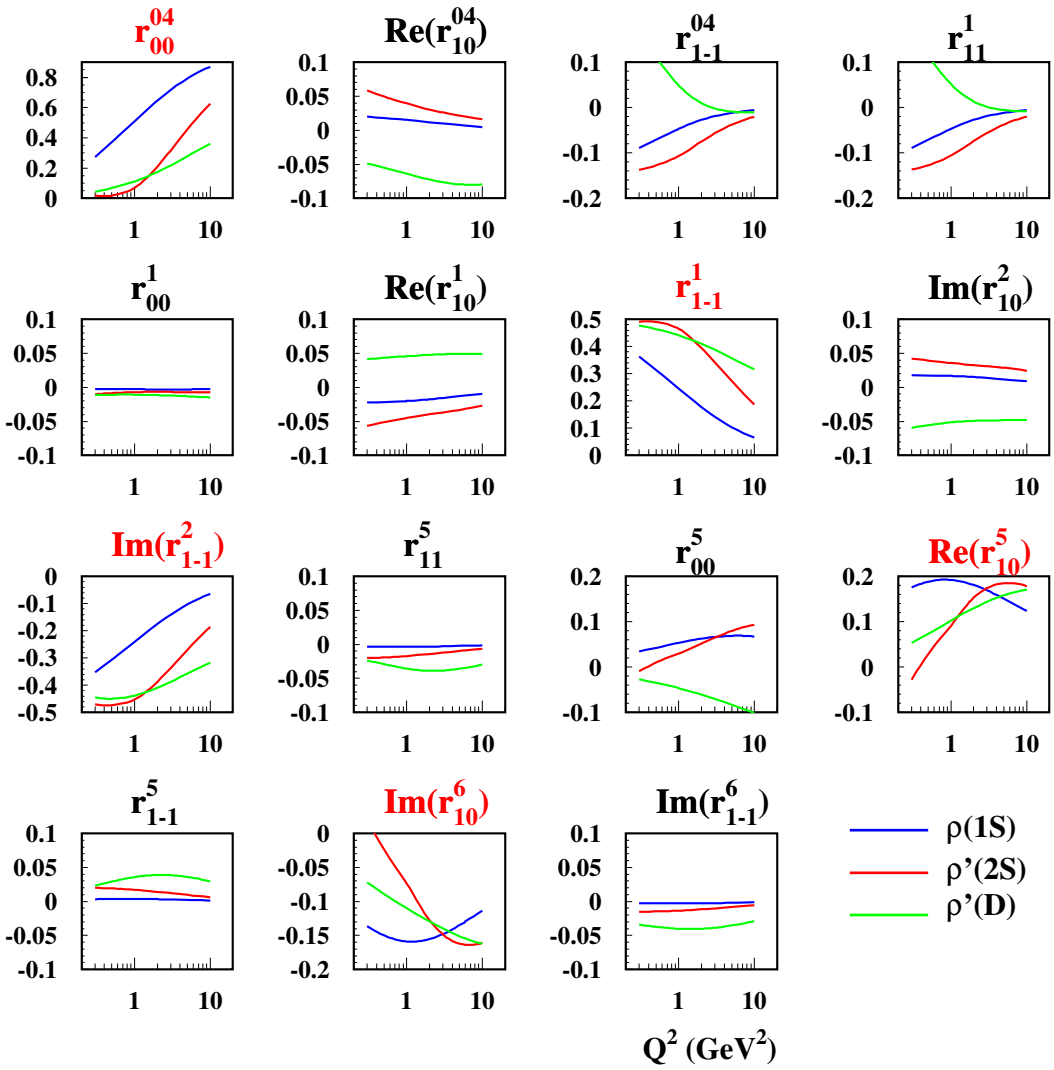

Figure 10.29: *The Q^2 behavior of the spin ensity matrix for $1S$, $2S$, and D wave states in the ρ system.*

Chapter 11

The σ_T puzzle

The detailed comparison of the numerical results for ρ meson production obtained in the k_t-factorization approach with the experimental data shows that the scheme used fails to reproduce the correct Q^2 behavior of the transverse cross section σ_T, which was dubbed by us the σ_T puzzle. In this chapter we explore two possible causes of this mismatch. Namely we explore the effect of color Coulomb interaction of a $q\bar{q}$ pair and show that it leads to an increase of σ_T with respect to σ_L. We then analyze the issue of possible S/D wave mixing in the ρ system and try to obtain a better description of σ_L/σ_T.

As we will see, the first method might turn out to be the remedy for the σ_T puzzle, but even an accurate formulation of this method forces us to go beyond the lowest Fock state, thus making only rough estimates of the effect possible. The second mechanism will be shown, indeed, to decrease the σ_L/σ_T ratio at higher Q^2 to acceptable values, but this happens at the expense of too low values of σ_L, rather than increased values of σ_T. Therefore, this mechanism does not provide the solution to the σ_T puzzle, at least in its pure form.

11.1 The Coulomb tail of the wave function

As we discussed before, the major source of ambiguity in our approach is the vector meson wave function. Without accurate knowledge of the radial wave function, one is limited to an educated guess.

In our treatment we used to the soft wave function Ansatz everywhere; that is, we assumed that any integral involving the wave function would be saturated by the small-p region ($|\boldsymbol{p}| \sim 1/R_V$). This implies that at large p the wave function must vanish fast enough, or to be precise, faster than any $\boldsymbol{p}^2$ power present in numerators of the above formulas. Since the highest momentum power is $\vec{k}^2$, which appears, for instance, in the transverse amplitudes, we conclude that the "softness" of the wave function means that

$$\psi(z,\vec{k})|_{\vec{k}^2\to\infty} = o\left(\frac{1}{\vec{k}^4}\right) . \tag{11.1}$$

The Gaussian wave function Ansatz used everywhere above certainly satisfies this requirement.

It turns out, however, that the above requirement is violated when the true short-range Coulomb-like interquark potential is taken into account. As is well-known, if the color Coulomb potential were the only source of the quark-antiquark interaction, the resulting Coulomb-type

wave function of the vector meson would look like

$$\psi(\boldsymbol{p}) \propto \frac{1}{(\boldsymbol{p}^2 + a^2)^2}. \tag{11.2}$$

In reality, the interquark forces are much more complicated. However, without any need to know the precise form of interquark forces, one can assert that at short distances there must be some resemblance of the Coulomb-like high-$\boldsymbol{p}^2$ tail.

11.1.1 The strategy

There is certainly a multitude of approaches that claim to account for the color Coulomb interaction at short distances. One of them would consist in obtaining an accurate numeric solution of a given potential model. If one prefers to used a fully QFT-based approach, one must deal then with a set of diagrams. Ideally, one should start with free quarks and then, by taking their interaction into account, arrive at the physical vector meson with a (presumably) uniquely defined $q\bar{q}$ wave function.

Realizing such a program is still an unresolved task, and attempts to accomplish it would certainly go far beyond this study. Moreover, even if we were capable of doing it, we would still run into interpretational difficulties, at least in the framework of our scheme. Indeed, when calculating the diagrams we will see the higher Fock states intrude into our $q\bar{q}$ description of the vector meson. Even if we still wanted to follow only quark-antiquark distribution in a meson, we will be forced to switch from the wave function to the density matrix description. Another problem would be the presence of higher angular momenta of the $q\bar{q}$ pair due to gluon radiation. This will leave no room for our simple S wave/D wave description of the vector meson. Finally, the $q\bar{q}$ wave function (or density matrix) will have no unique, process-independent definition. Indeed, in order to preserve the gauge invariance at any given order of perturbation theory, we will have to include corrections to the rest of a diagram (the kernel) as well as corrections that entangle the kernel with the wave function. As a result, the two-particle irreducibility of the process will be lost.

The conclusion is that we cannot expect a reasonable answer to the question of how to account for short range Coulomb interaction and still stay within the framework of our approach.

Nevertheless, the mere formulation of this question does not force us to go beyond our lowest Fock state, two-particle-irreducible approach. Our procedure can be justified by arguing that the Coulomb tail of the wave function must be there. Given that, can we develop a reasonable understanding of its impact on dynamics of the vector meson production? In this formulation, we now ask for a QFT-inspired model that would produce an estimate of the hard tail without forcing us to confront the problems just mentioned.

We suggest the following procedure that would satisfy this need. We start with the soft wave function Ansatz and perform an evolution procedure that will generate the hard tail. This evolution will basically consist of allowing for gluon exchange between the quark and the antiquark. The result will be interpreted as the hard piece of the vertex function Γ, and eventually as the hard piece of the wave function itself.

11.1.2 The quantum mechanics of the Coulomb tail

Suppose that our potential is a sum of an oscillator and Coulomb potential, the latter being a "perturbation" and bearing an intrinsic small parameter:

$$V(p) = V_{osc}(p) + V_{coul}(p)\,;$$
$$V_{osc}(p) = -\frac{\mu\omega^2}{2}\cdot\frac{12\pi^2}{p^2}\delta''(p)\,, \quad V_{coul}(p) = -\frac{4\pi}{p^2+\mu_G^2}\alpha_s(p^2)C_F\,. \tag{11.3}$$

Here the coupling constant is supposed to be the small parameter. The effective parameter μ_G accounts for confinement.

The total wave function is represented as sum of the soft part $\psi_s = c\cdot\exp(-k^2a^2/2)$, which is the solution of Schrodinger equation with oscillator potential only, and the hard part ψ_h, determined via:

$$\left(\frac{p^2}{2\mu} - E\right)\psi_h(p) = -\frac{1}{(2\pi)^3}\int dk V_{coul}(k)\psi_s(p-k) \tag{11.4}$$

Let's for a moment neglect running of the coupling constant. Then

$$\psi_h(p) = \frac{1}{\frac{p^2}{2\mu}-E}\cdot\frac{4\pi\alpha_s C_F}{(2\pi)^3}\cdot I(p)\,, \tag{11.5}$$

so that

$$\psi(p) = \exp\left(-\frac{k^2a^2}{2}\right) + \frac{1}{\frac{p^2}{2\mu}-E}\cdot\frac{4\pi\alpha_s C_F}{(2\pi)^3}\cdot I(p)\,, \tag{11.6}$$

where

$$\begin{aligned} I(p) &= \int\frac{d^3\vec{k}}{(\boldsymbol{p}-\vec{k})^2+\mu_G^2}\exp\left(-\frac{k^2a^2}{2}\right) = 2\pi\int_0^\infty k^2dk\frac{1}{2pk}\log\left[\frac{(p+k)^2+\mu_G^2}{(p-k)^2+\mu_G^2}\right]\exp\left(-\frac{k^2a^2}{2}\right) \\ &= 2\pi\int_0^\infty\frac{k^2dk}{k^2+\mu_G^2}\frac{e^{-\frac{(k-p)^2a^2}{2}} - e^{-\frac{(k+p)^2a^2}{2}}}{kpa^2}\,. \end{aligned} \tag{11.7}$$

This function cannot be evaluated exactly. One can, however, ask for its asymptotic large-p behavior, which can be evaluated directly from (11.4) by replacing $k \to p-k$ and taking $V_{coul}(p-k) \approx V_{coul}(p)$ out of the integral:

$$\psi_h(p\to\infty) = 4\pi C_F\alpha_s\frac{2\mu}{p^4}\cdot\psi(r=0)\,. \tag{11.8}$$

Note, however, that one should not use this simple analytic form because it spoils the large distance behavior of the wave function. The wave function (11.8), even when regularized as $p^2 \to p^2+\mu_G^2$, leads to exponential decrease of the wave function $\exp(-r\mu_G)$, while the true wave function exhibits gaussian decrease, $\exp(-r^2a^2/2)$.

11.1.3 Derivation of $\Delta\psi_{Coul}$

The diagrammatic representation of this procedure is show in Fig. 11.1. Instead of implementing the soft vertex function Γ^α_{soft}, we use a properly normalized one,

$$\Gamma^\alpha_{total} = \frac{1}{\sqrt{N}}(\Gamma^\alpha_{soft} + \Delta\Gamma^\alpha)\,, \tag{11.9}$$

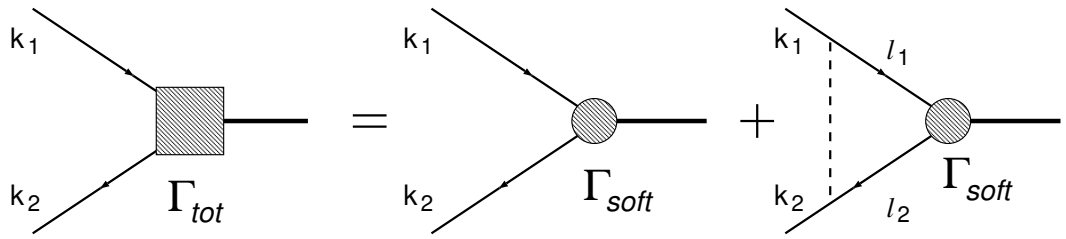

Figure 11.1: *Diagrmmatic representation of the effect of Coulomb tail at small distances*

where $1/\sqrt{N}$ factor accounts for the proper normalization. The Coulomb correction $\Delta\Gamma^\alpha$ is then

$$\Delta\Gamma(z,\vec{k})^\alpha = -i\int\frac{d^4l}{(2\pi)^4}\cdot g^2C_F\cdot\frac{\gamma^\mu(-\hat{l}_2+m)\Gamma^\alpha_{soft}(\hat{l}_1+m)\gamma_\mu}{(l_1^2-m^2+i\varepsilon)(l_2^2-m^2+i\varepsilon)[(k_1-l_1)^2-\mu_G^2+i\varepsilon]}\,. \quad (11.10)$$

The Sudakov decomposition of the momenta of the initial and intermediate particles' reads

$$\begin{aligned} k_1^\mu &= yp'^\mu + zq'^\mu + k_\perp^\mu\,; \\ k_2^\mu &= (1-y)p'^\mu + (1-z)q'^\mu - k_\perp^\mu\,; \\ l_1^\mu &= y'p'^\mu + z'q'^\mu + l_\perp^\mu\,; \\ l_2^\mu &= (1-y')p'^\mu + (1-z')q'^\mu - l_\perp^\mu\,; \\ (k_1-l_1)^\mu &= (y-y')p'^\mu + (z-z')q'^\mu + (k_\perp-l_\perp)^\mu\,. \end{aligned} \quad (11.11)$$

We know from the above analysis that one of the initial particles is on-mass-shell. Therefore, one of the two conditions

$$y=\frac{\vec{k}^2+m^2}{zm_V^2} \quad \text{or} \quad y=1-\frac{\vec{k}^2+m^2}{(1-z)m_V^2}$$

is fulfilled.

The numerator constitutes the most challenging part. Certainly, there is no problem to perform gluon index summation:

$$-\gamma^\mu(-\hat{l}_2+m)\gamma^\alpha(\hat{l}_1+m)\gamma_\mu = 2m^2\gamma^\alpha - 2\hat{l}_1\gamma^\alpha\hat{l}_2 - 4(l_1-l_2)^\alpha\,. \quad (11.12)$$

The problem, however, is that this spinorial structure cannot be reduced to the scalar multiplicative renormalization of the original structure γ^α. Moreover, after integration, the spinorial structure cannot be expressed in terms of S and D waves only. Finally, the resulting spinorial structure will lead to gauge non-invariant corrections to the wave function.

In order to go as far as we can in trying to obtain a reasonable estimate for the Coulomb tail and avoid trouble, we propose the following procedure. First, we look at the transverse vector meson production. Since the vector meson polarization vector V^α possesses only transverse components ($\vec{V}^\alpha$), only transverse terms

$$2m^2\vec{\gamma}^\alpha + 2\hat{\vec{l}}\vec{\gamma}^\alpha\hat{\vec{l}} - 2[z'(1-y')\hat{p}'\vec{\gamma}^\alpha\hat{q}' + y'(1-z')\hat{q}'\vec{\gamma}^\alpha\hat{p}'] - 8\vec{l}^\alpha\,. \quad (11.13)$$

will survive from the expression (11.12). Then, in order to simplify matters, we will proceed for the ρ meson as if it were a heavy quarkonium. That is, we will neglect $\vec{l}^2$ in comparison

with m^2 and put $z' = \frac{1}{2}$. Finally, the last stroke is to put $m_V^2 = 4m^2$ in the numerator, so that y' can be replaced by $1/2$ as well. The result of this procedure gives

$$-\gamma^\mu(-\hat{l}_2 + m)\vec{\gamma}^\alpha(\hat{l}_1 + m)\gamma_\mu \to 4m^2\vec{\gamma}^\alpha, . \tag{11.14}$$

Finally, we *postulate* that the same scalar renormalization holds for longitudinal vector mesons as well.

The denominator is calculated in the same way as before. We note that the numerator in our calculation does not depend on y'; the pole structure on the y' plane comes from the propagators only. The position of poles, however, changes with z': at $z' < 0$ or $z' > 1$ all poles lie in the same half-plane, and thus by closing the contour we can nullify the contribution of these z' regions to the integral. The interval $0 < z' < 1$ then naturally breaks into two parts: $z' < z$ and $z' > z$. In the former region we prefer to close the contour from below and take the residue at the position of pole 1. The two other propagators become

$$\begin{aligned} \text{pole 2} &\to (1-z')(m_V^2 - M'^2) + i\varepsilon\,; \\ \text{pole 3} &\to (z-z')\left(ym_V^2 - \frac{\vec{l}^2 + m^2}{z'}\right) - (\vec{k}-\vec{l})^2 - \mu_G^2 + i\varepsilon\,. \end{aligned} \tag{11.15}$$

In the second z' region we close the contour from above and take residue at $y' = 1 - (\vec{l}^2 + m^2)/[(1-z')m_V^2]$, so that the other poles become

$$\begin{aligned} \text{pole 1} &\to z'(m_V^2 - M'^2) + i\varepsilon\,; \\ \text{pole 3} &\to -(z'-z)(M'^2 - m_V^2) - (z'-z)\left(ym_V^2 - \frac{\vec{l}^2 + m^2}{z'}\right) - (\vec{k}-\vec{l})^2 - \mu_G^2 + i\varepsilon\,. \end{aligned} \tag{11.16}$$

Note that in both cases the familiar $M'^2 - m_V^2$ appears in the denominator, which fuses with $\Gamma_{soft}(M'^2)$ to produce $\psi_{soft}(M'^2)$. Thus, the result of the y' integration is

$$\begin{aligned} &\int dy' \frac{\Gamma_{soft}(M'^2)}{(l_1^2 - m^2 + i\varepsilon)(l_2^2 - m^2 + i\varepsilon)[(k_1 - l_1)^2 - \mu_G^2 + i\varepsilon]} \\ &= \theta(z-z')\frac{1}{\Delta_1 + (\vec{k}-\vec{l})^2 + \mu^2} + \theta(z'-z)\frac{1}{\Delta_2 + (\vec{k}-\vec{l})^2 + \mu^2} \end{aligned} \tag{11.17}$$

with

$$\left.\begin{aligned} \Delta_1 &= -(z-z')\left(\tfrac{\vec{k}^2+m^2}{z} - \tfrac{\vec{l}^2+m^2}{z'}\right) \\ \Delta_2 &= (z'-z)\left(\tfrac{\vec{k}^2+m^2}{z} - \tfrac{\vec{l}^2+m^2}{z'}\right) + (z'-z)(M'^2 - m_V^2) \end{aligned}\right\} \quad k_1 \text{ on-mass-shell;}$$

$$\left.\begin{aligned} \Delta_1 &= (z-z')\left(\tfrac{\vec{k}^2+m^2}{1-z} - \tfrac{\vec{l}^2+m^2}{1-z'}\right) + (z'-z)(M'^2 - m_V^2) \\ \Delta_2 &= -(z'-z)\left(\tfrac{\vec{k}^2+m^2}{1-z} - \tfrac{\vec{l}^2+m^2}{1-z'}\right) \end{aligned}\right\} \quad k_2 \text{ on-mass-shell.}$$

The analysis of the positive definiteness of the gluon propagator reveals that in one case the positiveness indeed holds due to the inequality

$$-\frac{z-z'}{z}\vec{k}^2 + \frac{z-z'}{z'}\vec{l}^2 + (\vec{k}-\vec{l})^2 = \left(\sqrt{\frac{z'}{z}}\vec{k} - \sqrt{\frac{z}{z'}}\vec{l}\right)^2 > 0\,,$$

while in the other case the gluon pole can, in principle, arise in the allowed kinematical region. Such a pole would correspond to the situation in which both quark and gluon are simultaneously on mass shell. However, in the case of ρ mesons such configurations are avoided due to the sufficiently small mass of the vector meson ($m_V^2 < 2\mu_G^2$).

Thus, the expression for $\Delta\Gamma(z,\vec{k})$ takes form

$$\begin{aligned}\Delta\Gamma(z,\vec{k}) &= C_F\frac{\alpha_s(\vec{k}^2)}{4\pi^2}\,4m^2\int\frac{dz'}{z'(1-z')}d^2\vec{l}\,\psi_{soft}(M'^2)\\ &\times\left[\theta(z-z')\frac{1}{\Delta_1+(\vec{k}-\vec{l})^2+\mu^2}+\theta(z'-z)\frac{1}{\Delta_2+(\vec{k}-\vec{l})^2+\mu^2}\right]. \quad (11.18)\end{aligned}$$

With $\Delta\Gamma(z,\vec{k})$ calculated according to (11.10), we can now construct the hard part of the wave function $\psi(z,\vec{k})$. However the straightforward answer, $\delta\psi = \Delta\Gamma/(M^2-m_V^2)$, will not be a satisfactory option due to the unphysical pole at $M^2 = m_V^2$. We remember that when constructing the soft wave function we forced the corresponding vertex function Γ_{soft} to have zero at $M^2 = m_V^2$ in order to cancel the unphysical pole. Here we do not have such freedom in manipulation with $\Delta\Gamma$, which is, by the way, always positive. However, we can again tune the *soft* vertex function Γ_{soft} so that the entire expression $\Gamma_{soft}+\Delta\Gamma$ does have zero at the required point. This can be achieved by shifting the node position of the soft vertex function

$$\Gamma_{soft}(z,\vec{k}^2)\to\psi_{soft}(M^2)\left[M^2-m_V^2-\frac{\Delta\Gamma(z,\vec{k}_0^2)}{\psi_{soft}(m_V^2)}\right], \quad (11.19)$$

where $\frac{k_0^2+m^2}{z(1-z)} = m_V^2$. The total wave function then becomes

$$\begin{aligned}\psi_{total}(z,\vec{k}^2) &= \frac{\psi_{soft}(M^2)\left[M^2-m_V^2-\frac{\Delta\Gamma(z,\vec{k}_0^2)}{\psi_{soft}(m_V^2)}\right]+\Delta\Gamma(z,\vec{k}^2)}{M^2-m_V^2}\\ &= \psi_{soft}(M^2)+\frac{1}{M^2-m_V^2}\left[\Delta\Gamma(z,\vec{k}^2)-\Delta\Gamma(z,\vec{k}_0^2)\frac{\psi_{soft}(M^2)}{\psi_{soft}(m_V^2)}\right]. \quad (11.20)\end{aligned}$$

The wave function constructed in this manner is regular at $M^2 = m_V^2$ and has the expected large M^2 behavior.

11.1.4 The large Q^2 asymptotics of σ_T: analytical result

The integration in (11.18) cannot be done analytically but, in order to grasp the asymptotics, a simple estimate can be performed.

For $\vec{k}^2 \gg \vec{l}^2,\ \mu_G^2,\ m^2$ the denominators turn into $\vec{k}^2z'/z$ and $\vec{k}^2(1-z')/(1-z)$ for on-mass-shell initial quarks 1 or 2, respectively. If we then suppose that the soft wave function is given by the Gaussian Ansatz with $R_V^2m^2 \gg 1$, we can put $z'\to 1/2$ and do the integration completely. The answer reads

$$\Delta\Gamma(z,\vec{k}^2) = C_F\frac{\alpha_s(\vec{k}^2)}{\pi^2}\cdot m^2\frac{2}{m}\frac{2z}{\vec{k}^2}\cdot\int d^3\boldsymbol{l}\,\psi_{soft}(M'^2) = \frac{z}{\vec{k}^2}\,C_F\frac{\alpha_s(\vec{k}^2)}{\pi^2}\cdot 4ma_\psi\cdot\left(\frac{2\pi}{R_V^2}\right)^{\frac{3}{2}}. \quad (11.21)$$

We see that the hard tail of the wave function $\Delta\Gamma$ falls off as $1/\vec{k}^4$ at large $\vec{k}^2$, in accordance with our expectations.

The Coulomb tail of the vector meson wave function being finally obtained, we are now ready to estimate the expected change in the σ_L/σ_T ratio for high-Q^2 production of ρ mesons. Before we examine the numerical values, let us make an analytical estimate of the Q^2 asymptotics. We plug the hard tail of the wave function $\Delta\psi(z,\vec{k}^2)$ into the leading twist expression for $A_{T\to T}$, which we write as

$$\begin{aligned} ImA_T &= s\frac{c_V\sqrt{4\pi\alpha_{em}}}{4\pi^2}\int\frac{dz}{z(1-z)}d^2\vec{k}\psi_{total}(z,\vec{k}^2)\cdot\int\frac{d^2\vec{\kappa}}{\vec{\kappa}^4}\alpha_s(\vec{\kappa}^2)\mathcal{F}(x_g,\vec{\kappa}^2) \\ &\quad\times\frac{2\vec{\kappa}^2}{[z(1-z)Q^2+\vec{\kappa}^2+\vec{k}^2]^2}\left\{m^2+2[z^2+(1-z)^2]\vec{k}^2\right\} \\ &\approx s\frac{c_V\sqrt{4\pi\alpha_{em}}}{4\pi^2}\cdot 2\pi\alpha(\overline{Q}^2)G(\overline{Q}^2)\cdot\mathcal{J}_{total}(Q^2)\,. \end{aligned} \tag{11.22}$$

The integral

$$\mathcal{J}_{total}(Q^2)\equiv\int_0^1\frac{dz}{z(1-z)}d^2\vec{k}\psi_{total}(z,\vec{k}^2)\frac{m^2+2[z^2+(1-z)^2]\vec{k}^2}{[z(1-z)Q^2+\vec{\kappa}^2+\vec{k}^2]^2}$$

is naturally split into $\mathcal{J}_{soft}(Q^2)$ and $\mathcal{J}_{hard}(Q^2)$. The former is calculated in the heavy-quarkonium approximation with a Gaussian wave function and yields

$$\mathcal{J}_{soft}(Q^2)=\int\frac{4}{m_V}d^3\vec{k}\psi_{soft}\frac{4m_V^2}{Q^4}=\frac{16m_V}{Q^4}a_\psi\cdot\left(\frac{2\pi}{R_V^2}\right)^{\frac{3}{2}}. \tag{11.23}$$

The hard piece is calculated as

$$\begin{aligned} \mathcal{J}_{hard}(Q^2) &= \int_0^1\frac{dz}{z(1-z)}\,\pi\int_{\mu^2}^{z(1-z)Q^2}d\vec{k}^2\frac{32[z^2+(1-z)^2]\vec{k}^2}{Q^4}\cdot\frac{z(1-z)}{\vec{k}^2} \\ &\quad\times\frac{1}{2\vec{k}^2}\,C_F\frac{\alpha_s(\vec{k}^2)}{\pi^2}\cdot 2m_Va_\psi\cdot\left(\frac{2\pi}{R_V^2}\right)^{\frac{3}{2}} \\ &= 2m_Va_\psi\cdot\left(\frac{2\pi}{R_V^2}\right)^{\frac{3}{2}}\cdot\frac{C_F}{\pi}\frac{16}{Q^4}\cdot\int_0^1 dz[z^2+(1-z)^2]\cdot\int_{\mu^2}^{Q^2/4}\frac{d\vec{k}^2}{\vec{k}^2}\alpha_s(\vec{k}^2) \end{aligned} \tag{11.24}$$

The ratio A_{hard}/A_{soft} is then

$$\frac{A_{hard}(Q^2)}{A_{soft}(Q^2)}=\frac{4C_F}{3\pi}\cdot\int_{\mu^2}^{Q^2/4}\frac{d\vec{k}^2}{\vec{k}^2}\alpha_s(\vec{k}^2)=\frac{64}{81}\log\left[\frac{\alpha_s(\mu^2)}{\alpha_s(\frac{1}{4}Q^2)}\right]. \tag{11.25}$$

This expression represents the asymptotic large-Q^2 behavior of the A_{hard}/A_{soft} ratio. As could be expected, it is governed by $\log\left[\frac{\alpha_s(\mu^2)}{\alpha_s(\frac{1}{4}Q^2)}\right]$, which rises with Q^2 growth, but extremely slowly. Within the experimentally studied region of Q^2 (not higher than 100 GeV^2), this logarithm, which is supposed to be large, is still less than unity ($\sim 0.5\div 0.7$). This indicates that the asymptotic regime is not reached at HERA, and the estimate just derived seems to

be irrelevant to the real magnitude of the hard tail effects. Nevertheless, this estimate tells us that no abnormal suppression factors appear in our problem.

The numerical analysis of the Coulomb tail impact on the production amplitudes will be given elsewhere.

11.2 The S/D wave mixing

The presence of tensor forces in two-fermion bound states is a natural consequence of relativistic corrections. They lead to mixing of states with definite angular momentum, which in the case of a vector particle translates into S wave – D wave mixing.

The most famous example is provided by the Breit potential in a hydrogen atom. Such forces are present in a deuteron, where they lead to about 5% admixture of D wave, and they can be present in vector meosns as well. Review [89] provides further examples.

How are we going to mix S and D waves? When calculating the normalization or decay constant for a vector meson, we observed a two-fold dependence on the vector meson state: in the spinorial structure and in the particular form of the radial wave function. In all cases, the rest was insensitive to the vector meson state. Therefore, the two quantities we should mix are $\mathcal{S}_\mu\psi_S(\mathbf{p}^2)$ and $\mathcal{D}_\mu\psi_D(\mathbf{p}^2)$:

$$|\Gamma_\mu\psi(\mathbf{p}^2)\rangle = |\mathcal{S}_\mu\psi_S(\mathbf{p}^2)\rangle\cos\theta + |\mathcal{D}_\mu\psi_D(\mathbf{p}^2)\sin\theta\rangle\,. \tag{11.26}$$

If mixing angle θ is constant, then this vector meson state automatically satisfies the normalization condition,

$$\langle\Gamma_\mu\psi|\Gamma_\nu\psi\rangle = \langle\mathcal{S}_\mu\psi_S|\mathcal{S}_\nu\psi_S\rangle\cos^2\theta + \langle\mathcal{D}_\mu\psi_D|\mathcal{D}_\nu\psi_D\rangle\sin^2\theta = g_{\mu\nu}\,. \tag{11.27}$$

There can be several types of S/D mixing. First, we can mix D state with $1S$, $2S$ or even higher S states. It is not clear *a priori* which mixing should be stronger. Therefore, in our analysis below, we accounted for possible $1S/D$ and $2S/D$ mixing on equal footing. Second, the mixing angle θ can be an explicit function of $\mathbf{p}^2$. This case is a bit more complicated but nothing seems to rule out such possibility.

11.2.1 Constructing the γ_μ vertex

The first issue we wish to elaborate is how to construct the γ_μ vertex from accurate $\mathcal{S}_\mu$ and $\mathcal{D}_\mu$ spinorial structures. This question arises when one tries to check how the naive $\bar{u}\gamma_\mu u$ treatment of the quark-antiquark-vector meson vertex differs from the accurate one. To do so, in the expression

$$\Gamma_\mu\psi(\mathbf{p}^2) = \left(\gamma_\mu - \frac{2p_\mu}{M+2m}\right)\psi_S(\mathbf{p}^2)\cos\theta(\mathbf{p}^2) + \left(\mathbf{p}^2\gamma_\mu + (M+m)p_\mu\right)\psi_D(\mathbf{p}^2)\sin\theta(\mathbf{p}^2)\,, \tag{11.28}$$

all terms with p_μ must be banished by properly adjusting mixing angle $\theta = \theta(\mathbf{p}^2)$. Assuming for simplicity that we use oscillator Ansatz wave functions with all a_i equal, one obtains for $1S/D$ mixing

$$\tan\theta(\mathbf{p}^2) = -\frac{2}{(M+2m)(M+m)}\frac{c_1}{c_D} = -\frac{\sqrt{30}}{(M+2m)(M+m)a^2}\,. \tag{11.29}$$

A very rough estimate for the ρ system gives $\tan\theta \sim 0.2$. For $2S/D$ mixing one has

$$\tan\theta(\mathbf{p}^2) = -\frac{\sqrt{45}\,(1 - 2\mathbf{p}^2 a^2/3)}{(M+2m)(M+m)a^2}\,. \tag{11.30}$$

This time the mixing angle even swings with $\mathbf{p}^2$ growth. After p_μ terms are canceled in (11.28), the residual expression is proportional only to γ_μ and has slightly modified $\mathbf{p}^2$ dependence via the explicitly $\mathbf{p}^2$-dependent mixing angle. However this modification is completely inessential. Moreover, for $2S/D$ mixing, this modification does not shift the position of the node. Therefore, it seems that the impact of this specific mixing on the radial wave function is minimal. The magnitude of this mixing can be also described with only one number — the integrated mixing angle:

$$\tan^2\theta^* = \frac{\langle \sin^2\theta(\mathbf{p}^2)\rangle_D}{\langle \cos^2\theta(\mathbf{p}^2)\rangle_S}\,, \tag{11.31}$$

where $\langle ... \rangle_{S,D}$ mean the normalization integral for S/D state. For $1S/D$ and $2S/D$ types of mixing, $\tan^2\theta^*$ is equal to 0.027 ($\theta^* = 9.3°$) and 0.062 ($\theta^* = 14°$), respectively.

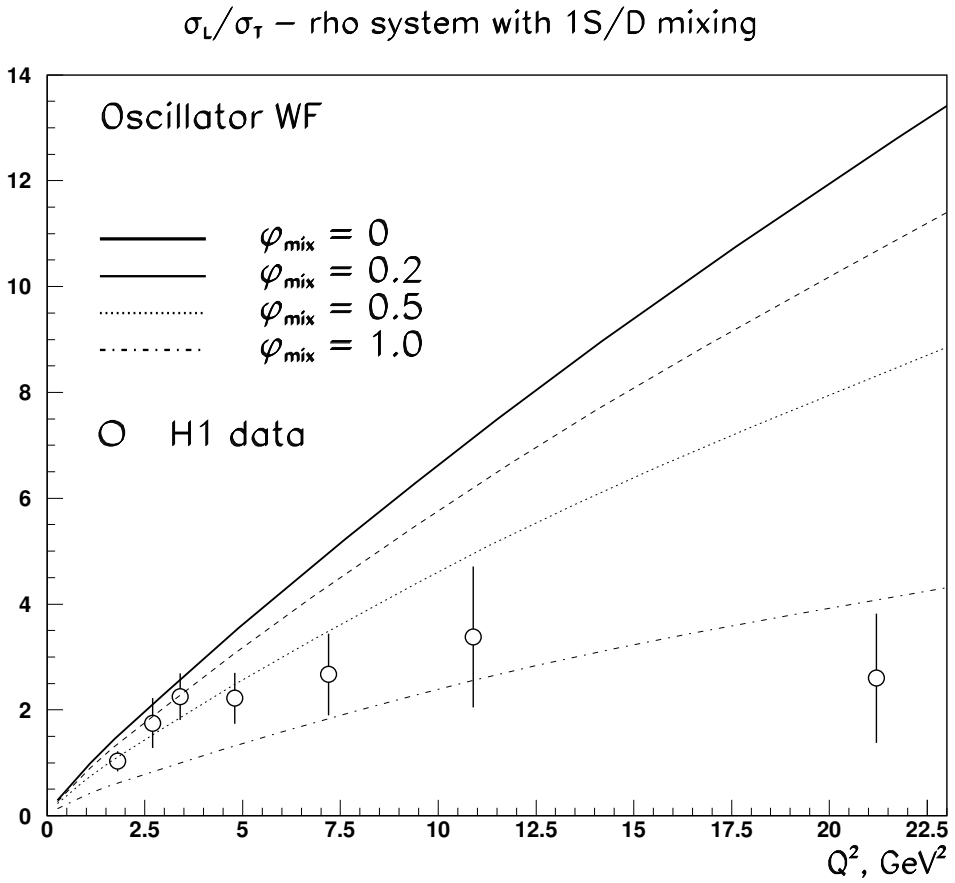

Figure 11.2: *The impact of $1S/D$ mixing in the ρ system on the σ_L/σ_T ratio for the lowest energy state production.*

11.2.2 Impact of S/D wave mixing on ρ meson production

For simplicity, we will restrict ourselves to the constant-angle variant of S/D wave mixing. As our primary motivation here is to check how mixing alters the σ_L/σ_T ratio in ρ production, we will focus only on ρ meson.

Since a generic ρ meson production amplitude is linear in the meson wave function (understood in its complete sense, i.e., spinorial structure times the scalar wave function), one immediately has

$$\mathcal{A}_\rho = \mathcal{A}_S \cos\theta + \mathcal{A}_D \sin\theta \,. \tag{11.32}$$

With this expression in mind we can now predict the effect of S/D wave mixing by simply looking at the pictures for pure S and D wave production.

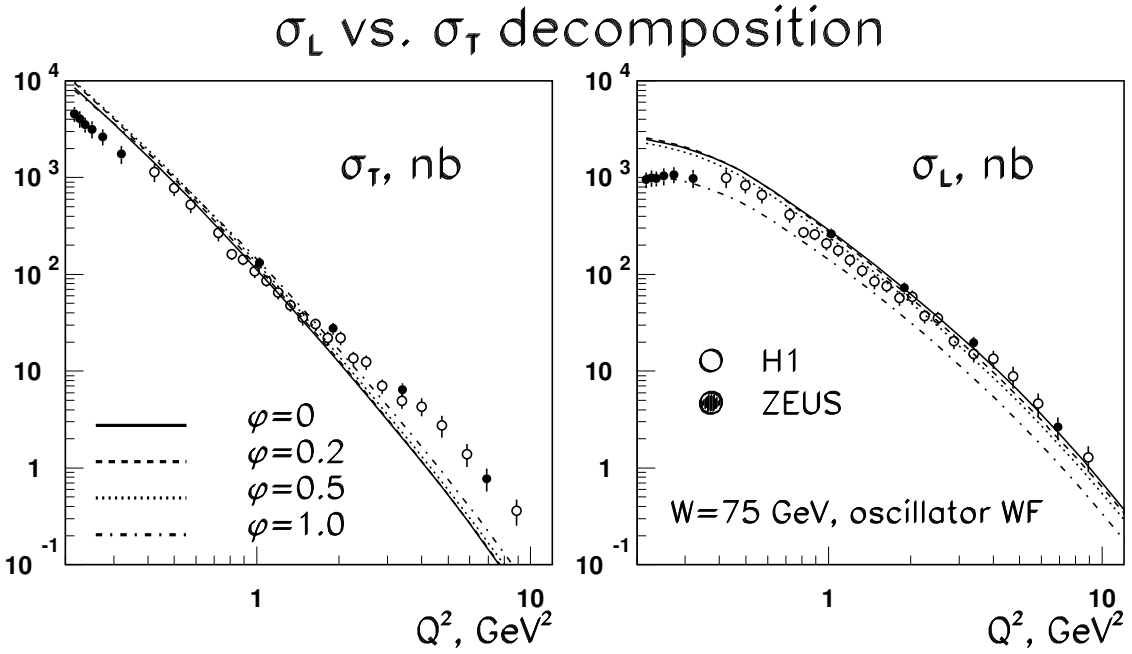

Figure 11.3: *Changes in Q^2 profiles of σ_T and σ_L cross sections for ρ system ground states caused by $1S/D$ mixing.*

Fig. 11.2 and Fig. 11.3 show the changes in the longitudinal and transverse ρ meson cross sections caused by the $1S/D$ mixing. One sees that as $\phi_{mix} > 0$ grows, the ratio σ_L/σ_T decreases. Fig. 11.2 implies that $\phi \sim 0.7$ would do the best job in describing the data points. Note, however, that the shape of σ_L/σ_T ratio remains the same and does not significantly flatten, which would be needed for a better description of the experimental points. Even more problems come from separate analysis of σ_L and σ_T cross sections. One sees that decrease of σ_L/σ_T arises not from making σ_T higher, but at the expense of making σ_L significantly lower than the data. Thus, although the ratio σ_L/σ_T can indeed be corrected in a simple mixing scenario, the cross sections themselves still deviate at large Q^2 from the measured values. This analysis leads us to conclude that the σ_T puzzle in ρ production still persists in our approach.

Although the S/D wave mixing failed to completely resolve the σ_T puzzle, it is still an interesting issue on its own. In constrast to all previous calculations of the vector meson production amplitudes, our approach allows for a clear formulation and detailed analysis of this phenomenon.

Chapter 12

Conclusion

In the present work we formulated the k_t-factorization approach to the calculation of the diffractive production of vector mesons in DIS. Since this approach is organically linked to the BFKL dynamics, no requirements were placed on the value of $Q^2 + m_V^2$, which allowed us to investigate the production cross sections from the photoproduction limit up to the highest Q^2 values attainable in the experiment.

When describing the vector meson, we limited ourselves to the lowest Fock state; that is, we treated a vector meson as a bound state of quark-antiquark pair. Being an approximation, this limitation allowed for the strict construction of the pure S-wave and D-wave states of the $q\bar{q}$ pair sitting inside the meson, which was then applied to the corresponding production amplitudes.

On the other side of the reaction, we related the production amplitudes to the unintegrated gluon structure function of the proton. We undertook an extensive study of the differential gluon density, which included its first-ever extraction from the experiment and detailed investigation of its properties. This was then used in the vector meson production calculations and yielded reliable numerical results.

Here we give a detailed list of main results of the present work.

1. Differential gluon structure function of the proton

   - First-ever extraction of the unintegrated gluon structure function and its casting into the form of simple and ready-to-use parametrizations;
   - detailed analysis of the soft-hard decomposition of various observables and the impact of soft-to-hard diffusion phenomenon on them;
   - observation of self-generated two-reggeon-like structure of F_{2p} predicted by k_t-factorization;
   - showing by means of χ^2 analysis that the high-precision experimental data on F_{2p} suggests rather strong separation of soft and hard parts of the unintegrated gluon density.

2. Diffractive vector meson production: analytical study

   - Developing for the first time a theory for vector meson spin-angular coupling and using it consistently in the derivation of the meson production amplitudes;

- observing remarkably different Q^2-dependence of S and D wave type amplitudes, thus providing a way to discern S and D states that are indistinguishable at e^+e^- colliders;
- observing a dramatic role, at large Q^2, of the higher twist contributions to the D wave vector mesons, which even forced sign change for the $L \to L$ amplitude and led to a non-monotonic σ_L/σ_T ratio;
- observation of very large helicity-violating effects for D wave vector states, which do not get suppressed even in the case of heavy quarkonia;
- confirmation of the soft dominance of the double spin flip amplitude in the case of both S and D wave states;
- establishing the borders of our approach during discussion of the hard Coulomb tail of the wave function.

3. Diffractive vector meson production: numerical study

- Showing that k_t-factorization approach leads to a good overall agreement with availble experimental data on all types of vector mesons. Namely we showed that the overall shape of the Q^2 dependence, energy growth, t-dependence, the picture of s-channel helicity-violation observed in ρ, ϕ, and J/ψ mesons production are in good agreement with k_t-factorization prediction.
- Recognizing that two particular issues — the transverse cross section σ_T for ρ mesons at higher Q^2 and the magnitude of $\Upsilon(1s)$ state — still remain unresolved. The causes of this discrepancy and the resolution possibilities were discussed.
- Predicting many previously unknown features of the excited vector meson production reactions, including opposite signs for the largest spin flip amplitude $T \to L$ for S and D wave vector mesons and dramatically different σ_L/σ_T ratio;
- investigating S/D-mixing induced phenomena; indicating that large S/D wave mixing in the ρ system can be the origin of σ_T puzzle.

Since the work contains a large number of predictions of the observables that have not yet been investigated in experiment, I hope that the thesis will serve as a guide to the directions of future experimental research. The dramatic differences between S and D wave vector meson production predicted in this work demand confirmation and offer a novel way to study the structure of hadrons.

Finally, in this work I intended not merely to list the results, but also give a detailed and pedagogical presentation of all steps. In particular, Part I, where I introduced the k_t-factorization scheme, Chapter 4, where I construct the theory of the vector meson spin-angular coupling, and Appendices contain very detailed intermediate calculations, so that everyone can follow the entire line of derivation. To this end, I hope that the present text can be used as a means of learning as well.

Appendix A

Denominator evaluation: details

Below we give the denominator calculus in full detail. The major guideline in this derivation will be the analysis of the pole positions and setting some of the propagators on-mass-shell by taking appropriate residues.

A.1 The forward Compton scattering

A.1.1 The s-channel diagram: all details

We first start with the forward virtual Compton scattering amplitude. The integral to be calculated is

$$\int dy\ dz\ d\alpha\ d\beta\ \frac{1}{[(q-k)^2-m^2+i\epsilon][k^2-m^2+i\epsilon][k^2-m^2+i\epsilon][(k+\kappa)^2-m^2+i\epsilon]} \frac{1}{[\kappa^2-\mu^2+i\epsilon]^2[(p-\kappa)^2-m^2+i\epsilon]}\,. \tag{A.1}$$

With the Sudakov decomposition

$$q_\mu = q'_\mu - \frac{Q^2}{s}p'_\mu\,,\quad p_\mu = p'_\mu + \frac{m^2}{s}q'_\mu\,,\quad k_\mu = yp_\mu{}' + zq_\mu{}' + \vec{k}_\mu\,,\quad \kappa_\mu = \alpha p_\mu{}' + \beta q_\mu{}' + \vec{\kappa}_\mu\,, \tag{A.2}$$

one can rewrite all 7 propagators as:

$$\begin{aligned}
\langle 1\rangle \qquad & (q-k)^2-m^2+i\epsilon = \left(-y-\frac{Q^2}{s}\right)(1-z)s - (\vec{k}^2+m^2)+i\epsilon\,,\\
\langle 2\rangle,\langle 4\rangle \qquad & k^2-m^2+i\epsilon = yzs-(\vec{k}^2+m^2)+i\epsilon\,,\\
\langle 3\rangle \qquad & (k+\kappa)^2-m^2+i\epsilon = (y+\alpha)(z+\beta)s-[(\vec{k}+\vec{\kappa})^2+m^2]+i\epsilon\,,\\
\langle 5\rangle,\langle 6\rangle \qquad & \kappa^2-\mu^2+i\epsilon = \alpha\beta s-(\vec{\kappa}^2+\mu^2)+i\epsilon\,,\\
\langle 7\rangle \qquad & (p-\kappa)^2-m^2+i\epsilon = (1-\alpha)\left(\frac{m^2}{s}-\beta\right)s-(\vec{\kappa}^2+m^2)+i\epsilon\,.
\end{aligned}$$

Let us analyze the position of propagator poles (namely the sign of $i\epsilon$) in complex y plane for different values of z and β. We get

$$\begin{aligned}
\langle 1\rangle \qquad & y = -\frac{Q^2}{s} - \frac{\vec{k}^2+m^2}{(1-z)s} + \frac{i\epsilon}{1-z}\,; \\
\langle 2\rangle, \langle 4\rangle \quad & y = \frac{\vec{k}^2+m^2}{zs} - \frac{i\epsilon}{z}\,; \\
\langle 3\rangle \qquad & y = -\alpha + \frac{(\vec{k}+\vec{\kappa})^2+m^2}{(\beta+z)s} - \frac{i\epsilon}{z+\beta}\,.
\end{aligned} \tag{A.3}$$

For the poles on α plane we get

$$\begin{aligned}
\langle 3\rangle \qquad & \alpha = -y + \frac{(\vec{k}+\vec{\kappa})^2+m^2}{(\beta+z)s} - \frac{i\epsilon}{z+\beta}\,; \\
\langle 5\rangle, \langle 6\rangle \quad & \alpha = \frac{\vec{\kappa}^2+\mu^2}{\beta s} - \frac{i\epsilon}{\beta}\,; \\
\langle 7\rangle \qquad & \alpha = 1 + \frac{\vec{\kappa}^2+m^2}{\beta s - m^2} - \frac{i\epsilon}{\beta - m^2/s}\,.
\end{aligned} \tag{A.4}$$

Since the function we integrate — namely the product of propagators — is analytic and decreases at large $|y|$ and large $|\alpha|$ sufficiently fast, we can switch from $(-\infty,+\infty)$ integration to the contour integration both on y and α complex planes. This is done by adding half-circle of infinite radius either on the upper or on the lower half planes. What we now have to done is just to trace how many poles we have inside the contours.

As seen from (A.3) and (A.4), the position of the poles on y and α planes depends on the values of z and β. If these are such that no poles fall inside the contours, the integral turns zero, and corresponding (z,β) region does not contribute to the total integral. Therefore, our task now transforms into searching for such (z,β) regions that both y and α contour integrations are non-zero.

A convenient way to perform this analysis is to do it graphically. Fig. A.1 illustrates the sign of $i\epsilon$ in $y = \ldots \pm i\epsilon$ (left panel) and $\alpha = \ldots \pm i\epsilon$ (right panel) for all values of (z,β). Each shaded line here corresponds to a propagator from (A.3) and (A.4), the shaded side indicating the half plane with positive value of $i\epsilon$. For example, propagator $\langle 1\rangle$ from (A.3) has positive $i\epsilon$ when $z < 1$.

If we now take a closer look at each of possible regions (z,β), we see that the only (z,β) pairs that result in a non-zero expression lie inside a triangle, which is shown in Fig. A.2. For convenience, we break up the whole area into three sub-regions A, B, and C. For each of these regions, we get only one pole inside y and one pole inside α contours:

$$\begin{aligned}
&\text{Region A:} \quad \left\{ \begin{array}{c} 0<z<1 \\ -z<\beta<0 \end{array} \right\} \qquad \text{pole } \langle 1\rangle \text{ for } y\text{; pole } \langle 3\rangle \text{ for } \alpha. \\
&\text{Region B:} \quad \left\{ \begin{array}{c} 0<z<1 \\ 0<\beta<m^2/s \end{array} \right\} \qquad \text{pole } \langle 1\rangle \text{ for } y\text{; pole } \langle 7\rangle \text{ for } \alpha. \\
&\text{Region C:} \quad \left\{ \begin{array}{c} 0<\beta<m^2/s \\ -\beta<z<0 \end{array} \right\} \qquad \text{pole } \langle 3\rangle \text{ for } y\text{; pole } \langle 7\rangle \text{ for } \alpha.
\end{aligned} \tag{A.5}$$

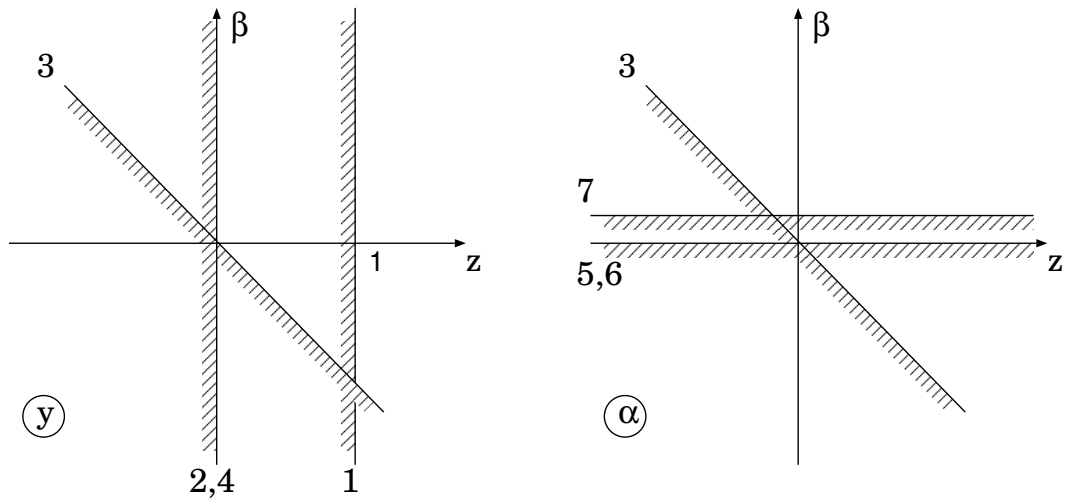

Figure A.1: The $i\epsilon$ signs of the poles in propagators on complex y (left panel) and α (right panel) planes as functions of z and β. At each line, the shaded region indicates (z,β) semiplane where the corresponding $i\epsilon$ sign is positive. The numbers refer to propagators.

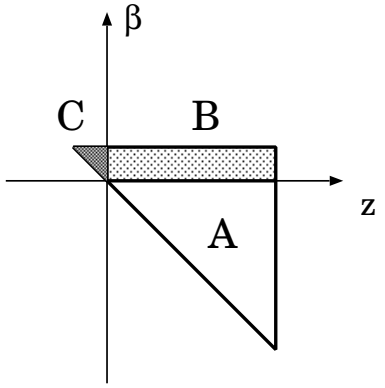

Figure A.2: The three subregions of (z,β) plane that contribute to the overall integral.

Thus, the evaluation of the integrals over y and α turns into taking the residues at certain poles. Let us write the result of this procedure for each of the three regions.

Region A

Here we get

$$y = -\frac{Q^2}{s} - \frac{\vec{k}^2+m^2}{(1-z)s}\,; \quad \alpha = \frac{Q^2}{s} + \frac{\vec{k}^2+m^2}{(1-z)s} + \frac{(\vec{k}+\vec{\kappa})^2+m^2}{(z-|\beta|)}\,. \tag{A.6}$$

Since $\beta<0$, we explicitly switch to a more clear notation $|\beta|$. The other five propagators turn into

$$\langle 2\rangle, \langle 4\rangle \;\to\; -\frac{1}{1-z}[\vec{k}^2+m^2-z(1-z)Q^2]+i\not{\epsilon}\,;$$

$$\langle 5\rangle, \langle 6\rangle \;\to\; -\vec{\kappa}^2-\mu^2-\left[Q^2+\frac{\vec{k}^2+m^2}{1-z}+\frac{(\vec{k}+\vec{\kappa})^2+m^2}{z-|\beta|}\right]+i\not{\epsilon}\,;$$

$$\langle 7\rangle \;\;\to\;\; -\vec{\kappa}^2 - m^2 + \left[s - Q^2 - \frac{\vec{k}^2+m^2}{1-z} - \frac{(\vec{k}+\vec{\kappa})^2+m^2}{z-|\beta|}\right]\left(\frac{m^2}{s}+|\beta|\right) + i\epsilon\,. \quad \text{(A.7)}$$

Here symbol $i\not\epsilon$ means that the rule for pole passing is not needed since the propagator has definite sign for the physical values of the parameters.

The result of the integration is

$$\int dy\; dz\; d\alpha\; d\beta\; \frac{1}{\text{propagators}} = \left(-\frac{2\pi i}{s}\right)^2 \int_0^1 dz \int_0^z d|\beta|\; \frac{1-z}{z-|\beta|}\; \frac{1}{[\vec{k}^2+m^2+z(1-z)Q^2]^2}$$
$$\times \frac{1}{\left\{\vec{\kappa}^2+\mu^2+|\beta|\left[Q^2+\frac{\vec{k}^2+m^2}{1-z}+\frac{(\vec{k}+\vec{\kappa})^2+m^2}{z-|\beta|}\right]\right\}^2}$$
$$\times \frac{1}{\vec{\kappa}^2+m^2-(m^2+|\beta|s)\left[1-\frac{Q^2}{s}-\frac{\vec{k}^2+m^2}{1-z}-\frac{(\vec{k}+\vec{\kappa})^2+m^2}{z-|\beta|}\right]-i\epsilon}\,. \quad \text{(A.8)}$$

Now comes the last step. The result (A.8) has both real and imaginary parts. Since we are looking for the imaginary part only, we extract it by means of

$$\frac{1}{X-i\epsilon} = \text{V.P.}\left(\frac{1}{X}\right) + i\pi\delta(X)$$

and by cancelling the β integral with aid of δ function. The value of β is

$$|\beta| \approx \frac{\vec{\kappa}^2}{s} \ll 1\,, \quad \text{(A.9)}$$

and therefore it can be neglected everywhere else in (A.8). The result is

$$Im\left\{\int \frac{dy\; dz\; d\alpha\; d\beta}{\text{propagators}}\right\} = \frac{4\pi^2}{s^3}\int_0^1 dz\; \frac{1-z}{z}\frac{1}{[\vec{k}^2+m^2+z(1-z)Q^2]^2}\frac{1}{[\vec{\kappa}^2+\mu^2]^2}\,. \quad \text{(A.10)}$$

The z integration limits in (A.10) should not be understood literally as 0 and 1. In fact, when z is sufficiently close to 0 or 1, β can no longer be neglected in comparison with z. Therefore, the integrand in (A.10) does not have the correct small z and small $1-z$ asymptotics. Nevertheless, since the physical quantities will have regular $z\to 0$ and $z\to 1$ behavior, the impact of this difference will be suppressed by $\sim m^2/s$ simply due to the small integration measure.

Regions B and C

Although region B has much smaller area than region A, one cannot guarantee a priori that the third pole, which produces the imaginary part of the integral, always lies outside this region. One can check, however, that it is the case.

We extract first the values of y and α according to (A.5)

$$y = -\frac{Q^2}{s} - \frac{\vec{k}^2+m^2}{(1-z)s}\,; \quad \alpha = -\frac{\beta s+\vec{\kappa}^2}{m^2-\beta s}\,. \quad \text{(A.11)}$$

We remind that $0<\beta<m^2/s$, so that no singularity arises here. The remaining propagators are

$$\langle 2\rangle, \langle 4\rangle \;\;\to\;\; -\frac{1}{1-z}[\vec{k}^2+m^2-z(1-z)Q^2]+i\not\epsilon\,;$$

$$\langle 5\rangle, \langle 6\rangle \;\to\; -\mu^2 - \frac{\beta^2 s^2 + m^2\vec{\kappa}^2}{m^2 - \beta s} + i\not{\epsilon}\,;$$

$$\langle 3\rangle \;\to\; -[(\vec{k}+\vec{\kappa})^2 + m^2] - \left(Q^2 + \frac{\vec{k}^2 + m^2}{1-z}\right)(z+\beta) - \frac{\vec{\kappa}^2 + \beta s}{m^2 - \beta s}(z+\beta)s + i\not{\epsilon}\,.$$

We see that throughout the whole phase space of the remaining kinematic parameters all the propagators have definite sign, which makes the answer purely real.

The similar picture occurs in region C as well. Therefore, regions B and C do not contribute to the imaginary part of our integral.

A.1.2 The other three s-channel diagrams

The evaluation scheme just described can be applied to the other three diagrams. There will be slight modifications in quark propagators, but the strategy remains unchanged.

For example, consider diagram (b) of Fig. 5.2. The only difference is the expression for propagator $\langle 4\rangle$:

$$\begin{aligned}
\langle 4\rangle \;&=\; (q-k-\kappa)^2 - m^2 + i\epsilon = (1-z-\beta)\left(-\frac{Q^2}{s} - y - \alpha\right) - [(\vec{k}+\vec{\kappa})^2 + m^2] + -\epsilon\,;\\
&\to\; y = -\alpha - \frac{Q^2}{s} - \frac{(\vec{k}+\vec{\kappa})^2 + m^2}{(1-z-\beta)s} + \frac{i\epsilon}{1-z-\beta}\,;\\
&\to\; \alpha = -y - \frac{Q^2}{s} - \frac{(\vec{k}+\vec{\kappa})^2 + m^2}{(1-z-\beta)s} + \frac{i\epsilon}{1-z-\beta}\,. \qquad \text{(A.12)}
\end{aligned}$$

Again, one can check that the main nonzero contribution comes from the same region A and the same residues. So, if one again calculates the imaginary part of the integral, one finds

$$\begin{aligned}
&Im\left\{\int \frac{dy\; dz\; d\alpha\; d\beta}{\text{propagators}}\right\} =\\
&= \frac{4\pi^2}{s^3}\int_0^1 dz \frac{1}{[\vec{k}^2 + m^2 + z(1-z)Q^2][(\vec{k}+\vec{\kappa})^2 + m^2 + z(1-z)Q^2]}\frac{1}{[\vec{\kappa}^2+\mu^2]^2} \qquad \text{(A.13)}
\end{aligned}$$

Again, one can make sure that the small regions B and C do not contribute to the imaginary part as well, although the proof might not appear as clean as before. Namely one can find that regions B or C will contain a propagator (namely propagator $\langle 4\rangle$) that can change its sign, and therefore will contribute to the imaginary part. However, this can happen at abnormally small $\vec{\kappa}^2$

$$\vec{\kappa}^2 \sim \frac{m^4}{s}\,.$$

Therefore the contribution of this configuration is $1/s$-suppressed, and we neglect it at our level of accuracy.

The results for the remaining two diagrams are

$$\frac{4\pi^2}{s^3}\int_0^1 dz \frac{1}{[(\vec{k}+\vec{\kappa})^2 + m^2 + z(1-z)Q^2][\vec{k}^2 + m^2 + z(1-z)Q^2]}\frac{1}{[\vec{\kappa}^2+\mu^2]^2} \quad \text{diagram C;}$$

$$\frac{4\pi^2}{s^3}\int_0^1 dz \frac{1}{[(\vec{k}+\vec{\kappa})^2 + m^2 + z(1-z)Q^2]^2}\frac{1}{[\vec{\kappa}^2+\mu^2]^2} \quad \text{diagram D.}$$

A.1.3 The u-channel diagrams

We claimed before that the u-channel diagrams do not contribute to the imaginary part. Here we show that it is indeed the case.

The only difference between t-channel and u-channel diagrams is that in the u-channel case we switch the direction of particle p. Propagator $\langle 7\rangle$ will now be

$$\begin{aligned}\langle 7\rangle &= (p+\kappa)^2 - m^2 + i\epsilon = (1+\alpha)\left(\frac{m^2}{s}+\beta\right)s - (\vec{\kappa}^2 + m_p^2) + i\epsilon\,;\\ \alpha &= -1 + \frac{\vec{\kappa}^2+m^2}{m^2+\beta s} - \frac{i\epsilon}{\beta + m^2/s}\,.\end{aligned} \tag{A.14}$$

Following the same line as before, we recognize three regions A, B, and C. In region A ($-1 < \beta < -m^2/s;\ -\beta < z < 1$) the last propagator turns into

$$\langle 7\rangle \to -\vec{\kappa}^2 - m^2 - \left[s + Q^2 + \frac{\vec{k}^2+m^2}{1-z} + \frac{(\vec{k}+\vec{\kappa})^2+m^2}{z-|\beta|}\right]\left(|\beta| - \frac{m^2}{s}\right) + i\not{\epsilon}\,, \tag{A.15}$$

which means we do not get any contribution to the imaginary part. One can check that no contribution to the imaginary part arises from the other regions on (z,β) plane (except for abnormal cases when $\vec{\kappa}^2 \sim m^4/s$). The conclusion is that the u-channel diagram gives no leading $\frac{1}{s}$ contributions to the imaginary part of the process.

A.1.4 The α-representation technique

Here, for the purpose of completeness, we show an alternate way to do the integrations over y and α. Sure enough, the underlying meaning of all manipulations are the same as before. In a certain sense, however, this way might appears simpler, since it does not require performing any graphic analysis. Everything is done algebraically. It seems that this method is similar to the so-called α representation of the loop integrals.

We start with expression (A.1) and use the following representation for each of the seven propagators

$$\frac{1}{X - i\epsilon} = \frac{i}{\epsilon + iX} = i\int_0^\infty dt \exp[-t\epsilon - itX]\,. \tag{A.16}$$

The integral (A.1) transforms into

$$\begin{aligned} i^7 \int dy\ dz\ d\alpha\ d\beta\ \int_0^\infty dt_1\cdots dt_7\ &\exp[-t_1\epsilon - it_1(ys+Q^2)(1-z) - it_1(\vec{k}^2+m^2)]\\ &\times\exp[-t_2\epsilon + it_2yzs - it_2(\vec{k}^2+m^2) - t_3\epsilon + it_3(y+\alpha)(z+\beta)s - it_1[(\vec{k}+\vec{\kappa})^2+m^2]]\\ &\times\exp[-t_4\epsilon + it_4yzs - it_2(\vec{k}^2+m^2) - t_5\epsilon + it_5\alpha\beta s - it_5(\vec{\kappa}^2+\mu^2)]\\ &\times\exp[-t_6\epsilon + it_6\alpha\beta s - it_6(\vec{\kappa}^2+\mu^2) - t_7\epsilon + it_7(m^2-\beta s)(1-\alpha) - it_7(\vec{\kappa}^2+m^2)] \end{aligned} \tag{A.17}$$

Since the total integral is convergent and thanks to the factorization of y and α dependencies, we can do the y and α integration first and obtain

$$\begin{aligned}&\int dy\ e^{iys[-t_1(1-z)+t_2z+t_3(z+\beta)+t_4z]}\int d\alpha\ e^{i\alpha s\left[t_3(z+\beta)+t_5\beta+t_6\beta+t_7(\beta-m^2/s)\right]} = \left(-\frac{2\pi i}{s}\right)^2\\ &\times\delta\left[-t_1(1-z)+t_2z+t_3(z+\beta)+t_4z\right]\ \delta\left[t_3(z+\beta)+t_5\beta+t_6\beta+t_7(\beta-m^2/s)\right]\,.\end{aligned}$$

Since all parameters t_i are positive, the two delta-functions can be simultaneously non-zero only for certain (z,β) pairs. As should be expected, these pairs lie precisely within the allowed regions.

We can now take two of $t_1 \ldots t_7$ integrations to cancel the two delta-functions. Let them be t_1 and t_3 (of course, one can take other pairs as well). We get

$$\begin{aligned} t_3 &= -\frac{\beta}{z+\beta}(t_5+t_6+t_7) + t_7\frac{m^2}{(z+\beta)s}\,; \\ t_1 &= \frac{z}{1-z}(t_2+t_4) - \frac{\beta}{1-z}(t_5+t_6+t_7) + t_7\frac{m^2}{(1-z)s}\,. \end{aligned} \tag{A.18}$$

Since the integrations in t_i remain factorized, we easily obtain

$$\int_0^\infty dt_2 e^{-t_2\epsilon} e^{-it_2(\vec{k}^2+m^2)-\frac{z}{1-z}(\vec{k}^2+m^2)-zQ^2} = \frac{-i}{\frac{1}{1-z}[\vec{k}^2+m^2+z(1-z)Q^2]-i\epsilon}\,;$$

$$\int_0^\infty dt_4 e^{-t_4\epsilon} e^{-it_4(\vec{k}^2+m^2)-\frac{z}{1-z}(\vec{k}^2+m^2)-zQ^2} = \frac{-i}{\frac{1}{1-z}[\vec{k}^2+m^2+z(1-z)Q^2]-i\epsilon}\,;$$

$$\begin{aligned} &\int_0^\infty dt_5 e^{-t_5\epsilon} e^{-it_5(\vec{\kappa}^2+\mu^2)+it_5\frac{\beta}{z+\beta}[\vec{k}^2+m^2+Q^2(1-z)+(\vec{k}+\vec{\kappa})^2+m^2]} \\ &\quad = \frac{-i}{\vec{\kappa}^2+\mu^2-i\epsilon-\frac{\beta}{z+\beta}[Q^2(1-z)+\vec{k}^2+m^2+(\vec{k}+\vec{\kappa})^2+m^2]}\,; \end{aligned}$$

$$\begin{aligned} &\int_0^\infty dt_6 e^{-t_6\epsilon} e^{-it_6(\vec{\kappa}^2+\mu^2)+it_6\frac{\beta}{z+\beta}[\vec{k}^2+m^2+Q^2(1-z)+(\vec{k}+\vec{\kappa})^2+m^2]} \\ &\quad = \frac{-i}{\vec{\kappa}^2+\mu^2-i\epsilon-\frac{\beta}{z+\beta}[Q^2(1-z)+\vec{k}^2+m^2+(\vec{k}+\vec{\kappa})^2+m^2]}\,; \end{aligned}$$

$$\begin{aligned} &\int_0^\infty dt_7 e^{-t_7\epsilon} e^{it_y(\mu^2-\beta s)-it_7(\vec{\kappa}^2+m^2)-it_7\frac{m^2/s-\beta}{z+\beta}[\vec{k}^2+m^2+Q^2(1-z)+(\vec{k}+\vec{\kappa})^2+m^2]} \\ &\quad = \frac{-i}{\vec{\kappa}^2+\beta s-i\epsilon+\frac{m^2/s-\beta}{z+\beta}[Q^2(1-z)+\vec{k}^2+m^2+(\vec{k}+\vec{\kappa})^2+m^2]}\,. \end{aligned} \tag{A.19}$$

If we now bring all pieces together, we will arrive at the expression obtained in the previous section.

A.2 Vector meson production: the fully off-forward case

The integration in this case is done similarly to the Compton scattering; therefore, we do all calculations in a less detailed fashion and pay special attention only to distinct features of vector meson production.

Strictly speaking, the (virtual) photoproduction of vector mesons is always an off-forward process, even though the final state might have no transverse momentum. The reason is that when the initial and final states have different masses the exchanged pomeron must carry a non-zero longitudinal momentum. In the language of two-gluon exchange, it means that the momenta of the gluons are not identical, in contract to what we had in previous section.

The integral we deal with is

$$\int dy\ dz\ d\alpha\ d\beta\ \frac{\Gamma(M^2)}{[(q-k)^2-m^2+i\epsilon][k^2-m^2+i\epsilon][(k+\Delta)^2-m^2+i\epsilon][(k+\kappa_1)^2-m^2+i\epsilon]}$$
$$\frac{1}{[\kappa_1^2-\mu^2+i\epsilon][\kappa_2^2-\mu^2+i\epsilon][(p-\kappa_1)^2-m^2+i\epsilon]} \tag{A.20}$$

With the Sudakov decomposition and notation $\kappa_1 \equiv \kappa + \Delta/2\,, \kappa_1 \equiv \kappa - \Delta/2$, we have the following seven propagators:

$$\langle 1\rangle \qquad (q-k)^2-m^2+i\epsilon = \left(-y-\frac{Q^2}{s}\right)(1-z)s-(\vec{k}^2+m^2)+i\epsilon\,,$$

$$\langle 2\rangle \qquad (k+\Delta)^2-m^2+i\epsilon = (y+\sigma)(z+\delta)s-[(\vec{k}+\vec{\Delta})^2+m^2]+i\epsilon\,,$$

$$\langle 3\rangle \qquad (k+\kappa_1)^2-m^2+i\epsilon = (y+\alpha+\frac{1}{2}\sigma)(z+\beta+\frac{1}{2}\delta)s-[(\vec{k}+\vec{\kappa}+\Delta/2)^2+m^2]+i\epsilon\,,$$

$$\langle 4\rangle \qquad k^2-m^2+i\epsilon = yzs-(\vec{k}^2+m^2)+i\epsilon\,,$$

$$\langle 5\rangle \qquad \kappa_1^2-\mu^2+i\epsilon = (\alpha+\frac{1}{2}\sigma)(\beta+\frac{1}{2}\delta)s-[(\vec{\kappa}+\frac{1}{2}\Delta)^2+\mu^2]+i\epsilon\,,$$

$$\langle 6\rangle \qquad \kappa_2^2-\mu^2+i\epsilon = (\alpha-\frac{1}{2}\sigma)(\beta-\frac{1}{2}\delta)s-[(\vec{\kappa}-\frac{1}{2}\Delta)^2+\mu^2]+i\epsilon\,,$$

$$\langle 7\rangle \qquad (p-\kappa_1)^2-m^2+i\epsilon = (1-\alpha-\frac{1}{2}\sigma)\left(-\beta-\frac{1}{2}\delta\right)s-[(\vec{\kappa}+\frac{1}{2}\vec{\Delta})^2+m^2]+i\epsilon\,.$$

One can write now poles on the y and α plane, draw the regions of positivity of the corresponding $i\epsilon$'s on the (z,β) plane, and select the regions that leads to non-zero contributions (there will be five of them in this case). One can again make sure that the leading $1/s$ contribution to the imaginary part comes from the main region. The presence of μ^2 — namely the fact that $\mu^2 > m_V^2 - 4m^2$ for all vector mesons — also helps avoid extra poles.

Setting propagators $\langle 1\rangle$ and $\langle 3\rangle$ on-mass-shell, we obtain

$$y = -\frac{Q^2}{s}-\frac{\vec{k}^2+m^2}{(1-z)s}\,; \quad \alpha = \frac{Q^2}{s}-\frac{1}{2}\sigma+\frac{\vec{k}^2+m^2}{(1-z)s}+\frac{(\vec{k}+\vec{\kappa}+\vec{\Delta}/2)^2+m^2}{(z+\beta+\delta/2)s}\,. \tag{A.21}$$

The resulting quark propagators are

$$\begin{aligned}\langle 4\rangle &= -\frac{1}{1-z}\left[\vec{k}^2+m^2+z(1-z)Q^2\right]+i\not{\epsilon}\,;\\ \langle 2\rangle &= (z+\delta)s\sigma-(z+\delta)sQ^2-(z+\delta)\frac{\vec{k}^2+m^2}{1-z}-[(\vec{k}+\vec{\Delta})^2+m^2]+i\epsilon\,.\end{aligned} \tag{A.22}$$

Note that since the invariant mass of the produced $q\bar{q}$ state is equal to

$$M^2 = \frac{\vec{k}^2+m^2}{1-z}+\frac{(\vec{k}+\vec{\Delta})^2+m^2}{z+\delta}-\vec{\Delta}^2\,,$$

propagator $\langle 2\rangle$ turns into $(z+\delta)(m_V^2-M^2)$. Together with the vertex factor $\Gamma(M^2)$, it gives rise to the wave function of the vector meson.

The gluon propagators are

$$\langle 5\rangle = (\beta+\frac{1}{2}\delta)\left(Q^2+\frac{\vec{k}^2+m^2}{1-z}+\frac{(\vec{k}+\vec{\kappa}+\vec{\Delta}/2)^2+m^2}{z+\beta+\delta/2}\right)-[(\vec{\kappa}+\frac{1}{2}\Delta)^2+\mu^2]+i\not{\epsilon}\,;$$

$$\langle 6\rangle = (\beta-\frac{1}{2}\delta)\left(-m_V^2-\vec{\Delta}^2+\frac{\vec{k}^2+m^2}{1-z}+\frac{(\vec{k}+\vec{\kappa}+\vec{\Delta}/2)^2+m^2}{z+\beta+\delta/2}\right)-[(\vec{\kappa}-\frac{1}{2}\Delta)^2+\mu^2]+i\not{\epsilon}\,.$$

In the case of gluon $\langle 5\rangle$ the absence of the pole was — ue to negativity of both β and δ — obvious. In the case of the second gluon, the pole can in principle arise. In our case however this is avoided due to large enough μ^2 (namely $\mu^2 > m_V^2 - 4m^2$ for all vector mesons).

Finally, the propagator $\langle 7\rangle$ takes the form

$$\langle 7\rangle = -(\beta+\frac{1}{2}\delta)\left[s-Q^2-\frac{\vec{k}^2+m^2}{1-z}-\frac{(\vec{k}+\vec{\kappa}+\vec{\Delta}/2)^2+m^2}{z+\beta+\delta/2}\right]-[(\vec{\kappa}+\frac{1}{2}\Delta)^2+\mu^2]+i\epsilon\,. \quad \text{(A.23)}$$

This propagator, as usual, is used to extract the imaginary part of the integral, which leads to

$$\beta \approx \frac{(\vec{\kappa}+\frac{1}{2}\vec{\Delta})^2}{s} \ll 1\,.$$

With all these manipulations done, we finally obtain

$$Im\int dy\ dz\ d\alpha\ d\beta\ \frac{\Gamma}{[\text{all propagators}]} \quad \text{(A.24)}$$
$$= \left(-\frac{\pi i}{s}\right)\left(-\frac{2\pi i}{s}\right)^2\cdot\int\frac{dz}{z(1-z)}\psi_V(z,\vec{k}^2)\cdot\frac{1}{[\vec{k}_1^2+m^2+z(1-z)Q^2]}\frac{1}{(\vec{\kappa}^2+\mu^2)^2}\,.$$

Appendix B

Helicity amplitude technique

Here we give the derivation of expression for traces of the following type

$$Sp\left\{\hat{e}\ (\hat{k}_4+m)\ \hat{p}'\ (\hat{k}_3+m)\ \hat{V}^*\ (\hat{k}_2+m)\ \hat{p}'\ (\hat{k}_1+m)\right\} \tag{B.1}$$

in full detail. Although one can calculate this trace covariantly, a particularly convenient way to do so is given by light cone helicity amplitude technique [25]. We emphasize that both ways are absolutely equivalent. In the helicity amplitude approach, we recall that all fermion lines in (B.1) can be taken on-mass-shell (see detailed derivation of LCWF normalization in Sect.4.5) and decomposed into a sum of light cone helicities

$$\begin{aligned}
&(\hat{k}+m) \to \sum_{\lambda=\pm} u_\lambda \bar{u}_\lambda \quad \text{for quark lines;} \\
&(\hat{k}+m) = -[(-\hat{k})-m] \to -\sum_{\lambda=\pm} v_\lambda \bar{v}_\lambda \quad \text{for antiquark lines.}
\end{aligned}$$

Since the specific choice of this decomposition does not affect the final result, we are free to take the most convenient choice of spinors (see [25] for details), namely

$$\begin{aligned}
u(p,\lambda) &= \frac{1}{\sqrt{\sqrt{2}p^+}}\left(\sqrt{2}p^+ + \beta m + \vec{\alpha}\vec{p}\right)\left\{\begin{array}{ll}\chi(\uparrow) & \lambda=+1\\ \chi(\downarrow) & \lambda=-1\end{array}\right. \\
v(p,\lambda) &= \frac{1}{\sqrt{\sqrt{2}p^+}}\left(\sqrt{2}p^+ - \beta m + \vec{\alpha}\vec{p}\right)\left\{\begin{array}{ll}\chi(\downarrow) & \lambda=+1\\ \chi(\uparrow) & \lambda=-1\end{array}\right.
\end{aligned} \tag{B.2}$$

where

$$\chi(\uparrow) = \frac{1}{\sqrt{2}}\begin{pmatrix}1\\0\\1\\0\end{pmatrix}; \quad \chi(\downarrow) = \frac{1}{\sqrt{2}}\begin{pmatrix}0\\1\\0\\-1\end{pmatrix}$$

We stress that we use here our normal convention for + components of 4-vectors. For convenience, we also give the explicit expressions for all these spinors in the Dirac representation of γ matrices:

$$\beta=\gamma^0=\begin{pmatrix}I & 0\\ 0 & -I\end{pmatrix}\ \gamma^k=\begin{pmatrix}0 & \sigma^k\\ -\sigma^k & 0\end{pmatrix}\ \alpha^k=\begin{pmatrix}0 & \sigma^k\\ \sigma^k & 0\end{pmatrix}\ \gamma^5=\begin{pmatrix}0 & I\\ I & 0\end{pmatrix} \tag{B.3}$$

The explicit expressions for all spinors $u^+(p),\ u^-(p),\ v^-(p),\ v^+(p)$ read:

$$\frac{1}{\sqrt{2}}\frac{1}{\sqrt{\sqrt{2}p^+}}\cdot\begin{pmatrix}\sqrt{2}p^+ + m\\ p_x + ip_y\\ \sqrt{2}p^+ - m\\ p_x + ip_y\end{pmatrix}\begin{pmatrix}-p_x + ip_y\\ \sqrt{2}p^+ + m\\ p_x - ip_y\\ -\sqrt{2}p^+ + m\end{pmatrix}\begin{pmatrix}\sqrt{2}p^+ - m\\ p_x + ip_y\\ \sqrt{2}p^+ + m\\ p_x + ip_y\end{pmatrix}\begin{pmatrix}-p_x + ip_y\\ \sqrt{2}p^+ - m\\ p_x - ip_y\\ -\sqrt{2}p^+ - m\end{pmatrix} \tag{B.4}$$

Using these explicit formulas, one can do straightforward calculations and indeed prove that comply with orthonormality and completeness rules:

$$\begin{aligned}&\bar{u}(p,\lambda)u(p,\lambda') = -\bar{v}(p,\lambda)v(p,\lambda') = 2m\delta_{\lambda\lambda'}\,;\\ &\sum_\lambda u(p,\lambda)\bar{u}(p,\lambda) = \hat{p} + m\,;\quad \sum_\lambda v(p,\lambda)\bar{v}(p,\lambda) = \hat{p} - m\,.\end{aligned} \tag{B.5}$$

For $\lambda = \pm 1$ we defined

$$a(\lambda) = -\lambda a_x - i a_y\ . \tag{B.6}$$

Cross product is defined as

$$[\vec{a}\vec{b}] = a_x b_y - b_x a_y\ . \tag{B.7}$$

Moreover **every** matrix element should be multiplied by common factor $\sqrt{p_+ q_+}$.
Some useful relations:

$$\begin{aligned}&\gamma^5 v_\lambda(q) = -\lambda u_{-\lambda}(q)\,;\quad \gamma^5 u_\lambda(q) = \lambda v_{-\lambda}(q)\,;\\ &a(-\lambda)b(\lambda) = -\vec{a}\vec{b} + i\lambda[\vec{a}\vec{b}]\,;\quad \sum_\lambda a(-\lambda)b(\lambda) = -2\vec{a}\vec{b}\,;\\ &a(-\lambda)\left(\vec{b}\vec{a} + i\lambda[\vec{b}\vec{a}]\right) = b(-\lambda)\vec{a}^2\,.\end{aligned} \tag{B.8}$$

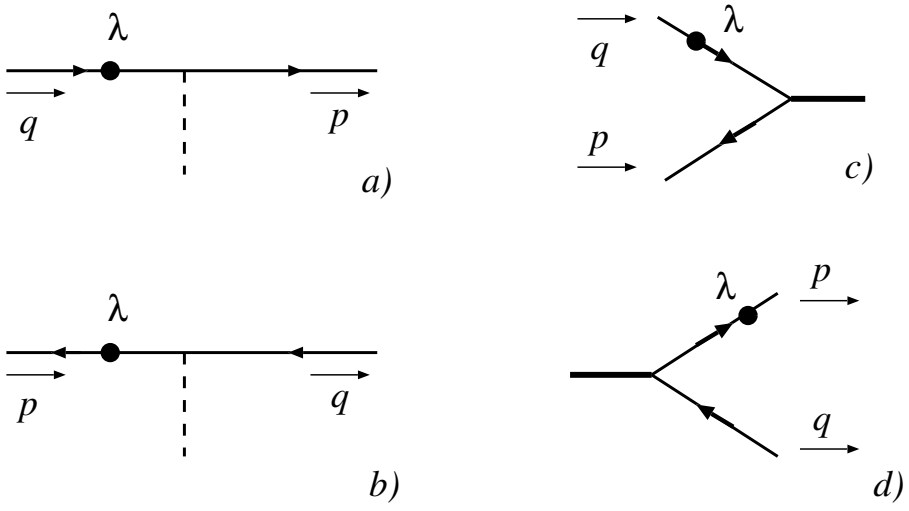

Figure B.1: Four types of transitions, for which we give the amplitudes. Dot with label λ indicates the spinor whose helicity is used as λ.

Straight line elements

For line in Fig.B.1a, one has

	$\bar{u}_\lambda(p)...u_\lambda(q)$	$\bar{u}_{-\lambda}(p)...u_\lambda(q)$
γ^+	2	0
γ^-	$\frac{1}{p_+q_+}\left(m^2+\vec{p}\vec{q}+i\lambda[\vec{p}\vec{q}]\right)$	$\frac{m}{p_+q_+}\left(p(\lambda)-q(\lambda)\right)$
$\vec{a}\cdot\vec{\gamma}$	$\frac{\vec{a}\vec{p}}{p_+}+\frac{\vec{a}\vec{q}}{q_+}-i\lambda\left(\frac{[\vec{a}\vec{p}]}{p_+}-\frac{[\vec{a}\vec{q}]}{q_+}\right)$	$-ma(\lambda)\left(\frac{1}{p_+}-\frac{1}{q_+}\right)$
1	$m\left(\frac{1}{p_+}+\frac{1}{q_+}\right)$	$\frac{p(\lambda)}{p_+}-\frac{q(\lambda)}{q_+}$
$\gamma^-\gamma^+\vec{\gamma}\cdot\vec{a}$	$\frac{2}{p_+}\left(\vec{a}\vec{p}-i\lambda[\vec{a}\vec{p}]\right)$	$-\frac{2m}{p_+}a(\lambda)$
$\vec{a}\cdot\vec{\gamma}\ \gamma^+\gamma^-$	$\frac{2}{q_+}\left(\vec{a}\vec{q}+i\lambda[\vec{a}\vec{q}]\right)$	$\frac{2m}{q_+}a(\lambda)$
$\vec{a}\cdot\vec{\gamma}\ \gamma^+\vec{\gamma}\cdot\vec{b}$	$2(\vec{a}\vec{b}+i\lambda[\vec{a}\vec{b}])$	0
$\gamma^+\gamma^5$	2λ	0

For line in Fig.B.1b, one has

	$\bar{v}_\lambda(p)...v_\lambda(q)$	$\bar{v}_\lambda(p)...v_{-\lambda}(q)$
γ^+	2	0
γ^-	$\frac{1}{p_+q_+}\left(m^2+\vec{p}\vec{q}-i\lambda[\vec{p}\vec{q}]\right)$	$-\frac{m}{p_+q_+}\left(p(\lambda)-q(\lambda)\right)$
$\vec{a}\cdot\vec{\gamma}$	$\frac{\vec{a}\vec{p}}{p_+}+\frac{\vec{a}\vec{q}}{q_+}+i\lambda\left(\frac{[\vec{a}\vec{p}]}{p_+}-\frac{[\vec{a}\vec{q}]}{q_+}\right)$	$ma(\lambda)\left(\frac{1}{p_+}-\frac{1}{q_+}\right)$
1	$-m\left(\frac{1}{p_+}+\frac{1}{q_+}\right)$	$\frac{p(\lambda)}{p_+}-\frac{q(\lambda)}{q_+}$
$\gamma^-\gamma^+\vec{\gamma}\cdot\vec{a}$	$\frac{2}{p_+}\left(\vec{a}\vec{p}+i\lambda[\vec{a}\vec{p}]\right)$	$\frac{2m}{p_+}a(\lambda)$
$\vec{a}\cdot\vec{\gamma}\ \gamma^+\gamma^-$	$\frac{2}{q_+}\left(\vec{a}\vec{q}-i\lambda[\vec{a}\vec{q}]\right)$	$-\frac{2m}{q_+}a(\lambda)$
$\vec{a}\cdot\vec{\gamma}\ \gamma^+\vec{\gamma}\cdot\vec{b}$	$2(\vec{a}\vec{b}-i\lambda[\vec{a}\vec{b}])$	0
$\gamma^+\gamma^5$	-2λ	0

Vertex lines

For vertex in Fig.B.1c, one has

	$\bar{v}_\lambda(p)...u_\lambda(q)$	$\bar{v}_{-\lambda}(p)...u_\lambda(q)$
γ^+	0	2
γ^-	$\frac{m}{p_+q_+}\left(p(\lambda)+q(\lambda)\right)$	$\frac{1}{p_+q_+}\left(-m^2+\vec{p}\vec{q}+i\lambda[\vec{p}\vec{q}]\right)$
$\vec{a}\cdot\vec{\gamma}$	$ma(\lambda)\left(\frac{1}{p_+}+\frac{1}{q_+}\right)$	$\frac{\vec{a}\vec{p}}{p_+}+\frac{\vec{a}\vec{q}}{q_+}-i\lambda\left(\frac{[\vec{a}\vec{p}]}{p_+}-\frac{[\vec{a}\vec{q}]}{q_+}\right)$
1	$\frac{p(\lambda)}{p_+}-\frac{q(\lambda)}{q_+}$	$-\frac{m}{p_+}+\frac{m}{q_+}$
$\gamma^-\gamma^+\vec{\gamma}\cdot\vec{a}$	$\frac{2m}{p_+}a(\lambda)$	$\frac{2}{p_+}\left(\vec{a}\vec{p}-i\lambda[\vec{a}\vec{p}]\right)$
$\vec{a}\cdot\vec{\gamma}\ \gamma^+\gamma^-$	$\frac{2}{q_+}a(\lambda)$	$\frac{2}{q_+}\left(\vec{a}\vec{q}+i\lambda[\vec{a}\vec{q}]\right)$
$\vec{a}\cdot\vec{\gamma}\ \gamma^+\vec{\gamma}\cdot\vec{b}$	0	$2(\vec{a}\vec{b}+i\lambda[\vec{a}\vec{b}])$
$\gamma^+\gamma^5$	0	2λ
γ^5	$\lambda\left(\frac{p(\lambda)}{p_+}-\frac{q(\lambda)}{q_+}\right)$	$-\lambda m\left(\frac{1}{p_+}+\frac{1}{q_+}\right)$

For vertex in Fig.B.1d, one has

	$\bar{u}_\lambda(p)...v_\lambda(q)$	$\bar{u}_\lambda(p)...v_{-\lambda}(q)$
γ^+	0	2
γ^-	$-\frac{m}{p_+q_+}\left(p(-\lambda)+q(-\lambda)\right)$	$\frac{1}{p_+q_+}\left(-m^2+\vec{p}\vec{q}+i\lambda[\vec{p}\vec{q}]\right)$
$\vec{a}\cdot\vec{\gamma}$	$-ma(-\lambda)\left(\frac{1}{p_+}+\frac{1}{q_+}\right)$	$\frac{\vec{a}\vec{p}}{p_+}+\frac{\vec{a}\vec{q}}{q_+}-i\lambda\left(\frac{[\vec{a}\vec{p}]}{p_+}-\frac{[\vec{a}\vec{q}]}{q_+}\right)$
1	$\frac{p(-\lambda)}{p_+}-\frac{q(-\lambda)}{q_+}$	$\frac{m}{p_+}-\frac{m}{q_+}$
$\gamma^-\gamma^+\vec{\gamma}\cdot\vec{a}$	$-\frac{2m}{p_+}a(-\lambda)$	$\frac{2}{p_+}\left(\vec{a}\vec{p}-i\lambda[\vec{a}\vec{p}]\right)$
$\vec{a}\cdot\vec{\gamma}\ \gamma^+\gamma^-$	$-\frac{2m}{q_+}a(-\lambda)$	$\frac{2}{q_+}\left(\vec{a}\vec{q}+i\lambda[\vec{a}\vec{q}]\right)$
$\vec{a}\cdot\vec{\gamma}\ \gamma^+\vec{\gamma}\cdot\vec{b}$	0	$2(\vec{a}\vec{b}+i\lambda[\vec{a}\vec{b}])$
$\gamma^+\gamma^5$	0	2λ
γ^5	$-\lambda\left(\frac{p(-\lambda)}{p_+}-\frac{q(-\lambda)}{q_+}\right)$	$\lambda m\left(\frac{1}{p_+}+\frac{1}{q_+}\right)$

Transverse photon polarization

As we see from the table, neither of gluon legs can flip quark helicity. Therefore, there are 4 combinations of all possible helicity assignments.

In the case both $q\bar{q}$ helicities are the same, one gets

$$2zq_+p_- \cdot 2zq_+p_- \cdot \frac{\sqrt{z(1-z)}q_+}{z(1-z)q_+} me^*(\lambda) \cdot \frac{\sqrt{z(1-z)}q_+}{z(1-z)q_+}(-m)e(-\lambda)$$
$$= \frac{z}{1-z}s^2(-m^2)e^*(\lambda)e(-\lambda) \tag{B.9}$$

In the case quark and antiquark helicities are opposite, one obtains

$$2zq_+p_- \cdot 2zq_+p_- \cdot \frac{\sqrt{z(1-z)}q_+}{z(1-z)q_+}\left[(-e^*k)z + (e^*k)(1-z) - i\lambda(-[e^*k]z - [e^*k](1-z))\right]$$
$$\cdot\frac{\sqrt{z(1-z)}q_+}{z(1-z)q_+}\left[(ek)(1-z) - (ek)z - i\lambda([e^*k](1-z) + [e^*k]z)\right]$$
$$= \frac{z}{1-z}s^2\left[(e^*k)(1-2z) + i\lambda[e^*k]\right]\left[(ek)(1-2z) - i\lambda[ek]\right] \tag{B.10}$$

Thus, performing summation over $q\bar{q}$ helicities, one obtains

$$2s^2\frac{z}{1-z}\left[m^2(ee^*) + (ek)(e^*k)(1-2z)^2 + [ek][e^*k]\right]$$

Finally, averaging over azymuthal angle, omitting factor $2s^2$ and including (-1) due to one antiquark propagator reveals

$$\frac{1-z}{z}I^{(a)} = -\left[m^2 + (z^2 + (1-z)^2)k^2\right] \tag{B.11}$$

Note that the expression for Diagr.(d) can be instantly obtained from the above expressions by replacement $\vec{k} \to -\vec{k}$; $z \to 1-z$. In this case 3 antiquark propagators also give factor $(-1)^3 = -1$. So, the answer for this diagram is

$$\frac{z}{1-z}I^{(d)} = -\left[m^2 + (z^2 + (1-z)^2)k^2\right] \tag{B.12}$$

Finally, one has

$$m^2 + (z^2 + (1-z)^2)(k, k+\kappa)$$
$$m^2 + (z^2 + (1-z)^2)(k, k-\kappa)$$

for Diagrams (b) and (c) respectively.

With all these results, Eq.(2.21) turns into

$$A^T = is\frac{32}{(2\pi)^2}e_f^2 \cdot \alpha_s^2\alpha_{em} \cdot 2 \cdot \int dz \frac{d^2\vec{k}}{\left[\vec{k}^2 + m^2 + z(1-z)Q^2\right]} \int \frac{d^2\vec{\kappa}V(\kappa)}{(\vec{\kappa}^2 + \mu^2)^2}$$
$$\times\left[-\frac{m^2 + (z^2 + (1-z)^2)\vec{k}^2}{[\vec{k}^2 + m^2 + z(1-z)Q^2]} + \frac{m^2 + (z^2 + (1-z)^2)(\vec{k}^2 + (\vec{k}\vec{\kappa}))}{[(\vec{k}+\vec{\kappa})^2 + m^2 + z(1-z)Q^2]}\right]. \tag{B.13}$$

Note that we changed $\kappa \to -\kappa$ in Diagr.(c), so that it became identical to Diagr.(b).

Scalar photon polarization

The virtual photon scalar polarization is described by

$$e_0^\mu = \frac{1}{Q}(q'^\mu + xp'^\mu) = \frac{1}{Q}(q_+ n_+^\mu + xp_- n_-^\mu) \tag{B.14}$$

One notes that in this case only $q\bar{q}$ states with opposite helicities do contribute. For Diagr.(a) an amplitude reads

$$\begin{aligned} & 2zq_+p_- \cdot 2zq_+p_- \cdot \left(\frac{\sqrt{z(1-z)}q_+}{Q}\right)^2 \left[\frac{q_+(-m^2-\vec{k}^2)}{z(1-z)q_+^2} + 2xp_-\right]\left[\frac{q_+(-m^2-\vec{k}^2)}{z(1-z)q_+^2} + 2xp_-\right] \\ & = s^2 \frac{1}{Q^2}\frac{z}{1-z}\left[m^2+\vec{k}^2 - z(1-z)Q^2\right]^2 . \end{aligned} \tag{B.15}$$

Therefore,

$$\frac{1-z}{z} I^{(a)} = -\frac{1}{Q^2}\left[m^2+\vec{k}^2 - z(1-z)Q^2\right]^2 . \tag{B.16}$$

Obviously, for Diagr.(d) one has

$$\frac{z}{1-z} I^{(d)} = -\frac{1}{Q^2}\left[m^2+\vec{k}^2 - z(1-z)Q^2\right]^2 . \tag{B.17}$$

The expressions for Diagrs.(b) and (c) can be obtained in the same way and give

$$\begin{aligned} I^{(b)} &= \frac{1}{Q^2}\left[m^2+\vec{k}^2 - z(1-z)Q^2\right]\left[m^2+(\vec{k}+\vec{\kappa})^2 - z(1-z)Q^2\right] ; \\ I^{(c)} &= \frac{1}{Q^2}\left[m^2+\vec{k}^2 - z(1-z)Q^2\right]\left[m^2+(\vec{k}-\vec{\kappa})^2 - z(1-z)Q^2\right] . \end{aligned} \tag{B.18}$$

Therefore Eq.(2.21) now reads

$$\begin{aligned} A^0 &= is\frac{32}{(2\pi)^2} e_f^2 \cdot \alpha_s^2 \alpha_{em} \cdot \int dz d^2\vec{k} \frac{\left[m^2+\vec{k}^2 - z(1-z)Q^2\right]}{\left[\vec{k}^2+m^2+z(1-z)Q^2\right]} \int \frac{d^2\vec{\kappa} V(\kappa)}{(\vec{\kappa}^2+\mu^2)^2} \\ &\quad \times \frac{2}{Q^2}\left[-\frac{\left[m^2+\vec{k}^2 - z(1-z)Q^2\right]}{\left[\vec{k}^2+m^2+z(1-z)Q^2\right]} + \frac{\left[m^2+(\vec{k}-\vec{\kappa})^2 - z(1-z)Q^2\right]}{\left[(\vec{k}-\vec{\kappa})^2+m^2+z(1-z)Q^2\right]}\right] . \end{aligned} \tag{B.19}$$

In fact, this expression in brackets can be greatly simplified. First, trivial algebra leads to

$$\begin{aligned} & -\frac{\left[m^2+\vec{k}^2 - z(1-z)Q^2\right]}{\left[\vec{k}^2+m^2+z(1-z)Q^2\right]} + \frac{\left[m^2+(\vec{k}-\vec{\kappa})^2 - z(1-z)Q^2\right]}{\left[(\vec{k}-\vec{\kappa})^2+m^2+z(1-z)Q^2\right]} \\ & = -1 + \frac{2z(1-z)Q^2]}{\left[\vec{k}^2+m^2+z(1-z)Q^2\right]} + 1 - \frac{2z(1-z)Q^2}{\left[(\vec{k}-\vec{\kappa})^2+m^2+z(1-z)Q^2\right]} \\ & = 2z(1-z)Q^2\left[\frac{1}{\left[\vec{k}^2+m^2+z(1-z)Q^2\right]} - \frac{1}{\left[(\vec{k}-\vec{\kappa})^2+m^2+z(1-z)Q^2\right]}\right] . \end{aligned}$$

Second, in we replace $e_0 \propto (q'+xp')$ by $q = (q'-xp')$, we will get zero due to the gauge invariance of the totaf sum of all diagrams. Effectively, it means that residual $[m^2+\vec{k}^2 -$

$z(1-z)Q^2]$ can be replaced by $-2z(1-z)Q^2$. Of course, it does not mean that these two expressions are identical by themselves. Only after integration over quark momenta they give the same answer. Thus, the final answer for scalar photons reads

$$A^0 = is\frac{128Q^2}{(2\pi)^2}e_f^2\cdot\alpha_s^2\alpha_{em}\cdot 2\cdot\int dz z^2(1-z)^2 d^2\vec{k}\frac{1}{\left[\vec{k}^2+m^2+z(1-z)Q^2\right]}\int\frac{d^2\vec{\kappa}V(\kappa)}{(\vec{\kappa}^2+\mu^2)^2}$$
$$\times\left[\frac{1}{[\vec{k}^2+m^2+z(1-z)Q^2]}-\frac{1}{[(\vec{k}-\vec{\kappa})^2+m^2+z(1-z)Q^2]}\right]. \qquad \text{(B.20)}$$

B.1 Photon vertex amplitudes

Notation is given in Fig.5.3. We start with transverse photon.

$$\bar{u}'\hat{e}_T v = \bar{u}'(-\vec{\gamma}\vec{e})v\,.$$

Equal $q\bar{q}$ helicities give

$$-\frac{\sqrt{z(1-z)}q_+}{z(1-z)q_+}\cdot(-m)e(-\lambda) = \frac{1}{\sqrt{z(1-z)}}me(-\lambda) \qquad \text{(B.21)}$$

Opposite $q\bar{q}$ helicities give

$$-\frac{\sqrt{z(1-z)}q_+}{z(1-z)q_+}\cdot\left[(\vec{e}\vec{k}_1)(1-z)-(\vec{e}\vec{k}_1)z-i\lambda\left([\vec{e}\vec{k}_1](1-z)+[\vec{e}\vec{k}_1]z\right)\right]$$
$$=-\frac{1}{\sqrt{z(1-z)}}\left[(\vec{e}\vec{k}_1)(1-2z)-i\lambda[\vec{e}\vec{k}_1]\right] \qquad \text{(B.22)}$$

In the case of scalar photon

$$\bar{u}'\hat{e}_0 v = \bar{u}'\frac{1}{Q}(q_+\gamma_- + xp_-\gamma_+)v$$

the same helicities give exactly zero while opposite helicities result in

$$\frac{\sqrt{z(1-z)}q_+}{z(1-z)q_+}\cdot\frac{1}{Q}\cdot\left[\frac{q_+}{q_+}(-m^2-\vec{k}_1^2)+x2z(1-z)p_-q_+\right]$$
$$=-\frac{1}{\sqrt{z(1-z)}}\frac{1}{Q}\left[m^2+\vec{k}_1^2-z(1-z)Q^2\right] \qquad \text{(B.23)}$$

B.2 Vector meson vertex amplitudes

This case is more tricky due to the nonzero vector meson transverse momentum $\vec{\Delta}$. We start with the transverse vector meson polarization:

$$\hat{V}_T^* = -\vec{\gamma}\vec{V}^* + \frac{2(\vec{V}^*\vec{\Delta})}{s}p_-\gamma_+\,.$$

The same $q\bar{q}$ helicities give again

$$-\frac{\sqrt{z(1-z)}q_+}{z(1-z)q_+}\cdot mV^*(\lambda) = -\frac{1}{\sqrt{z(1-z)}}mV^*(\lambda) \tag{B.24}$$

while opposite helicities give

$$\begin{aligned}
&\frac{\sqrt{z(1-z)}q_+}{z(1-z)q_+}\Big\{-[(\vec{V}^*\vec{k}_3)z+(\vec{V}^*\vec{k}_2)(1-z)-i\lambda\left([\vec{V}^*\vec{k}_3]z-[\vec{V}^*\vec{k}_2](1-z)\right)] \\
&+\frac{2(\vec{V}^*\vec{\Delta})}{s}p_-2z(1-z)q_+\Big\} \\
&= -\frac{1}{\sqrt{z(1-z)}}\Big\{(\vec{V}^*\vec{k})(1-2z)+i\lambda[V\vec{k}]\Big\}
\end{aligned} \tag{B.25}$$

Here we used definitions and properties (see also Fig.5.3):

$$\begin{aligned}
&\vec{k}_2 = \vec{k}+z\vec{\Delta}\,; \quad \vec{k}_3 = -\vec{k}+(1-z)\vec{\Delta} \\
\Rightarrow\ &(1-z)\vec{k}_2 - z\vec{k}_3 = \vec{k}\,; \quad (1-z)\vec{k}_2 + z\vec{k}_3 = (1-2z)\vec{k}+2z(1-z)\vec{\Delta}\,; \\
&(\vec{k}_2\vec{k}_3) = -\vec{k}^2+(1-2z)(\vec{k}\vec{\Delta})+z(1-z)\vec{\Delta}^2 \\
&M^2+\vec{\Delta}^2 = \frac{\vec{k}_2^2+m^2}{z}+\frac{\vec{k}_3^2+m^2}{(1-z)} = \frac{\vec{k}^2+m^2}{z(1-z)}+\vec{\Delta}^2\,.
\end{aligned} \tag{B.26}$$

For the longitudinal vector mesons one has for equal quark-antiquark helicities

$$\frac{\sqrt{z(1-z)}q_+}{z(1-z)q_+}\frac{1}{M}\cdot\left[-m\vec{\Delta}(\lambda)+m\frac{q_+}{q_+}[k_2(\lambda)+k_3(\lambda)]\right] = 0 \tag{B.27}$$

and for opposite helicities

$$\begin{aligned}
&\frac{\sqrt{z(1-z)}q_+}{z(1-z)q_+}\frac{1}{M}\Big\{-[(\vec{\Delta}\vec{k}_3)z+(\vec{\Delta}\vec{k}_2)(1-z)+i\lambda[\vec{\Delta}\vec{k}]]+\frac{q_+}{q_+}[-m^2+(\vec{k}_2\vec{k}_3)+i\lambda[\vec{k}_3\vec{k}_2]] \\
&+\frac{\vec{\Delta}^2-M^2}{s}p_-2z(1-z)q_+\Big\} \\
&= -\frac{1}{\sqrt{z(1-z)}}2z(1-z)M
\end{aligned} \tag{B.28}$$

B.3 Final trace calculation

Once we have the expressions for vertex amplitudes, the rest is done quickly. We first note that each gluon vertex attached to the lower or upper line gives factor

$$2zq_+\cdot p_- = sz\,; \quad 2(1-z)q_+\cdot p_- = s(1-z) \tag{B.29}$$

correspondingly.

So. let's start with $T \to T$ amplitude and calculate it for Diagr.(c) at Fig.5.2.

Equal $q\bar{q}$ helicities give

$$s(1-z)\cdot sz\cdot\frac{-1}{\sqrt{z(1-z)}}mV^*(\lambda)\frac{1}{\sqrt{z(1-z)}}me(-\lambda) = -s^2m^2e(-\lambda)V^*(\lambda) \tag{B.30}$$

Summing over λ gives

$$2s^2m^2(\vec{e}\vec{V}^*)\,. \tag{B.31}$$

The opposite helicities yield

$$s^2\left[(\vec{V}^*\vec{k})(1-2z)+i\lambda[\vec{V}^*\vec{k}]\right]\left[(\vec{e}\vec{k}_1)(1-2z)-i\lambda[\vec{e}\vec{k}_1]\right] \tag{B.32}$$

Summing over helicities and making use of identity

$$[\vec{a}\vec{b}][\vec{c}\vec{d}] = (\vec{a}\vec{c})(\vec{b}\vec{d})-(\vec{a}\vec{d})(\vec{b}\vec{c}) \tag{B.33}$$

one obtains

$$2s^2\left[(\vec{V}^*\vec{k})(\vec{e}\vec{k}_1)(1-2z)^2+(\vec{e}\vec{V}^*)(\vec{k}\vec{k}_1)-(\vec{e}\vec{k})(\vec{V}^*\vec{k}_1)\right]\,. \tag{B.34}$$

Since we factored out $2s^2$ when deriving (5.18), we finally get

$$I^{(c)}_{T\to T} = -\left[(\vec{e}\vec{V}^*)(m^2+\vec{k}\vec{k}_1)+(\vec{V}^*\vec{k})(\vec{e}\vec{k}_1)(1-2z)^2-(\vec{e}\vec{k})(\vec{V}^*\vec{k}_1)\right]\,. \tag{B.35}$$

We included factor (-1) since in this diagram we have one antiquark propagator.

An important observation here is that all other integrands, namely $I^{(a)}\cdot(1-z)/z$, $I^{(c)}$, $I^{(d)}\cdot z/(1-z)$ give absolutely the same result (with their own definitions of $\vec{k}_1$ of course). The only thing one should not forget is that diagrams (a,d) enter with sign '$-$' while diagrams (b,c) enter with sign '$+$':

$$-\frac{1-z}{z}I^{(a)} = I^{(b)} = I^{(c)} = -\frac{z}{1-z}I^{(d)}\,.$$

For $L \to L$ amplitude one has immediately

$$I^{(c)}_{L\to L} = -\frac{1}{Q}[m^2+\vec{k}_1^2-z(1-z)Q^2]\cdot\frac{1}{M}2z(1-z)M^2 \tag{B.36}$$

In fact, using simple relation

$$\frac{m^2+\vec{k}_1^2-z(1-z)Q^2}{m^2+\vec{k}_1^2+z(1-z)Q^2} = 1+\frac{-2z(1-z)Q^2}{m^2+\vec{k}_1^2+z(1-z)Q^2} \tag{B.37}$$

and noting that all unity terms will eventually cancel out in (5.24), one can rewrite (B.36) as

$$I^{(c)}_{L\to L} = -4QMz^2(1-z)^2\,. \tag{B.38}$$

For $T \to L$ amplitude one has

$$I^{(c)}_{T\to L} = 2z(1-z)M(\vec{e}\vec{k}_1)(1-2z) \tag{B.39}$$

and for $L \to T$ amplitude one has

$$I^{(c)}_{L\to T} = \frac{1}{Q}[m^2+\vec{k}_1^2-z(1-z)Q^2](1-2z)(\vec{V}^*\vec{k})\,. \tag{B.40}$$

The same transformation as in $L \to L$ amplitude, leads to

$$I^{(c)}_{L\to T} = -2z(1-z)Q^2(1-2z)(\vec{V}^*\vec{k})\,. \tag{B.41}$$

Note that in the last three amplitudes only opposite $q\bar{q}$ helicities contributed.

Bibliography

[1] N.N. Nikolaev and B.G. Zakharov, "Phenomenology of Diffractive DIS", Talk given at 5th International Workshop on Deep Inelastic Scattering and QCD (DIS 97), Chicago, IL, 14-18 Apr 1997, **hep-ph/9706343**.

[2] A.C. Irving, R.P. Worden, *Phys.Rept.* **34** (1977) 117-231.

[3] V.S. Fadin, E.A. Kuraev, L.N. Lipatov, *Phys.Lett.* **B 60** (1975) 60; E.A. Kuraev, L.N. Lipatov, V.S. Fadin, *Sov. Phys. JETP* **44**, (1976) 443; **72** (1977) 377; Ya.Ya. Balitskii, L.N.Lipatov, *Sov.J.Nucl.Phys.* **28** (1978) 822.

[4] L.N. Lipatov and V.S. Fadin, *JETP Lett.* **49** (1995); L.N. Lipatov, *Phys.Rept.* **286** (1997) 131-198.

[5] *for an introductory text see* E. Levin, *Heavy Ion Phys.* **8**:265-283,1998, hep-ph/9808483; E. Levin, *"The pomeron: yesterday, today and tomorrow"*, Lectures given at 3rd Gleb Wataghin School on High Energy Phenomenology, Campinas, Brazil, 11-16 Jul 1994, **hep-ph/9503399**

[6] D.Yu. Ivanov, R. Kirschner, *Phys.Rev.* **D58** (1998),114026.

[7] E.V. Kuraev, N.N. Nikolaev, and B.G. Zakharov, *JETF Lett.* 68(1998) 667.

[8] N.N. Nikolaev, *Comments on Nucl.Part.Phys.* **21** (1992) 41; B.Z. Kopeliovich, J. Nemchik, N.N. Nikolaev and B.G. Zakharov, *Phys. Lett.* **B 309** (1993) 179; *Phys. Lett.* **B 324** (1994) 469.

[9] D.Yu. Ivanov, *Phys. Rev.* **D 53** (1996) 3564; I. Ginzburg, S. Panfil and V. Serbo, *Nucl. Phys.* **B 284** (1987) 685; **B 296** (1988) 569.

[10] K. Schilling, G. Wolf, *Nucl.Phys.* **B 61**(1973) 381.

[11] J. Nemchik, N.N. Nikolaev and B.G. Zakharov, *Phys. Lett.* **B339** (1994) 194-200.

[12] D.O. Riska, *Acta Phys.Polon.* **B29** (1998) 2389.

[13] I.P. Ivanov, N.N. Nikolaev, *Pis'ma ZhETF (JETP Lett.)* **69** (1999) 268.

[14] I.P.Ivanov, N.N.Nikolaev, *Phys Rev.* **D65** (2002) 054004.

[15] I.P.Ivanov and N.N.Nikolaev, *"Improved determination of the differential gluon structure function of the proton"*; I.P. Ivanov and N.N. Nikolaev, *"Vector meson production in the k_t-factorization approach"*; I.P. Ivanov and N.N. Nikolaev, *"The effects of Coulomb tail on the vector meson production"*; I.P. Ivanov and N.N. Nikolaev, *"S/D wave mixing in vector mesons and its impact on diffractive vector meson production"*; all works in progress.

[16] I.P. Ivanov and N.N. Nikolaev, Talk given at 8th International Workshop on Deep Inelastic Scattering and QCD (DIS 2000), Liverpool, England, 25-30 Apr 2000. Published in "Liverpool 2000, Deep inelastic scattering", 119-120, hep-ph/0006100.

[17] I.P. Ivanov and N.N. Nikolaev, Talk given at Low-x Workshop, Krakow, Poland, 27-30 June 2001.

[18] V.N. Gribov and L.N. Lipatov, *Sov. J. Nucl. Phys.* **15** (1972) 438; L.N. Lipatov, *Sov. J. Nucl. Phys.* **20** (1974) 181; Yu.L. Dokshitser, *Sov. Phys. JETP* **46** (1977) 641; G. Altarelli and G. Parisi, *Nucl. Phys.* **B126** (1977) 298, for the review see R.G.Roberts, The structure of the proton. (Cambridge Univ. Press, 1990).

[19] V.S.Fadin, E.A.Kuraev and L.N.Lipatov *Phys. Lett.* **B60**, 50 (1975); E.A.Kuraev, L.N.Lipatov and V.S.Fadin, *Sov.Phys. JETP* **44**, 443 (1976); **45**, 199 (1977).

[20] J.Nemchik, N.N.Nikolaev, E.Predazzi and B.G.Zakharov, *Phys. Lett.* **B374** (1996) 199.

[21] V.M. Budnev, I.F. Ginzburg, G.V. Meledin and V.G. Serbo, *Phys. Rept.* **15**, 181 (1974)

[22] N.N. Nikolaev, B.G. Zakharov, V.R. Zoller, *JETP* **105** (1994) 1498.

[23] N.N.Nikolaev and B.G.Zakharov, *Phys. Lett.* **B327** (1994) 157.

[24] M.V. Terentev, *Sov. J. Nucl. Phys.* **24** (1976) 106; **Yad. Fiz. 24** (1976) 207; V.B. Berestetskii and M.V. Terentev, **Yad. Fiz. 25** (1977) 653; L.A. Kondratyuk and M.V. Terentev, *Sov. J. Nucl. Phys.* **31** (1980) 561; **Yad. Fiz. 31** (1980) 1087.

[25] J. Bjorken, J. Kogut, D. Soper, *Phys. Rev.* **D 3**(1971) 1382; G.P. Lepage, S.J. Brodsky, *Phys. Rev.* **D 22**(1980) 2157; S. Brodsky, H.-Ch. Pauli, S. Pinsky, *Phys. Rept.* **301**, (1998), 299-486; T. Heinzl, **hep-th/9812190**, 1998.

[26] V.V. Sudakov, *Sov.Phys.JETP* **3**, 65 (1956)/*Zh.Eksp.Teor.Fiz.* **30**, 87 (1956).

[27] V.V. Anisovich *et al.*, *Nucl. Phys.* **A 563** (1993) 549–583; W. Jaus, *Phys. Rev.* **D 41**(1990) 3394; *Phys. Rev.* **D 44**(1990) 2851.

[28] A.V. Radyushkin, *Phys.Rev.* **D56**, 5524 (1997).

[29] A.G. Shuvaev, K.J. Golec-Biernat, A.D. Martin, M.G. Ryskin, *Phys.Rev.* **D60**, 014015 (1999).

[30] Ya.Ya.Balitskii and L.N.Lipatov, *Sov. J. Nucl. Phys.* **28** (1978) 822

[31] N.N.Nikolaev and B.G.Zakharov and V.R.Zoller, *JETP Letters* **59**, 8 (1994)

[32] N.N.Nikolaev and B.G.Zakharov, *JETP* **78** (1994) 598; *Z. Phys.* **C64** (1994)631.

[33] A.H. Mueller and B. Patel, *Nucl. Phys.* **B425** (1994) 471

[34] N.Nikolaev and B.G.Zakharov, *Phys. Lett.* **B332** (1994) 177; *Z. Phys.* **C53** (1992) 331.

[35] N.N. Nikolaev, A.V. Pronyaev and B.G. Zakharov, *Phys. Rev.* **D59** 091501 (1999)

[36] M. Bertini, M. Genovese, N.N. Nikolaev, A.V. Pronyaev and B.G. Zakharov, *Phys. Lett.* **B422**, 238 (1998)

[37] E.V.Kuraev, N.N.Nikolaev, and B.G.Zakharov, *JETF Lett.* 68(1998) 667; I.P.Ivanov, N.N.Nikolaev, *Pis'ma ZhETF (JETP Lett.)* **69** (1999) 268

[38] J. Nemchik, N.N. Nikolaev, E. Predazzi, B.G. Zakharov and V.R. Zoller, *J. Exp. Theor. Phys.* **86**, 1054 (1998)

[39] N.N. Nikolaev, in: Hamburg 1998/1999, Monte Carlo generators for HERA physics, pp. 377-381; *hep-ph/9905562.*

[40] S.P. Baranov and N.P. Zotov, *Phys. Lett. B458* (1999) 389; M.G. Ryskin, A.G. Shuvaev and Yu.M. Shabelski, *Phys.Atom.Nucl.* **64**, 1995 (2001)/ *Yad.Fiz.* **64**, 2080 (2001)

[41] J.R Forshaw and R.G. Roberts, *Phys. Lett.* **B335** (1994) 494; A.J. Askew, D. Graudenz, J. Kwiecinski and A.D. Martin, *Phys. Lett.* **B338** (1994) 92.

[42] J. Kwiecinski, A.D. Martin and A.M. Stasto, **B459** (1999) 644.

[43] M. Glueck, E. Reya, A. Vogt, *Eur.Phys.J.* **C5**, 461 (1998)

[44] H.L. Lai, W.K. Tung, *Z.Phys.* **C74**, 463 (1997)

[45] A.D. Martin, R.G. Roberts, W.J. Stirling, R.S. Thorne, *Phys.Lett.* **B443**, 301 (1998)

[46] V. Barone, C. Pascaud and F. Zomer, *Eur. Phys. J.* **C12**, 243 (2000)

[47] N.N. Nikolaev and V.R. Zoller, *JETP Lett.* **69**, 103 (1999); E. Gotsman, E. Levin, U. Maor and E. Naftali, *Nucl. Phys.* **B539**, 535 (1999)

[48] H. Abramowicz and A. Caldwell, *Rev. Mod. Phys.* **71**, 1275 (1999); ZEUS Collab., J. Breitweg et al., *Eur. Phys. J.* **C7**, 609 (1999).

[49] E.M. Levin, M.G. Ryskin, Yu.M. Shabelski and A.G. Shuvaev, *Sov. J. Nucl. Phys.* **54** (1991) 867; S. Catani, M. Ciafaloni and F. Hautmann, *Nucl. Phys.* **B366** (1991) 135; S. Catani and F. Hautmann, *Nucl. Phys.* **B427** (1994) 475; J.C. Collins and R.K. Ellis, *Nucl. Phys.* **B360** (1991) 3.

[50] N.N. Nikolaev, B.G. Zakharov, *Phys. Lett.* **B327** (1994) 157.

[51] N.N. Nikolaev, B.G. Zakharov, V.R. Zoller, *JETP Letters* **66** (1997) 138; N.N. Nikolaev, J. Speth and V.R. Zoller, *Phys. Lett.* **B473** (2000) 157.

[52] N.N.Nikolaev and B.G.Zakharov, *Phys. Lett.* **B332** (1994) 184.

[53] V.Barone, M.Genovese, N.N.Nikolaev, E.Predazzi and B.G.Zakharov, *Phys.Lett.* **B326** (1994) 161.

[54] J.Nemchik, N.N.Nikolaev, E.Predazzi and B.G.Zakharov, *Z. Phys.* **C75** (1997) 71.

[55] E. Meggiolaro, *Phys.Lett.* **B451** (1999) 414

[56] N.N. Nikolaev and B.G. Zakharov, *Z. Phys.* **C49** (1991) 607.

[57] V.N. Gribov, *Eur. Phys. J.* **C10** (1999) 71; D.V. Shirkov, *Phys. Atom. Nucl.* **62** (1999) 1928; Yu.L. Dokshitzer, G. Marchesini and B.R. Webber, *JHEP* **07** (1999) 012;

[58] P.V.Landshoff and O.Nachtmann, *Z. Phys.* **C35** (1987) 405; H.G.Dosch, T.Gousset, G.Kulzinger and H.J.Pirner *Phys. Rev.* **D55** (1997) 2602.

[59] A. Donnachie and P.V. Landshoff, *Phys.Lett.* **B437** (1998) 408

[60] ZEUS coll., M. Derrick et al., Z. Phys. **C72** (1996) 399.

[61] ZEUS coll., J. Breitweg et al., Eur.Phys.J. **C7** (1999) 609.

[62] ZEUS coll., J. Breitweg et al., Phys. Lett. **B407** (1997) 432.

[63] H1 coll., S. Aid et al., Nucl. Phys. **B470** (1996) 3.

[64] H1 coll., C. Adloff et al., Nucl. Phys. **B497** (1996) 3.

[65] E665 coll., M.R. Adams et al., Phys. Rev. **D54** (1996) 3006.

[66] NMC coll., M. Arneodo et al., Nucl. Phys. **B483** (1997) 3.

[67] J.Nemchik, N.N. Nikolaev and B.G. Zakharov, *Phys. Lett.* **B341** (1994) 228

[68] J. Kwiecinski, A.D. Martin and A.M. Stasto, *Phys.Rev.* **D56** (1997) 3991.

[69] ZEUS Collab., J.Breitweg et al., Eur. Phys. J.**C 12** (2000) 35.

[70] ZEUS Coll., *Phys.Lett.* **B487**, 52 (2000).

[71] ZEUS Coll., *Eur.Phys.J.* **C21**, 443 (2001).

[72] H1 Coll., *Eur.Phys.J.* **C21**, 33 (2001).

[73] H1 Coll., *Phys.Lett.* **B520**, 183 (2001).

[74] H1 Coll., *Nucl.Phys.* **B463**, 3 (1996).

[75] ZEUS Coll., *Z.Phys.* **C73**, 253 (1997).

[76] H1 Coll., *Eur.Phys.J.* **C13**, 371 (2000).

[77] ZEUS Coll., *Eur.Phys.J.* **C6**, 603 (1999).

[78] H1 Coll., *Phys.Lett.* **B483**, 360 (1996).

[79] ZEUS Coll., *Phys.Lett.* **B377**, 259 (1996).

[80] ZEUS Coll., *Phys.Lett.* **B380**, 220 (1996).

[81] H1 Coll., *Phys.Lett.* **B483**, 23 (2000).

[82] H1 Coll., *Nucl.Phys.* **B468**, 3 (1996).

[83] ZEUS Coll., *Z.Phys.* **C75**, 215 (1997).

[84] ZEUS Coll., *Phys.Lett.* **B437**, 432 (1998).

[85] B. Clerbaux, talk given at Workshop on Low-x Physics, June 1999, Tel-Aviv, Israel; *hep-ph/9908519*.

[86] ZEUS Coll., *Eur.Phys.J.* **C12**, 393 (2000).

[87] H1 Coll., *Phys.Lett.* **B421**, 385 (1998).

[88] H1 Coll., *Eur.Phys.J.* **C10**, 373 (1998).

[89] V.A. Novikov, L.B. Okun, M.A. Shifman, A.I. Vainshtein, M.B. Voloshin, V.I. Zakharov, *Phys.Rept.* **41**, 1-133 (1978).

Acknowledgements

It is an honor for me to thank Prof. J.Speth for his perpetual desire to see me as a member of Jülich theory group and for making my entire stay at Forschungszentrum so comfortable and scientifically fruitful.

Million of thanks must undoubtedly go to Kolya Nikolaev for pulling me in the midst of his turbulent scientific activity and making me immediately start contributing, for infecting me with his desire to look for a clear physical meaning behind every formula, and for innumerable discussion we have had during these years.

I want to thank all my colleagues at IKP and in Novosibirsk, in particularly, Ilya Ginzburg, who discussed with me details of my work, or just listened to what I've been saying.

I wish to thank all members of the wonderful company that grew up in Jülich — Vadim, Achot, Pasha, Fedya, Dmitro, Lena, Tanya and many others. Thanks for all those parties and journeys together!

Anuta! Thanks to you too! For your continuous and many-sided help and support. Well, most of time it actually looked rather like distracting from studies than supporting them, but thanks anyway! Without relaxing at home, I would get completely crazy with all these vector mesons!

Finally, I want to collectively thank all those people who have helped me in various ways during my work, but whom I failed to recollect in this acknoledgement due to my innate forgetfulness.